ISSN 1349-113X
JAXA-SP-07-030
宇宙航空研究開発機構特別資料

第4回「宇宙環境シンポジウム」講演論文集

Proceedings of the 4th Spacecraft Environment Symposium

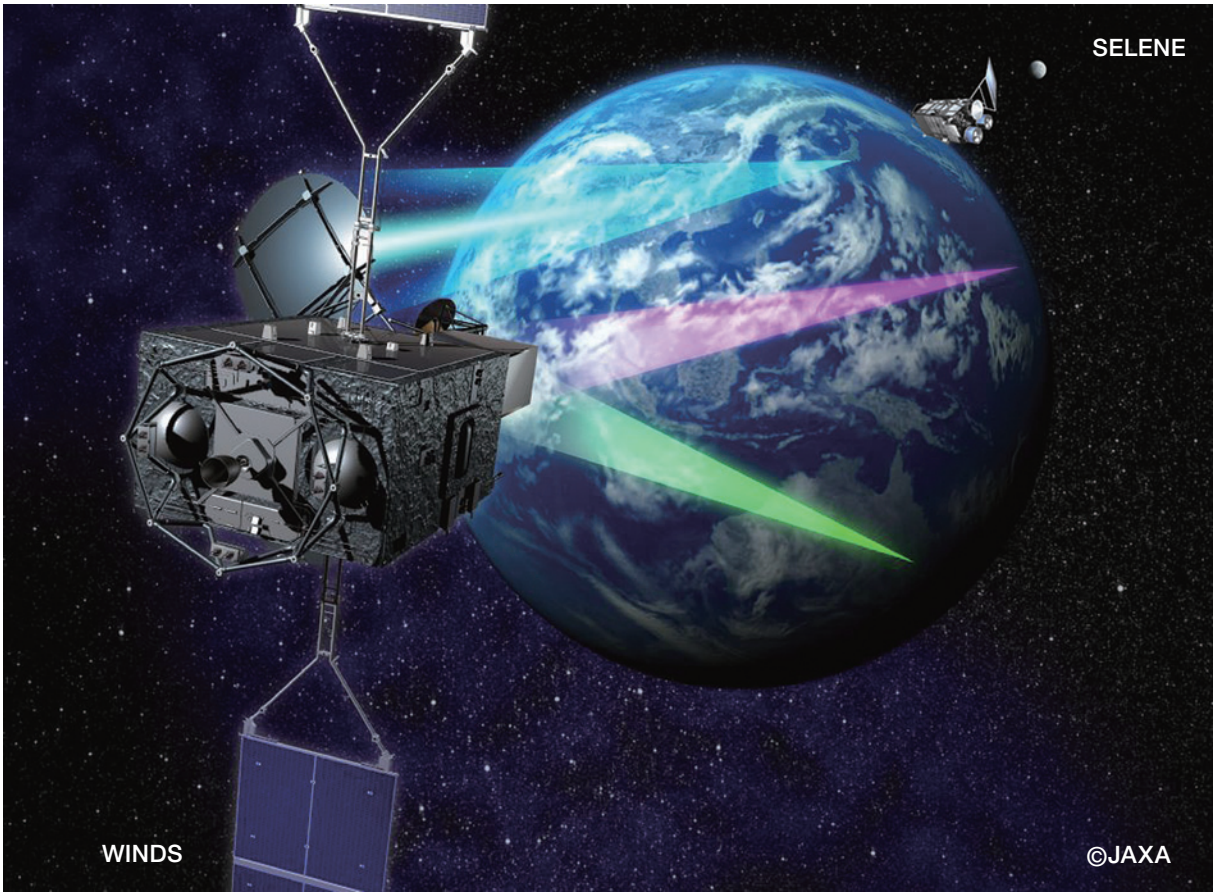

2008年1月22日、23日
日本科学未来館

宇宙航空研究開発機構
総合技術研究本部　環境計測グループ
Japan Aerospace Exploration Agency

JAXA-SP-07-030

宇宙航空研究開発機構特別資料
JAXA Special Publication

第4回「宇宙環境シンポジウム」講演論文集

Proceedings of the 4th Spacecraft Environment Symposium

作成元　総合技術研究本部 環境計測グループ

Prepared by
Space Environment Measurement Group
Institute of Aerospace Technology

2008年3月
March 2008

宇宙航空研究開発機構
Japan Aerospace Exploration Agency

目　次

帯電･放電

Charging & Discharging

－ＭＥＭＯ－

特集－世界の宇宙環境の研究最前線－

Special Session

Effects of Low Temperature on Charging of Spacecraft Dielectrics

Dale C. Ferguson, Todd A. Schneider, and Jason A. Vaughn
NASA / JPL
dale.c.ferguson@nasa.gov

Abstract

Spacecraft dielectric charging, sometimes called deep-dielectric-charging or bulk-charging, occurs when high energy electrons imbed themselves in dielectric materials, and the charge density builds up, sometimes to breakdown levels. Charges usually bleed off slowly due to material conductivity. At very low (cryogenic) temperatures, the dielectric conductivity decreases until charges may reamin and build up over weeks, months, or years. In those cases, the guidelines given in NASA and industry documents for when dielectric charging may become important are misleading. Arcing tests of spacecraft cables at liquid nitrogen temperatures and very low flux levels have been done at NASA MSFC for the JWST Project. In this paper, we describe the results of those tests and analyze their important implications for cryogenic spacecraft cable design and construction.

Visualizing Root Causes for Satellite Anomalies, Spacecraft Charging, and Mitigation Methods to Prevent ESD

Richard Briet
Aerospace Corp.
2350 East El Segundo Blud. USA
E-mail: richard.briet@aero.org

The contents of the presentation are:

1) There is a strong correlation between on-orbit anomalies and meteor showers
2) It is certain that some process is responsible for on-orbit anomalies during meteor showers
3) Micrometeoroid Impacts is a Possible Root Cause for on-orbit satellite anomalies: This is an unproven hypothesis that must still be proven.
4) Spacecraft Charging leading up to ESD is a Possible Root Cause for on-orbit anomalies Spacecraft Charging is better understood, it is predictable, and therefore controllable
5) Conventional spacecraft charging mitigation can be improved upon: "Best Grounding Methods" may not be "Good enough!"
6) Simple Circuit Models that some people use to analyze and assess spacecraft charging concerns lead to false conclusions

'Spacecraft Plasma Interaction eXperiment in India - an Introduction'

SURESH E.PUTHANVEETTIL[1*], S. MUKHERJEE[2], S.P. DESHPANDE[2], BHOOMI MEHTA[2], M. RANJAN[2], N. VAGHELA[2], R.S. RANE[2], V. ACHARYA[2], R.BANDYOPADHYAY[2], B.R.UMA[1], M. SANKARAN[1], M. SUDHAKAR[1]

[1]ISRO Satellite Center, Bangalore 560 017 (INDIA)
[2]Institute for Plasma Research, Gandhinagar, Gujarat (INDIA)
[*]Email: eps@isac.gov.in

ABSTRACT:
Possibility of arcing in high voltage arrays have necessitated the theoretical and experimental study of charging and arcing by Indian Space research Organisation (ISRO), which is planning to increase the satellite bus voltage above the current level of 42 volt. The study, named Spacecraft Plasma Interaction eXperiment (SPIX) was undertaken, together with Institute for Plasma Research (IPR), India to (i) develop software, which is able to predict the floating potential of an object of simplified geometry in space plasma typically of geosynchronous bimaxwellian type, which is also able to calculate the differential potential between two such objects, (ii) to develop software to solve the differential equations describing primary arcing phenomena developed by Cho, a pioneer in the field [1], (iii) to study the primary arcing threshold and frequency and to identify the arcing sites of a solar array coupon immersed in a LEO like laboratory plasma and to (iv) find out the arcing threshold of sustained arcs by introducing a solar array simulator voltage between adjacent strings in a solar array coupon immersed in a LEO-like plasma environment. The experiments have largely yielded results akin to that of other investigators, although some differences have been observed in some experiments. A short term future aim would be to increase the sample space in the last type of experiments mentioned above.

1. INTRODUCTION

Indian Space Research Organisation (ISRO), the primary agency doing space related work in India, has made arrays of up to 6kW and successfully flown them. Conventionally, ISRO has the 42 volt array. Higher power requirements and some specific payload constraints have necessitated the development of high voltage array. Since high voltage arrays are much more likely to arc and get destroyed compared to those operating at lower voltages in the presence of space plasma, a study project was undertaken, which has been named SPIX, an acronym for Spacecraft Plasma Interaction eXperiment. This project was executed jointly by ISRO and Institute for Plasma Research, Gandhinagar, Gujarat, India. The project had elements of theoretical and modeling work and experimental study. The theoretical study was aimed at calculating the potential of a conducting body of simple geometry in space plasma as well as finding the potential difference between a conductor and a tiny patch of dielectric present on its surface. This was aimed at arriving at a simple but reasonably accurate model of the potential

difference that is found between the metallic and insulating parts of the solar array, the latter typified by, for example, the coverglass of the solar cell. Another aim was to find a simple way of solving the differential equations developed by Cho [1], which relates the shapes of the oscilloscope traces of the primary arcs to the electrical parameters that make up the solar cell coupon, thereby gaining a deeper understanding of the arcing phenomenon. The experimental study was aimed at studying the primary and secondary arcing thresholds and their relation to the coupon configuration and identification of the arcing sites so as to arrive at mitigating techniques.

2. CHARGING AND ARCING CODES

The charging code calculates the floating potential of a spherical conductor placed in the geosynchronous orbit plasma. The plasma parameters which can be given as input are either single or double maxwellian. The currents to and from the conductor considered by the software are:

1. Flux due to ambient electrons
2. Flux due to ambient ions
3. Emission of secondary electrons due to the electron impact
4. Backscattering of electrons
5. Emission of ion-induced secondary electrons and
6. Emission of photo-electrons due to UV radiation.

The other currents are neglected as their contributions in a realistic case are negligible. In the equilibrium condition the total current to the body is zero. The voltage at which this happens is the floating potential. All except the first two among the above are strong functions of the material and different formulas like Whipple-Dionne formula are used to calculate these currents.

The potential difference between two adjacent materials: one -a conductor and another- a dielectric is calculated by another module. This is done by a ‘patch-on-sphere’ code where the geometry is very much simplified. The dielectric is a very small patch on the conductor. A small leakage current goes from the dielectric to the conductor. This gives a different equilibrium potential for the dielectric. The results of the code have been compared against the European SPENVIS code and are in good agreement [2].

We have used the circuit model for the primary arcs from [1] and we have solved the circuit equations using Scilab routines unlike the author himself who had used Laplace transforms to do the same. We feel that this is an easier and simpler way. Our results, naturally, are the same.

3. EXPERIMENTAL SET-UP

In the experimental setup, test solar array coupons were exposed to plasma interaction experiments. These experiments were performed to develop LEO like condition in the laboratory. Plasma of density ~ $1x10^{12}m^{-3}$ was obtained using argon gas. This was developed in the test chamber of size 1 m in length and 1 m in diameter. The chamber could be opened at both ends, with dome shaped end flanges having view ports and access ports for various diagnostics. The chamber was evacuated by a diffusion pump with pumping speed of 3000 l/s backed by rotary pump. The chamber was cooled by

copper tubes brazed on the outer surface. The solar panel coupons (300 mm x 300 mm) were mounted on insulating supports, facing towards the view ports. Position of the coupon was such that it could be focused completely from one of the view ports using a CCD camera. The ends of the solar cells were connected with insulating cables to high voltage vacuum compatible feed-throughs.

Experiments were carried out in what we denote as Cho's configuration [1] and NASA configuration [3]. Cho's configuration corresponds to the set up where the feed-throughs were shorted and were connected to an external capacitor (0 or 33 pF), which in turn was connected to an external power supply (0 to -600 V) through a variable resistance (1 – 200 kilo ohm). The solar cell arrays in this case could be biased from -300 V to -600 V. NASA configuration corresponds to the case where, in addition to the above, a solar array simulator voltage is introduced between two adjacent strings. (Fig 1) The former configuration is designed to study the primary arcing phenomena and the latter to study secondary arcs. The pulsed arc current was measured with two current transformers CT-1 (having response of 1.0V/A) and CT-2 (having response of 1.0 V/A). A Tektronix make (Model no: P6015A) 1000 X HV probe was used to monitor the applied voltage wave form on oscilloscope. A 350 MHz digital oscilloscope with 1 Gb/s sampling rate was used for fast data acquisition during arcing event. The output of 1000 X HV probe, CT-1 and CT-2 are connected to different channels of the oscilloscope. After pumping the chamber to the base pressure, argon gas was introduced to the operating pressure of 5 x 10^{-5} mbar. Thoriated tungsten filaments were heated to emit primary electrons which were accelerated to impact-ionize the background gas to form plasma. The plasma density was measured using Langmuir probes. The plasma density was controlled by controlling the total discharge power.

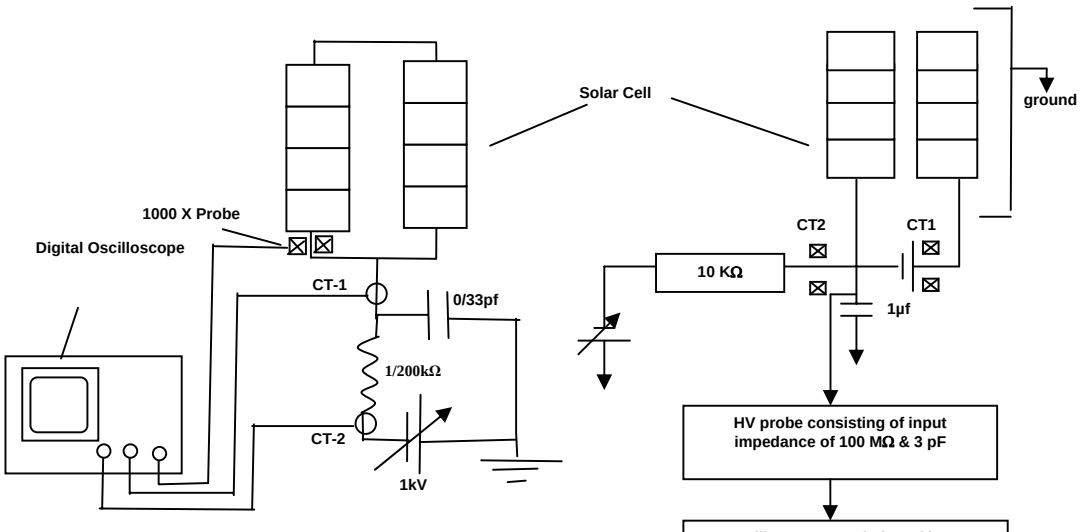

▪ **Cho's configuration: Both terminals of solar panel coupons are shorted and negatively biased.**

▪ **NASA configuration: A potential is applied between to solar cell to simulate actual conditions.**

Figure 1: Schematic diagram of the circuits used.

4. RESULTS AND DISCUSSION

In Cho's configuration we found that the number of primary arcs is least for GaAs cells rather than Si or multijunction cells. This may be because GaAs cells which we have used have smaller area. It was also found that grouting reduces the number of primary arcs. We have two types of grouting – partial and full. In the first one all portions except the coverglass and interconnect are immersed in RTV adhesive. In the second case, even the interconnect is immersed in adhesive. We found that even partial grouting helps reduce the number of primary arcs and with full grouting the numbers of arcs are even lower. Even without grouting also, the number of arcs we observed was less than that in [1]. This is very surprising to us.

We have done some preliminary studies in NASA configuration but the sample space is not high. Here we found that the no arcing occurs in any coupon ever below 20VA. With higher gap less number of major arcs occurred with same capacitor and current limit values. With large value of external capacitor and low value of current limit, there may be more chances of major or sustained arcs. The probable reason is that large value of capacitor charges more and at the time of arc it gives more charge/current to the circuit and in this condition low value current limit is not effective. No major arc was observed even after removing current limit from fully grouted coupon with triple junction cells up to 100V. So full grouting is a better option rather than increasing the string gaps from the point of view of preventing major arcs. However, the grouting should not stress the interconnects during temperature cycling and it should not peel off due to the space environment. More experiments needs to be done before we finalize on our option.

5.ACKNOWLEDGEMENT

The authors are grateful to the Director, Deputy Director (IPA), Group Director (PSG) of ISRO Satellite Center for their constant encouragement and support to this investigation and permission to present this work. The authors are also grateful to the Director, Institute for Plasma Research for unfailing support.

6 BIBLIOGRAPHY

[1] Mengu Cho, 'Arcing on High Voltage Solar Arrays in Low Earth Orbit: Theory and Computer Particle Simulation', Ph.D. Thesis (1992).
[2] www.spenvis.oma.be
[3] David B. Snyder, Dale C. Ferguson, Boris V. Vayner and Joel T. Galofaro, 'New Spacecraft-Charging Solar Array Failure Mechanism', 6th Spacecraft Charging Technology conference, September 2000

ARCING ON SOLAR ARRAY SURFACES: GROUND TESTS

Boris VAYNER
Ohio Aerospace Institute, Cleveland, OH 44142, USA

Joel GALOFARO
NASA Glenn Research Center, Cleveland, OH 44135, USA

OUTLINE

- Historical overview
- NASA Glenn: Chambers and Coupons
- Trigger arcs
  a) inception on different samples;
  b) optical spectra;
- Sustained arcs
  a) inception
  b) assessment of damage.
- Prevention vs. Statistics
- Conclusions

History

1968, *R. Cole et al, NASA CR-72376 (ESD on GEO sat.)*
1978, *N. Stevens, NASA CP-2071 (basic ground tests)*
1984, *C. Purvis et al, NASA Guidelines*
1985, *D. Snyder & E. Tyree, NASA TM 86887 (scaling)*
1989, *D. Ferguson, SOAR 89 (threshold)*
1990-1993, *D. Hastings et al, M. Cho & D. Hastings, R. Mong & D. Hastings – series of publications in JSR- theory of inception*
1996 *B. Kaufman et al., NASA TM 3635, ISS Panel under UV and LEO Plasma, 400 cells (8x8 sq.cm.) GRC Tank 5*
1997 *Failure of SS/LORAL SC- Sustained discharge, I.Katz suggested test at NASA Glenn (D.Snyder et al., 6th SCTC) C.Hoeber et al, AIAA Paper 98-1401*
1998 *D. Ferguson et al., Inception of Snapover, AIAA Paper 98-1045*
2001 *B.Vayner et al., Optical Spectra, 7th SCTC*
2004 *B.Vayner et al., Large Array in Plume Plasma, 6th FLTPD*
2005 *J. Galofaro et al, Thin Film Array in LEO Plasma, 4th WCPEC*

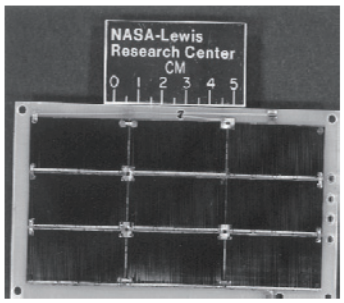

Bell Jar, D=0.6 m, H=1 m

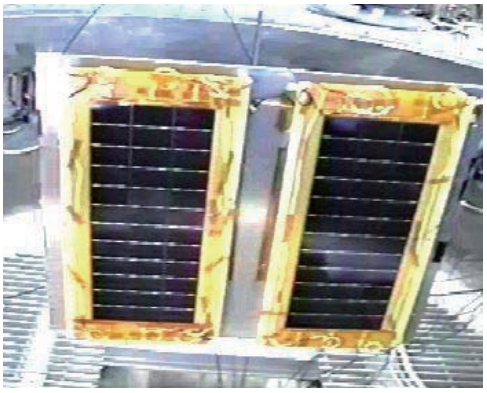

Vertical Tank, D=2 m, H=3 m

Horizontal Tank, D=2 m, L=2 m

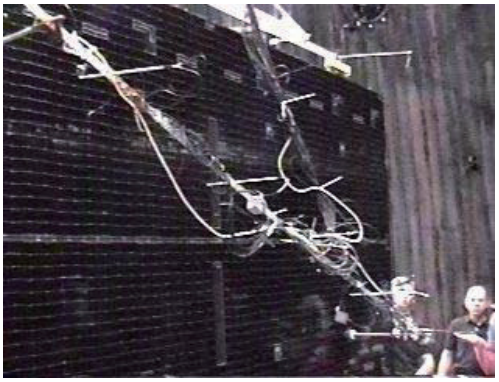

Vertical Tank B-2, D=12 m, H=18 m

National Aeronautics and Space Administration

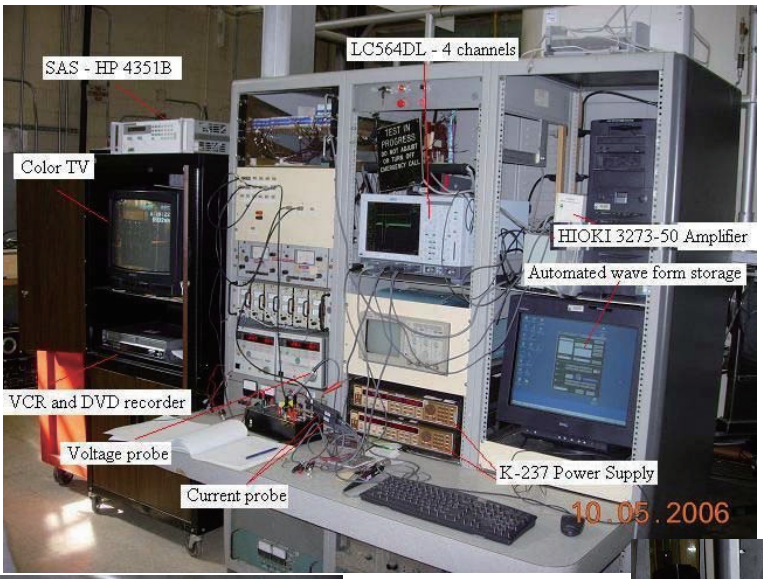

RGA

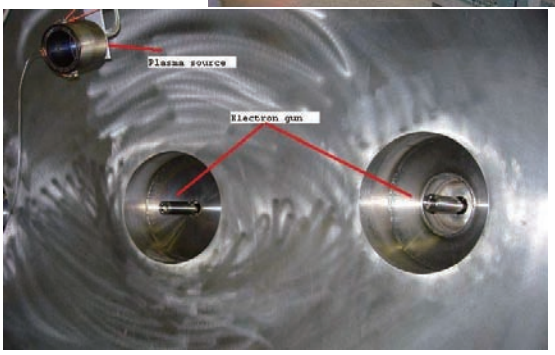

National Aeronautics and Space Administration

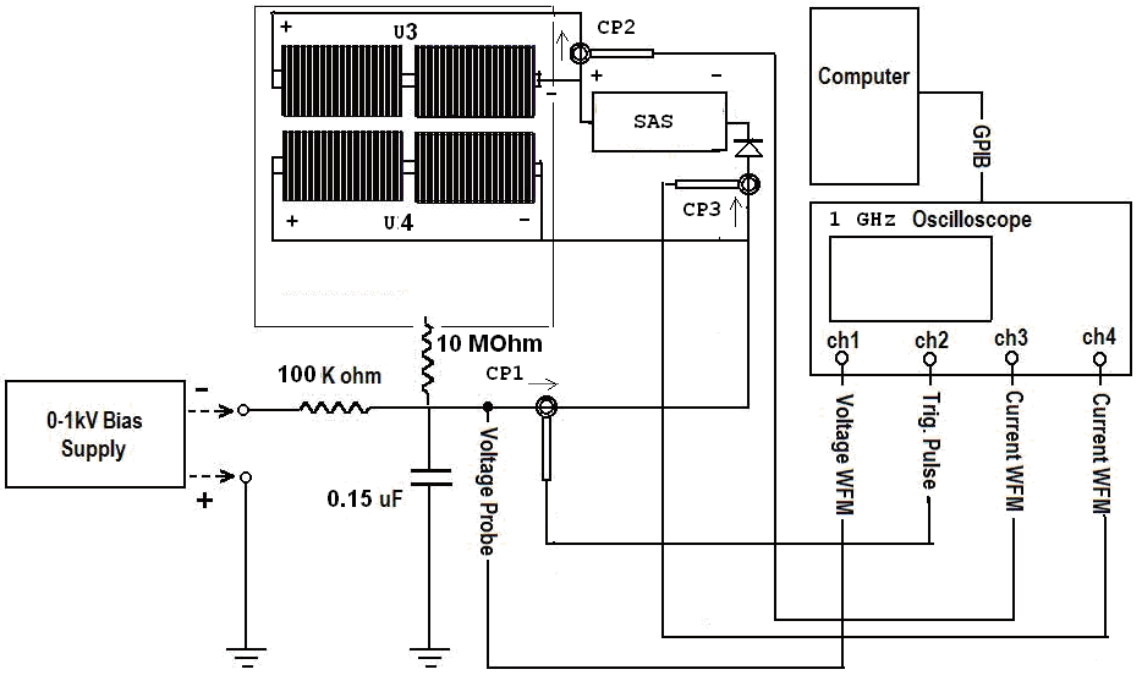

Circuitry diagram for arc parameter measurements (diode 1N4723).

Cabling and setup see: *D. Ferguson et al., NASA Testing Procedures, 9th SCTC*

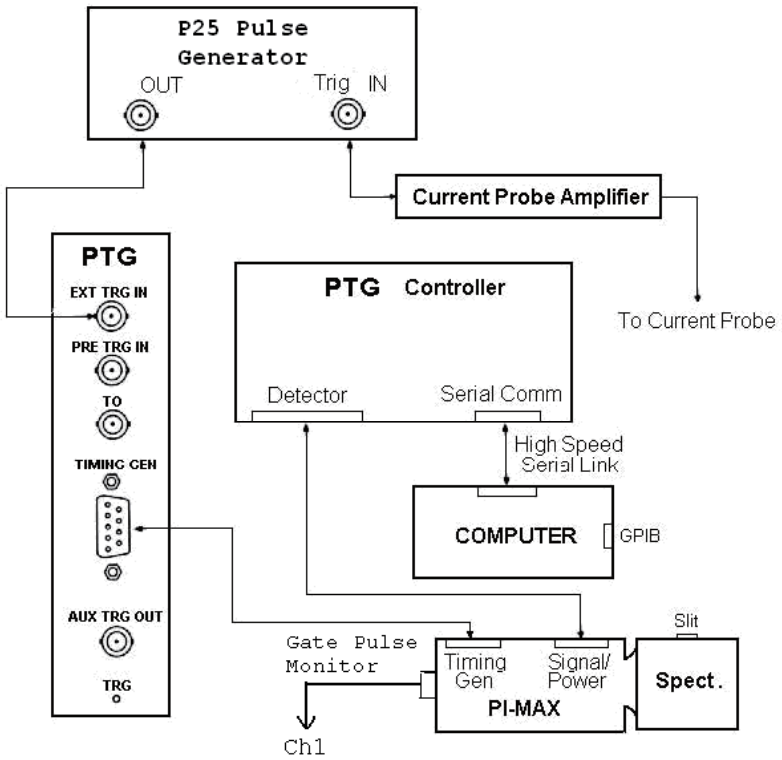

Diagram showing the experimental setup used for obtaining individual arc spectra

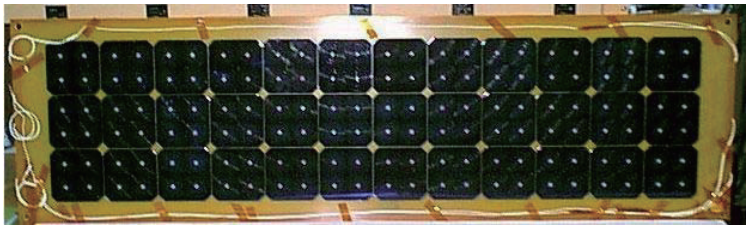

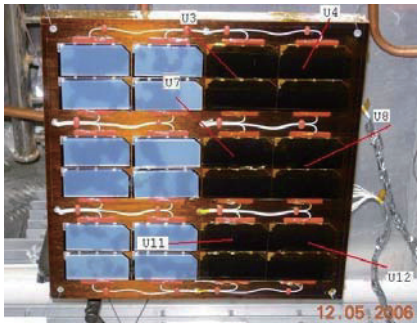

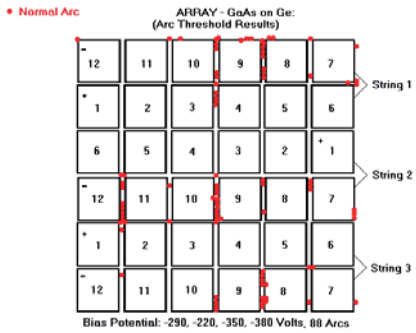

Fig.4. SAS is off. Most arcs occured on interconnects.

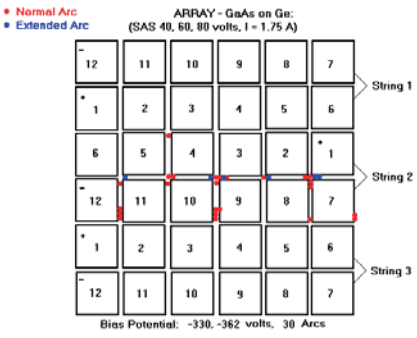

Fig. 5. Arcs occure between cells due to SAS voltage

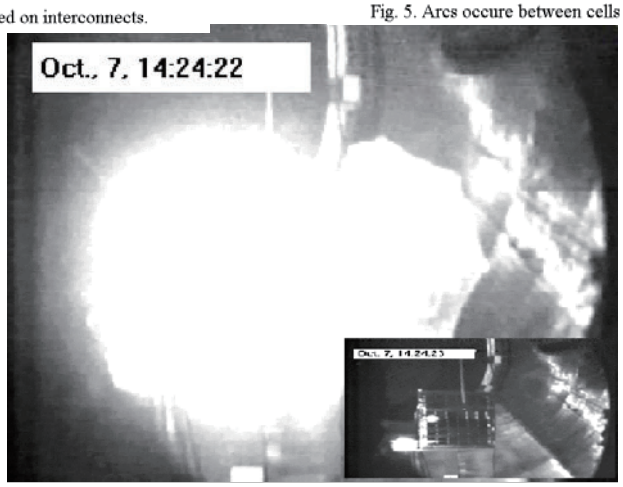

Fig.3. Sustained arc on GaAs array. Bias voltage –350 V, SAS voltage 80 V, SAS current limit 2.25 A.

Table 1. Seven types of solar array samples tested in two large chambers.

Sample No.(Type)	Coverglass Thickness (µm): Material	Overhang (µm)	Cell size (cm)	Interconnect	Mfg.
1(Si)	300 UVR	0	4x6	exposed	Tecstar
2(Si)	150 UVR	0	4x6	exposed	
3(Si)	150 CMX UVR	0	4x6	exposed	
4(Si)	150 UVR	250	4x6	exposed	
5(Si)	150 UVR	0	8x8	wraptrough	
6(TJ)	150 UVR	0	4x6	exposed	SS/Loral
7(TJ)	150 UVR	0	4x6	exposed	Toshiba

Table 2. Arc inception parameters.

Sample No.	Primary Arc InceptionV	Sustained Arc Inception V	A
1	250	60	2.0
2	265	80	1.6
3	280		
4	340		
5	300(530)	>120	>4
6	170	80	2.25
7	200	50	2.0
		50	2.6

Catastrophic damage due to sustained arcs

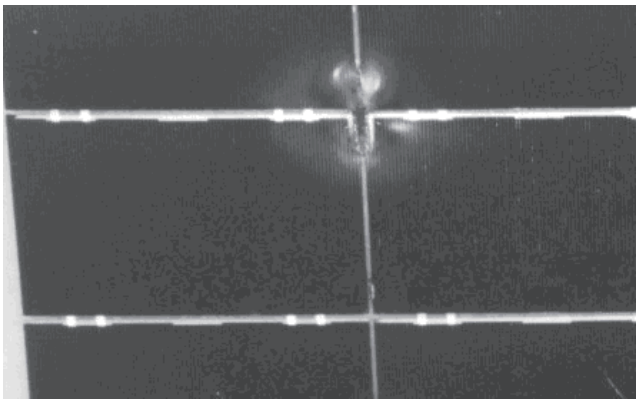

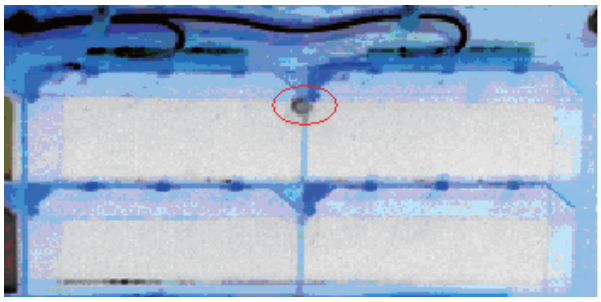

Preventing sustained arcs:

1) Prevent primary ESD

2),3) *Statistics and so on - Possible but risky*.

See: D. Ferguson et al., NASA GUIDELINES

Optical Spectra

Motivation: 1) to determine atomic (molecular) species involved;
2) to elucidate difference between vacuum arc and ESD on triple junction;
3)to advance our understanding of ESD inception.

History: ***1994, B.L. Upschulte et al, JSR, Vol.31, p.493*** **–** established correlation between bolometric luminosity and arc current temporal behaviors, identified silver spectral lines, and suggested the possibility of molecular emission patterns.

2002, E. Amorim et al, J.Phys.D:Appl.Phys., Vol.35, p.L21 –identified atomic metal spectral lines, and stressed commonality between vacuum arc and ESD on triple junction. H_α was also observed but not discussed.

2002, B.Vayner et al, AIAA Paper 2002- 0631 – identified atomic and ion metal spectral lines, molecular and radical lines and bands including hydroxyl.

Influence of adsorbed water vapor on arc inception summarized in: ***2004, B.Vayner et al, JSR, Vol.41, p.1031.***

National Aeronautics and Space Administration

Arcs on triple junction

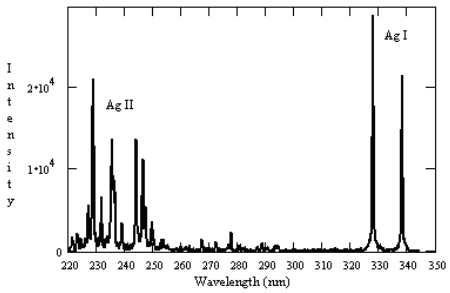

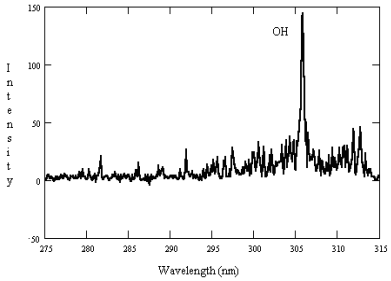

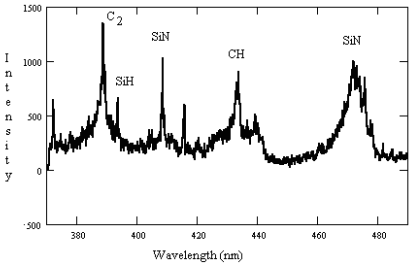

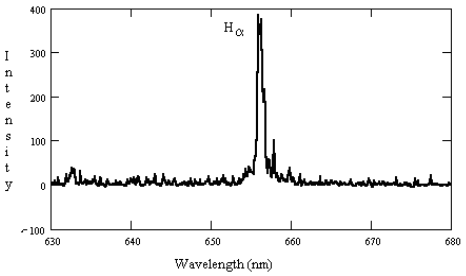

Solar array sample

National Aeronautics and Space Administration

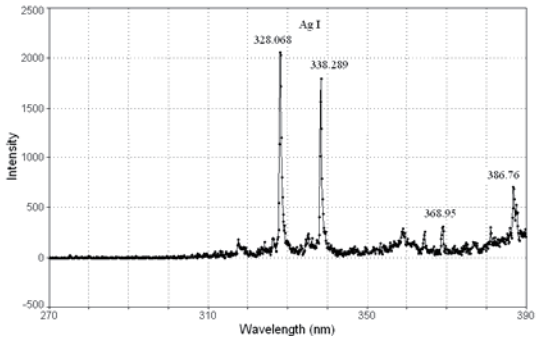

a)

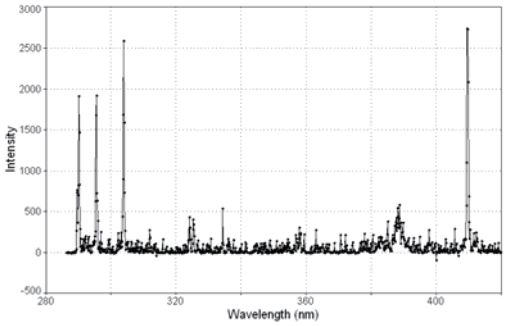

b)

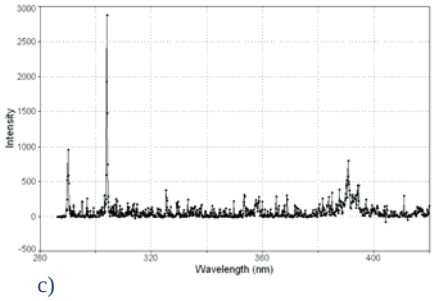

c)

Emission spectra of arc plasma**:** a) arc on interconnect; b) arc between strings U3-U4; c) temporary sustained arc (>500 μs). Spectral lines of Ge I (303.9) and Si I (390.6) are identified.

National Aeronautics and Space Administration

Individual arcs

In LEO: *a few hundred arcs per sample with no damage*

In GEO: visual damage but no significant changes in voltage

(no flash test)

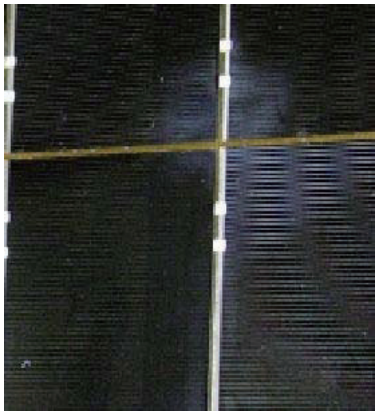

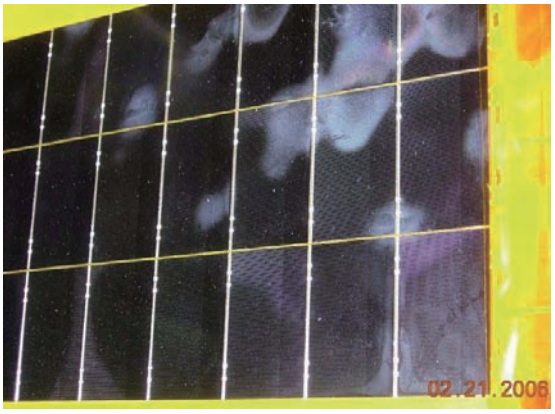

National Aeronautics and Space Administration

Test for separate cells

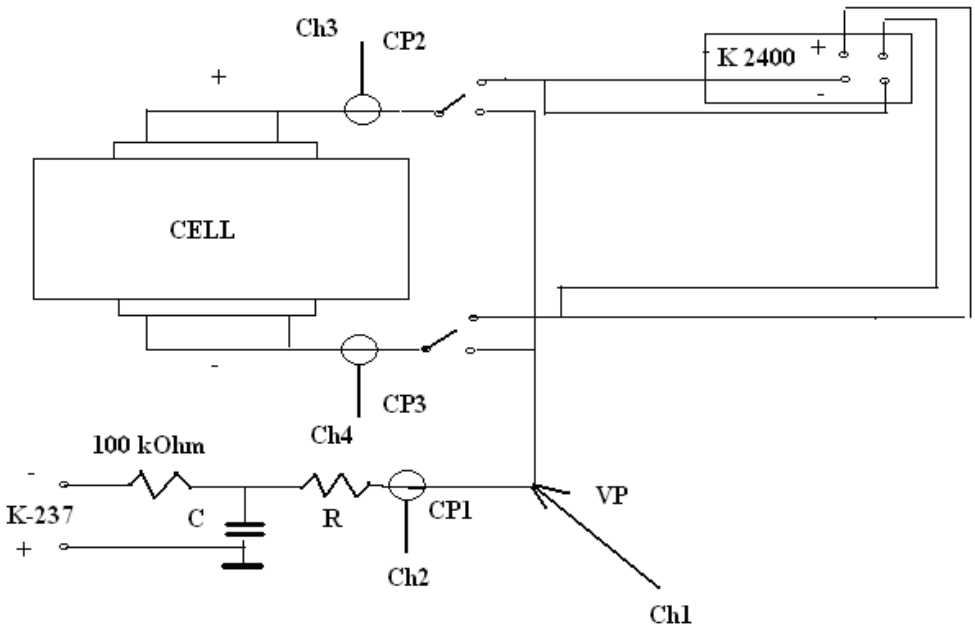

National Aeronautics and Space Administration

Dark I-V curves for one cell

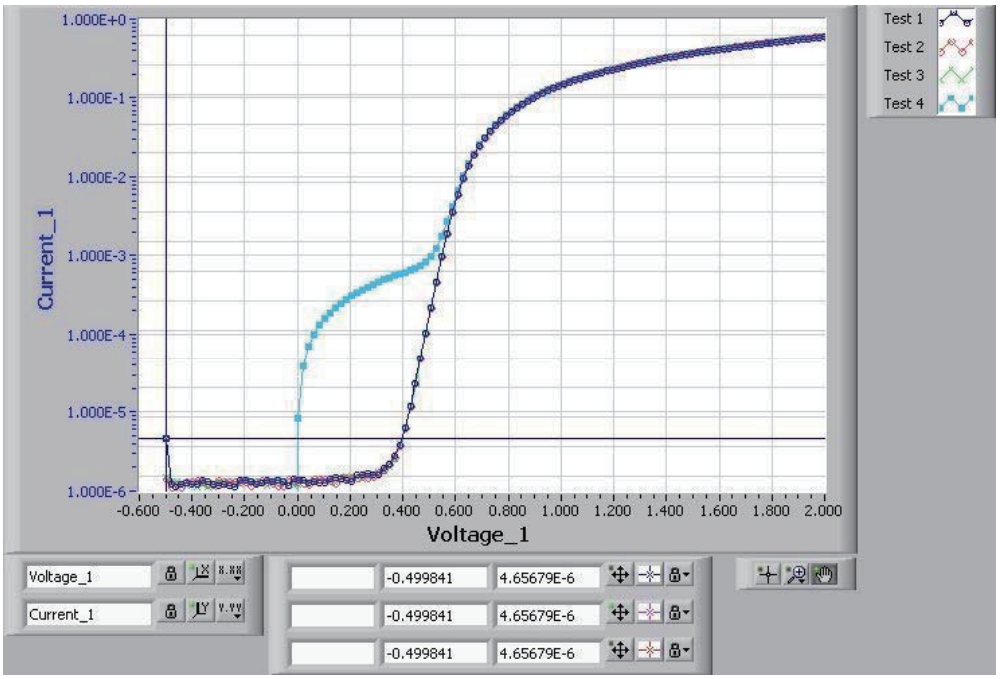

Initial three tests revealed no changes but the fourth one demonstrated significant “damage” to the cell.

National Aeronautics and Space Administration

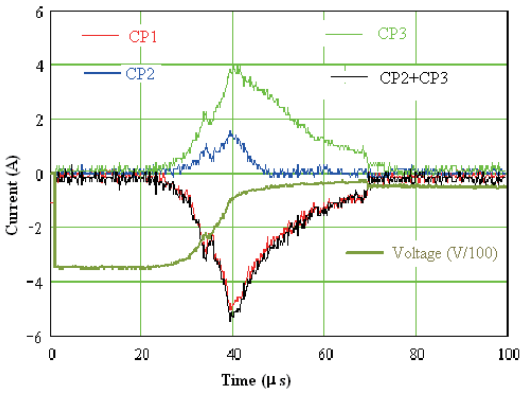

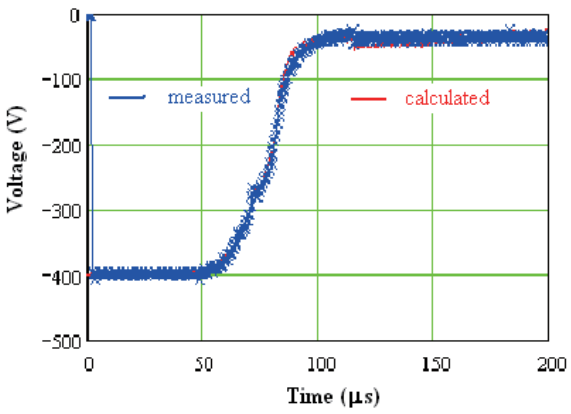

$$U(t) = U_0 - \left(\frac{1}{C} \cdot \int_0^t I(t')dt' + I(t) \cdot R \right)$$

$$W(t) = I(t) \cdot U(t)$$

$$E = \int_{t_1}^{t_2} W(t)dt$$

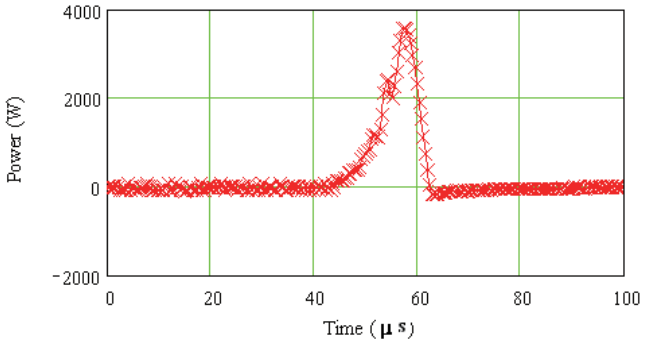

National Aeronautics and Space Administration

“Damage” and Damage

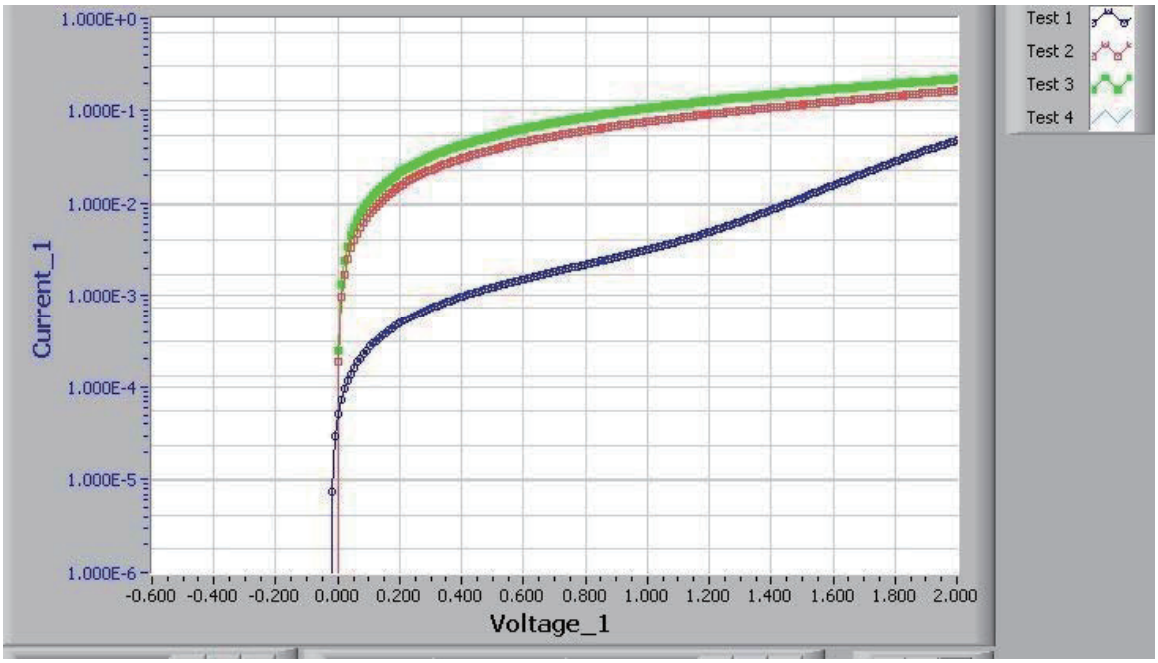

One example of consecutive four DIV curves measured during one run and usually characterized as “severe damage”.

National Aeronautics and Space Administration

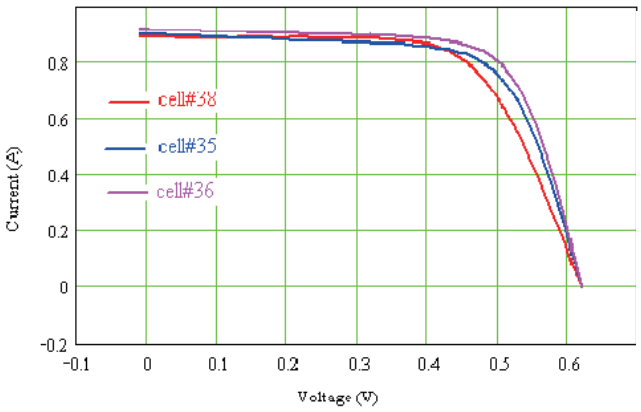

PV I-V characteristics for three Si-N cells: #38-virgin state; ##35 and 36 –“severely damaged”.

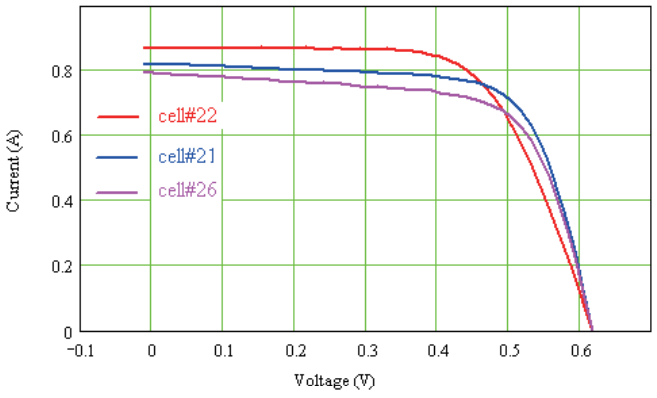

PV I-V characteristics for three Si-IBF cells: #22-virgin state; ##21and 26 –“severely damaged”.

Real damage assessment must be performed with flash test

Table 1. The results of the test for Si cells

Cel#	Bias (V)	Capacitor (nF)	## arcs edge/total	I peak (A)	Width I (μs)	Power (kW)	Energy (mJ)	Remark
21a,b	400/500	150	2\19	6,8(0.9)	12.8(1.8)	1.3(0.27)	9(1.3)	
21c	500	220	2\19	14.9(1)	11(1.6)	3.6(0.45)	23(0.4)	
21d	500	470	2\20	29(1.9)	12.2(1.2)	6,8(0.6)	45.5(0.8)	
21e	500	470	9\20	28(2.40)	12.3(0.9)	6.7(0.5)	45.1(0,7)	
21f	700	1000	10\20					
21g	700	2000	14\20					
21h	700	2000	11\20	146(7)	17.2(0.7)	61.3(7.2)	463(40)	severe damage
22a	400	470	0\20					
22b	400	1000	2\20					
22c	500	1000	2\20					
22d	600	1000	1\20					
22e	600	1000	17\20					
22f	600	2000	11\20	138(4.4)	17(0.9)	40(3)	316(11)	
22g	600	2000	8\20					
22h	700	2000	8\20					no damage
23a	600	2000	5\20					
23b	600	2000	15\20					
23c	700	2000	14\20	154(15)	17.2(0.7)	51.5(8.6)	407(58)	severe damage
24a	700	1000	16\20	106(6)	14.2(0.48)	38.9(3.8)	285(24)	no damage
26a	400	2000	9\20	77.7(11.4)	19(1.9)	19.4(2.4)	181(15)	severe damage after 3 arc on edge
34a	500	1000	9\20					
34b	500	1000	8\20					no damage
34c	600	2000	13\20	138(5)	16.7(0.8)	58(2.6)	499(11)	severe damage after 4 arcs on edge
35a	500	2000	14\20	107(7.6)	17(1.4)	30(2.5)	259(6)	sev.dam
36a	500	1000	7\20	70.6(8.2)	14.4(1)	17.6(2.4)	136(1.9)	sev.dam. After 1 arc on edge. Further da
40a	500	1000	12\20					sev.dam.after 5 arcs on edge
42a	500	470	0\20					no damage
42b	500	470	4\20					no damage
42c	500	470	8\20					no damage
42d	500/600	470	14\20					no damage

Table 2. Test results for TJ cells.

Capacitance (μF)	PeakCurr (A)	Width (μs)	Power (W)	Energy (mJ)	
0.075	3.9	16	1231	8.8	
0.22	12.2	15	3731	26.5	
0.47	24.5	15.5	7559	61.7	
			no damage		
0.15	6.2	16.9	1765	14	
0.3	11.8	16.7	3460	31	
0.3	12.9	15.9	3714	31	
0.3	12.7	17	3697	32	
0.47	26	14.2	7863	61.2	
1	49.6	15	15711	138	damage

Capacitance (μF)	Resistance (Ohm)	PeakCur (A)	Width (μs)	Power (W)	Energy (mJ)	
0.22	20	4.6	38	739	9.2	
0.22	20	4.6	38	715	13.5	
			no damage			
0.22	10	7.6	23	1272	13.1	
0.3	25	4.2	54	666	9.5	
0.3	17	5	43	703	9	
0.3	17	5.6	42	866	11.4	damage

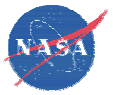

CONCLUSIONS

Sustained discharges between adjacent strings are certainly catastrophic events for solar array operation, and they must be prevented by any means. Individual arcs can cause a gradual decrease in solar array efficiency but a significant loss of power output due to such events is highly improbable. Tests revealed wide variations in the robustness of individual “identical” cells against electrostatic discharges. Thus, the ability of a solar array to withstand multiple arcs is determined by its “weakest” cells, which can be found by testing a statistically representative coupon in a plasma chamber. However, it is almost impossible to determine the size of a statistically representative coupon to represent a real solar array of large size. The ultimate solution to this problem is the adoption of a solar panel design that prevents arcing on its surfaces.

Space Environment Effects on Thermal Control Materials

Weiquan FENG, Yigang DING, Dekui YAN，Xuechao LIU, Wei WANG，Dongmei LI

Beijing Institute of Spacecraft Environment Engineering

P.O.Box9832,Beijing 100029,China

e-mail:weiquan_feng@yahoo.com.cn, Tel:(8610)68746635, Fax :(8610)68746751

Abstract:

Space environments such as electron, proton and UV have degradation actions as increase of solar absorptance parameter of thermal control coatings which would result in temperature increase of satellite. In order to protect satellite from over-heating on the orbit, the degradation of thermal control coatings at the end of life must be simulated correctly by irradiation test. A combined space environment test facility has been developed in BISEE. The combined and single environment test of electron, proton, UV have been performed in spacecraft thermal control materials. This paper introduces the combined test facility and test results. Comparison studies of these effects have been performed. Proton irradiation has been found to have the severest degradation effects on thermal control coatings. The degradation of thermal control coatings will be saturated for a long NUV irradiation. Combined irradiation effects was found to be less than the sum of single environmental effects.

SOLAR CELL R&D ACTIVITIES AT ESA

C. Baur
ESA/ESTEC, Keplerlaan 1, NL-2200 AG Noordwijk, The Netherlands
e-mail: carsten.baur@esa.int

ABSTRACT

III-V multi-junction solar cells have taken over the lead in today's solar cell market for space. Due to the significantly higher efficiencies and higher radiation hardness the higher manufacturing costs in comparison with silicon solar cells are overcompensated. However, the development of the current state-of-the-art triple-junction solar cell for space applications consisting of the material combination $Ga_{0.5}In_{0.5}P/Ga_{0.99}In_{0.01}As/Ge$ has been driven close to its practical efficiency limits of 30%.

In order to decrease the overall solar array costs further, new concepts have to be developed and investigated. The European Space Agency (ESA) follows different promising approaches which are firstly related to the increase of solar cell efficiencies. In addition, ways to reduce the cell thickness are investigated in order to bring down the specific power given in power/mass. Finally, larger cell areas could lead to cost savings in the integration process of the solar cells onto the panel substrate.

INTRODUCTION

Since the beginning of space exploration by spacecrafts, photovoltaics played the most important role for the power generation of on board instruments. For many years the space market was almost exclusively dominated by silicon (Si) solar cells. Only since the beginning of the 90ies the situation started to change. III-V GaAs cells began to enter the market and finally outrun the Si based technology especially after the development and introduction of III-V multi-junction cells.

This success story is mainly related to the higher conversion efficiencies of III-V multi-junction solar cells and the higher radiation hardness of these material combinations. Both characteristics of the III-V multi-junction cells result in higher specific power given in power/mass or power/area especially at end-of-life (EOL), i.e. after 15 years in geostationary orbit. Since the specific power is inversely proportional to the launch costs of the solar generator alone the higher manufacturing costs are completely overcompensated by the reduced launch costs.

Currently, the III-V triple-junction cell based on the material combination $Ga_{0.5}In_{0.5}P/Ga_{0.99}In_{0.01}As/Ge$ is the state-of-the-art solar cell used for space application having reached a begin-of-life (BOL) efficiency of about 30 % and remaining factors at EOL of 84%-88% in power taking into account an equivalent 1 MeV electron fluence of $1 \cdot 10^{15}$ cm^{-2}.

However, with this value also the practical limit of this band gap combination is reached. Thus, to reduce costs of the solar array further, new designs leading to higher efficiencies have to be developed, together with ways to reduce manufacturing costs of the given and future concepts. Those points are reflected in various R&D activities run by the European Space Agency (ESA) which are discussed in this paper.

WAYS TO HIGHER CONVERSION EFFICIENCIES

In theory, disregarding all manufacturing related losses of solar cells the efficiency is solely determined by the temperature, the incident spectrum and the band gap of the semiconductor material used. Thus, one way to identify material or band gap combinations with higher efficiency potentials is to compare them on a pure theoretical basis. Figure 1 shows theoretical efficiency limits of triple-junction solar cells with germanium as a bottom cell (0.66 eV) for different band gap values of top and middle cell. The efficiency limits are calculated with the computer code etaOpt [1] that is based on the detailed balance method first introduced by Shockley and Queisser [2]. Spectrum and temperature were AM0 [3] 25°C. As a rule of thumb 70-75% of the theoretical values can be reached in praxis.

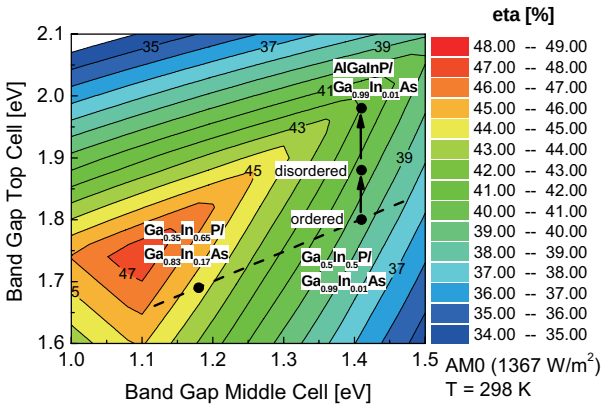

Fig. 1: Theoretical efficiency limits of different band gap combinations of top and middle cell of a 3J cell. The bottom cell is assumed to be germanium with a band gap of 0.66 eV.

Introducing the band gap combinations of the current state-of-the-art 3J solar cell into Figure 1 a theoretical maximum efficiency of 40.6-41.9 % can be obtained. Depending on the top cell manufacturing process which has an influence of the grade of regularity in the crystal and then on the band gap or by the additional introduction of aluminium its band gap can be varied. In any case, the current state-of-the-art 3J cell is far from the optimum band gap combination and as stated before, with about 42 % maximum theoretical efficiency, applying the rule of thumb, the maximum practical efficiency of more or less 30 % is already reached.

The highest theoretical values of up 47.7 % is obtained with a 3J cell based on Ge as bottom cell when the band gap combination would be 1.74 eV for the top cell and 1.1 eV for the middle cell.

Although almost all band gaps between 0.2 eV and 2.5 eV are accessible by III-V compounds (Figure 2), not all combinations can practically be combined without any problems.

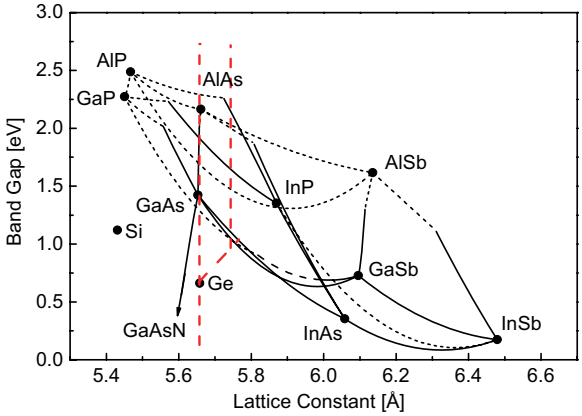

Fig. 2: Band gap versus lattice constant for different III-V material combinations. The dashed lines correspond to the lattice-matched and lattice-mismatched approaches.

From the band gap engineering map of III-V compound semiconductors given in Figure 2 the optimum material combination could be obtained with GaInP and GaInAs both with fairly high indium content. However, the lattice constant of both materials would be slightly different from each other and clearly different from the one of Germanium. Since the different subcells of a 3J cell are grown layer by layer in an epitaxial process on top of each other, differences in lattice-constant cause strain and tensile stress in the material that lead to defects in the crystal and therefore poor material qualities and also efficiencies. Nevertheless, lattice-mismatched approaches are investigated with the constraint that top and middle cell still have to have the same lattice constant. In Figure 1 all band gap combinations where this requirement is fulfilled are represented by the dashed line. The structure currently under investigation consists of the material combination of $Ga_{0.35}In_{0.65}P/Ga_{0.83}In_{0.17}As/Ge$ with a theoretical maximum efficiency of 44.5 %.

Apart from this lattice-mismatched approach another idea to increase efficiencies of the lattice-matched design is to add additional junctions to the structure. Since the Ge subcell of the current 3J cell has just twice the current of the top and the middle cell it is quite obvious to introduce a junction between the middle and the bottom cell that just absorbs half of the Ge bottom cell in the current 3J cell design. This would result in a current matching of all subcells leading to very high efficiencies.

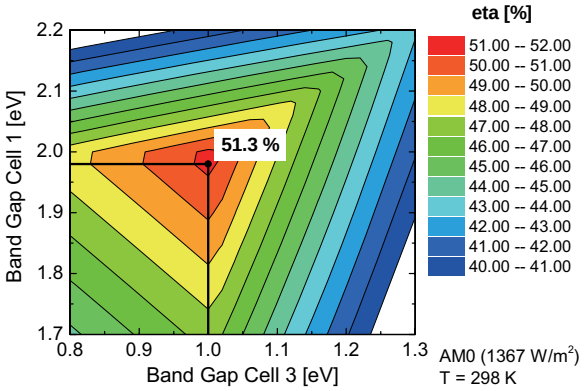

Fig. 3: Theoretical efficiency limits of different band gap combinations of the first and the third cell of quadruple (4J) cell. The bottom cell is assumed to be germanium with a band gap of 0.66 eV and the second cell is $Ga_{0.99}In_{0.01}As$ with a band gap of 1.41 eV.

Figure 3 shows the efficiency limits of a quadruple (4J) cell with Ge as a bottom cell (0.66 eV) and $Ga_{0.99}In_{0.01}As$ as the second junction (1.41 eV) in the stack. Obviously, the optimum band gaps for the first and the third junction are 1.98 eV and 1.0 eV, respectively, resulting in an efficiency limit of 51.3 %. The first junction can be obtained by an AlGaInP cell lattice matched to Ge while the most promising candidate for the 1 eV material was identified already in 1998 to be GaInNAs [4,5], which can also be grown lattice-matched to the other subcells. Since then a lot of effort was put in developing high quality GaInNAs. However, it turned out that this material combination suffers from very poor electrical properties.

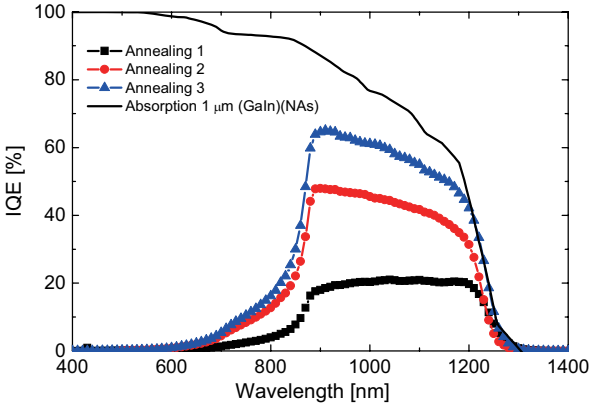

Fig. 4: Internal quantum efficiencies (IQE) of (GaIn)(NAs) solar cells, annealed under different conditions. The light was filtered by a 700 nm thick GaAs cap.

Figure 4 shows internal quantum efficienies (IQE) of differently annealed GaInNAs solar cells with an overall

thickness of 1 μm under a GaAs filter to simulate the situation in a real 4J cell [6]. By adjusting the annealing conditions after the growth a clear improvement is visible.

However, diffusion lengths are still not large enough to provide the photocurrent density of 16 mA/cm^2 required for a beneficial implementation into a 4J cell. Highest photocurrent densities are still only in the range between 10-12 mA/cm^2 for those cells.

With the long-term target of developing the 4J cell as intermediate steps on this path the quintuple (5J) and sextuple (6J) cell are under consideration.

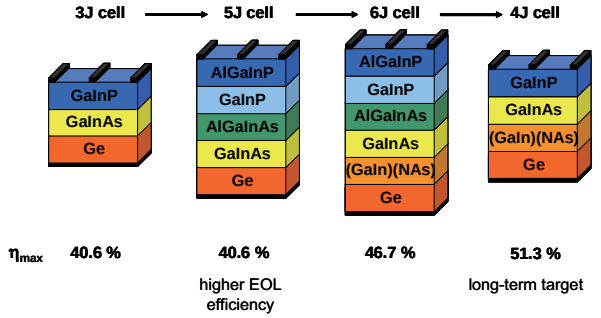

Fig. 5: Roadmap to higher efficiencies of lattice-matched solar cell designs. The 5J and 6J cell are considered intermediate steps on the long-term target of developing the current-matched 4J cell.

Starting from the 3J cell, the 5J cell is obtained by splitting each of the top two junctions of the 3J cell into two. Thereby, the current of a 5J is halved while voltage is doubled. The BOL efficiency of this 5J cell will be identical to the current 3J cell. The benefit of the 5J cells should become visible EOL where the thinner absorber layers are likely to improve the radiation hardness compared the 3J cell which was already shown in first experiments [7].

From the 5J cell then it is only a small step to the 6J solar cell. Since the current is halved, only 8 mA/cm^2 are now required from the GaInNAs subcell in order to make a contribution to the overall efficiency. With the values reached so far it should be feasible to introduce the GaInNAs subcell already. The 6J cell would then have clearly higher BOL and EOL efficiencies. The overall roadmap for the lattice-matched approach is summarized in Figure 5 [8].

OTHER COST REDUCTION ACTIVITIES

Other possibilities to reduce launch, manufacturing and integration costs are identified in thinning down the solar cell structure or to increase their area.

There are different ways to obtain thin solar cells which are investigated in various research activities followed by ESA:

1. Use of thinner Ge substrates
2. Grinding down the backside of solar cell after epitaxial growth
3. Grinding down before epitaxial growth
4. Substrate removal approaches

All of these points have related problems that have to be solved in order to maintain in the first place a yield that is comparable to the current technology. While the thickness limit for the first point in the list is about 70-100 μm, for the second and third approach one might expect reduced thicknesses of down to 20 μm. Even thinner are the cells that are obtained from carrier removal approaches (5-10 μm).

Figure 6 shows an example of a 100 μm thin solar cell manufactured by Azur Space [8]. Here the thickness is just reduced to a level where the solar cell starts to become flexible, what might have additional advantages for future panel concepts.

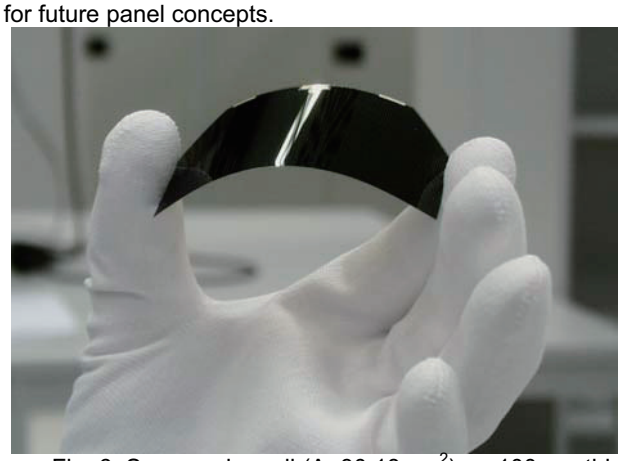

Fig. 6: Space solar cell (A=30.18 cm^2) on 100 μm thin Ge substrate weighing 1.8 g. The weight reduction compared to 150 μm Ge substrates is 28% [8].

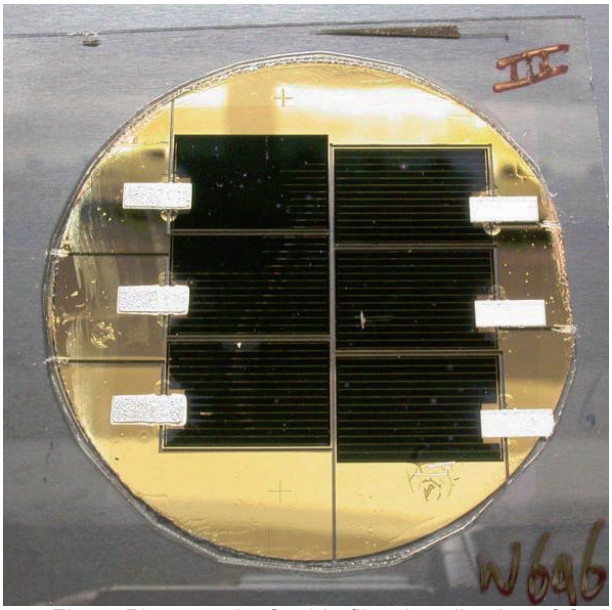

Fig. 7: Photograph of a thin-film six cell string of GaAs single-junction cells [9]. The thickness of one solar cell is less then 5 μm in this case.

Figure 7 shows an example of a solar cell string manufactured at the Radboud University in Nijmegen [9]. The research group there developed a process to remove the solar cells from the substrate without destroying the

substrate. So, it could be reused for additional manufacturing runs reducing costs even further.

Another interesting approach is the inverted metamorphic solar cell [10]. A 3J solar cell is here grown upside down on a Ge substrate. That means Ge in this case is no longer a subcell of the device. The material combination in this case is AlGaInP/GaInAs/GaInAs with a band gap combination of 2.0eV/1.4eV/1.0eV. Therefore, the In content of the last cell to be grown has to be increased significantly which also results in an increase of the lattice constant. The advantage of this approach is that the most delicate subcells – the top and the middle cell – in the stack are still grown lattice-matched to Ge maintaining a very high material quality comparable to the those in the current 3J cell structure. Since now the bottom cell has a higher band gap of 1.0 eV higher efficiencies of about 33-34 % should be in reach in praxis under AM0. After growth the metallization of the top side of the cell is made and the cell is placed on a thin substrate. Then, the Ge substrate has to be removed (cp. Figure 8). Also in this approach it might be possible to reuse the substrate.

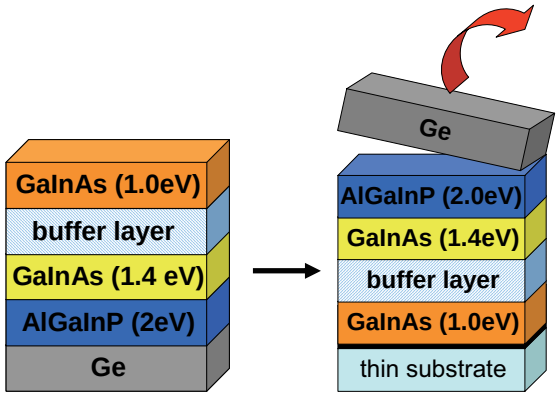

Fig. 8: Inverted metamorphic 3J solar cell. The cell is grown upside down on a Ge substrate which is removed in a later step.

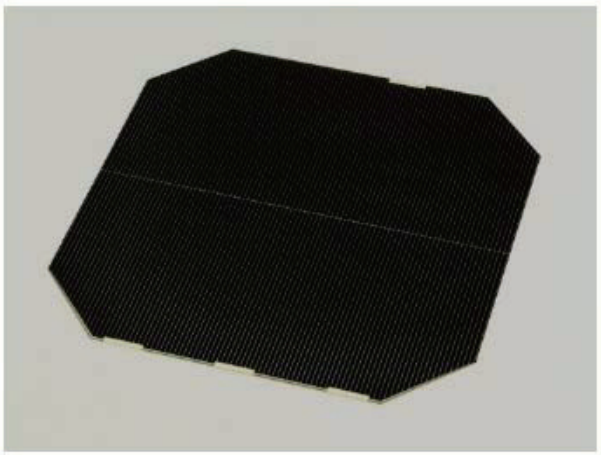

Fig. 9: Large area triple-junction space solar cell (8cm x 8cm with cropped corners) [8].

Finally, another future trend is the usage of larger cell areas which allows a reduction of the integration costs since then only half of the number of solar cells have to be handled (see Figure 9).

SUMMARY

The current 3J cell concept based on the lattice-matched material combination $Ga_{0.5}In_{0.5}P/Ga_{0.99}In_{0.01}As/Ge$ is driven close to its practical efficiency limit of about 30 %. For future improvements in terms of efficiency new concepts have to be investigated. ESA is currently following both, lattice-matched approaches with the 4J cell as a long-term target and the lattice-mismatched approach in conventional and inverted configuration. Additional cost reductions are expected from a reduced cell thickness which would increase the power/mass ratio. Various approaches to obtain thin solar cells are under investigation. Going to larger solar cell areas seem to be an option for the future by which integration costs could be reduced.

REFERENCES

[1] G. Létay and A. W. Bett, "EtaOpt - a program for calculating limiting efficiency and optimum bandgap structure for multi-bandgap solar cells and TPV cells", *Proc. 17th EC PVSEC*, Vol. 1, No. 3, 2001, pp. 178-181.

[2] W. Shockley and H. J. Queisser, "Detailed balance limit of efficiency of p-n junction solar cells", *J. Appl. Phys.* **32**(3), 1961, pp. 510-519.

[3] ISO 15387, "Space systems - Single-junction solar cells - Measurement and calibration procedures", *International Organization for Standardization*, 2005.

[4] D. J. Friedman, J. F. Geisz, S. R. Kurtz and J. M. Olson, "1-eV GaInNAs solar cells for ultrahigh-efficiency multijunction devices", *Proc. 2nd WCPEC*, Vol. 1, No. 3, 1998, pp. 3-7.

[5] H. Q. Hou, K. C. Reinhardt, S. R. Kurtz, J. M. Gee, A. A. Allerman, B. E. Hammons, P. C. Chang and E. D. Jones, "Novel InGaAsN pn junction for high-efficiency multiple-junction solar cells", *Proc. 2nd WCPEC*, 1998, pp. 3600-3603.

[6] K. Volz, D. Lackner, O. Rubel, W. Stolz, C. Baur, F. Dimroth, S. Müller and A. W. Bett, "Improving the material quality of MOVPE grown (GaIn)(NAs)", *Proc. 21st EC PVSEC*, 2006, pp. 497-500.

[7] C. Baur, M. Meusel, F. Dimroth, A. W. Bett, M. Nell, G. Strobl, S. Taylor and C. Signorini, "Analysis of the radiation hardness of triple- and quintuple-junction space solar cells", *Proc. 31st IEEE PVSC*, 2005, pp. 548-551.

[8] M. Meusel, W. Bensch, T. Bergunde, R. Kern, V. Khorenko, W. Köstler, G. La Roche, T. Torunski, W. Zimmermann, G. Strobl, W. Guter, M. Hermle, R. Hoheisel, G. Siefer, E. Welser, F. Dimroth, A. W. Bett, W. Geens, C. Baur, S. Taylor and G. Hey, "Development and production of European III-V multi-junction solar cells", *Proc. 22nd EC PVSEC*, 2007, pp. 16-21.

[9] G. J. Bauhuis, P. Mulder, E. J. Haverkamp and J. J. Schermer, "Substrate reuse for epitaxial lift-off of III-V solar cells", *Proc. 22nd EC PVSEC*, 2007.
[10] M. W. Wanlass, S. P. Ahrenkiel, R. K. Ahrenkiel, D. S. Albin, J. J. Carapella, A. Duda, J. F. Geisz, S. Kurtz, T. Moriarty, R. J. Wehrer and B. Wernsman, "Lattice-mismatched approaches for high-performance, III-V photovoltaic energy converters", *Proc. 31st IEEE PVSC*, 2005, pp. 530-535.

ESD RELATED R&D STUDIES AT CNES AND ONERA

Denis PAYAN[(1)], Virginie INGUIMBERT [(2)], Jean-Charles MATEO-VELEZ [(2)], Daniel SARRAIL [(2)], Thierry PAULMIER [(2)], Jean-François ROUSSEL [(2)], Bernard DIRASSEN [(2)], Françoise BOULAY [(2)], Laurence GIRARD [(3)]

[(1)] CNES
18 Avenue Edouard Belin
31 401 Toulouse cedex 9
France

[(2)] ONERA DESP
2 Avenue Edouard Belin
31055 Toulouse cedex 4
France

[(3)] CRIL ALYOTECH
6 rue Brindejonc les moulinais
31500 Toulouse
France

1 - INTRODUCTION

The paper presents the experimental and numerical capabilities of CNES and ONERA Space Environment Department on charging and Electrostatic discharges (ESD) studies. In a first part, the SIRENE spectrum is presented; dose and temperature effects on material conductivity are studied. In the second part, the Inverted Voltage Gradient situation is obtained on a large solar array in the plasma chamber JONAS and the flash over is measured. Finally, the last numerical simulations (plasma chamber and ESD inception) performed with SPIS are presented.

2 - DEEP DIELECTRICS CHARGING

2.1 - GEOSTATIONARY ORBIT ELECTRON FLUX - REFERENCE SPECTRUM

The utilization in the SIRENE facility of a realistic spectrum sets the problem of choosing the best worst case energy spectrum of the GEO like environment. Tests has to be representative for all the experimental simulation of the electrostatic charging and discharging phenomena made in laboratory. The CNES and ONERA DESP has adopted the spectrum SIRENE presented in Figure 1.

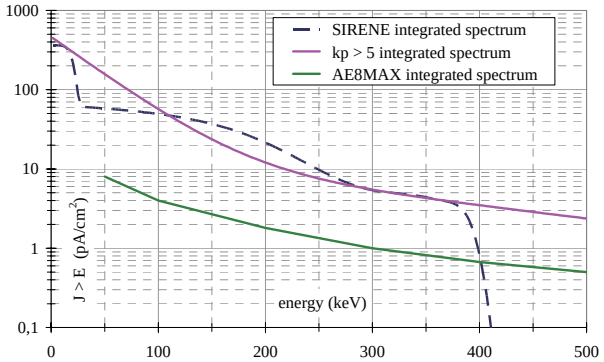

Figure 1 – SIRENE spectrum

2.2 - SIRENE EXPERIMENTAL FACILITY

The originality of the SIRENE experimental simulation facility is that it includes equipment making it possible to reproduce the effects of the charges induced by the electrons from the space

environment in an energy range lower than or equal to 400 keV. The SIRENE facility has the following main components:

- A large-dimension cylindrical vacuum chamber (L≈1.5 m, Ø≈0.5 m) designed in 3 sections to ensure modularity. The horizontal opening of the chamber makes it easy to set up experiments *in situ*. At the level of the vessel, the influence of the terrestrial magnetic field on the electron flow trajectory is compensated for by the magnetic field induced by the two pairs of windings (vertical and horizontal) surrounding the chamber. The body of the chamber is fitted with several standardised diameter extensions enabling the installation of various control and metrology instruments (vacuum gauge, visualisation camera, electrical outputs, analysis probes, connections to the radiation sources, etc.).
- A primary and secondary pumping unit which ensures a pressure of the order of 10^{-6} hPa after some hours in operation.
- A specimen door, with temperature regulation within a range comprised between -180°C and +100°C.
- The facility is equipped with two electron sources:
  - a Van de Graaff type accelerator capable of delivering a monoenergetic electron beam whose energy level can be adjusted between 100 and 400 keV. In the case of experiments carried out using a simulation of electron flux from space whose energy spectrum is distributed, the accelerator's operating energy is of the order of 400 keV (most frequent case).
  - a low-energy electron gun which delivers a beam whose energy level can be adjusted between 1 and 35 keV. This electron beam can be used alone (many tests are requested on the basis of specifications such as: E=20 keV, Φ=1 nA/cm^2). It is also used to complete the flow of the Van de Graaff accelerator's electron beam at low energy levels.
- A set of "complex" diffusion windows designed to transform the 400 keV monoenergetic beam delivered by the accelerator into an energy-distributed beam according to a reference spectrum chosen to simulate a type of orbit.
- The analysis instruments specific to the electrostatic studies, that is to say:
  - current probes for detecting discharges and analysing current transients,
  - a potential probe used for analysing charge potentials along a vertical axis.

A further development phase being carried out at present with the CNES concerns the metrology of the charge potentials. The instruments currently in place only enable *in situ* measurements of the potentials according to a vertical axis (d ≤ 15 cm) and no other analysis probe movements are possible. In the case of studies on a relatively large number of simple specimens, or on more complex structures (solar arrays, antennas, etc.), these instruments are insufficient. Consequently, a new potential probe movement system is in the process of being designed. It should make it possible to analyse charge potentials in a 20 cm x 20 cm plane.

A general view of the SIRENE experimental facility is shown in Figure 2.

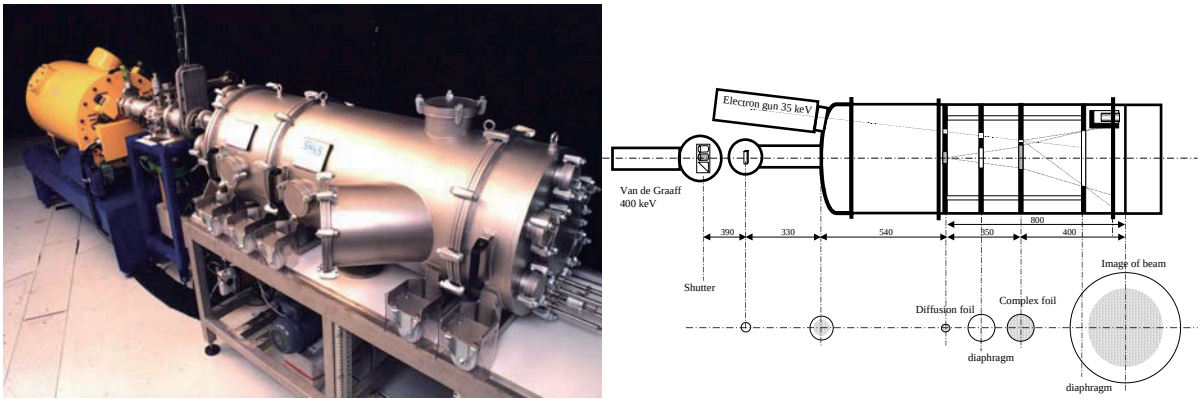

Figure 2: General view & schematic diagram of SIRENE

The facility's various components with the positioning and the trajectory of the two electron beams delivered by the electron gun and the Van de Graaff accelerator are symbolised in Figure 2 (shown in the horizontal plane). The SIRENE integrated spectrum (GEO orbit) is compared with the Kp>5 integrated reference spectrum in Figure 1, and a good match can be seen between the two spectrums.

2.3 - TEMPERATURE EFFECT

The influence of the temperature on deep dielectrics charging is studied using the SIRENE integrated spectrum. The effect is weak in the case of a 50 µm thick layer of Kapton® because this material has a good Radiated Induced Conductivity (RIC). On the contrary, the effect is strong on a solar cell like device, composed of glued CMX. The conductivity is highly decreased for temperatures less than 0°C, Figure 3.

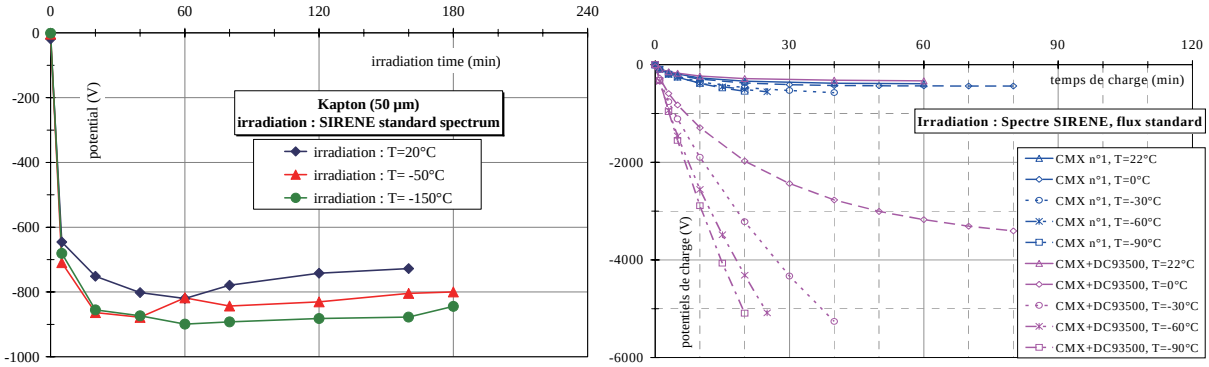

Figure 3 – Temperature effect on Kapton conductivity (left) and on CMX and glued CMX (right)

3 - FLASH-OVER ON SOLAR ARRAY COUPONS

3.1 - JONAS PLASMA CHAMBER

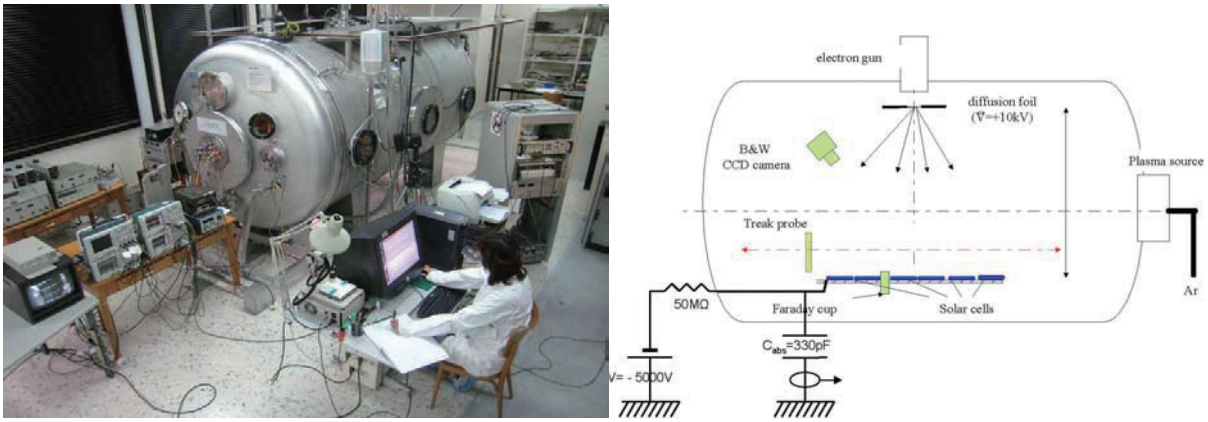

Figure 4 – JONAS Plasma chamber (left); solar panel test (right)

This set-up is a large chamber (L=3.5 m, Ø=1,85 m) built in a nonmagnetic stainless steel. A set of Helmoltz coils can compensate the earth magnetic field. A high capacity cryogenic pumping system (12000 l/s for argon gas) insures a limit pressure of 2.10^{-8} hPa after about fifteen hours of pumping. The set-up allows us to reproduce the Inverted Potential Gradient (IPG) situation observed in flight, i.e. while the satellite body (here sample structure and cells) is negatively charged up to several kilovolts, the dielectrics (here cover-glasses protecting the cells) build up a differential charge as high as 1000V. This can be reproduced either with plasma or electrons (ref). For this purpose, both plasma source and electron gun are implanted in the chamber. The plasma source is implanted in chamber axis (at one end) and allows us to reproduce low earth orbit plasma conditions with regards with electrostatic problems. On the other end of the chamber, the door is equipped with high voltage

and high current feedthroughs and receives the sample holder. On the top of the chamber are placed the electron gun and its diffusion foil. A photograph of JONAS chamber with all instruments required for ESD tests on solar arrays coupons and the schematics are presented in Figure 4. It shows a side view of the chamber with the implantation of all the different instruments.

3.2 - MAIN RESULTS

A large amount of tests have been performed on different size samples (from 2 X 3 cells to 19 X 16 cells coupons). The main results shows that:

- the flash-over can neutralize more than 1 m^2,

- it extends more than 1.4 m with a velocity of about 10^4 m/s,

- the flash-over can jump from a solar panel to another, even if these two panels have a 0.2 m gap distance.

- the secondary arcs durations is strongly dependant on coupon size (i.e. flash-over duration) : for the same couple (V, I) applied in the active gap, large coupon produces longer discharges than small one. Complementary tests have been performed using external capacitor as missing coverglasses simulator. The conclusion of this campaign is that this device is not realistic because using high values of external capacitance induces the creation of anodic spots on nearby ground leading to high plasma density increasing strongly the plasma conductivity and the available current in the ESD which becomes a Coupling with ground ESD (CwG ESD) as reported in our papers in 10^{th} SCTC.

4 - SPIS LAST SIMULATIONS

4.1 - GLOBAL SIMULATION OF JONAS

The Spacecraft Plasma Interaction Software (SPIS) has been used to numerically simulate the physics in the plasma tank JONAS. The goal is to simulate both fast and slow ions co-existing in such ground plasma chamber. The plasma source is derived from the experimental results (density measurements with Langmuir probes upstream and downstream a plate). These fast ions are computed through a Monte-Carlo method. The neutral are injected in the whole plasma tank volume. Their density is estimated by the measured residual pressure P_n.

The plasma dynamics consists in a PIC (Particle-In-Cell, Monte-Carlo) method for fast and slow ions. The electrons follow a Boltzmann distribution:

$$N_e = N_0 \exp\left(\frac{e\phi}{k_B T_e}\right)$$

where N_0 is a numerical parameter for the cutting of the Boltzmann distribution. When the plasma potential is positive, the electron density is set equal to N_0.

The neutral dynamics is not calculated (constant pressure). The only volumetric reaction considered is the charge exchange (CEX) between fast ions and neutrals : $Ar^+_f + Ar \rightarrow Ar + Ar^+_s$. The variation of the slow ion density during the time step *dt* is proportional to the neutral and fast ion densities $N(Ar^+_f)$ and N(Ar):

$$\Delta N(Ar_s^+) = N(Ar_f^+).N(Ar).\sigma.V_{rel}.dt$$

where σ is the cross section of CEX reaction and V_{rel} the relative velocity of neutrals and fast ions. Fast ion and neutral densities are assumed to be conserved. Indeed, for $\sigma=10^{-18}m^2$ and $N(Ar) = 10^{17}m^{-3}$, the CEX ions reach 10% of the fast ions over a distance of 1m. The reaction rate is to small to have a strong effect on fast ions.

The electric field follows the non-linear Poisson equation:

$$-\Delta\phi = \frac{e}{\varepsilon_0}\left(N_+ - N_0 \exp\left(\frac{e\phi}{k_B T_e}\right)\right)$$

The numerical parameters used in this study are presented on the following table. The fit of the fast ion beam measurement is used as an input data. The SPIS model is an axisymmetric source.

Simulation time (s)	Max integration time step (s)	N_0 (m^{-3})
$2.5.10^{-3}$	10^{-4}	10^{14}
σ (m^2)	Fast ion current (mA)	P_n (mbar)
$0.4.10^{-18}$	1,1	$4.3.10^{-6}$
Electron temperature (eV)	Tank voltage (V)	
0,2	-2	

4.2 - NUMERICAL RESULTS

The space distributions of fast and slow ion densities are presented in Figure 5. They are represented in the same logarithmic scale range so as to compare them.

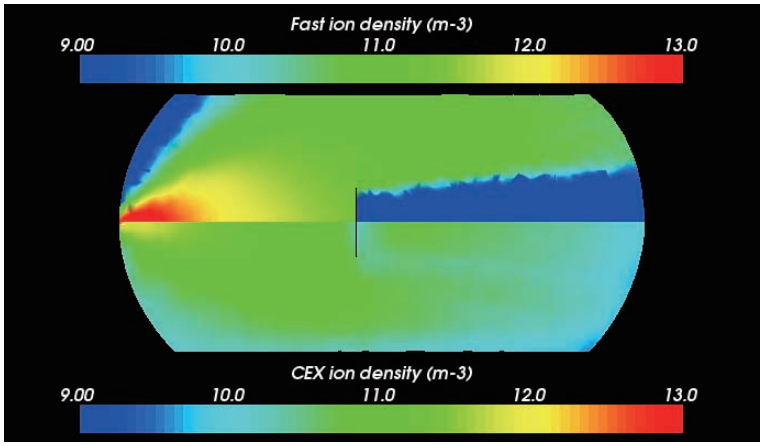

Figure 5- Fast (up) and slow (down) ion densities (logarithm scale)

The fast ion beam clearly shows a spatial decay corresponding to the divergence of the plasma plume. The fast ion density decreases from $10^{14}m^{-3}$ to $10^{11}m^{-3}$ at the back of the plasma tank. The aperture angle of 80° is well represented and the wake effect due to the plate is clearly demonstrated. The slow ions reach the whole tank due to their slow temperature. They are created in the vicinity of the plasma source and are submitted to potential gradients created by the fast ions. That makes them drift slowly towards the whole tank. Their density is about 10^{10}-$10^{11}m^{-3}$.

4.3 - ESD TRIGGERING MODEL

SPIS has been used to simulate the first step of the ESD on the IVG obtained on solar cells. The geometrical model takes into account the triple point existing between the cell, the coverglass and the vacuum. This situation is enhanced by a micro tip, Figure 6.

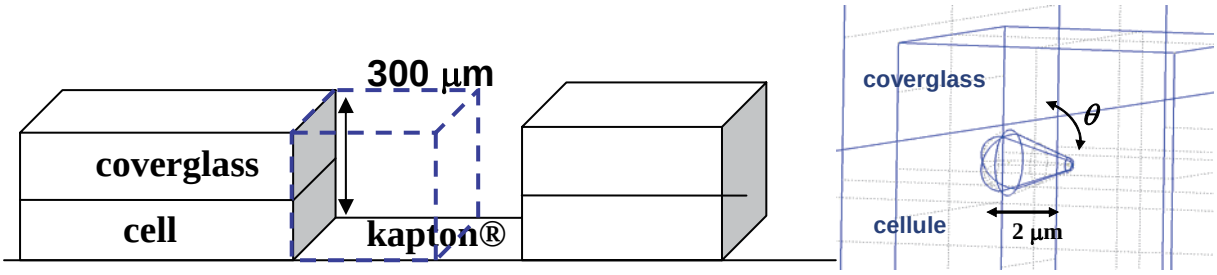

Figure 6 – Numerical model for the triple point geometry on solar cell

Electron dynamics is influenced by photoemission, secondary emission yield more than one in the coverglass and field effect on the cathode tip. The results, cf. Figure 7, show that the electric field is highly enhanced if the tip is oriented towards the coverglass. This situation amplifies the field effect electron emission. These so created electrons collide with the dielectrics and produce secondary emission. The positive charge induced then increases the electric field and so on, up to the beginning of the ESD.

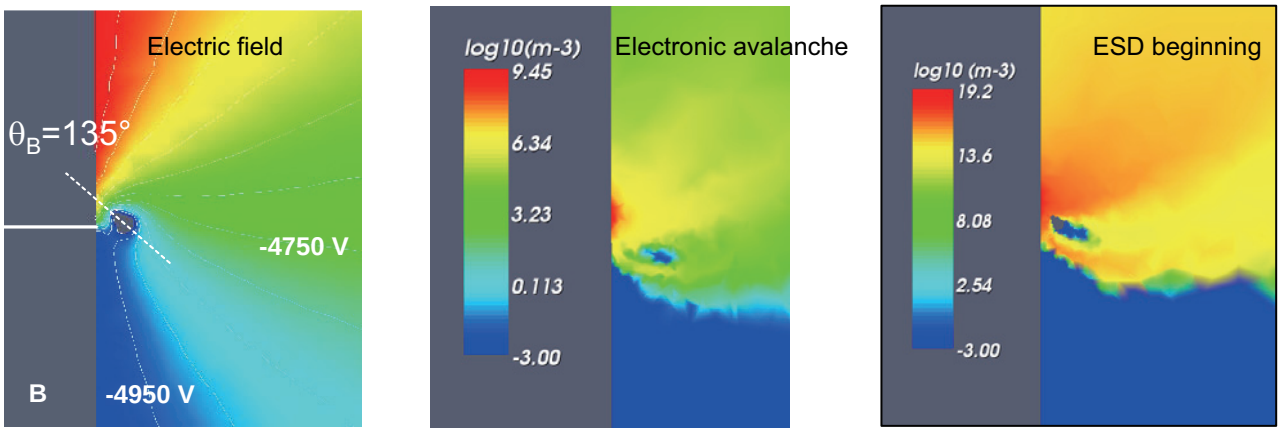

Figure 7 – Electric field amplification (left), elctronic avalanche (middle) and ESD inception (right) in the IVG model

5 - CONCLUSION

For each study at CNES and ONERA, we follow a global approach consisting in:

- understanding and modelling the physics,

- developing flight representative facilities (SIRENE, JONAS, ...) and associated setups,

- performing flight representative experiments,

because all R&D studies depend strongly on test setup configurations especially ESD qualification of materials and assemblies.

6 - REFERENCES

[1] Effect of a realistic charging environment on electrostatic qualification for space dielectrics, Payan et al., 10th Spacecraft Charging Technology Conference, Biarritz, France, June 2007

[2] Electrotatic discharge and secondary arcing on solar array - Flash-over measurement and consequences on arc occurrence - Dependence with the test set-up, Payan et al., 10th Spacecraft Charging Technology Conference, Biarritz, France, June 2007

[3] Ground plasma tank modelling and comparison to measurements. J.C. Matéo-Vélez et al., 10th Spacecraft Charging Technology Conference, Biarritz, France, June 2007

[4] Simulation of an electrostatic discharge initiation with software SPIS, L. Girard et al., 10th Spacecraft Charging Technology Conference, Biarritz, France, June 2007

In-situ Space Environment Measurement of Near Earth and SEDA

Tateo Goka, Haruhisa Matsumoto, Kiyokazu Koga, Hideki Koshiishi, Yugo Kimoto, Yasutomo Sasaki,
Tatsuto Komiyama
Japan Aerospace Exploration Agency, Sengen 2-2-1, Ibaraki, 305-8505, Japan

ABSTRACT

The current status of measuring radiation using JAXA satellites is reviewed. Starting with Engineering Test Satellite-V (ETS-V; KIKU-5 in Japanese) in 1987, efforts to conduct radiation measurements in space have continued using almost all Japan Aerospace Exploration Agency (JAXA formerly NASDA) satellites (ETS-VI, ADEOS, ADEOS-II, MDS-1, DRTS(ongoing) and ETS-VIII(ongoing), and ALOS (ongoing)), in geostationary orbit (GEO), geostationary-transfer orbit (GTO), and low-Earth orbit (LEO). Electrons, protons, alpha particles, and heavy ions have been the main objects of study. Future plans for radiation monitoring in JAXA, including GOSAT, Jason-2 (in collaboration with CNES), and ISS/JEM/Exposure Facility/SEDA-AP, are presented.

1. Introduction

JAXA (formerly NASDA) developed TEDA (Technical Data Acquisition Equipment), which is able to measure the space radiation environment and its effects on newly developed electronic devices onboard a satellite. TEDA was designed to acquire engineering data useful to the design of future spacecraft, to diagnose the anomalies encountered on orbit, and to collect data to make new radiation belt models (electrons, protons, and alpha particles) to augment NASA radiation belt models. TEDA is composed of various instruments for every spacecraft mission. TEDA was reviewed by two papers, Kohno [1] and Fukuda et al. [2] almost ten years ago. This paper reviews current TEDA instruments and data over the past ten years, and presents our future measurement plan.

II. TEDA Post-Flight Measurement Data

TEDA instruments have flown on board ten spacecraft (Table 1). All measured data are available on the SEES (Space Environment and Effects System) website (http:// sees.tksc.jaxa.jp/).

Table 1: Spacecraft carrying TEDA

Spacecraft		ETS-V	ETS-VI	ADEOS	ETS-VII	Shuttle	ADEOS II	DRTS	ISS	MDS-1	ALOS
Launch		1987	1994	1996	1997	1998	2002	2002	2002	2002	2006
Orbit		GEO	GTO	LEO	LEO	LEO	LEO	GEO	LEO	GTO	LEO
Altitude		36k	8k-38k	800	500	400	800	36k	400	250-36k	700
DOM	DOse Monitor	◎	◎				◎	◎		◎	
HPM	High energy Particle Monitor			◎							
LPT	Light Particle Telescope										◎
HIT	Heavy Ion Telescope		◎	◎						◎	◎
DOS	DOSimeter (RadFET)			◎			◎			◎	◎
MAM	Magneto Meter		◎							◎	
AOM	Atomic Oxygen Monitor				◎						
NEM	NEutron Monitor					◎			◎		
PLA	Plasma Monitor										
POM	POtential Monitor	◎	◎	◎							
DIM	DIscharge Monitor	◎									
SUM	Single event Upset Monitor	◎	◎	◎			◎			◎	
ICM	Integrated Circuit Monitor	◎	◎								
SCM	Solar Cell Monitor	◎	◎								
COM	COntamination Monitor	◎	◎	◎							

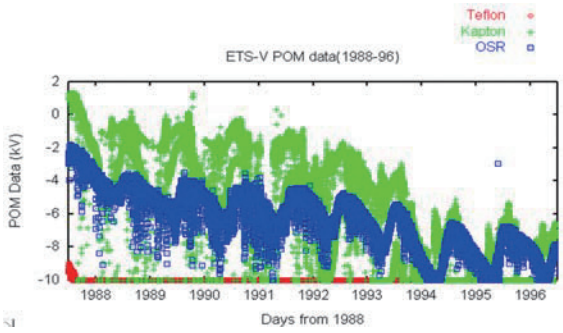

Fig. 1: POM/ETS-V measured data

2.1 KIKU-5 (Engineering Test Satellite-V) (GEO, longitude: 150 deg. E)

A dose monitor (DOM) composed of two silicon detectors was installed on this satellite [1-2]. The measurement data were gathered from August 1987 to September 1997 (ten years). Single-event latch-up data acquired by a Single-Event Upset Monitor (SUM) were reported for the first time [3].

The Potential Monitor (POM) measures differences electrostatic potential on the surface of spacecraft. Figure 1 presents the POM instrument measured data for ten years. Three samples (Teflon (lowest), Kapton (highest), and OSR(middle in y axis)) were mounted on the POM. The electric field leaking from an aperture of each sample was modulated by a chopper at 1kHz, and the electrostatic electrode detected the weak electric field. POM data shows a time-trend to decrease in figure 1.The authors think that is why the radiation damage (or/and contamination) effects a decrease of secondary electron emission yields of the cover glasses for the solar cell, or/and a decrease of photo-emission yields. We are now verifying the effects on the ground test, [4].

2.2 KIKU-6 (Engineering Test Satellite-VI) (GTO: perigee 8,600 km, apogee 38,600 km)

A DOM composed of six silicon detectors and a Magnetometer (MAM) were installed on this satellite. The data were gathered from August 1994 to July 1996. The measurement data were mainly reported in three papers [5-7]. We made the first empirical radiation belt models (electrons, protons, and alpha particles in a solar minimum period) by using this data and scientific satellite AKEBONO data [8].

2.3 MIDORI (Advanced Earth Observing Satellite (ADEOS)) (LEO-POLAR: altitude: 800 km, inclination: 98.6 deg.)

A DOM and a Heavy Ion Telescope (HIT) were installed on this satellite. The data were gathered from August 1996 to July 1997. The HIT measured the interplanetary anomalous cosmic ray (ACR), oxygen, and nitrogen, with results quite similar to those of SAMPEX (Figure 2) [9].

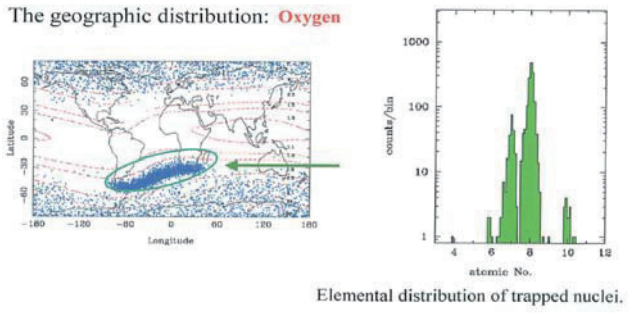

Fig. 2: Geographic distribution of oxygen and elemental distribution of trapped Anomalous Cosmic Ray (O, N, C, Ne) observed by MIDORI /HIT[9].

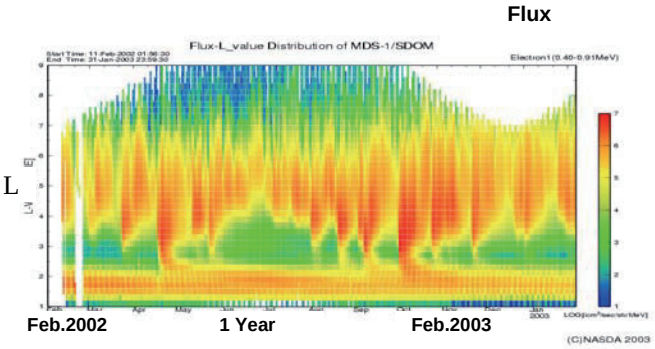

Fig. 3 : Electron Flux (0.4-0.9MeV) L-t Diagram

2.4 MIDORI-2 (ADEOS-2) (LEO-POLAR: altitude 800 km, inclination 98.6 deg.)

A DOM was installed on this satellite; data were gathered from December 2002 to September 2003[10]. The DOM data were used for diagnosis of the ADEOS-2 total loss anomaly [11].

2.5 TSUBASA (Mission Demonstration Satellite (MDS-1)) (GTO: perigee 500 km, apogee 36,000 km)

A Standard Dose Monitor (SDOM)[12], a HIT, and a MAM were installed on this satellite. The data were gathered from February 2002 to September 2003. There are many reports on these data [13-15].

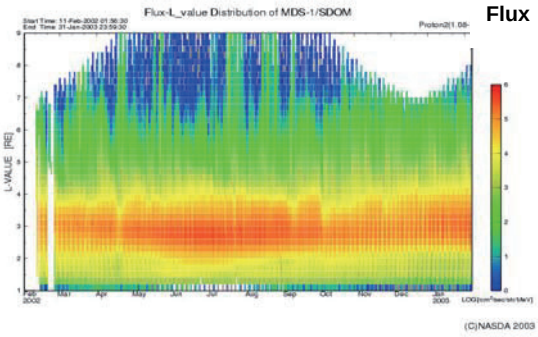

Fig. 4 : Proton Flux (1-1.5MeV) L-t Diagram

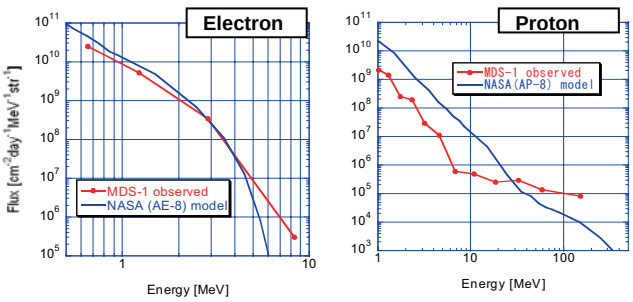

Fig. 5: Comparison between MDS-1 Observed Energy Spectrum and NASA Model

The SDOM measurement results are given in Figures 3 and 4. The electron flux (0.4-0.9 MeV) and the proton flux (1-1.5MeV) are indicated on the L-t diagram, where the vertical axis gives McIlwain's L-value ranging from L=1 to 9, and the horizontal axis gives time covering one year, starting in February 2002. Figure 5 depicts the observed and averaged electron (right) and proton (left) energy spectra, compared to the spectra calculated from the NASA AE-8 MAX[16] and AP-8 MAX[17] models, the fluxes of which were integrated along all data points of the MDS-1 orbit. The measured averaged proton fluxes were ten times lower than those of the AP-8 MAX model for energy levels below 20 MeV. However, we found that both electron and proton fluxes were broadly consistent with AE-8 MAX and AP-8 MAX models on the geomagnetic equator [18].

2.6 KODAMA (Data Relay Test Satellite; DRTS) (GEO; longitude 90.75 deg. E)

An SDOM was installed on this satellite. Data have been gathered since September 2002. Figure 6 depicts proton channel 11ch-15ch data (8MeV-211MeV) from October 2002 to January 2006. You can see 2 major peaks correspond with the Holloween Solar Flare (Oct. 2003), and the Tatina Flare (20 Jan. 2005) .

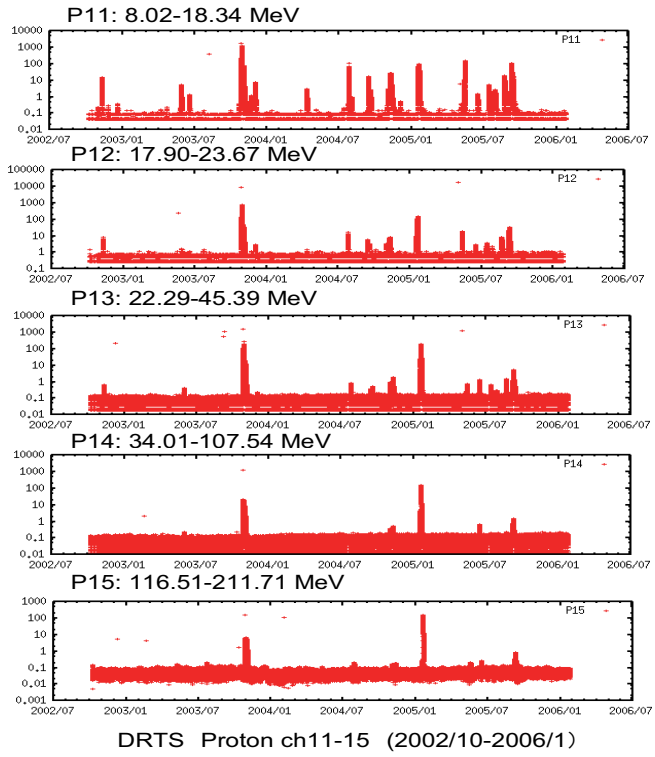

Fig. 6: Proton Ch. 11-15 (8-211MeV) data from October 2002 to January 2006, obtained by DRTS/SDOM

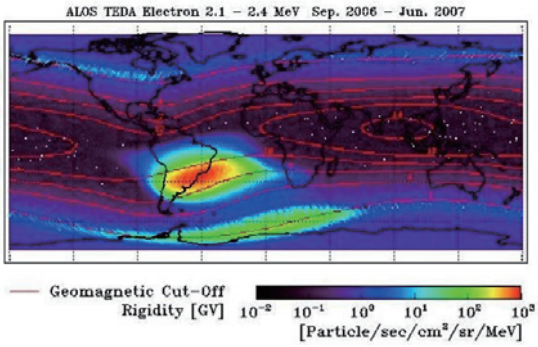

Fig. 7: LPT (ALOS) Electron (2.1-2.4MeV) 1month data (Dec.2006-Jan.2007) and geomagnetic cut off rigidity contour on a world map.

2.7 DAITI (ALOS) (LEO-POLAR: altitude 690 km, inclination 98 deg.)

TEDA consists of a Light Particle Telescope (LPT) and a HIT. Data have been gathered since February 2006. Figure 7 shows electron (2.1-2.4MeV) 1 month data and geomagnetic cut off rigidity contour on a world map, respectively. These data cleary the increased flux in the South Atlantic Anomaly (SAA).

2.8 KIKU-8 (Engineering Test Satellite-VIII) (GEO longitude 146 deg. E)

ETS-8 was successfully launched in 18, December 2006. TEDA has four components: a MAM, a POM, a DOM, and a SUM. The MAM, a fluxgate magnetometer, was placed on the upper antenna tower. The measurement range was 256, 1024, 4096, and 65536nT, the same range as that of ETS-6. The MAM data are showed in Figure 8. The POM instrument was the same instrument as ETS-V,-VI, and ADEOS, except samples. Three cover glasses (BRR/s-0213, CMX-BRR, and CMG-AR) were selected for ETS-8.

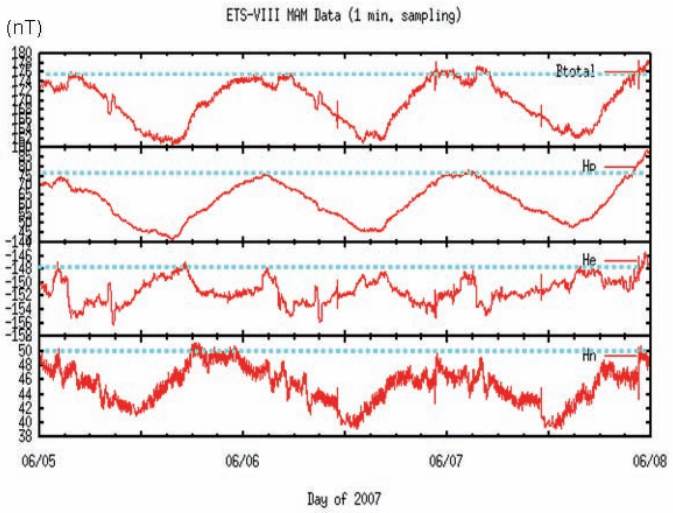

Fig. 8: Magnetometer Data (ETS-8) on 3 days (5-8, Jun. 2007), that mean B total, Hp, He, Hn, In nT, from upper to bottom panel.

III. TEDA Future Plan

JAXA are planned to be flown on various missions in the following years. Table 2 lists the confirmed TEDA mission to date.

Table 2. Planned TEDA Mission Plan

Spacecraft		ETS-8	Jason-2	GOSAT	SmartSat	ISS/JEM
Launch		2006	2008	2008	2008-2009	2008-2009
Orbit		GEO	LEO	LEO	GTO	LEO
Altitude		36k	1.3k	666		400
DOM	DOse Monitor					◎
HPM	High energy Particle Monitor					
LPT	Light Particle Telescope		◎	◎	◎	
HIT	Heavy Ion Telescope			◎		◎
DOS	DOSimeter (RadFET)	◎				
MAM	Magneto Meter	◎				
AOM	Atomic Oxygen Monitor					◎
NEM	NEutron Monitor					◎
PLA	Plasma Monitor					◎
POM	POtential Monitor	◎				
DIM	DIscharge Monitor					
SUM	Single event Upset Monitor	◎				◎
ICM	Integrated Circuit Monitor					◎
SCM	Solar Cell Monitor					
COM	COntamination Monitor					

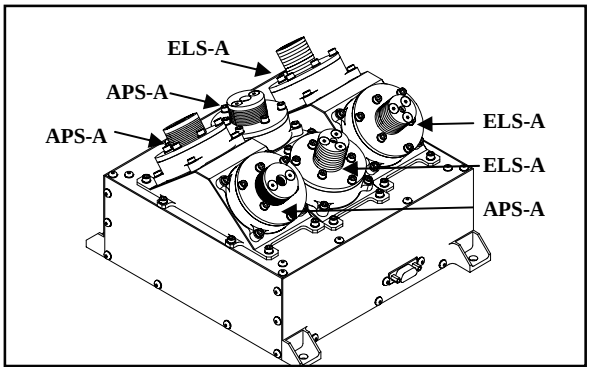

Fig. 8. LPT-3 onboard GOSAT

4.1 Greenhouse Gases Observing Satellite (GOSAT) (LEO, Polar)

GOSAT will be launched in mid-2008 into sun-synchronous sub-recurrent orbit with an altitude of 666km and an inclination of 98deg. The nominal lifetime will be five years. TEDA is composed of an LPT and a HIT. The LPT measures electron, proton, and alpha particles, and identifies the types of particles and energy. It is composed of four instruments (LPT1～4). LPT1 and LPT2 have the same configuration, composed of ELS-A, ELS-B, APS-A, and APS-B; but LPT1 and LPT2 have different fields of view. LPT3 is composed of three ELS-As and three APS-As. LPT4 is composed of APS-C [19].

Each LPT is composed of compact and high-performance sensors (Table 3). LPT3 has three fields of view to observe the distribution of pitch angle of particle flux with a geomagnetic field (Fig. 8).

Table 3 : Sensors used in LPT

Sensor	Energy range
ELS-A	Electron: 30keV～1.3MeV, 1.3MeV<
ELS-B	Electron: 280keV～20MeV
APS-A	Proton: 400keV～37MeV, Alpha: 3MeV～16MeV
APS-B	Proton: 1.5MeV～250MeV, Alpha: 20.7MeV～400MeV
APS-C	Proton: 100MeV～500MeV, Alpha: 25MeV/n～500MeV/n

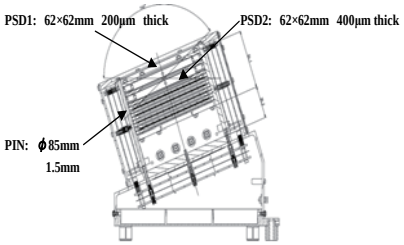

Fig. 9. HIT onvboard GOSAT

The measurement ranges of the HIT(fig. 9) are:

- He: 7～48MeV/n
- Li: 8.5～56MeV/n
- C: 13～90MeV/n
- O: 16～106MeV/n
- Fe: 28～201MeV/n.

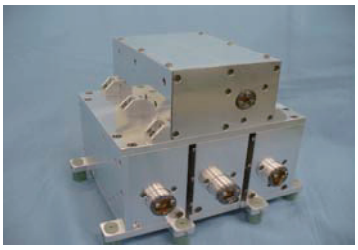

Fig. 10. LPT onboard Jason-2

4.2 Jason-2 (CNES/JAXA joint project)

CNES and JAXA agreed that the radiation particle monitor, the LPT, would be accommodated in the CNES satellite Jason-2. The mission of the JASON-2 is dedicated to ocean and climate forecasting, in continuation of the successful TOPEX-POSEIDON satellite launched in 1992 and the Jason-1 launched in 2001. Jason-2 is planned to be launched in June 2008. The altitude of its orbit will be 1,336km, and the inclination will be 66 degrees. It was decided to load the LPT on the Jason-2 with the same specifications as the GOSAT LPT1, which consists of four sensors (ELS-A, ELS-B, APS-A, and APS-B) (Fig.10) [20].

4.3 ISS JEM Exposed Facility and SEDA-AP

Development of the SEDA that will be mounted on the Exposed Facility (EF) of the Japanese Experiment Module (JEM, also known as “Kibo”) on the ISS has been completed. This payload module is called SEDA–Attached Payload (AP). The SEDA-AP will be launched by space shuttle and attached to the JEM-EF in 2008-2009. It will measure space environment data on the ISS orbit. The SEDA-AP is composed of common bus equipment that supports launch, RMS handling, power and communication interfaces

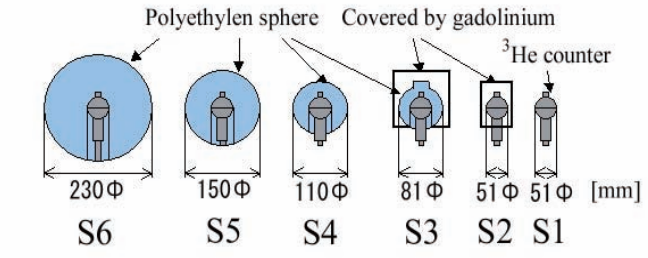

Fig。 11. A two-inch spherical He^3 proportional counter covered with a moderator of polyethylene sphere.

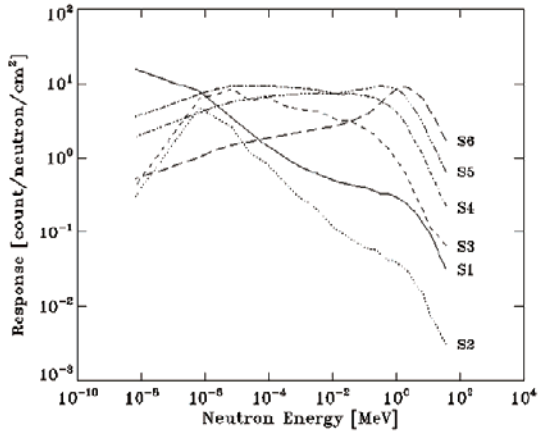

Fig。 12. Energy-response functions of each sensor for incident neutrons.

with JEM-EF, an extendible mast that extends the neutron monitor sensor 1m from the bus structure, and equipment that measures space environment data.

(1) Neutron Monitor (NM)

The NM measures the energy of neutrons from thermal to 100 MeV by two detectors, the Bonner Ball Detector (Thermal-15MeV) and the Scintillation Fiber Detector (15MeV- 100MeV) in real time. The Bonner Ball Detector discriminates neutrons from other charged particles by ^{3}He proportional gas counters, which have high sensitivity to thermal neutrons, and measures the energy of neutrons by using relative responses that correspond to different polyethylene moderator thicknesses, with the same specifications as the precursor measurements on space-shuttle (1998)and ISS inside(2001). The next paragraph shows more detail. The Scintillation Fiber Detector measures tracks of incident particles by a cubic arrangement sensor (consisting of a stack of 512 scintillator sticks), discriminates neutrons by using differences of these tracks, and measures energy of neutrons by measuring track length.

The BBND has six sensors. A two-inch spherical He^3 proportional counter is placed at the center of each sensor. Some sensors are covered with two neutron moderators as shown in Figure 11
. One is polyethylene spheres with thickness of 1.5mm, 3mm, 5mm, and 9mm, to make each sensor have different energy-response functions for incident neutrons in Figure 12. Another is a gadolinium cover with 1mm thickness in order to eliminate thermal neutrons. The energy-response functions of each sensor for incident neutrons in the assembled configuration in Figure 13 were evaluated by the numerical calculation based on the individual calibration result of each sensor obtained from irradiation experiments. The available energy range is from thermal neutron (0.025eV) through 15MeV.

The BBND hardware was launched on 8th Mar. 2001 by STS-102, and was onboard US Laboratory Module of ISS on 14th Mar. The investigation was carried out from 23rd Mar. through 14th Nov. for over eight months, corresponding to solar-activity maximum period. By applying the energy-response functions of each sensor in Figure 1 to the obtained raw data via an unfolding code NEUPAC-83[4], the differential neutron energy spectrum is obtained. Armstrong's data[5] as an initial conditions, and the assumption of the shield-thickness to be 20g/cm^2 of Alminum[6] are used in the unfolding procedure. The dose-quivqlent is also evaluated by using ICRP-74 coefficient.

Figure 14 shows the neutron energy spectrum averaged for the whole investigation period compared with the result of precursor investigation on board the STS-89[3] in 1998. The major cause of secondary neutrons inside the ISS measured by the BBND is galactic cosmic rays[7], which have the anti-correlation variation with the 11-year solar-activity. The flux obtained by the BBND is, therefore, consistently lower than that in the precursor investigation though the actual shied thickness both for the ISS and the STS-89 are not known. Figure 15 depicts the variation of the dose-equivalent rate through the investigation. The average dose-equivalent rate is 3.9 micro Sv/hour. The highest rate is 96 micro Sv/hour which appears in the SAA region. Figure 6 illustrates the distribution of the

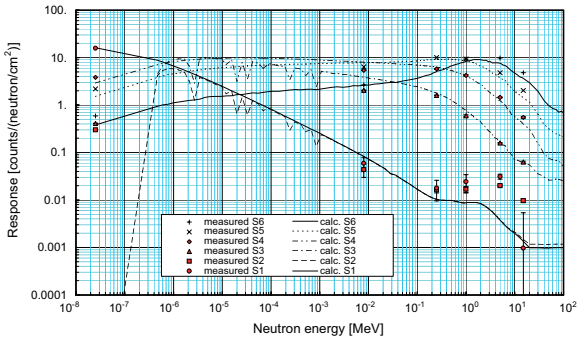

Fig. 13. Assembled configuration of the BBND sensors.

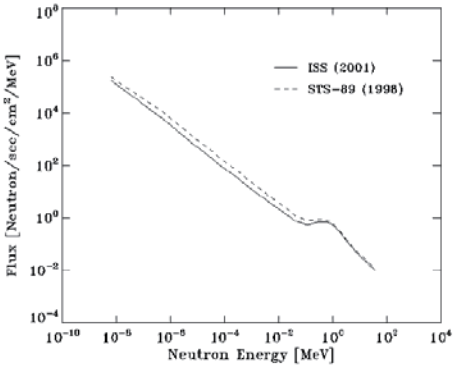

Fig. 14. Neutron energy spectrum averaged for the whole investigation period in comparison with the result of precursor investigation on board the STS-89 in 1998.

dose-equivalent rate averaged for the whole investigation period. The whole aspect of distribution is due to the geomagnetic rigidity cut off for galactic cosmic rays at the ISS orbital altitude except in the SAA region where the trapped protons cause the high rate.

(2) Heavy Ion Telescope (HIT)
The HIT uses a solid-state detector to measure the energy distribution of heavy ions (Li-Fe) that cause single-event anomalies and damage of electronic devices. The solid-state detector converts loss energy of heavy ions in the detector to electrical signals. The HIT measures incident particle mass from loss energy in each layer (delta-E) and total loss energy of each layer (E) by the delta-ExE method, with the same specifications as the ALOS.
(3) Plasma Monitor (PLAM)
The PLAM measures density and electron temperature of space plasma, which cause charging and discharging of spacecraft, by the Langmuir probe.
(4) Standard Dose Monitor (SDOM)
The SDOM measures energy distribution of high-energy light particles such as electrons, protons, and particles that cause single-event anomalies and damage electronic devices, by a solid-state detector and a scintillator, with the same specifications as the DRTS and the MDS-1.
(5) Atomic Oxygen Monitor (AOM)
The AOM measures the amount of atomic oxygen on the orbit of the ISS. The atomic oxygen interacts with the thermal control materials and paints, and lowers their thermal control ability. AOM measures the resistance of a thin carbon film that is decreased by atomic oxygen erosion.
(6) Electronic Device Evaluation Equipment (EDEE)
The EDEE measures the single-event phenomena and radiation damage of electronic parts. Single-event phenomena are induced by the impact of an energetic heavy ion or proton. The occurrence of single-event phenomena is detected by bit flips of memorized data or sudden increases of power supply current.
(7) Micro-Particles Capturer (MPAC)
The MPAC captures micro-particles that exist on orbit. Silica-aerogel and metal plates are used to capture micro-particles. After the retrieval of MPAC, size, composition, and collision energy of captured particles will be estimated.
(8) Space Environment Exposure Device (SEED)
The SEED exposes materials for space use to the real space environment. After the retrieval of SEED, degradation of these materials caused by the space environments (e.g. radiation and atomic oxygen) will be estimated.

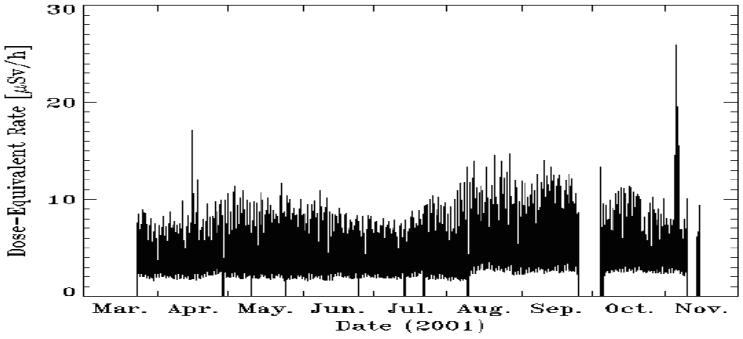

Fig. 15.　Variation of the dose-equivalent rate.

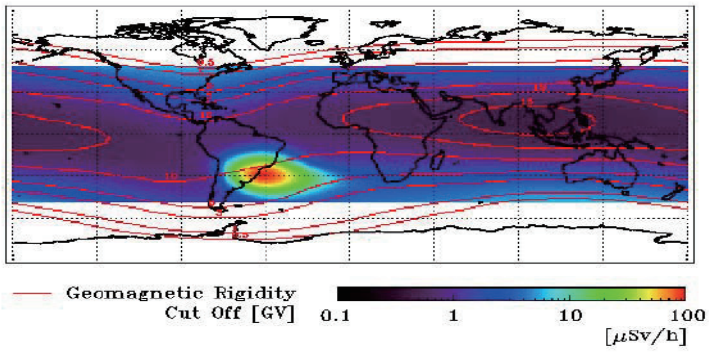

Fig. 16.　Distribution of the dose-equivalent rate averaged for the whole investigation period and overlaid with the geomagnetic rigidity cut off..

Concluding Remarks

Space environment and radiation effects measurement has been a long-term effort since 1987. Radiation monitors have been flown with almost all JAXA satellites for 20 years. This effort will be justified when new JAXA radiation belt models (electrons, protons, and alpha particles with pitch angle distributions) are developed in the very near future.

This resource will be further expanded with the instrument's flight plan on a future mission, as presented in this paper. The final goal is the creation of an international network of complementary radiation monitors providing continuous and long-term measurement of the space environment.

References

[1] Kohno, T., (1996), Current and future data available in Japan, Geophysical Monograph 97, Radiation Belts Models and Standards, J.F. Lemaire, D. Heynderickx, and D.N Baker, editors, American Geophysical Union, 217-222.

[2] Fukuda, T., T. Goka, H. Matsumoto, (1996), The Measurement of Space Environment and Effect in NASDA, IAF-96-U.3.05, 47th IAC Beijing.

[3] Goka, T., S. kuboyama, Y. Shimano, T. Kawanishi, (1991), The On-Orbit Measurement of Single Event Phenomena by ETS-V Spacecraft, IEEE Trans. On Nucl. Sci., NS-38, 1393-1699.

[4] Kawakita S., M. Imaizumi, M. Takahashi, S. Matsuda, S. Michizono, Y. Saito, (2002), Influence of High Energy Electrons and Protons on Secondary Electron Emission of Cover Glasses for Space Solar Cells, XXth International Symposium on Discharges and Electrical Insuration in Vacuum-Tours. pp. 84-87.

[5] Goka, T., H. Matsumoto, T. Fukuda, S. Takagi,(1996), Measurement of Radiation Belt Particles with ETS-6 Onboard Dosimeter, Geophysical Monograph 97, Radiation Belts Models and Standards, J.F. Lemaire, D. Heynderickx, and D.N Baker editors, American Geophysical Union, 251-254.

[6] Goka, T., H. Matsumoto, T. Fukuda, S. Takagi(1996), ,Space Environment and Effect Measurements from ETS-6 Satellite, ESA Symposium Proceedings on Environment Modelling for Space-based Applications, ESA SP-392, 51-57.

[7] Goka, T., H. Matsumoto, T. Fukuda, S. Takagi, (1996), Predictions of the Radiation Belt Particle Flux Variations from ETS-6 In-flight Measurements, Proceedings of a workshop Solar-Terrestrial Predictions-V edited by G. Heckman, K. Marubashi, M. A. Sh ea, D. F. Smart, R. Thompson, 476-479.

[8] Goka, T., H. Matsumoto, S. Takagi, (1999), Empirical model based on the measurements of the Japanese spacecraft, Radiation Measurements 30, pp.617-624.

[9] Kohno, T., H. Miyasaka, H. Kato, C. Kato, T.Goka, H. Matsumoto, (1998), Heavy Ion Radiation in Space Obseved by Japanese Satellite, Proceedings of the 3rd International Workshop on Radiation Effects on Semicinductor Devices for Space Application, 90-95.

[10] Kimoto, T., H. Matsumoto, et al, (2002), Outline of Space Radiation & Effect Monitor on board ADEOS-II, 23rd ISTS proceeding, pp.1730-1734.

[11] Goka, T., H. Matsumoto, K. Koga, Y. Kimoto,(2005), Space Environment Effects on two Satellite Anomalies in Oct. 2003 Stor m, AIAA, IAC-04-IAA.4.9.3.U.6.01, 56th IAC, Vancover,

[12] Matsumoto. H., H. Koshiishi, T. Goka, Y. Kimoto, B. D. Green, G.E. Galica,T. Nakamura, T. Abe, S. Badono,S.Murata, J. D. Sulliban, (2001), Compact, Lightweight Spectrometer for Energetic Particles, IEEE Trans. Nuclear Science, N S-48, No.6, 2043-2049.

[13] Goka, T., et al, (2002), Space Environment & Effect Measurements From The MDS-1 (Tsubasa) Satellite, 23rd ISTS proceeding, pp.1747-1754.

[14] Koshiishi, H, H. Matsumoto, Y. Kimoto, H. Liu and T. Goka, (2002), Space Environment Data Acquisition Equipment on Board Mission Demonstration Test Satellite, COSPAR Colloquia Series, Solar-Terrestrial Magnetic Activity and Space Environment, edited by H. Wang, R. Xu, pp.369-371.

[15] Kimoto, Y., H. Koshiishi, H.. Matsumoto, T.Goka, (2003), Total dose orbital data by dosimeter onboard tsubasa (MDS-1) satellite, IEEE Trans. Nucl. Sci. vol.50, No6, pp.2301-2305.

[16] Vette, J. I., (1991), The AE-8 trapped electron model environment, NSSDC/WDC-A-R&S76-06, NASA /Goddard Space Flight Center.

[17] Sawyer, D. M., Vette, J. I., (1991), AP-8 trapped proton environment for solar maximum and solar minmum, NSS DC/WDC-A-R&S76-06, NASA /Goddard Space Flight Center.

[18] Matsumoto, H., H. Koshiishi, T. Goka, (2006), MDS-1 Data Base and Radiation Belts Model, CO.1-0015-16, 36th COSPAR, Beijing China, 2006.

[19] Sasaki Y., H. Matsumoto, T. Nakamura, T. Goka, Development of Technical Data Acquisition Equipment on board GOSAT, (2006), IEICE General Conference 2006.

[20] Komiyama T., H. Matsumoto, T. Goka, JAXA/CNES Joint Radiations experiment onboard Jason-2 satellite, (2006), IEICE General Conference 2006.

[21] Bramblett, R.L., Ewing, R.I. and Bonner, T.W. (1960). A New Type Neutron Spectrometer. Nucl. Instr. and Meth. 9, 1.

[22] Lockwood, J.A. (1973). Neutron Measurements in Space. Space. Sci. Rev. 14, 663.

[23] Matsumoto, H., Goka, T., Koga, K., Iwai, S., Uehara. T., Sato, O. and Takagi, S. (2001). Real-Time Measurement of Low-Energy-Range Neutron Spectra on board the Space Shuttle STS-89 (S/MM-8). Radiat. Meas. 33, 321.

[24] Taniguchi, T., Ueda, N., Nakazawa, M. and Sekiguchi, A. (1983). Neutron Unfolding Package Code "NEUPAC-83". NEUT Research Report 83.

[25] Armstrong, T.W., Chandler, K.C. and Barish, J. (1973). Calculations of Neutron Flux Spectra Induced in the Earth's Atmosphere by Galactic Cosmic Rays. J. Geophys. Res. 78, 2715.

[26] Armstrong, T.W.and Colborn, B.L. (2001). Predictions of Secondary Neutrons and Their Importance to Radiation Effects inside the International Space Station. Radiat. Meas. 33, 229.

[27] Benton, E.R. and Benton, E.V. (2001). Space radiation dosimetry in low-earth orbit and beyond. Nucl. Instr. and Meth. B184, 255.

[28] Koshiishi, H., H. Matsumoto, A. Chishiki, T. Goka, T. Omodaka, Evaluation of the neutron radiation environment inside the International Space station based on the Bonner Ball Neutron Detector experiment, Radiation Measurenment 42 (2007) 1510-1520.

Spacecraft design guideline in JAXA ;Quality assurance design guideline for solar panel , Insulation and spacecraft charging

Japan Aerospace Exploration Agency
Space power engineering group
K. Nitta[1]

JAXA design guideline

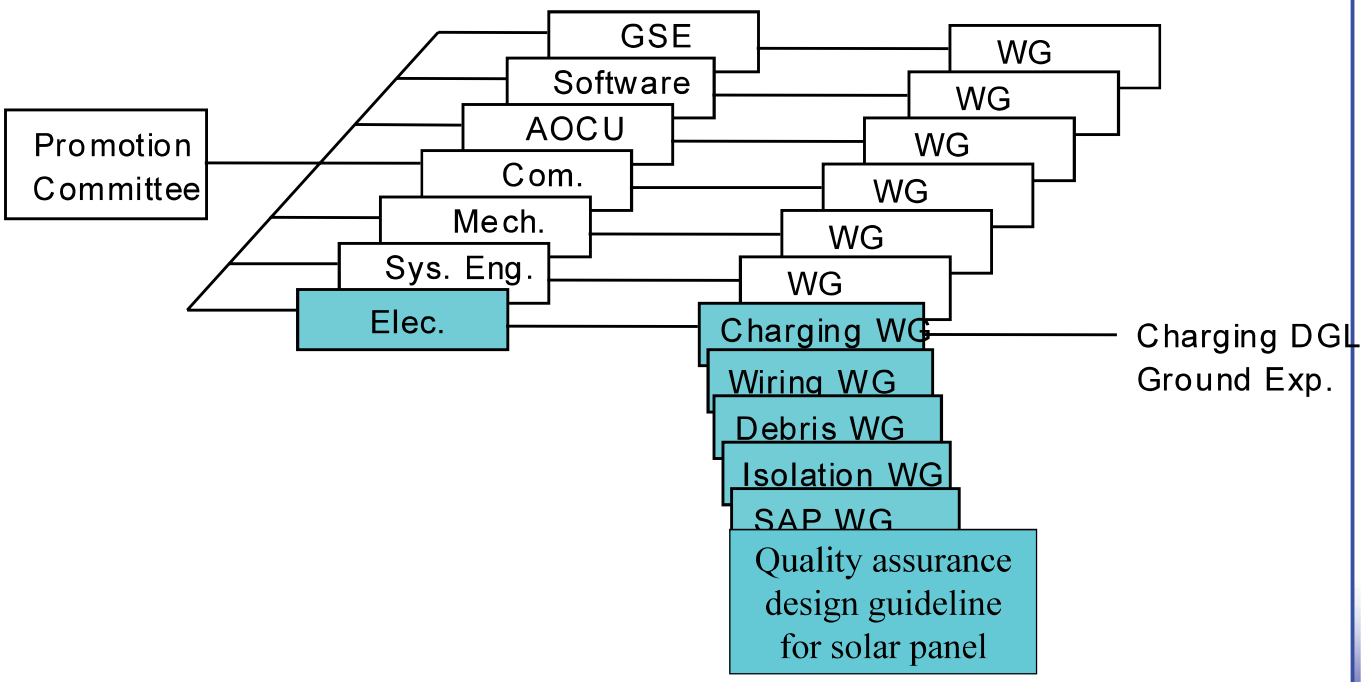

2

Applicable Documents

The following normative documents contain previsions which, through reference in this guideline, constitute provisions of this JAXA design guideline.

- ISO 15387(Single-junction space solar cells-Measurement and calibration procedures)
- ISO 23038 Space Solar Cells-Electron & proton irradiation test methods)
- JAXA-QTS2130
- WG1 JAXA charging design guideline
- WG11 JAXA electric power design guideline

3

Quality assurance guideline

- Objective
  - This guideline provide quality assurance approach for solar panel
- Scope
  - This guideline provides general requirements for solar panel, built with processes, materials, and components that are flight-qualified or proposed flight qualification. The requirements allow for the tailoring in accordance with the aim of each spacecraft projects.

4

Terms and definitions

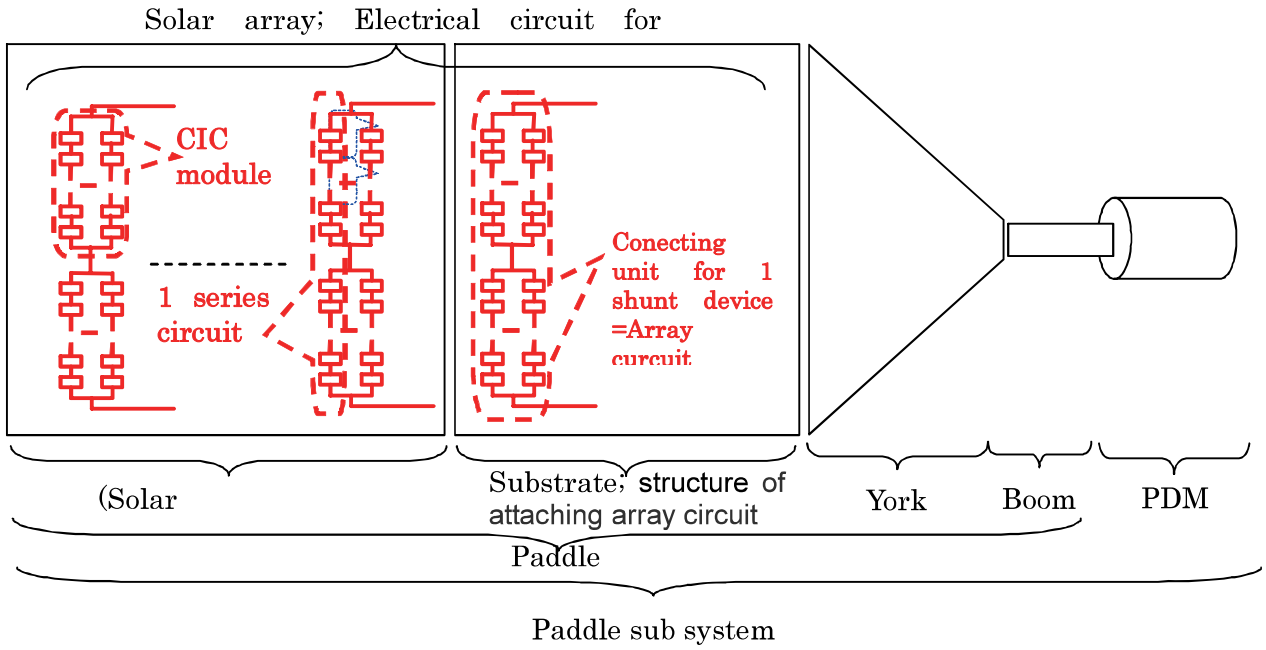

5

Flow on Development of Solar Array Panel

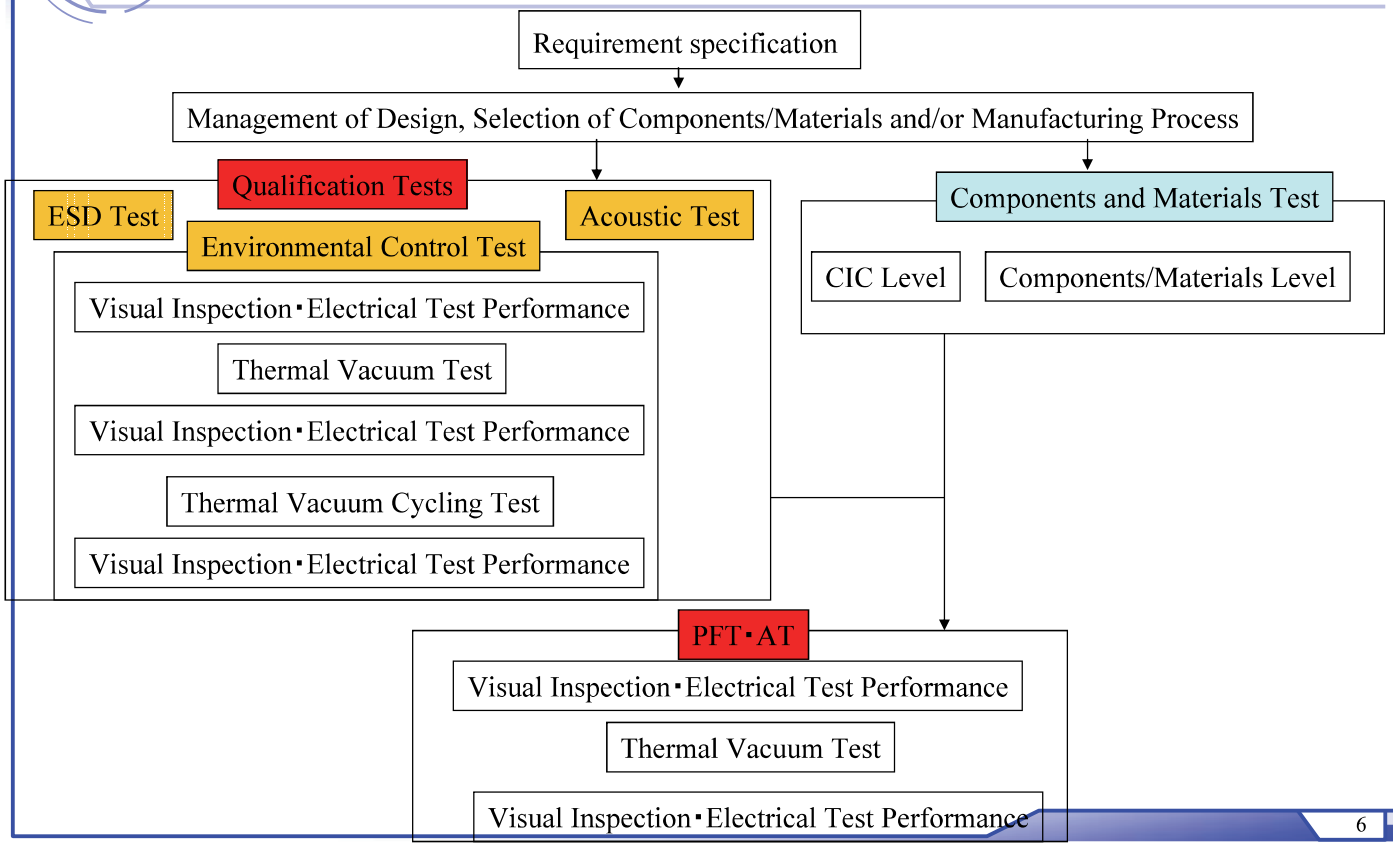

6

Summary of Qualification and Characterization Tests

No	Qualification and Characterization Test	Test specimen	Status		
			Development	QT	PFT/AT
1	Electrical test performance	Coupon、CIC、Full-sized flight panel	O	O	O
2	Visual inspection	Coupon、CIC、Full-sized flight panel	O	O	O
3	Thermal vacuum test	Coupon、Full-sized flight panel	O	O	O
4	Thermal vacuum cycling Test	Coupon	O	O	
5	Acoustic test	Full-sized flight panel	O	O/Paddle	Paddle
6	ESD(Charging･discharging experiment)	Coupon	O	O	
7	hemispherical emissivity characterization	CIC(Electronic, mechanical components)	O		
8	Solar absorptance characterization	CIC(Electronic, mechanical components)	O		
9	UV radiation effect characterization	CIC(Electronic, mechanical components)	O		
10	Atomic oxygen exposure	Electronic, mechanical components	O		
11	Angle of incidence characterization	CIC(Electronic, mechanical components)	O		
12	(＊)CIC electrostatic discharge sensitivity characterization	CIC(Electronic, mechanical components)	O		
13	(＊)Four-point bending(Three point bending)	CIC(Electronic, mechanical components)	O		
14	Humidity test	CIC(Electronic, mechanical components)	O		
15	Out-gases	Electronic, mechanical components	O		

7

Conclusion and Future for quality assurance guideline of solar panel

- We introduced a project for quality assurance guideline of solar panel in JAXA.
- We explained about the quality assurance guideline
- We decide to the detail based on the some experiments, analysis and Experience.
- We will not only conducts experiments, but designs the research and analyzes the results as needed from next year like the charging design WG1 and WG5.

8

Insulation design guideline

・Objective

Principal and accessory power source bus

Primary power source bus upper and including separator circuit for short-circuit fault

Double insulation

Vacuum insulation, plastic mold, coating etc….

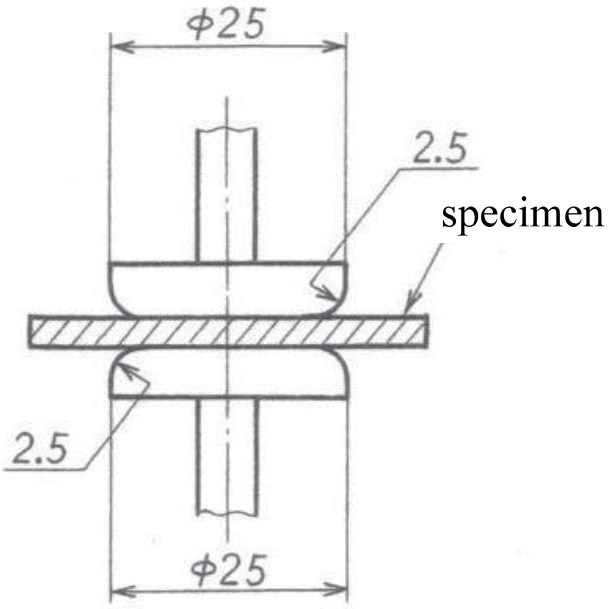

9

Dielectric Strength on Space Materials on WG5

Materials:
PTFE tape, Kapton tape, CHO THERM, SOLITHANE, PARYLENE, Mica, URALANE, LUMIRROR, Thermal Shrink tube, Glass epoxy, RTV, ETFE wire

Factors:
Temperature, Thickness, Frequency, Time, Electron Beam, UV

Test Methods:

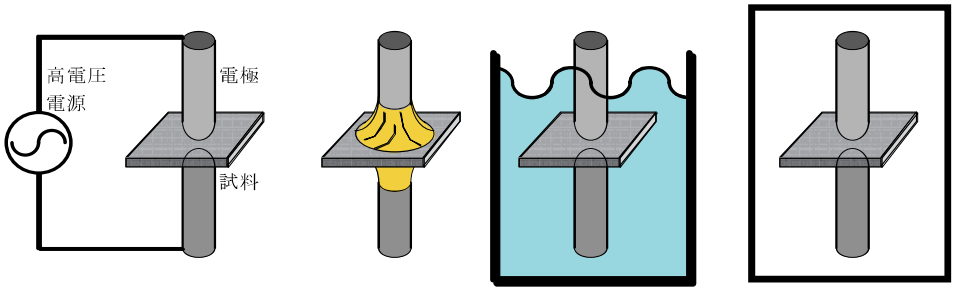

in air　resin coating　oil dip　in vacuum

10

Design Flow on Insulation design

- Depend on Insulation material, thickness, actuation temperature, and transmission frequency
- Electrical field strength coefficient Rt at 6mil

1mil=＝0.0254mm

- Temperature delating coefficient Rc
- Frequency delaiting coefficient Rf
- Electrical field strength E for operating time

Maximum allowable actuation voltage
=Rt × Rc × Rf × E × t

11

Proposed Design on Isolation Voltage

Example
Material : Mica
Isolation Voltage : 8kV@0.07mm
Thickness : 0.15mm
Max. Temperature : 50℃
Frequency : 100Hz
Electron Beam : 100kGy
Time : 10year

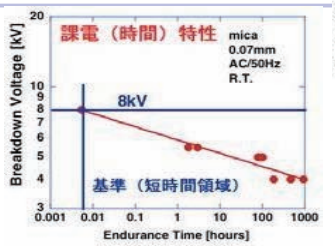

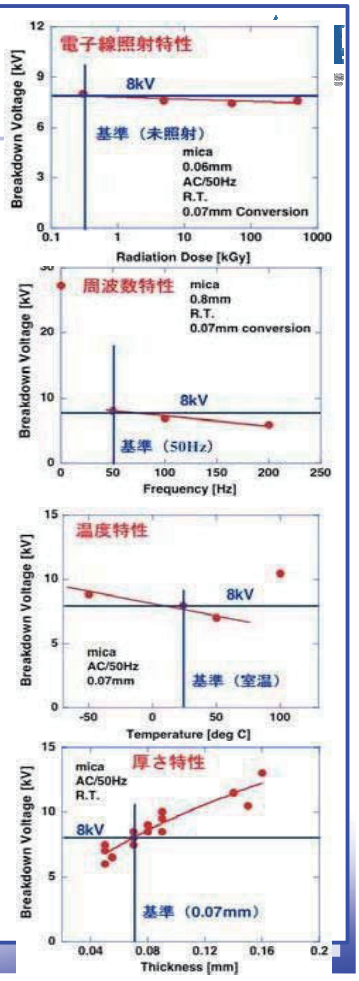

Thickness Effect	$R_t = 1.60$
Temperature Effect	$R_c = 0.88$
Frequency Effect	$R_f = 0.94$
Electron Beam Effect	$R_e = 0.95$
Time Effect	$R_h = 0.44$

Maximum Isolation Voltage V_m

$$V_m = 8[kV] \times R_t \times R_c \times R_f \times R_e \times R_h = 4.4[kV]$$

JAXA Activities on Spacecraft Charging

Design Flow on Satellite Charging

Case of ALOS (Daichi Satellite)

Redesign of diode boards in rear of SAP

Requirements
Polar 700km alt.
4ton
7kW BOL

Design Guidelines

Numerical Assessment

Launched Jan. 2006

Laboratory test in KIT

13

MUSCAT Satellite Charging Analysis Tool on WG1

Secondary Electron Emission on WINDS GEOsat.

Emax=800(eV), δemax=11 on CG

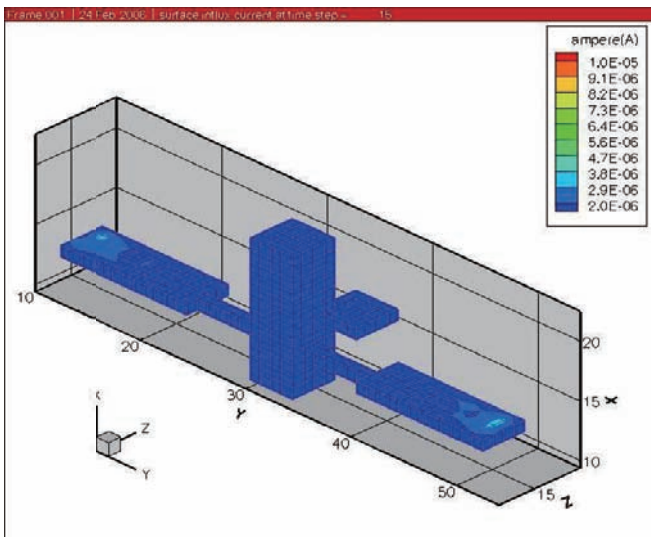

12 sec

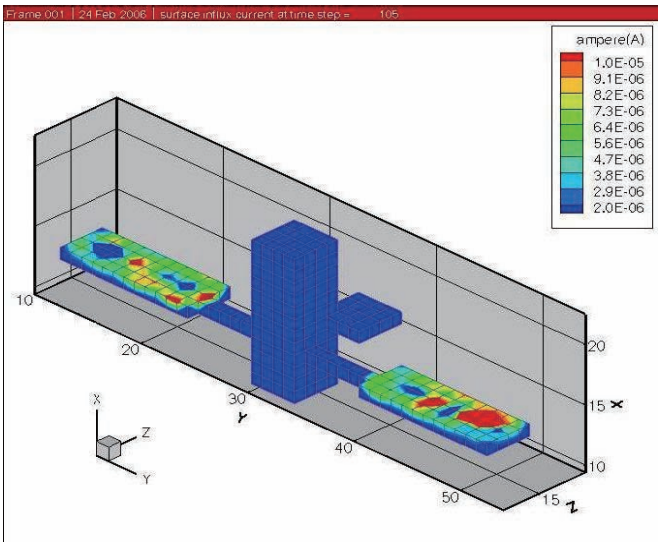

84 sec

14

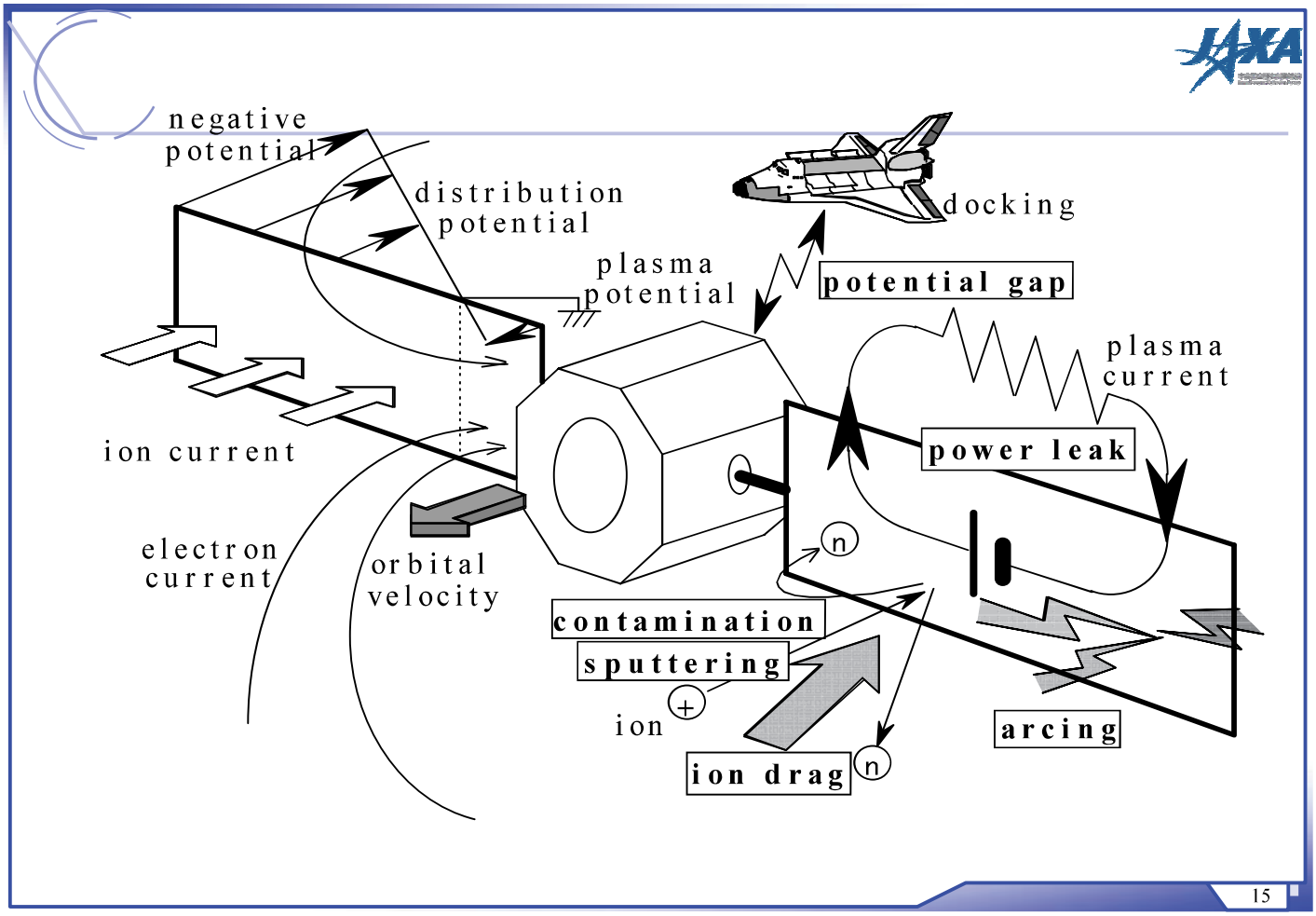

SCP Design example: Hayabusa

In order to protect the plasma interaction between SCP and EP

Triple junction cells
Max. operational voltage 120V
The voltage gap between the neighboring cells is less than 50V.
No care of canceling on the magnetic field due to the current loop on SCP
The cells along the SCP edge expose voltage less than 30V.
Bus bars of the solar cells are coated by RTV.

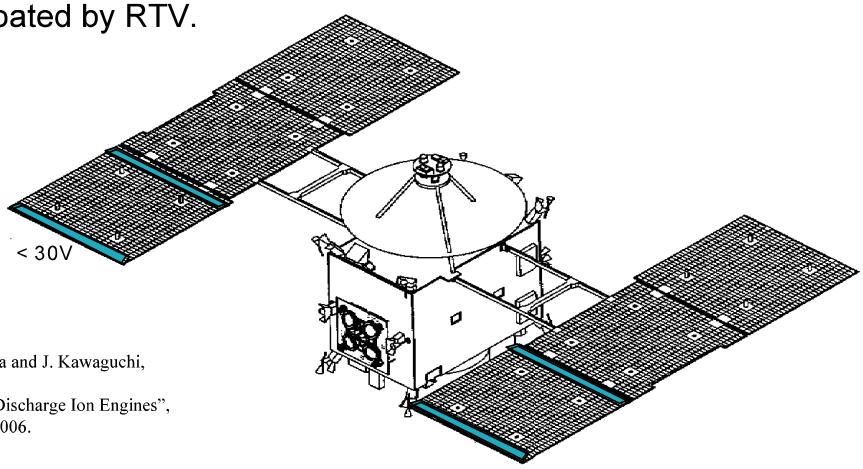

H. Kuninaka, K. Nishiyama, I. Funaki, Y. Shimizu, T. Yamada and J. Kawaguchi, "Assessment of Plasma Interactions and Flight Status of HAYABUSA Asteroid Explorer Propelled by Microwave Discharge Ion Engines", IEEE Transaction of plasma Science, Vol.34, No.5, October 2006.

Material properties measurements related to spacecraft charging

To make database of pure (BOL) or deterioration (EOL) material properties of spacecraft surface related to the electrostatic charge phenomena

MUSCAT
(Multi-Utility Spacecraft Charging Analysis Tool)

input	output
Ambient plasma Material property Structure	Surface potential Inner potential difference

17

List of material properties needed for Charging analysis

- **Secondary electron emission ("Delta Max" and "E-Max")**
- **Photoelectron emission**
- **Bulk resistivity**
- **Surface resistivity**
- **Diel**
- **A**

We can not measure the mean atomic numbers for chemical compounds, the elect… induced

We have to ask the mean atomic numbers, the mean atomic weight (AMU) and the material density to material companies

etc.

18

Framework for the Measurements of Materials Properties Parameter

We conduct joint studies for the following

Material property	The range of primary energy	Place
Secondary electron emission (SEE)	Accelerating voltage : 600V-5kV	The High Energy Accelerator Research Organization (KEK)
	Accelerating voltage : 200V-1kV	Musashi Institute of Technology
Photoelectron emission (PE)	Wavelength 110 to 400 nm	Musashi Institute of Technology
Bulk resistivity, Surface resistivity		Saitama University
Dielectric Constant		Sumitomo Metal Technology Inc.

19

Conclusion

- We introduced a project for quality assurance guideline of solar panel in JAXA.
- We explained about a part of the research and analyzes the results for the charging design WG1 and insulation design WG5.

20

－ＭＥＭＯ－

宇宙環境計測・宇宙天気

Space environment measurement & Space weather

Highly Energetic Electron Environment in the Inner Magnetosphere

T.Obara[1,2], H.Matsumoto[2] , K. Koga[2], H, Koshiishi[2] and T.Goka[2]

[1] *National Institutive of Information and Communications Technology, Koganei, Tokyo 184-8795, Japan*
[2] *Japan Aerospace Exploration Agency, Tsukuba, Ibaraki 305-8505, Japan*

ABSTRACT

Highly energetic electrons in the outer radiation disappear during the main phase of the magnetic storm, and rebuilding of the highly energetic electrons is made during the recovery phase of the magnetic storm. A distribution of the new peak of highly energetic electron flux with respect to the distance from the Earth is inversely proportional to the magnitude of the magnetic storm. In case of the super storm, the outer electron belt is pushed toward the Earth, filling so-called slot region. It is of interest to identify that the location of the intense low frequency plasma waves, which appear during the storm recovery phase, coincides with the location of the peak intensity of the highly energetic electrons in the outer radiation belt. This coincidence strongly suggests that an internal acceleration process takes place which leads to a large increase in the intensity of highly energetic electrons in the outer radiation belt during the storm recovery phase. A seasonal variation of the outer radiation belt is identified. The increase in the intensity of the highly energetic electrons is large both in spring and autumn seasons. The magnetic activity is also large both in spring and autumn seasons. Correlation of the increase in the intensity of highly energetic electrons with the magnetic activity is identified. A solar cycle variation of the outer radiation belt is identified. The location of the outer radiation belt was found closer to the Earth during the solar maximum periods and far from the Earth during the solar minimum periods. This variation is due to the evidence that large magnetic storms occur largely during the solar maximum periods, while small magnetic storms take place largely during the solar minimum periods, resulting a long-term solar cycle variation with respect to the distance from the Earth.

DYNAMIC BEHAVIOR OF THE HIGHLY ENERGETIC ELECTRON OUTER BELT DURING THE MAGNETIC STORM

Mission demonstration satellite 1 (MDS-1) was launched on Feb.4, 2002 into the geostationary transfer orbit (GTO) with an inclination of 28 degree and an orbital period of 10 hours. The MDS-1 satellite was renamed TSUBASA, meaning wings after launch. On this satellite a high energy particle detector was installed. The results are given in Fig.1. Top panel in the figure shows *L* - t diagram, where the vertical axis shows *L* - value ranging from *L* = 1 to 9 and the horizontal axis gives time covering three months with a start of April 1, 2002. We can see electron flux enhancements many times. These enhancements are caused by the magnetic storms. One example showing the dynamic variation of the electron outer radiation is given in Fig.2. Vertical axis shows the flux of 0.4-0.91 MeV electrons and horizontal axis is *L*-value. Around noon of April 17, a magnetic storm started and the *Dst* reached –120

nT early of April 18. The storm developed once again on April 19 and the *Dst* reached its minimum (-150nT) early on April 20 and then recovered gradually.

Individual measurements of MDS-1 are given in Fig. 2. Around 18UT on April 16, there was a peak of outer electron belt at L = 5 and it persisted till 09UT on April 17. The flux then decreased largely by 15UT on April 17; only a few hours after the commencement of the storm. The peak flux decreased more than one order of the

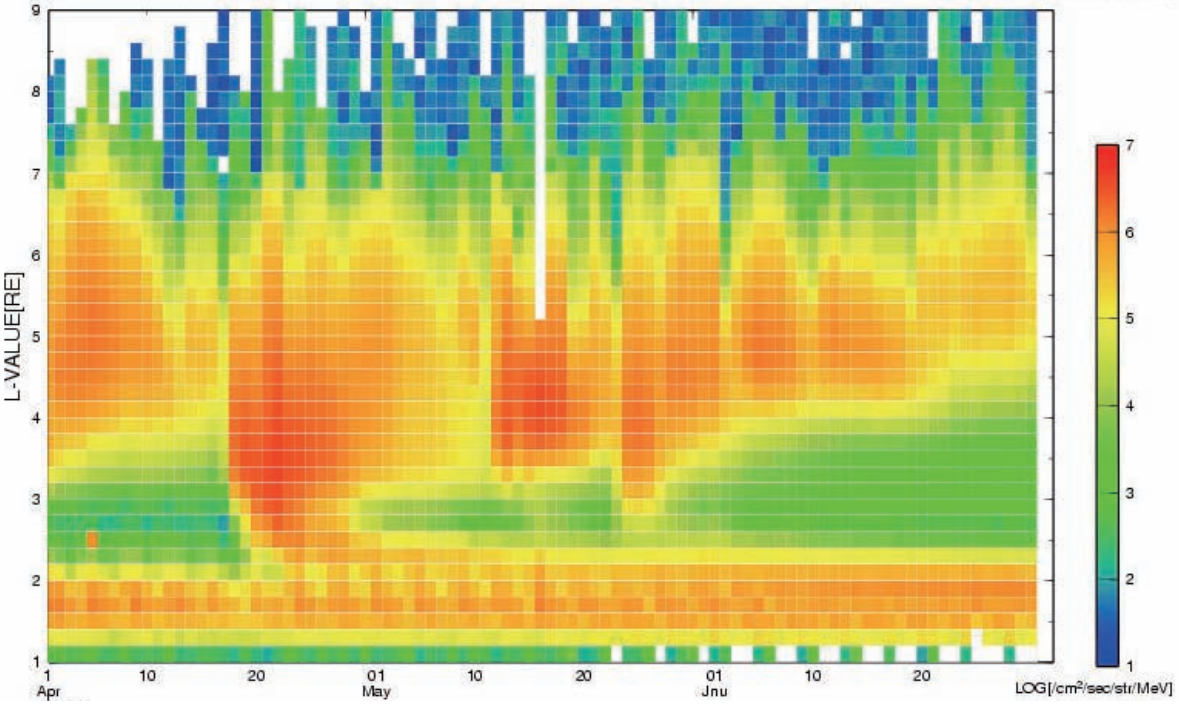

Fig.1. *L*-t diagram of 0.4 MeV to 0.91 MeV electrons and *Dst* index in 2002.

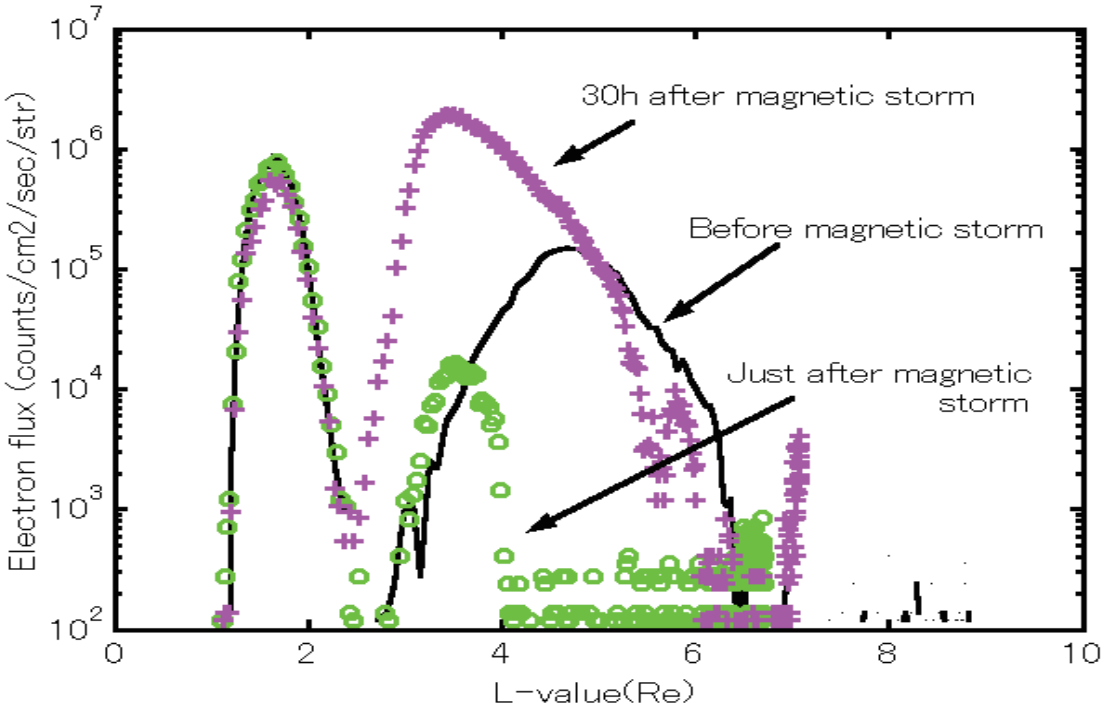

Fig.2. Variation of radiation belt profile measured by MDS-1 satellite. Each line demonstrates flux of electrons in the unit of $(cm^2\ sec\ st.\ MeV)^{-1}$, covering three days from April 16 to April 18.

magnitude and the peak location approached the Earth: i.e. L = 3.5. The magnetic storm continued on April 18, keeping *Dst* index around –100 nT. There were prolonged magnetic activities over April 18 producing quasi-periodic substorm injections every three hours or so. First injection was identified around 3UT by the LANL satellite and strong disturbances of the magnetic field were seen by the ground-based magnetometer. Due to this prolonged magnetic activities the flux of outer belt electrons increased significantly, exceeding pre-storm level. It should be mentioned that a new peak location of the outer radiation belt shifted toward the Earth; i.e. L = 3.5, which is consistent with Akebono simultaneous measurements and also consistent with statistical result (Obara et al., 2000).

During the life-time of MDS-1 satellite; i.e. one year and half, there were almost 30 enhancements in the flux of outer belt electrons with energy of 0.4 – 0.95 MeV. The results are given in Fig. 3, in which a peak position of newly formed outer belt during the storm recovery phase is plotted as a function of minimum *Dst* of each storm. There seems to be a correlation of the peak position and *Dst* value; a large storm produces a new outer electron belt closer to the Earth. This result is largely consistent with Obara et al. (2000) and O'Brian et al. (2003).

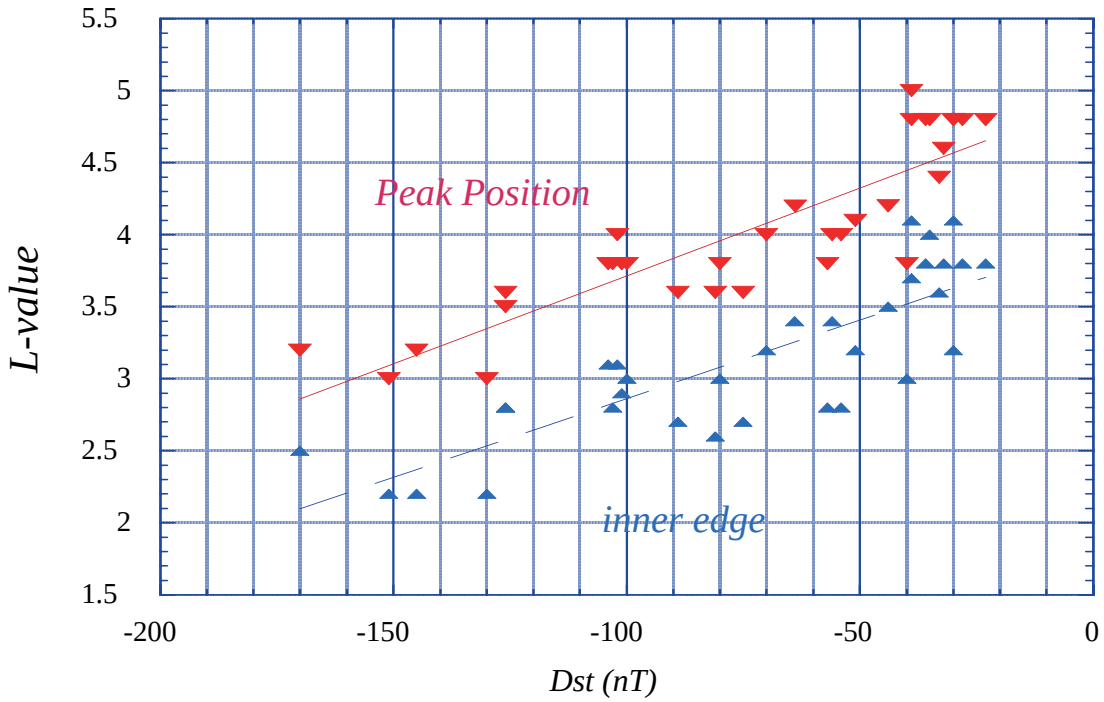

Fig. 3. Peak position of newly developed outer belt as a function of *Dst*. Inner edge of the newly formed belt is also plotted.

MDS-1 measurements show a clear relationship between the peak position of the energetic electron flux and *Dst* variations. This tendency is largely consistent with previous works Obara et al. (2000), O'Brian et al. (2003) and Tverskaya (2002). This is consistent with being caused by the transport of seed electrons during the main phase or early recovery phase (Obara et al., 2001). Advantage of MDS-1 measurement is that the observation has been made near the magnetic equator. We can clearly identify the inner edge of newly developed outer electron belt as given in Fig. 3. Location of inner edge is much closer to the Earth than that of peak location. This means that the transport of seed electrons is quite efficient near the Earth than as expected. Detail processes are however unclear at present. We need to investigate energetic electron transport mechanisms much more thoroughly.

The Akebono satellite measured VLF (very low frequency) chorus emissions along the orbit. The peak location

of wave amplitude largely coincides with that of energetic electrons (Obara et al., 2006). Whistler mode chorus emission can accelerate seed electrons up to MeV range (Obara et al., 2000 and 2001, Miyoshi et al., 2003). MDS-1 and Akebono measurements show the coexistence of energetic electron enhancements and the VLF chorus emissions. These observations confirm many results found using the previous satellites in the different orbit. Next step will be the quantitative study how the VLF waves produce relativistic electrons in the outer radiation belt.

Important physics of the outer electron radiation belt includes injection or transportation of seed electrons, acceleration of electrons. We have examined these issues by investigating super storm events. Outer belt electrons are pushed toward the Earth very rapidly at the commencement of the super storms, filling the slot region. One example is given in Fig.4, where electron fluxes with energy of >300 keV is demonstrated in the top of the figure as a function of time. *Dst* index is given in the bottom panel. On day of 197 in 2000 an intense interplanetary shock wave hit the Earth, causing a terrible large magnetic storm. The *Dst* index reached down to –300 nT. NOAA satellite measured the >300 keV electrons on the morning-evening meridian plane with an orbital period of 90 min. With a development of the storm main phase, energetic electrons were pushed toward the Earth, forming a new radiation belt in the slot region. By day of 199 additional population of 300 keV electrons has been produced in the outer radiation zone; i.e. ranging up to L=5 or so. On day of 202 a slight but significant depletion of 300 keV electrons is identified around L=3, which became slot (Obara et al., 2005).

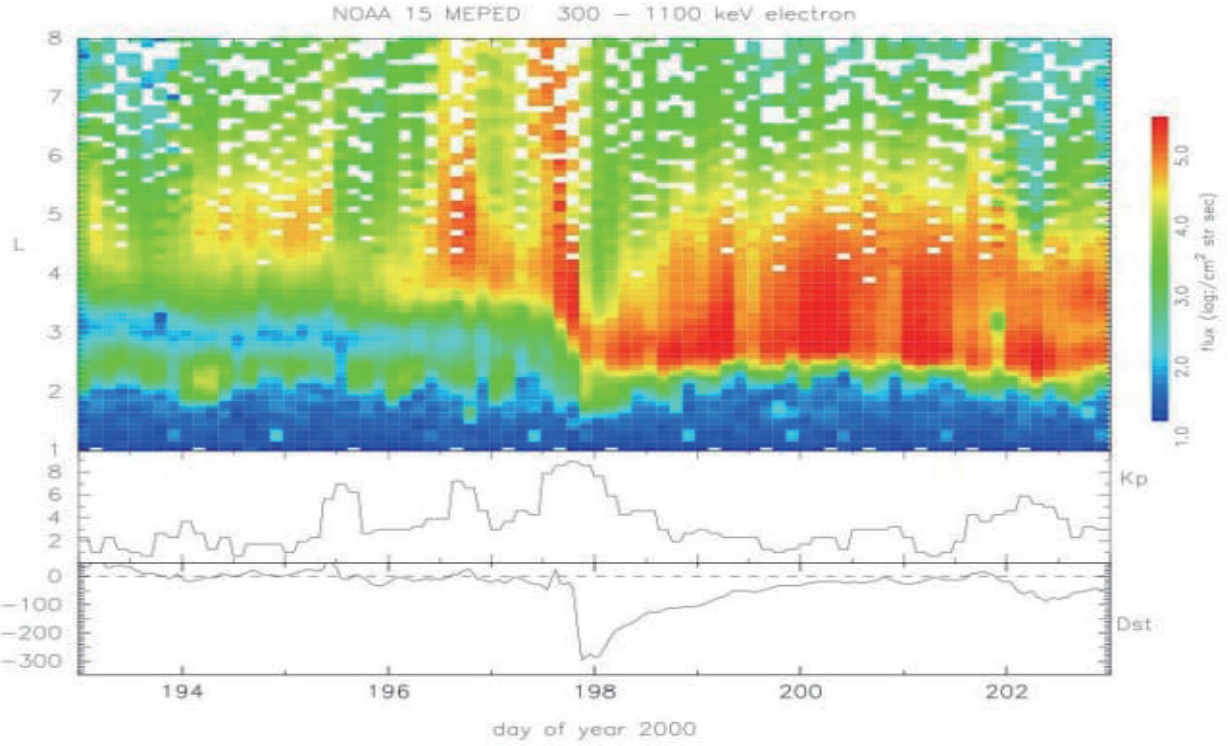

Fig. 4. *L*-t diagram for electrons with energies of >300keV (top), *Kp* index (middle) and *Dst* index (bottom) for the Bastille day super storm. Electron data were measured by NOAA 15 satellite.

Large transport of outer radiation belt electrons might be caused by the enhanced convection which reaches down to L=2.5 during the main phase of the super storm. Several satellites such as DMSP and Akebono have observed such enhanced convection in a subauroral and middle latitude zone. We believe the transport is made by this enhanced convection rather than the SC induced electric field proposed by Hudson et al. (1997), since it took several

hours for the movement of the inner edge of outer electron belt to the slot region. During the recovery phase of the super storm, a large enhancement in the intensity of energetic electrons around L=4 was seen. By analyzing Akebono radiation electron data we have obtained a large increase of phase space density, which means additional internal acceleration actually took place in the heart of outer radiation belt (Obara et al., 2005).

LONG-TERM VARIATIONS IN THE OUTER RADIATION BELT ELECTRONS

Interesting feature of the outer electron radiation belt in a long-time scale has been identified in the MDS-1 data. Fig. 5 demonstrates observations of highly energetic electrons by the MDS-1 together with MEO. MED is a geostationary transfer orbit satellite which is largely same with MDS-1 but one difference is inclination of the orbit.

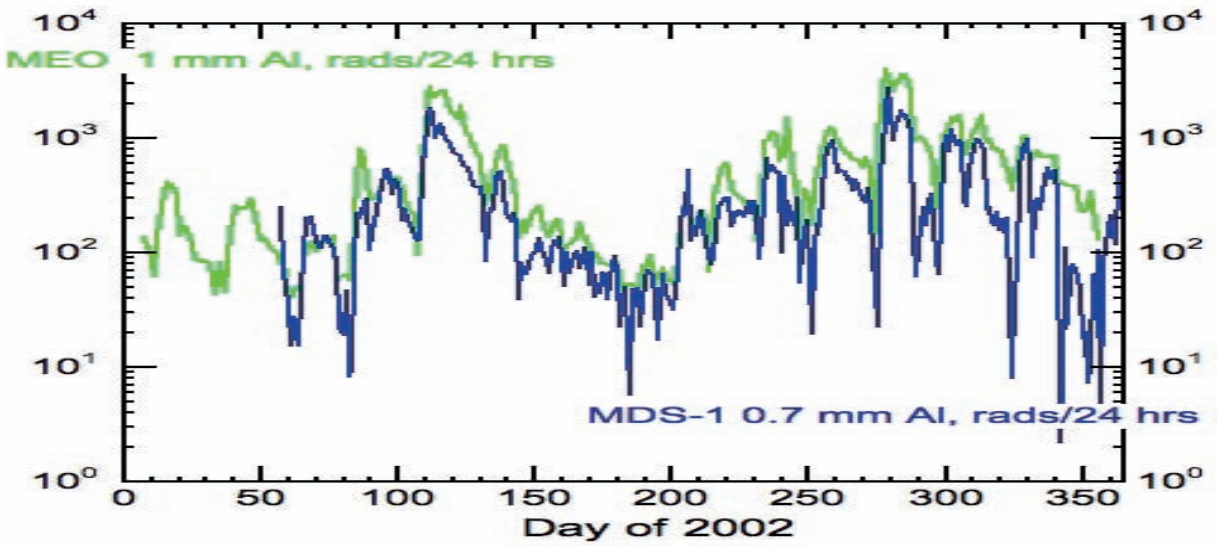

Fig. 5. Variation of total dose form MDS-1 and MEO satellites. Large increase is seen both in spring and autumn seasons.

We can see two peaks in the intensity of total dose. Peak appears both in spring and autumn seasons. Though inclinations of both satellites are differ, two lines in Fig. 5 show almost same intensity. This means that highly energetic electrons have isotropic nature, and this is consistent with pitch angle measurements by MDS-1 (Obara et al., 2006). Why the magnetic activities are high both in spring and autumn is the effect of the tilting of the Earth's magnetic field. If the intensity of highly energetic electrons increases due to the large magnetic activities, this evidence supports the internal acceleration model proposed by Obara et al. (2001).

Interesting feature of the outer electron radiation belt in a long-time scale has been identified in the NOAA data. Fig. 6 demonstrates observations of >300 keV electrons for more than 20 years. A location of the outer radiation belt was found to be closer to the Earth during the solar maximum periods and far from the Earth during the solar minimum periods. Location of the outer radiation belt is decided by the magnitude of magnetic storm (Obara et al., 2000) and the occurrence probability of the large magnetic storm is high during the solar maximum periods. Portions with red circles in Fig.6 demonstrate the periods when the big magnetic storms actually took place.

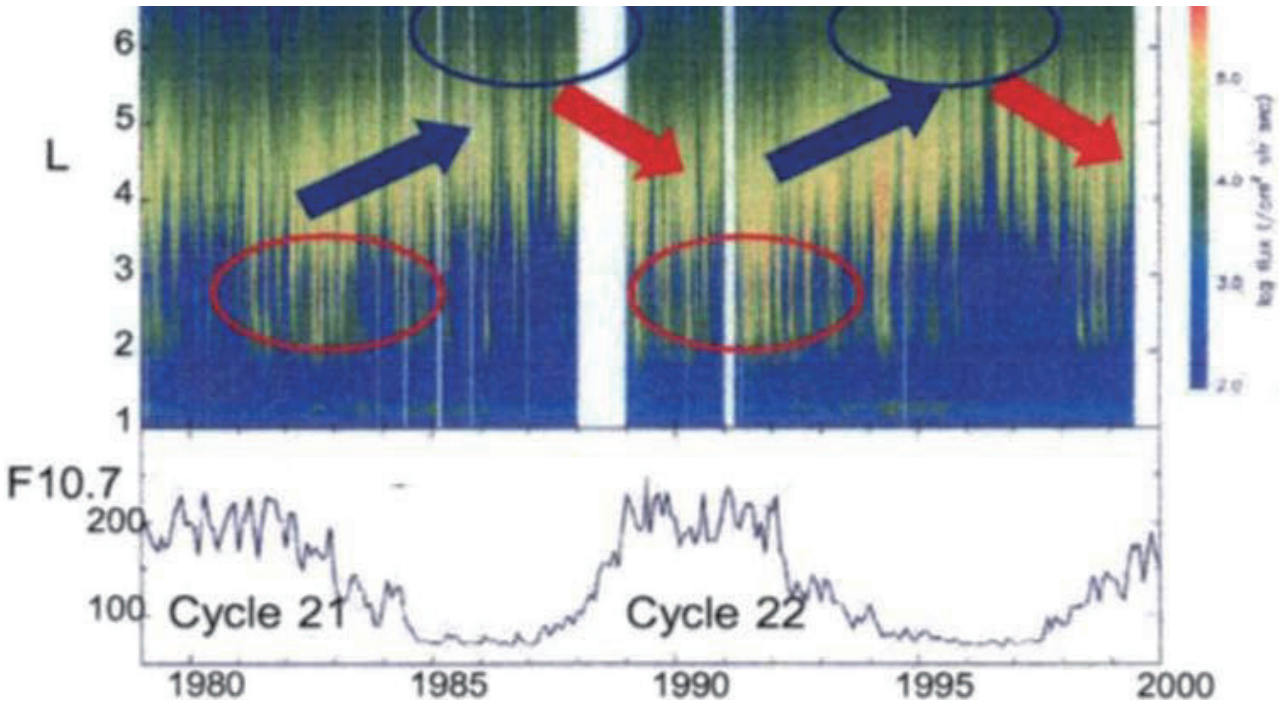

Fig. 6. Lon-term variation of >300keV electrons fort he last two decades. Bottom panel shows F10.7 flux. Enhancement of the electrons in the slot region is evident during the solar maximum periods (Miyoshi et al., 2004).

A highly energetic electron at geostationary orbit altitude is enhanced during the high-speed solar wind velocity periods. The high-speed solar wind is mainly caused by the coronal holes and they are evident during the declining phase of the solar activity. With the lack of the large magnetic storms during the solar minimum periods, the outer radiation belt moves outward compared with the solar maximum periods. Miyoshi et al. (2004) also demonstrated that there is a good coincidence between the plasma pause location and the peak location of >300 keV electrons. This evidence suggests that plasma pause takes an important role in making strong VLF emissions during the magnetic storm and the electron acceleration is possible to make highly energetic electrons there.

Non-adiabatic acceleration by VLF waves (Obara et al., 2001 and Miyoshi et al., 2003) is still one explanation in making relativistic electrons in the outer radiation belt during the storm recovery phase and we should like to confirm this by an international array of geostationary transfer orbit (GTO) satellites such as ERG satellite by ISAS/JAXA, ORBITALS satellite by CAS, RBSP satellites by NASA and RESONANCE satellite by IKI in very near future.

Acknowledgement

We are grateful to Dr. T.G.Onsager and Dr. Y. Miyoshi who provided NOAA data and friutful suggestions.

REFERENCES

Hudson, M. K., S. R. Elkington, J. G. Lyon et al., Simulations of radiation belt formation during storm sudden commencements, *J.Geophys. Res*., **102**, 14087-14102, 1997

Miyoshi, Y., A.Morioka, T. Obara et al., Rebulding process of the outer belt during November 3, 1993 magnetic storm, *J.Geophys.Res*., **108**, 1004 , doi:10.1029/2001JA007542, 2003

Miyoshi Y. S., V. K. Jordanova, A. Morioka, D. S. Evans, Solar cycle variations of the electron radiation belts: Observations and radial diffusion simulation, *Space Weather*, **2**, S10S02, doi:10.1029/2004SW000070, 2004

Obara, T., M. Den, Y. Miyoshi, and A. Morioka, Energetic electron variation in the outer radiation zone during early May 1998 magnetic storm, *JASTP*, **65**, pp.1407-1412, 2000.

Obara, T., Y. Miyoshi, and A. Morioka, Large enhancement of the outer belt electrons during magnetic storms, *Earth Planets Space*, **53**, pp.1163-1170, 2001.

Obara, T., H.Matsumoto and T.Goka, Coupling of energetic electrons in the inner magnetosphere to space weather phenomena, *Multiscale coupling of Sun Earth processes edt by Lui,T. and Y.Kamide*, Elsevier, pp.135-144, 2004

Obara, T., Y. Miyoshi and T.G.Onsager, Generation and loss of new electron radiation belt in the slot region during the Bastille day magnetic storm, *Space Radiation*, **4**, No. 3, 145- 152, 2005

Obara, T., M.Nakamura, H.Matsumoto, T.Goka, Relativistic electron variation in the radiation belt inferred from MDS-1 (TSUBASA), *Space Radiation*, **5**, No. 2, 101-109, 2006

O'Brien, T. P., K. R. Lorentzen, I. R. Mann, N. P. Meridith, J. B. Blake, J. F. Fennell, M. D. Looper, D. K. Milling, and R. R. Anderson, Energization of relativistic electrons in the presence of ULF power and MeV mibcrobursts: Evidence for dual ULF and VLF acceleration, *J. Geophys. Res.*, **108**, 1329, doi:10.1029 /2002JA009784, 2003.

Tverskaya, L. V., The latitude position dependence of the relativistic electron maximum as a function of *Dst*, *Adv. Space Res*., **18**, pp.135-140, 2002.

Statistical Data Analysis of the Aurora Electrons and Thermal Ions for Spacecraft Charging Analysis

Takamitsu Hamanaga and Mengu Cho
Department of Electrical Engineering, Kyushu Institute of Technology, 1-1 Sensui-cho Tobata-ku Kitakyushu, 804-8550, Japan

Polar Earth orbit (PEO) is a peculiar orbit where energetic auroral electrons and low-temperature ionospheric plasma coexist. There is a risk of charging and subsequent arcing in PEO, which was demonstrated unfortunately by the total loss of ADEOS-II satellite in 2003. Charging in PEO must be properly assessed in the early satellite design phase by a spacecraft charging analysis tool. The plasma environment, namely its density and energy, is the crucial parameter for the spacecraft charging analysis. The balance between the auroral electrons and the low temperature ionospheric ions determine the charging potential of a PEO satellite. We statistically analyzed the environmental condition in PEO using the data of auroral electrons and thermal ions measured by DMSP (Defense Meteorological Satellite Program) satellites. Probability of a given combination of current densities of auroral electrons and thermal ions has been derived. The energy spectrum of the auroral electrons are also classified into several types and correlation with the thermal ions is analyzed. Combinations of the plasma parameters used by a spacecraft charging simulation software have been identified and database regarding the probability of occurrence of each combination has been formulated.

I. Introduction

Compared to spacecraft charging in GEO, charging in LEO has not been given serious consideration because of presence of high density and low temperature ionospheric plasma. The balance of negative and positive currents to the spacecraft determines its potential with respect to the surrounding plasma. If a spacecraft is in low-inclination orbit that does not cross with the aurora zone, defined as the region between 60 and 75 degrees of magnetic latitude (MLAT), the ionspheric plasma dominates the current and the spacecraft potential is within the solar array power generation voltage[1].

Polar Earth orbit (PEO) that crosses the aurora zone is a peculiar orbit where the low-temperature plasma and energetic auroral electrons coexist. Therefore, a PEO spacecraft may charge to hundreds or thousands of volts negative when the density of thermal ions is reduced or the flux of auroral electrons become large[2,3]. In such a situation, if a potential difference between the spacecraft body and the spacecraft insulator material exceeds the arc inception threshold, an arc occurs. This may lead to a serious accident. In October 2003, a Japanese Earth observation satellite, ADEOS-II, suffered fatal power system failure because of sustained arc in cable harness phenomena triggered by charging of ungrounded thermal insulator by auroral electrons[4]. Since the accident of ADEOS-II, Japanese space sector takes spacecraft charging in PEO very seriously.

To prevent such an accident, charging in PEO must be properly assessed in the early satellite design phase by a spacecraft charging analysis tool. If the charging analysis predicts that the probability of arcing in orbit cannot be ignored, proper ground tests must be carried out[5,6]. In the Japanese space sector, JAXA decided to develop MUSCAT (Multi-Utility Spacecraft Charging Analysis Tool) [7] based on the lessons learned from the ADEOS-II failure. There are several ways of using the charging simulation code. One is to know whether the spacecraft reaches the critical charging situation where arcs are inevitable by simulating the worst plasma condition. Another is to know how many arcs a spacecraft suffers during the total lifetime. The later information is used to plan the ground test and assess the cumulative effects, such as surface deterioration or solar cell degradation, at the end of life[8].

Knowing the correct plasma environment a spacecraft encounters in orbit is very important to make use of the charging simulation code. Not only the worst condition but also statistical distribution of the plasma parameters are important if we like to derive the statistical prediction from the charging analysis and the ground test. The purpose of the present paper is to formulate a database regarding the PEO plasma environment suitable for the charging simulation code.

MUSCAT can simulate the spacecraft plasma interaction by modeling the ionosphere plasma by Maxwellian plasma and the auroral electron either by a single Maxwellian or a double Maxwellian plasma. In the MUSCAT simulation, the auroral electrons are injected from the numerical boundary donwnward only along the magnetic field line[8]. Therefore, we need at least a combination of ionospheric plasma density, auroral electron density and its temperature. In Ref.9 Cho et al carried out statistical analysis of GEO plasma environment using the data measured by LANL (Los Alamos National Laboratory) satellites. In Ref.9, the probability of each combination of electron density, electron temperature, ion density and ion temperature was derived assuming the GEO plasma was made by single Maxwellian electrons and ions. In the present paper, we carry out statistical analysis similar to Ref.9 using the data measured by DMSP (Defense Meteorological Satellite Program) satellites.

In the second section, we describe the DMSP data we used. In the third section, we describe the result of correlation analysis on the auroral electron current and thermal (ionospheric) ion current from 1996 to 2003.

II. Data Description

The data we used comes from data of SSJ/4 (precipitating electron and ion sensor), and SSIES (Special Sensor for Ion Scintillation monitor) onboard DMSP[#]. DMSP is a group of satellites orbiting the Earth at approximately 840 km altitude with 99° inclination and 101 minute orbital period. More than two DMSP satellites are always operated. Each DMSP satellite is classified by a number like F6 or F7 and so on.

SSJ/4 measures the energy spectrum of precipitating particles between 30 eV and 30 keV using 20 channels and records each channel every second[#]. Each channel covers a specific energy band and is logarithmically spaced between 30 eV and 30 keV. Each channel records the magnitude of the particle energy flux. We calculate the current density of the auroral electrons using the data of SSJ/4 according to the following process.

We assume that the velocity distribution of the energetic electrons is isotropic within 2π solid angle, which is defined by $0 < \Phi < 2$ and $0 < \theta < /2$, in polar coordinate shown in Figure 1.

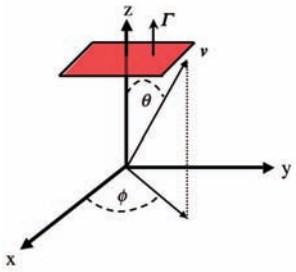

Fig.1 Particle flux and velocity vector

The energy flux in polar coordinates is given by the following equation.

$$\begin{aligned} &EnergyFlux(J/s/m^2) \\ &= \int_{v_{\min}}^{v_{\max}} \int_0^{\pi/2} \int_0^{2\pi} (\frac{1}{2}mv^2)(v^2 \sin\theta d\theta d\phi) dv\, f(v) v \cos\theta \\ &= \pi \int_{v_{\min}}^{v_{\max}} \frac{1}{2} m v^5 f(v) dv \\ &= 2\pi \Gamma_{flux} \end{aligned} \quad (1)$$

where Γ_{flux} is the value observed by SSJ/4 and v is a speed that corresponds to each channel energy.

The solid angle of 2 is used assuming that particles are unidirectional along the magnetic field lines. From Eq (1), the distribution function f(v) is given by the following equation (2).

$$f(v) = \frac{2\Gamma_e(E)}{v^3 \frac{1}{2} m v^2} \bullet \frac{1}{v_{i,\max} - v_{i,\min}} \quad (2)$$

where $v_{i,min}$ is the velocity corresponding to the minimum energy that a channel i can observe, $v_{i,max}$ is the velocity corresponding to the maximum energy that a channel i can observe and E is the channel energy. One might argue that energetic electrons in aurora may not be isotropic, and more oriented along the magnetic field line. As SSJ/4 measures only the energy flux in a limited solid angle, it is very difficult to estimate the angular width of the precipitating electrons. As the first step we multiply Γ_{flux} by 2 as in Eq (1) and it should be noted that this treatment leads to overestimation of the electron density and current to a certain degree.

We can derive the density by integrating the distribution function of electrons.

$$n = 4\pi \int_{v_i,\min}^{v_{i,\max}} f(v) v^2 dv \quad (3)$$

Average energy and current density is derived from the density and the distribution function. They are

$$< \frac{mv^2}{2} >= \frac{2\pi m \int_{v_{i,\min}}^{v_{i,\max}} f(v) v^4 dv}{n} \quad (4)$$

[#] http://www.ngdc.noaa.gov/dmsp/dmsp.html

where $<\frac{mv^2}{2}>$ is the average energy. The total current density i is given by

$$i = e < nv >= \int_{v_{i,\min}}^{v_{i,\max}} \int_0^{\pi/2} \int_0^{2\pi} e(v\cos\theta)(v^2 \sin\theta d\theta d\phi) dv f(v) \quad (5)$$
$$= e\pi \int_{v_{i,\min}}^{v_{i,\max}} v^3 f(v) dv$$

SSIES measures density, temperature, and velocity of the background thermal plasma. Sampling rate is 4 second[15]. We used the data of the thermal ion density.

The SSJ/4 data was obtained from the website* of "The Johns Hopkins University Applied Physics Laboratory" and SSIES data was obtained from the website§ of "DMSP SSIES Data Distribution Website". The data is from January, April, July, and October in 1996, 2000, and 2003 so that we can cover the maximum, the minimum and the middle of one solar cycle and four seasons. We analyzed only the data observed at the same time by both SSJ/4 and SSIES in the magnetic latitude between 60° and 75° in the southern and northern hemisphere. Number of data points we used is listed in table 1.

Table.1 Number of data points between 60° and 75° MLAT. (North and South) used in the analysis of sections 4 and 5.

	Jan	Apr	Jul	Oct	Satellites
96	266975	256811	217662	280040	F12,13
00	453929	500041	371375	372608	F12,13,14,15
03	234357	261944	255331	226339	F13,14,15

III. Concurrent Statistical Data Analysis of the Current Density of Auroral Electrons and Thermal Ions

In this section, we first classify the scale of the aurora into 5 types, Extreme, Severe, Strong, Moderate, and Weak (table 2). We made no distinction between the northern and the southern hemisphere. Moderate is the most probable type as scaling of the aurora. When the aurora becomes active, the scale changes in the order of Strong, Extreme and Severe, where the current to spacecraft is dominated by the auroral electrons. Weak is the case when auroal electrons hardly precipitate into the spacecraft.

Table 3 shows the probability that a spacecraft encounters a certain aurora condition at daytime or at nighttime in magnetic local time (MLT). Extreme and Severe show no significant dependence on MLT. Strong tends to occur more during nighttime than daytime. In addition, the probability of Strong type aurora becomes higher during the solar maximum (2000 and 2003) than the solar minimum (1996) (see Table 4).

Figure 2 shows the ion density in July 1996 and in July 2000. In July, the northern hemisphere is always illuminated. Therefore the ion density is high and stable. In contrast, the southern hemisphere is not illuminated, which makes the ion density low and fluctuating.

We classified the ion density into 3 types, Rare, Medium, and Dense (Table.5). The ion current was calculated by multiplying the density by 8 km/s, the orbital velocity. When the ion density becomes Rare, the auroral current of Strong, Severe, and Extreme exceeds the ion current. Figure 3 shows the relationship between the scale of the aurora and the scale of the thermal ion in the southern hemisphere in July 2000 between 21 MLT and 24 MLT. The southern hemisphere is not illuminated in July. Table 6 shows the probability that a spacecraft encounters a certain plasma environment in July 2000 in the southern hemisphere between 21MLT and 24MLT. The ion density becomes lower if the scale of the aurora becomes weaker and the ion density becomes higher if the scale of the aurora becomes stronger. This is caused by the increase of the ion density due to ionization of the atmosphere by the energetic auroral electrons. In the same way, the northern hemisphere in January have the same tendency.

The ion density in the illuminated region doesn't have this tendency, because the effect of the solar illumination is much stronger than the effect of ionization by auroral electrons.

From Tables 2 and 6, it is found that Severe and Extreme aurora scale and even Strong if accompanied by the ion density less than 8×10^8 m^{-3} may lead to serious negative charging of a spacecraft body. In Table 6 those cases are enclosed in the thick line. The total percentage of those charging cases is 0.84% in July 2000 in the southern hemisphere between 21MLT and 24MLT. A major part of this charging case is dominated by the Strong scale aurora. Thus, most charging event occur due to the decrease of ion density rather than the increase of the auroral current. Although it is very rare, less than 0.01%, in the Extreme case, spacecraft may charge to over -10kV because the auroral electrons energy is above 10keV.

* http://sd-www.jhuapl.edu/Aurora/dataset_list.html
§ http://cindispace.utdallas.edu/DMSP/

Table 2. Definition of aurora scale and its conditions.

Scale	Current Density (A/m^2)	Average Energy (keV)
Extreme	$>10^{-4}$	>10
Severe	$>10^{-4}$	<10
Strong	10^{-6}~10^{-4}	
Moderate	10^{-8}~10^{-6}	
Weak	$<10^{-8}$	

Table 3. Scale of aurora and probability (%) in 9~12 MLT and 21~24 MLT.

Scale	9~12 MLT			21~24 MLT		
	1996	2000	2003	1996	2000	2003
Extreme	0	0.006	0	0	0.005	0
Severe	0.08	0.14	0.4	0.09	0.16	0.22
Strong	9	22	34	34	41	53
Moderate	91	78	65	58	57	45
Weak	0.02	0.06	0.9	8	1.7	2.1

Table 4. Probability of each aurora scale (%) .

Scale	Probability (%)		
	1996	2000	2003
Extreme	0.0002	0.0035	0.0001
Severe	0.08	0.14	0.23
Strong	24	35	41
Moderate	73	64	57
Weak	2.5	0.5	1.1

Table 5. Scale of thermal ion and its conditions.

Scale	Current Density (A/m^2)	Density (m^{-3})
Rare	$<10^{-6}$	$<8\times10^{8}$
Medium	10^{-6}~10^{-4}	8×10^{8}~8×10^{10}
Dense	$>10^{-4}$	$>8\times10^{10}$

Table 6. Statistical correlation probability(%) between ion and electron current. (July 2000 in the southern hemisphere between 21MLT and 24MLT)

	Weak	Moderate	Strong	Severe	Extreme
Rare	0.11	0.69	0.64	0.003	0.0
Medium	1.1	54	40	0.17	0.005
Dense	0.023	1.6	2.1	0.021	0.003

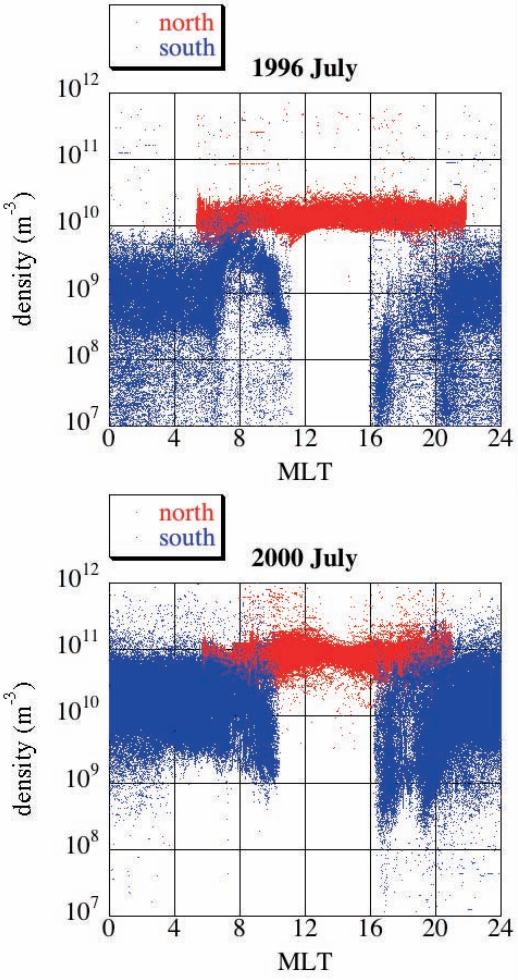

Fig.2. Relation between thermal ion density and MLT in July.(top:1996,July,north, 2nd low:1996,July,south, 3rd low:2000,July,north, bottom: 2000,July,south)

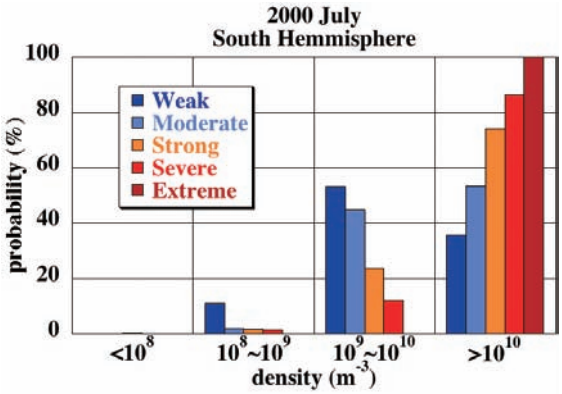

Fig. 3. Relation between the scale of the aurora and the ion density (July 2000 in the southern hemisphere between 21MLT and 24MLT.)

Table 7 shows the probability of the auroral current exceeding the ion current. The percentage of Strong type aurora to each probability is listed in the parentheses. For an example, in October in the southern hemisphere in 1996 between 0 MLT and 3 MLT, the probability of the auroral electron current exceeding the thermal ion current is 0.07%. In the 0.07%, 22.2% corresponds to Strong scale aurora and the rest corresponds to Severe and Extreme aurora. The charging probability due to the decreasing ion density is evident during the solar minimum in January 1996 in the northern hemisphere and in July in the southern hemisphere. In contrast, the charging probability due to the active aurora is evident during the solar maximum in July 2000 in the northern hemisphere where no Strong case exists. For the case of charging due to the active aurora, the ratio of Extreme and Severe cases in the probability increases compared to charging due to the decreasing ion density.

Table 7. Probability of auroral current exceeding ion current (%)

MLT	1996							
	North				South			
	Jan	Apr	Jul	Oct	Jan	Apr	Jul	Oct
0~3	n/a	n/a	n/a	n/a	0.02(0.0)	8.08(99.0)	28.13(99.8)	0.07(22.2)
3~6	19.53(100)	0.12(14.3)	0.22(14.3)	1.86(95.2)	0.04(0.0)	4.50(98.5)	16.77(99.8)	0.06(18.8)
6~9	15.10(99.1)	0.16(0.0)	0.11(0.0)	1.80(92.9)	0.09(0.0)	5.80(99.1)	8.84(99.5)	0.17(62.8)
9~12	2.04(96.6)	0.01(2.6)	0.13(0.0)	0.29(54.9)	0.00(0.0)	0.44(93.6)	2.27(100)	0.01(0.0)
12~15	1.21(90.1)	0.16(0.0)	0.11(0.0)	0.21(11.1)	n/a	n/a	n/a	n/a
15~18	2.10(93.0)	0.09(0.0)	0.05(0.0)	0.24(68.1)	0.01(0.0)	7.56(99.9)	7.70(100)	0.35(97.4)
18~21	4.93(99.1)	0.13(0.0)	0.04(0.0)	1.00(87.0)	0.10(79.2)	10.37(99.5)	13.96(99.9)	1.80(95.9)
21~24	5.17(98.6)	0.07(0.0)	0.01(0.0)	4.09(95.5)	0.09(4.5)	13.66(99.4)	18.42(99.4)	0.47(81.4)

MLT	2000							
	North				South			
	Jan	Apr	Jul	Oct	Jan	Apr	Jul	Oct
0~3	n/a	n/a	n/a	n/a	0.06(0.0)	0.12(0.0)	0.39(48.9)	0.09(0.0)
3~6	0.07(0.0)	0.09(0.0)	0.27(0.0)	n/a	0.07(0.0)	0.05(3.4)	0.16(10.1)	0.11(0.0)
6~9	0.18(3.2)	0.11(0.0)	0.25(0.0)	0.22(0.0)	0.14(0.0)	0.09(0.0)	0.18(2.4)	0.18(0.0)
9~12	0.13(0.0)	0.16(0.0)	0.28(0.0)	0.08(0.0)	0.18(0.0)	0.08(0.0)	0.23(24.0)	0.10(0.0)
12~15	0.43(0.0)	0.34(0.0)	1.11(0.0)	0.26(0.0)	n/a	n/a	n/a	n/a
15~18	0.19(1.4)	0.07(0.0)	0.32(0.0)	0.12(0.0)	0.03(0.0)	0.26(96.4)	0.91(92.7)	0.10(0.0)
18~21	0.15(0.0)	0.07(0.0)	0.18(0.0)	0.10(0.0)	0.10(0.0)	0.98(97.0)	1.31(90.1)	0.05(5.9)
21~24	0.09(0.0)	0.21(0.0)	0.00(0.0)	0.92(0.0)	0.16(0.0)	0.17(36.5)	0.84(75.9)	0.18(0.0)

MLT	2003							
	North				South			
	Jan	Apr	Jul	Oct	Jan	Apr	Jul	Oct
0~3	n/a	n/a	n/a	n/a	0.16(0.0)	0.08(17.6)	2.25(89.8)	0.09(0.0)
3~6	0.00(0.0)	n/a	n/a	n/a	0.08(0.0)	0.06(0.0)	0.92(86.7)	0.17(0.0)
6~9	0.23(1.2)	0.15(0.0)	0.43(0.0)	0.47(0.0)	0.17(0.0)	0.16(7.7)	1.32(66.7)	0.38(0.0)
9~12	0.37(0.0)	0.21(0.0)	0.72(0.0)	0.27(1.6)	0.69(0.0)	0.05(0.0)	2.03(60.0)	0.09(0.0)
12~15	0.90(2.9)	0.43(0.0)	0.95(0.0)	0.32(0.0)	0.00(0.0)	n/a	n/a	n/a
15~18	0.28(3.5)	0.15(0.0)	0.39(0.0)	0.17(0.0)	0.07(0.0)	2.64(99.6)	6.15(00.6)	0.38(0.0)
18~21	0.17(0.0)	0.07(0.0)	0.20(0.0)	0.38(0.0)	0.07(0.0)	2.24(97.5)	5.56(98.0)	0.18(11.6)
21~24	n/a	n/a	n/a	n/a	0.23(0.0)	0.44(70.2)	3.52(91.3)	0.20(0.0(0.0))

IV. Database for Spacecraft Charging Anaysis Parameter for MUSCAT

Finally, we formulate the database of input parameters of PEO plasma environment suitable for a parametric run by a spacecraft charging analysis tool such as MUSCAT.

In MUSCAT, the input plasma parameters for PEO analysis are the current density and average energy of aurora and surrounding thermal plasma density. The aurora electrons are modeled by a Maxwellian distribution. The temperature of surrounding plasma may vary between 0.1 to 0.2eV. Because the difference is negligible compared to the possible charging potential and the thermal speed is negligible compared to the orbital velocity, we fix the temperature to 0.2eV.

The purpose of the parametric run is to investigate as many cases as possible to derive the number of charging events in orbit. By knowing the time for the differential voltage between spacecraft surface insulator and the spacecraft body to reach the threshold for primary arc inception, we can also derive the expected number of primary arcs in orbit. This practice was once carried out for a GEO satellite in Ref.13. We can derive those numbers if we know the probability of occurrence for each set of the plasma environment parameters.

To formulate the database of possible combinations of the plasma parameters, we used the DMSP data of January, April, July and October in 1996, 2000, and 2003 between 60° MLAT and 75° MLAT in both hemispheres. In this way, we can cover four seasons in the northern and southern aurora zones during the solar maximum (2000), the solar minimum (1996) and the intermediate time (2003). To resolve the local time dependence, we divided the data into 8 MLT zones that have duration of 3 hours. In this way, the number of temporal and spatial combinations are 3x4x8x2=192 cases.

At each of 192 cases, we further divide the plasma environment depending on the aurora current density, average energy, spectra and thermal ion density. The ranges of each plasma parameter used to categorize are shown in table 8. For the aurora current density, we combined all the cases below 10^{-6}A/m^2 because the current density below 10^{-6}A/m^2 has little effect on negative charging. When we carry out the simulation for the case representing the aurora current density less than 10^{-6}A/m^2, we choose the aurora current density $1x10^{-6}$A/m^2 as the input value for the simulation. For the case of aurora current density from $1x10^{-6}$ to $1x10^{-5}$A/m^2, we choose $1x10^{-5}$A/m^2 as the input value of the aurora current density. The other input values are listed in Table 7. For the thermal plasma density above 10^{10}m^{-3} is combined into $1x10^{10}$m^{-3} as the dense plasma relaxes the negative charging. Choosing the aurora current density at the upper-bound of each range and the thermal ion density at the lower bound gives more cases of negative charging, leading to the conservative (safe-side) estimate on the number of charging events in orbit.

We divided the aurora spectrum into three cases to consider the correlation between spectrum of auroral electrons and thermal ions. We represent the energy flux by two-Maxwellian distribution. The formulation is following.

$$flux(\varepsilon) = M_1\left(\frac{1}{2\pi}\right)^{\frac{3}{2}}\sqrt{\frac{kT_1}{m}}\left(\frac{\varepsilon}{kT_1}\right)^{\frac{3}{2}}\exp\left(-\frac{\varepsilon}{kT_1}\right)$$

$$+M_2\left(\frac{1}{2\pi}\right)^{\frac{3}{2}}\sqrt{\frac{kT_2}{m}}\left(\frac{\varepsilon}{kT_2}\right)^{\frac{3}{2}}\exp\left(-\frac{\varepsilon}{kT_2}\right)$$

where $flux(\varepsilon)$ is the energy distribution function, M_1 and M_2 are electron density and T_1 and T_2 are electron temperature. T_1 is greater than T_2. Spectra are represented by the Maxwellian distribution of low temperature T_1 and high temperature T_2. We consider 3 cases. Case1; $M_1 \times 10 < M_2$, case2; $M_1 \times 10 \geqq M_2$ and $M_2 \times 10 \geqq M_1$, and case3; $M_1 > M_2 \times 10$. Case1 is the environment dominated by high energy electrons. Case2 is the environment that various energy electrons are precipitating. Case3 is the environment dominated by low energy electrons

We fitted M_1, M_2, T_1, and T_3 to the observational value of SSJ/4 using genetic algorithm fitting. The range for M_1 and M_2 are from 10^4m^{-3} to 10^{10}m^{-3}. The range for T_1 is from 10eV to 1keV. The range for T_2 is from 1keV to 80keV. Figure 4 shows the observational value and fitting value of case1, case2, and case3.

If the spectrum is categorized as the Case1, the temperature is further divided into the four cases listed in Table 8. The aurora electrons are modeled by a single Maxwellian with the temperature listed in the next column in Table 8. Likewise, if the spectrum is categorized as the Case3, the temperature is further divided into three cases. If the spectrum is categorized as the Case2, we multiply the average energy defined by Eq. (4) by 2/3 to obtain single temperature to be used to model the electron energy distribution by a single Maxwellian. For the case where the aurora current density is below 10^{-6}A/m^2, we neglect the difference of the aurora energy spectrum and treat all the spectrum type as case 2 for simplicity.

For each thermal plasma density, the number of combination for the aurora current density and temperature is 8+3x16=56. Therefore, the total number of combination for the plasma parameter is 4x56=224. Therefore, the total number of combination considering the solar activity, the season, the local time, the hemisphere and the plasma parameters is

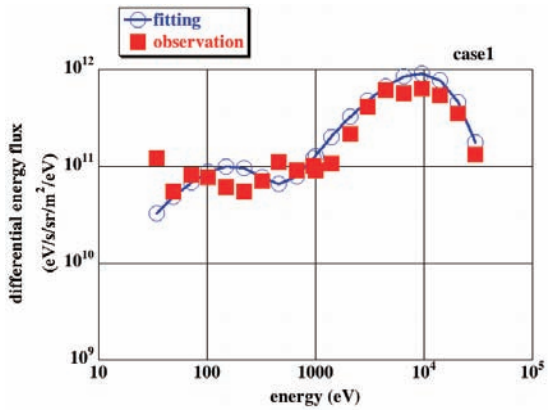

(a) case1

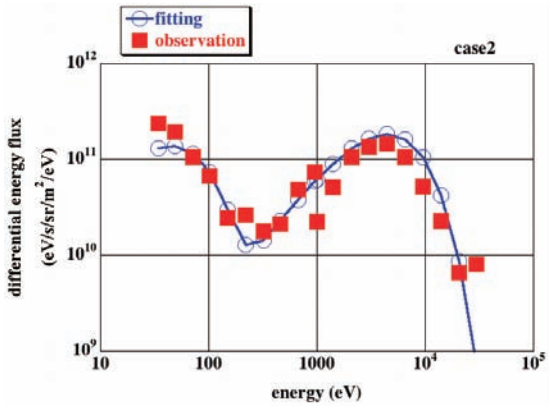

(b) case2

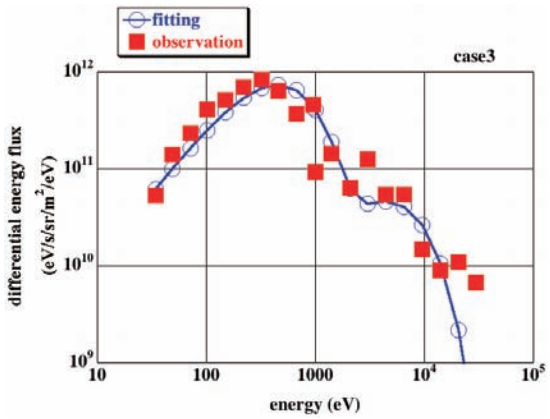

(c) case3

Fig 4. Fitting spectrum

192x224=43008. We calculate the probability of occurrence of each of 224 combinations of plasma parameters at each case of the 192 temporal and spatial combinations. Among the 192 temporal and spatial combinations, unfortunately, there are cases where no DMSP data is available. We compensate the no data region using adjacent time zones. No data regions are 0~3MLT, 3~6MLT, and 21~24MLT in the northern hemisphere and 12~15MLT in the southern hemisphere. Figure 2 shows little dependency on MLT, so we compensated no data regions considering only the aurora activity referring to the probability of 'the worst case' in Ref.10. Data of 0~3MLT, 3~6MLT, and 21~24MLT in the northern hemisphere are compensated by data of 18~21MLT, 15~18MLT, 18~21MLT in the northern hemisphere respectively. Data of 12~15MLT in the southern hemisphere is compensated by data of 9~12MLT in the southern hemisphere.

Among the 43008 combinations, there are cases where the probability of occurrence is zero. After we delete the cases with zero probability, there are only 2858 cases left. For parametric run, we can reduce the number of simulation to 930 cases because we have only to consider the plasma density, the auroral current, the temperature, time region, and the hemisphere in the calculation. We can further reduce the number of simulation by ignoring the cases where little negative charging is expected with the aurora current density much lower than the thermal ion current density. Deleting such cases, the number of simulation necessary is approximately 400. If we can finish each simulation case in 15 minutes, all the simulations can be done in less than 5 days.

V. Conclusion

It is necessary to characterize the plasma parameters in PEO to correctly access the risk of spacecraft charging in orbit and draft an appropriate ground test plan if necessary. Whether a spacecraft in PEO suffers serious negative charging beyond the solar array power generation voltage, depends on the balance between energetic auroral electrons and ionospheric ions. The plasma conditions have statistical distribution depending on the solar activity, orbital position, season and local time. To carry out quantitative analysis to derive the probability of serious charge events in orbit, we need to know not only the worst-case condition but also the probability of occurrence of each combination of the plasma parameters. In the present paper, we have statistically analyzed the current density of the aurora and background thermal ion in PEO using data of DMSP to produce a database suitable for series of spacecraft charging simulations to derive the number of charging events and the estimated number of primary arcs in orbit.

The statistical analysis of DMSP SSJ/4 and SSIES data revealed that during the solar maximum, the probability of negative charging due to active aurora rises. During the solar minimum, the probability of negative charging due to decrease of ion density rises especially in the southern hemisphere.

We have formulated a database to be used as input parameters of spacecraft charging simulation code,

MUSCAT. We have derived the probability of occurrence of each combination of season, solar activity, hemisphere, magnetic local time, auroral current density, ionospeheric ion density and auroral electron temperature. In the database, we have divided the seasons into 4, the solar activity into 3 levels, the hemispheres into south and north, the magnetic local to 8 time zones, the auroral current density into 4 levels, the ion density into 4 levels and the auroral electron temperature into 16 levels. Although the total number of combinations is more than 50,000, if we consider only the cases with non-zero probability of occurrence and possibility of auroral current density exceeding the ionospheric ion density, the number of case reduces to 400.

Our next task is to carry out the simulation runs of the 400 cases by MUSCAT and calculate the spacecraft charging potential and time for the differential voltage to reach the arcing threshold for each case.

In the present paper, the data we used for the statistical analysis is limited to DMSP. Therefore, strictly speaking the database we formulated is applicable only to the altitude of 840km. Correction would become necessary whenever we carry out the charging simulation for spacecraft in a different altitude. We have used only a limited amount of DMSP data to carry out the concurrent analysis of the auroral current and the ionospheric ion density. In future, it is necessary to refine the accuracy of database by increasing the number of observation data involved.

Acknowledgments

We thank Dr. Patrick Newell of Johns Hopkins University Applied Physics Laboratory for helping us analyze the data of SSJ/4.

References

[1]D. E. Hastings and H. Garrett, “Spacecraft-Environmental Interactions”, *Cambridge Univ.Press*, New York, 1996.

[2]P. C. Anderson, “A Survey of Surface Charging Events on the DMSP Spacecraft in LEO”, Proceedings of 7th Spacecraft Charging Technology Conference, ESA, SP476, 2001, pp.331-336.

[3] J. E. Wahlund, L. J. Wedin, T. Carrozi, A. I. Eriksson, B. Holback, L. Andersson and H. Laakso, “Analysis of Freja Charging Events: Statistical Occurrence of Charging Events”, *ESA TECHNICAL NOTE*, SPEE-WP130-TN, 1999.

[4]S. Kawakita, H. Kusawake, M. Takahashi, H. Maejima, T. Kurosaki, Y. Kojima, D. Goto, Y. Kimoto, J. Ishizawa, M. Nakamura, J. Kim, S. Hosoda, M. Cho, K. Toyoda and Y. Nozaki, “Investigation of an Operational Anomaly of the ADEOS-II Satellite”, 9th SCTC, Tsukuba, 2005.

[5]Mengu Cho, Jeong-ho Kim, Satoshi Hosoda, Yukishige Nozaki, takeshi Miura, and Takanori Iwata, “Electrostatic Discharge Ground Test of a Polar Orbit Satellite Solar Panel” IEEE Transaction on Plasma Science, Vol.34, pp.2011-2030, 2006

[6]Kazuhiro Toyoda, Hirokazu Masui, Takanobu Muranaka, and Mengu Cho, Tomoyuki Urabe, Takeshi Miura, and Shirou Kawakita, Yuichiro Gonohe and Tooru Kikuchi, ”Esd Ground Test of Solar Array Coupons for a Greenhouse Gases Observing Satellite in PEO”10th Spacecraft Charging Technology Conference, Biarritz, France, June 2007

[7]Takanobu MURANAKA, Shinji HATTA, Jeongho KIM,Satoshi HOSODA, Koichiro IKEDA, Mengu CHO, Hiroko O. UEDA, Kiyokazu KOGA, Tateo GOKA, ”Final Version of Multi-Utility Spacecraft Charging Analysis Tool (MUSCAT)”, 10th Spacecraft Charging Technology Conference, Biarritz, France, June 2007

[8]Mengu CHO**,** “Status of ISO Standardization Efforts of Solar Panel ESD Test Methods”, 10th Spacecraft Charging Technology Conference, Biarritz, France, June 2007

[9]Mengu Cho, Shirou Kawakita, Masao Nakamura, Masato Takahashi, Tetsuo Sato, Yukishige Nozaki, “Number of arcs estimated on solar array of a geostationary satellite” 2005, Journal of Spacecraft and Rockets, vol.42 no.4, pp.740-748

[10]Takamitsu Hamanaga, Shinji Hatta, Mengu Cho, “Analysis of the Plasma Environment in Polar Earth Orbit Using Data of Defense Meteorological Satellite Program”, The 25th International Symposium on Space Technology and Science, 2006

Table 8. Range and input value of each case of plasma parameters

Range of aurora current density (A/m^2)	Input value of aurora current density (A/m^2)	Range of thermal plasma density (m^{-3})	Input value of thermal plasma density (m^{-3})	Aurora electron spectrum and temperature (eV)		Input value of aurora electron temperature (eV)
~$1x10^{-6}$	$1x10^{-6}$	~$1x10^{8}$	$5x10^{7}$	Case 1	1000~2000	2000
$1x10^{-6}$~$1x10^{-5}$	$1x10^{-5}$	$1x10^{8}$~$1x10^{9}$	$1x10^{8}$		2000~4500	4500
$1x10^{-5}$~$1x10^{-4}$	$1x10^{-4}$	$1x10^{9}$~$1x10^{10}$	$1x10^{9}$		4500~10000	10000
$1x10^{-4}$~	$5x10^{-4}$	$1x10^{10}$~	$1x10^{10}$		10000~20000	20000
					20000~	30000
				Case 2	10~200	200
					200~450	450
					450~1000	1000
					1000~2000	2000
					2000~4500	4500
					4500~10000	10000
					10000~20000	20000
					20000~	30000
				Case 3	10~200	200
					200~450	450
					450~1000	1000

朝側から昼側領域の静止軌道における電子密度増加
Electron density enhancements in the pre-noon sector of GEO

中村　雅夫（大阪府立大学）
Masao Nakamura (Osaka Prefecture University)

はじめに

衛星の表面帯電は、静止軌道上の不具合の大きな原因の１つである。静止軌道衛星の表面帯電は、地球の日陰に入ったときや夜側から朝側の軌道領域へ磁気圏サブストームにともなう高温電子が流入したときに引き起こされると考えられている。しかし、観測データと帯電解析ソフトとを組み合わせた研究から、朝側から昼側領域にかけても無視できない頻度で帯電が発生する可能性が示され、この領域の帯電発生頻度の上昇は電子密度の異常増加に関係があることが示唆されていた。本研究では、この朝側から昼側領域の静止軌道において帯電を引き起こす電子密度の増加現象について調べた。

観測と解析結果

趙等[1]による Los Alamos National Laboratory(LANL)静止軌道衛星の観測データと衛星帯電解析ソフト NASA Charging Analyzer Program (NASCAP)による解析とを組み合わせた研究では、従来知られていた通り、主として地球の日陰および夜側から朝側にかけた領域で表面帯電が起こることが示された。これらは、日陰で光電子放出による帯電緩和効果が働かないことと、夜側から朝側にかけた領域で磁気圏サブストームにともなう高温電子が衛星軌道に侵入することで表面帯電が引き起こされるためである。さらに、その研究では、朝側から昼側領域にかけても無視できない頻度で表面帯電が起こる可能性があることを明らかにした。この領域でも、サブストームによる高温電子の一部が、昼側までドリフトしてくることにより帯電を引き起こしている場合もあるが、趙等の解析結果では 4.5 keV 程度（3-6 keV 範囲の代表値）の温度の電子による帯電発生頻度が、他の領域に比べて高くなっていることが示された。趙等は、電子密度が 10 個/cc を越えて異常増加するイベントの発生が朝側から昼側にかけて集中していることを突き止め、数 keV 程度の電子温度でも密度が増加することで、衛星に流れ込む電子による電流が増え、衛星帯電を引き起こしていることを示唆した。本研究では、それらのイベントを、趙等と同じ NASA の Coordinated Data Analysis (CDA) Web[2]にある LANL 静止軌道衛星の Magnetospheric Plasma Analyzer (MPA) Key Parameters を用いて解析をおこなった。表 1 に解析に用いたデータ期間を示す。このデータの中から、衛星が地方時で 8～14 時の間の朝側から昼側にかけた領域に位置し、電子密度が 10 個/cc 以上、衛星のポテンシャルが-100V 以下を同時に満たす観測点が 2 点以上連続しているイベントを選び出した。これらの条件を満たすイベントは、75 イベント見つかり、通常 1 衛星のみで観測され、異なる地方時で同時観測

している他の LANL 衛星では観測されない局所的な現象であった。

衛星	解析データ期間
LANL89	April, 1996 - December, 2002
LANL90	March, 1993 - December, 2002
LANL91	October, 1993 - September, 2003
LANL94	February, 1996 - October, 2003
LANL97	July, 1997 – September, 2003

表１：解析に用いた各 LANL 衛星のデータ期間。

図１に、第 22-23 期太陽活動周期の太陽黒点数のグラフに、全解析データ期間（黒矢印の範囲）と選択したイベントが得られた期間（赤矢印の範囲）とを重ねて示した。これらイベントは､解析データ期間中の(a)(b)の２つの期間に分かれて分布している｡(a)の期間は、太陽活動が極大期から極小期に向かう減衰期にあたり、全 75 イベント中 24 イベントが分布している。残りの 51 イベントは、(b)の太陽活動極大期周辺に集中している。しかし、(a)と(b)の間の太陽極小期には１イベントも見つからなかった。

さらに、個々のイベントと磁気圏活動との関係を調べた。磁気嵐の強度の指標である Dst 指数が、-50 nT 以下となる中規模程度以上の磁気嵐との相関を調べた。(b)の太陽極大期周辺では、51 イベント中 36 イベントが、中程度以上の磁気嵐の主相から 1 日以内に起こっており、よい相関を示した。それに対して、(a)の太陽活動減衰期では、24 イベント中 7 イベントしか中程度以上の磁気嵐の主相から 1 日以内におこっておらず、必ずしも相関がよくなかった。この 2 つの期間のイベントと磁気嵐との相関の違いは、太陽活動のそれぞれの時期で、磁気嵐を引き起こす原因が異なることに起因していると考えられる。つまり、太陽活動極大期の磁気嵐の多くは、Coronal Mass Ejection (CME)が磁気圏を通過することにより引き起こされ、太陽活動減衰期の磁気嵐の多くは、Corotating Interaction Region (CIR)が磁気圏を通過することにより引き起こされる。これら CME と CIR により引き起こされる磁気嵐は、異なる特徴を持つことが最近の研究で明らかになってきている[3,4]。しかし、全イベントの半数近くが太陽活動極大期の磁気嵐で起きていることは、朝側から昼側にかけての電子密度の異常増大が、磁気嵐などによる磁気圏対流の増大に何らかの関連があることを示していると考えられる。しかし、これらの電子密度の異常増加の特徴を同時に説明できるような物理メカニズムは、今のところわかっておらず、個々のイベント毎に他の観測などと合わせて詳細に解析していく必要がある。

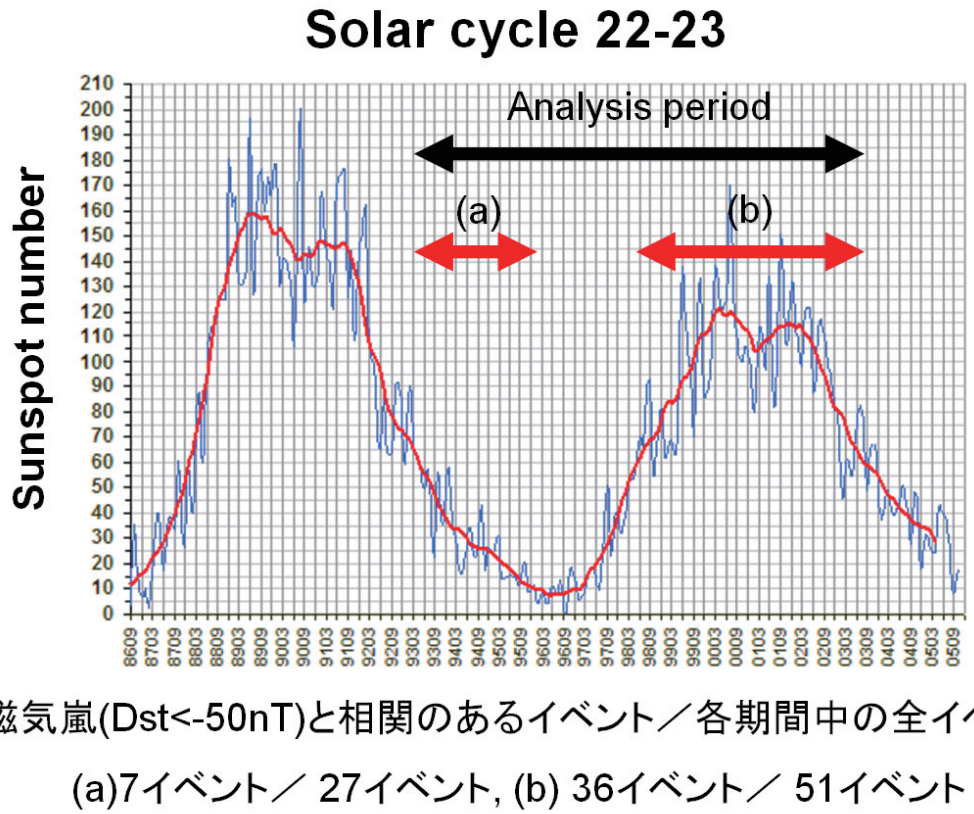

図１：第 22-23 期太陽活動周期の太陽黒点数の月平均値（青）とその平滑値（赤）のグラフ。本研究で解析に用いた全データ期間を黒矢印で、選択したイベントが得られた 2 つの期間を(a)、(b)の赤矢印で示した。

まとめ

静止軌道衛星の表面帯電現象の予測では、これまで磁気圏サブストームによる高温電子の夜側から朝側にかけての軌道上への流入に着目してきた。しかし、朝側から昼側にかけての領域でも、特に太陽極大期の磁気嵐時に、電子密度が急激に増大し、表面帯電を引き起こす可能性が高いことがわかった。現在は、第 24 太陽活動周期の始まりで、太陽極小期付近にあるが、今後、太陽活動が活発になり極大期に近づくにつれて、これらイベントがまた発生するようになると考えられる。そのため、本現象の物理メカニズムの解明が急がれ、衛星帯電予報に取り入れていく必要である。

参考文献

[1] M. Cho, S. Kawakita, M. S. Nakamura, M.Takahashi, T. Sato, Y. Nozaki, Estimate on number of arcs on solar array for a geostationary satellite, J. Spacecraft and Rockets, Vol. 42, No. 4, PAGES 740-748, 2005

[2] http://cdaweb.gsfc.nasa.gov/cdaweb/

[3] Miyoshi Y., R. Kataoka, Ring current ions and radiation belt electrons during geomagnetic storms driven by coronal mass ejections and corotating interaction regions, Geophys. Res. Lett., 32, L21105, 2005.

[4] Borovsky J. E., M. H. Denton, Differences between CME-driven storms and CIR-driven storms, J. Geophys. Res., 111, A07S08, 2006.

STEREO 探査機データの宇宙天気予報への応用

STEREO Data Applied to Space Weather Forecasting

長妻　努、秋岡　眞樹、大高　一弘
情報通信研究機構
T. Nagatsuma, M. Akioka, K. Ohtaka
National Institute of Information and Communications Technology

はじめに

宇宙天気予報は、主に太陽が駆動源となって生じる地球近傍の宇宙環境の変動を把握し、予測することで、通信・放送衛星等の宇宙機器や有人宇宙活動、社会インフラに対する宇宙環境擾乱の影響の低減に資することを目指している（**図 1**）。わが国では情報通信研究機構が宇宙天気予報に関する研究開発を推進すると共に、国際宇宙環境サービス（ISES）の一員として予報業務を実施している。

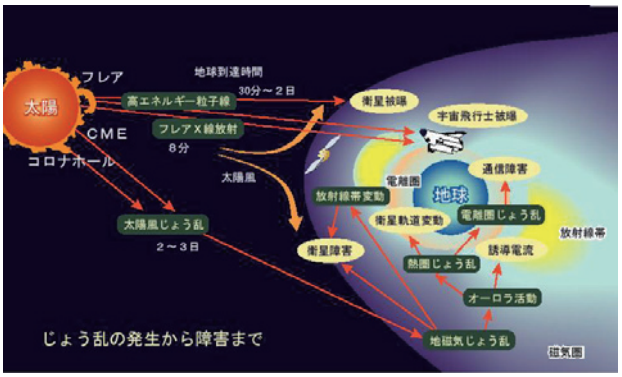

図 1　宇宙環境擾乱の発生から障害まで

宇宙天気予報は地球の天気予報に比べて、50 年くらい遅れていると言われる。これは取組みが始まった年代の隔たりに依る所が大きいが、それ以外にも両者の間には本質的な違いが存在する。宇宙天気予報と地球の天気予報の最も大きな違いは、閉鎖系で近似することができない点にある。地球の天気予報の場合、初期条件を定めてシミュレーションやモデルを走らせれば、計算精度に関しては議論があるにせよ、原理的にはいくらでも長期の予測が可能である。一方、宇宙天気予報の場合、どんなに精密な地球磁気圏シミュレーションを開発したとしても、太陽風や太陽面の情報が定常的に存在しなければ、30 分先を予測することすらおぼつかない。そのため、宇宙天気予報において予測のリードタイムを長くするには、太陽風や太陽の情報を得ることが本質的に重要である。しかしながら、これまではL1 点の ACE 探査機による太陽風の直接計測、惑星間空間シンチレーション（IPS）観測による太陽風のリモートセンシング、地上観測や人工衛星等による太陽及び太陽近傍のコロナのリモートセンシングのみで、内部太陽圏と呼ばれる太陽と地球の間の空間のカバレージが観測的には不十分な状況にある。

NASA の STEREO 探査機はサイエンス目的のミッションではあるが、宇宙天気予報及びその研究にとっても有効な情報を提供する。ここでは STEREO 探査機データの宇宙天気予報への応用の概念について述べる。

STEREO 探査機

STEREO（Solar-TErrestrial RElations Observatory）探査機は、太陽及び内部太陽圏を 2 機の探査機を用いてリモートセンシングと直接（in-situ）計測によって立体的に観測するユニークなミッションである。STEREO 探査機は、地球より少し内側の軌道を少しずつ先に進んでいく探査機（STEREO-A）と、地球より少し外側の軌道を少しずつ後ろに遅れていく探査機（STEREO-B）によって、異なる角度から太陽及び内部太陽圏を立体的に観測する。地球と太陽と探査機のなす角度は 1 年に約 22 度ずつ増加し、3 年で地球と探査機の距離は約 1 天文単位まで離れる。探査機には、以下の 4 つの装置及び装置群が搭載されている（**図 2**）。

SECCHI（Sun Earth Connection Coronal and Heliospheric Investigation）：太陽面及び内部太陽圏を撮像するための計測装置群

SWAVES（STEREO/WAVES）：プラズマ波動計測装置

IMPACT（In-situ Measurements of Particles and CME Transients）：磁場、電子、及び高エネルギー粒子の計測装置群

PLASTIC（Plasma and Suprathermal Ion Composition）：太陽風及び超熱的プラズマのイオン組成計測装置

STEREO 探査機は 2006 年 10 月 25 日に打ち上げられ、2-3 ヶ月間地球周回軌道を飛翔した後、月スイングバイを用いて太陽周回軌道に投入され、その後順調に太陽及び内部太陽圏の観測を継続している。

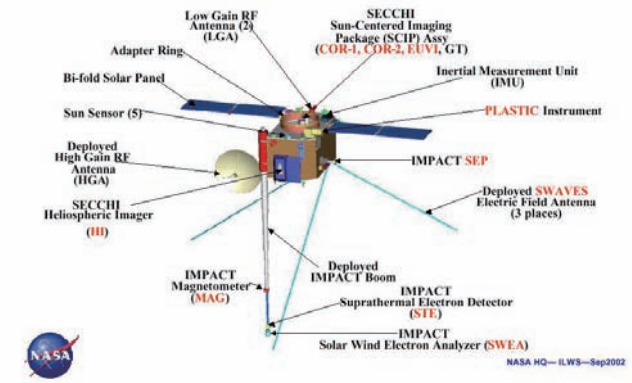

図 2　STEREO 探査機

図 3　NICT 小金井本部の受信設備

宇宙天気ビーコンモード

STEREO 探査機は本来ミッションに加えて、宇宙環境計測の空白域である内部太陽圏をモニターする上でも重要な役割を果たしうる。そのため、NASA は NOAA/SWPC（米国の宇宙天気予報センター）と協力して STEREO 探査機にリアルタイムビーコンモードを実装した。これはビットレートを低くおさえて（633bps）観測データを垂れ流しにし、宇宙環境を常時モニターできるようにしたものである。同様の機能は ACE 探査機、IMAGE 衛星でも既に導入され利用されている。特に ACE 探査機の太陽風データは宇宙天気予報機関にとって無くてはならないリアルタイムデータとして大いに利用されている。NASA は LWS(Living with a star)計画で今後打ち上げる予定の衛星・探査機に関して、同様の機能を実装することを検討中とのことである。

24 時間 365 日出来る限り欠落のないようにリアルタイムビーコンデータを取得するためには、NASA の DSN（Deep space network：深宇宙ネットワーク）の地上局だけではカバーしきれないために、他国の宇宙機関や宇宙天気予報機関にも協力が求められていた。我が国では、宇宙天気予報の研究及び業務を担当している NICT（(独) 情報通信研究機構）が協力を申し出て、2007 年 1 月末から小金井本部にある VLBI 実験用の 11m アンテナ設備（**図 3**）を使ってデータ受信の試験等を開始し、現在はほぼ順調に小金井本部での可視時間帯の運用を実施している。

他には英国の RAL（ラザフォード・アップルトン研究所）がデータ受信に協力しており、フランスの CNES もデータ受信の準備を進めつつある。これらの地上局のネットワークによって、1 日のうち、かなりの時間帯がカバーできるようになりつつある。

受信したデータは NASA の GSFC/SSC に集約され、データアーカイブと公開用のデータ処理が行われている。処理された準リアルタイムの画像データ、時系列プロットは以下の URL で公開されている。

画像データ：

http://stereo-ssc.nascom.nasa.gov/beacon/beacon_secchi.shtml

時系列プロット：

http://stereo-ssc.nascom.nasa.gov/beacon/beacon_insitu.shtml

図4にビーコンデータ画像の Web ページを一例として示す。

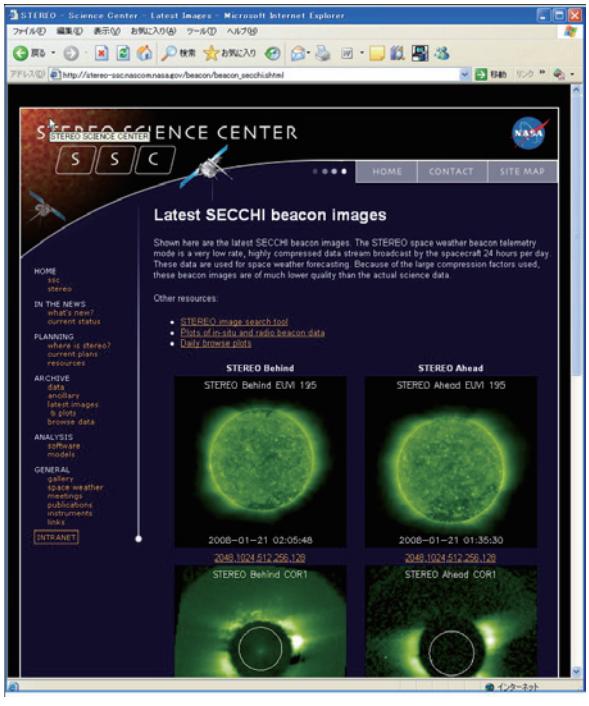

図 4　ビーコンデータ画像の Web ページ

宇宙天気予報の利用実験

現在のところデータが欠落する時間帯も存在するが、リアルタイムデータ受信は概ね順調に運用されている。

NICT の地上局も、少なくともここ 1-2 年はデータの受信が可能と思われる。そこで、リアルタイムビーコンデータを用いた宇宙天気予報への利用実験を検討している。以下に、いくつかの利用概念について述べる。

1) 太陽活動の先行監視

太陽活動の状況把握としては、太陽フレアやプロトン現象の源である活動領域の現況と推移の監視が重要となる。しかし、地球近傍の観測からは地球の裏側の領域での活動の様子を直接的に知ることができない。STEREO-B のデータを用いると地球近傍からは見ることが出来ない東のリムから回りこんでくる活動領域をいち早くモニターすることができるため、活動領域の

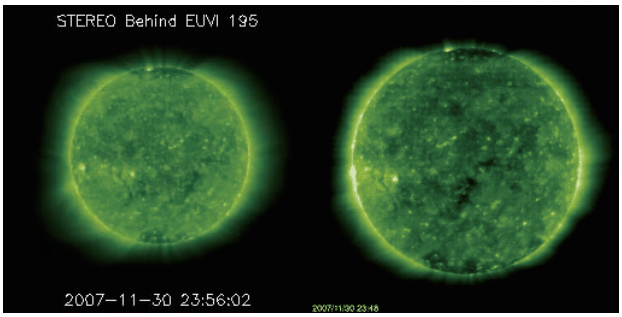

活動度や今後の推移を予測する上で有益である(**図 5**)。

図 5 STEREO-B(左)と SOHO(右)の太陽 EUV 画像

2) 太陽風の先行監視

太陽は約 27 日で自転しており、これに伴って太陽風の速度や密度、磁場強度やセクター構造が変化する(**図 6**)。もし、「惑星間空間の構造が定常的である(時間変化しない)」と仮定できるのであれば、STEREO-B で観測された太陽風パラメータはタイムラグ t_{lag} 後に地球に到来することが予測できる。Lag time の推定式は次の通りである。

$$t_{lag} = (T/2\pi)\theta - (l_1 - l_0)/Vsw$$

ここで、T は地球から見た太陽の自転周期、θ は地球－太陽－STEREO 探査機のなす角度、l_1 は太陽から STEREO 探査機までの距離、l_0 は太陽から地球までの距離、Vsw は太陽風速度である。STEREO－B のデータを用いることで、地球に到来する太陽風の状態を数日前に予測することが可能となり、地磁気活動度予測モデルやグローバル MHD シミュレーションの入力パラメータとして利用すれば、定量的な宇宙環境予測へと応用範囲は広がる。但し、現実的には Alfven 波動に伴う時間変化が重畳していたり、CME 等の突発的な現象には対応できない等の問題もあるため、実装に向けてこれらの課題を克服していく必要がある。

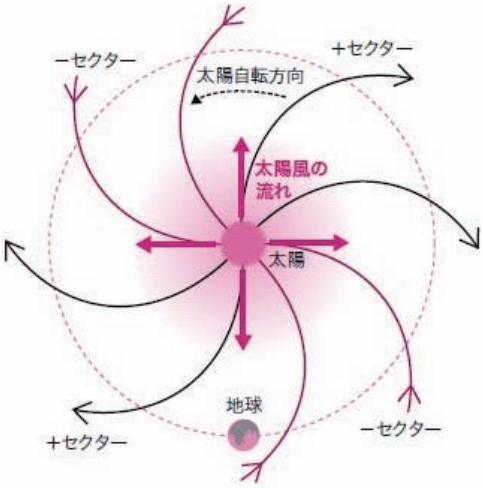

図 6 太陽風の構造

3) CME の先行監視

CME(コロナ質量放出)は地磁気嵐の要因の一つであり、CME 前面の衝撃波は、高エネルギープロトンの生成に重要な役割を担っていると考えられている。CME はコロナガス中の電子が太陽光を散乱することで可視化されるため、地球に到来する CME は、地球近傍から観測した場合、コロナガスが同心円状に拡がる Halo CME として見えることが多い。ところが、太陽から地球と反対方向に放出される CME も同様の見え方をするため、コロナグラフの画像のみで両者を区別することは困難である。加えて、CME が太陽から離れるにつれて見えにくくなるため、CME が地球へ到来するまでの状況をモニターすることは難しい。2 機の STEREO 探査機観測ならば、地球と離れた角度からの観測なので、CME の移動方向や CME が太陽から地球に到来するまでの様子をモニターすることが可能となる(**図 7**)。

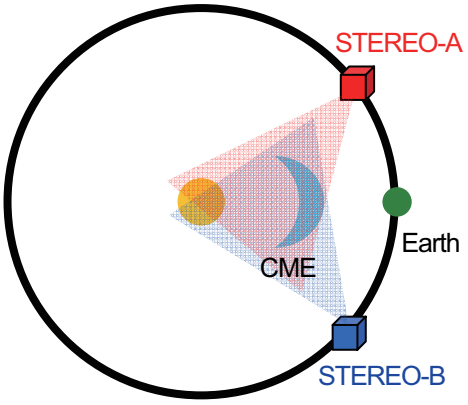

図 7 地球到来 CME の監視

4) プロトン現象の先行監視

プロトン現象は、人工衛星の機器の劣化や動作の不具合、有人宇宙活動におけるリスク要因となる。プロトン現象はこれまでに観測されている事例が限られているため、その空間的な広がりや時間発展・衰退、粒子の加速メカニズム等で未知の要素が多く残されており、STEREO 探査機を用いて異なる経度帯でプロトン現象を同時観測すること自体が重要な研究テーマである。

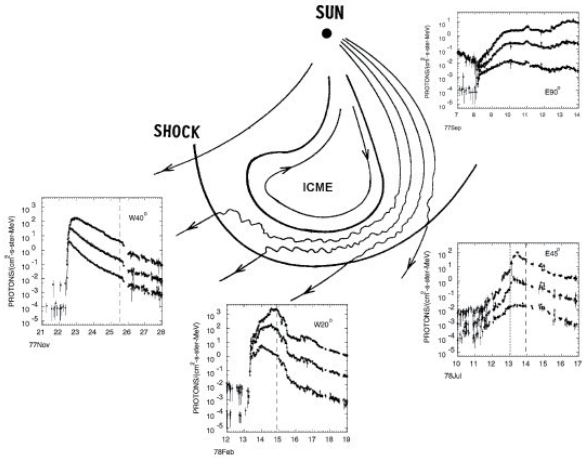

図8 フレア発生経度と CME、プロトン現象の関係
[*Cane et al.*, 1988]

一方、**図 8** に示すように経験的にはプロトン現象の要因となる太陽フレアの発生経度によって、地球への高エネルギープロトンの到来時刻が異なる。地球から見て西 45 度付近の活動領域に起因して発生するプロトン現象の到来時刻が一番早く、そこから離れるにつれて、到来時刻は遅くなる。そのため、STEREO 探査機のように異なる経度で高エネルギープロトンをモニターすることが出来れば、プロトン現象の発生・衰退の状況やその推移を先行的に検出できる可能性がある。

まとめ

STEREO 探査機データは、観測情報が著しく不足している内部太陽圏の監視において貴重な情報を提供し、宇宙天気予報の研究開発のみならず、オペレーショナルな予報業務にとっても有益な情報を提供しうる。

また、STEREO 探査機の太陽風パラメータに時刻補正や座標変換を行い、ACE 探査機と同様にモデルやシミュレーションに入力することで、磁気圏や電離圏の状態の予測へと可能性が広がる。

STEREO 探査機を一つの要素として内部太陽圏監視ネットワークを構築することで、宇宙環境の状況把握を充実させるとともに、宇宙天気予報のリードタイムを長くするための試みが可能になることが期待される。

参考文献

Cane, H. V., Reames, D. V., and von Rosenvinege, T. T.: 1988, *J. Geophys. Res.*, **93**, 9555-9567

DEVELOPMENT OF A LIGHT WEIGHT, LARGE AREA IN-SITU DUST/DEBRIS DETECTOR

Hideo Ohashi[1)], Sho Sasaki[2)], Takayuki Hirai[1)], Hiromi Shibata[3)], Ken-ichi Nogami[4)] and Takeo Iwai[5)]

1) *Tokyo University of Marine Science and Technology*, 2) *National Astronomical Observatory of Japan*, 3)*Kyoto University*, 4) *Dokkyo Medical University*, 5)*University of Tokyo*

1. Introduction

There exists inner- and extra-solar origin cosmic dust (hereafter “dust”) in the solar system. These dust particles have pristine material information and are the clues to understand the evolution of the solar system. High speed dust and/or debris impact on the satellite might hazardous to the operation of the satellite; therefore dust/debris study is important to evaluate the possible risk on the human activities in space.

There are two types of in-situ dust/debris detector; 1) a counter to measure the physical parameters such as mass, velocity and incident direction, as onboard GALILEO, NOZOMI, 2) an analyzer to measure chemical composition of the dust, as onboard HELIOS, STARDUST, CASSINI, etc. In both cases high velocity dust particles are impacted on the metal target plate, plasma cloud was formed (impact ionization), positive/negative ion are collected and measured. Impact ionization type of detector is the main stream for in-situ dust/debris measurement.

Future dust measurement in space, some restrictions such as “effective dust measurement with large aperture”, “light weighed to minimize the cost” are required. To fulfill these requirements, simplification of the structure is necessary. Determination of target shape, distance between target and grid, applied voltage are crucial for the development. But conventional detector, such as MDC onboard NOZOMI was box shaped with low symmetry, this caused the impact position dependence of signal and was the deficit of this detector. Our objective of study is to determine the optimum shape and applied voltage condition based on the experiment for the impact ionization detector (IID).

2. Principle of impact ionization detector

The first generation IID is composed of a circular metallic plate (target) of 5cm in diameter, side wall and an entrance grid. Dust with velocity higher than a few km/s impacting on the target generates plasma. For the easiness of handling, entrance grid is grounded, while the target is biased with high voltage (Fig.1). From the target signal, we can calculate rise-time t and generated total charge Q. Where t and Q/m are functions of dust impact velocity v, and is empirically noted as follows:

$$t = c_g v^{\alpha} \qquad (1)$$

$$Q/m = c_r v^{\beta} \qquad (2)$$

where c_g, c_r, α and β are determined by the calibration experiment [1,2]. From the measured rise-time t, we obtain impacting dust velocity v by applying v-t calibration curve, and this v is applied to v-Q/m curve we can obtain impacting dust mass m, while generated charge Q is already known.

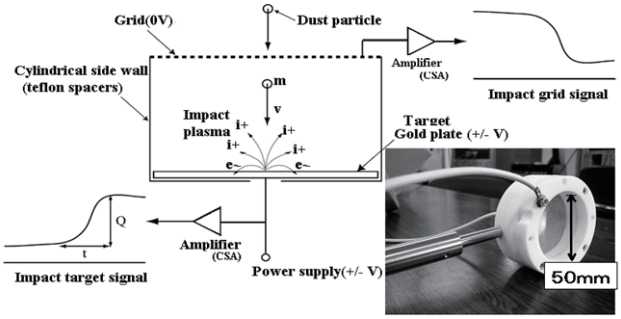

Fig.1 Principle of impact ionization detector

3. Experiments

Van de Graaff accelerators at HIT (High Fluence Irradiation Facility, the University of Tokyo, Tokai-mura, Japan) and MPI-K (Max-Planck Institute for Nuclear Physics, Heidelberg Germany) are used for calibration experiment. Micron sized conductive particles are accelerated to a few km/s to tens of km/s and are impacted onto metallic target. Inserted photograph in Fig.1 is the first generation IID. Applied voltage on the target, and target-grid distance were changed. Basic study proved this parallel-plane type of detector is superior to MDC which is asymmetric inside the detector.

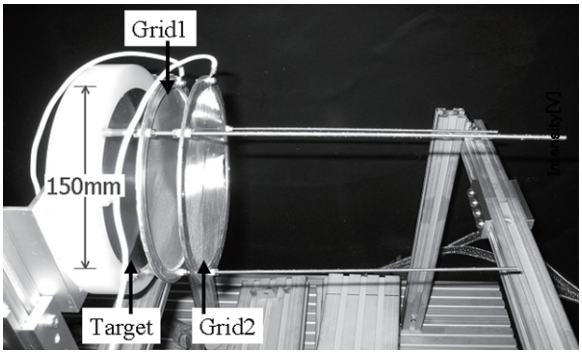

Fig.2 Second generation IID

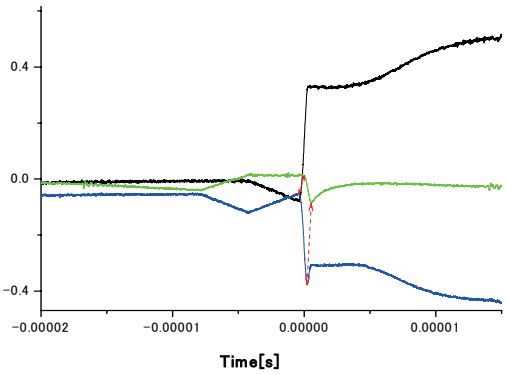

Fig.3 Typical signals

Second generation IID has an aperture of 15 cm in diameter, and has two grids to study the plasma cloud behavior. For charged particles, we can calculate their velocity from the signals. Side wall was removed to keep it light-weighed (Fig.2). Typical signals are show in Fig.3.

Third generation IID has an aperture of 30 cm in diameter, cylindrical side wall, and two grids with a total mass of 2kg (Fig.4).

Fourth generation IID has an aperture of 20 cm square, side wall, and two grids with a total mass of 2kg (Fig.5). Square type aperture was adopted to maximize the target area.

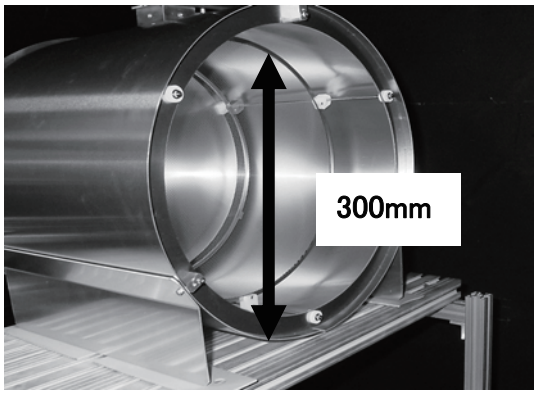

Fig.4 Third generation IID

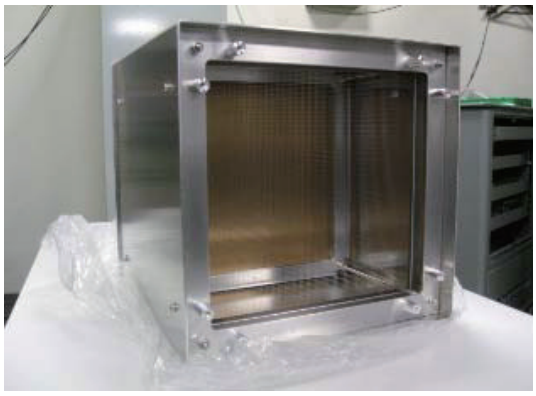

Fig.5 Fourth generation IID

4. Results and discussions

Rise-time t vs particle velocity v with different particles, different applied high voltages, and impact position dependence are shown in Fig.6 to Fig.8. Charge to mass ratio Q/m vs particle velocity v with different particles, different applied high voltages, and impact position dependence are shown in Fig.9 to Fig.11.

From these figures it is clear that empirical formulae (1) and (2) fit well in general. From Fig.6 and Fig.7, there is little dependence of the incident particle, nor applied high voltage. For the safety to satellite applied voltage is preferable as low as possible. From Fig.8 it is clear that there is little impact position dependence, therefore this type of detector has effective area nearly equal to that of the target area. Charge to mass ratio Q/m vs particle velocity v data (Fig.9) is incident particle material dependence. This feature proves us that this detector would work as a simple chemical analyzer. Cosmic dust with metallic composition

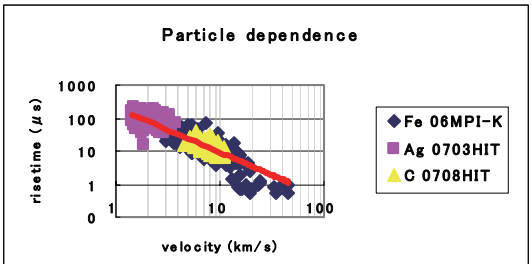

Fig.6 v-t Particle dependence

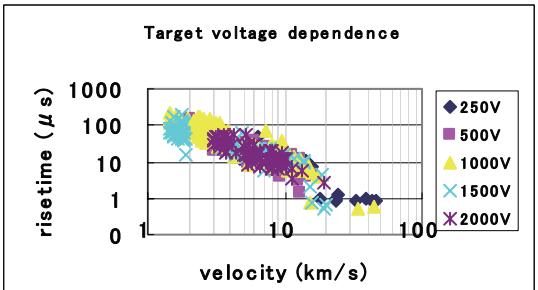

Fig.7 v-t Target voltage dependence

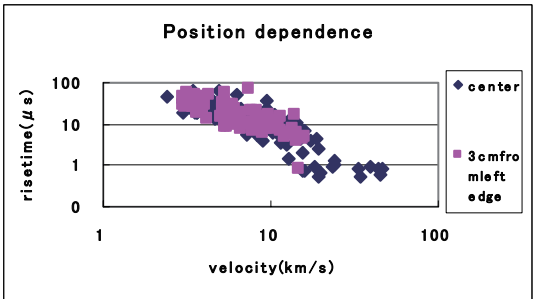

Fig.8 v-t Position dependence

and chondritic or stony composition would be differentiated by measuring *Q/m* vs velocity *v* for each impact signal. To prove this feature we are planning to perform further experiments with conductive latex particles to simulate chondritic dust particles.

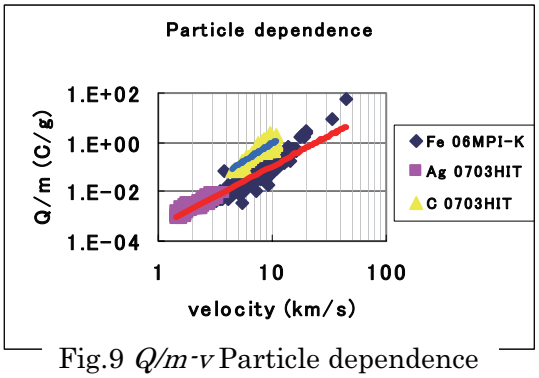

Fig.9 *Q/m-v* Particle dependence

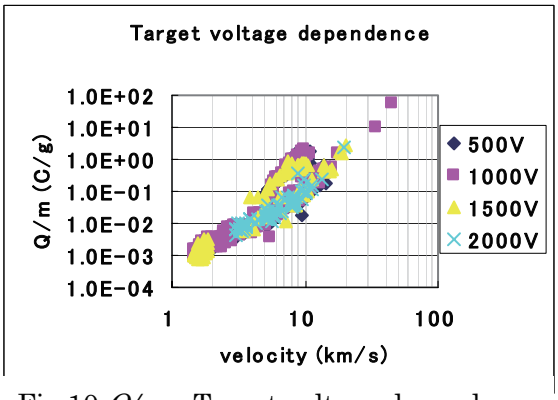

Fig.10 *Q/m-v* Target voltage dependence

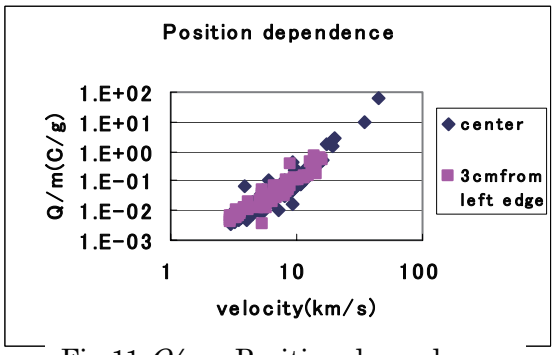

Fig.11 *Q/m-v* Position dependence

5. Conclusions

There is a good correlation between target rise-time *t*, charge to mass ratio *Q/m* and impacting particle velocity *v*. From rise-time *t*, dust impacting velocity *v* is deduced. From total charge produced *Q*, we can deduce impacting dust mass *m*. There is little dependence on impact position, as well as incident angle. These features prove that parallel-plane type of detector has enough performance for dust/debris impact ionization detector. From impacting particle material dependence data of charge to mass ratio *Q/m* vs particle velocity *v*, tit might work as chemical analyzer. If this feature is proven, IID would work as a simplest chemical analyzer compared to the sophisticated instrument ever developed.

References

[1] R. Srama, E. Gruen, and the CASSINI Dust Science Team; Phyics, chemistry and dynamics of interplanetary dust, ASP Conference, 104 (1996) 227-231.

[2] E. Igenbergs, et al., Mars Dust Counter, Earth Planets Space, 50 (1998) 241-245.

ニューラルネットワークによる静止軌道の高エネルギー電子フラックス予測について

Forecast of high-energy electron flux at geosynchronous orbit using neural network

亘　慎一（情報通信研究機構）、徳光政弘（豊橋技術科学大学）
北村健太郎（徳山工業高等専門学校）、石田好輝（豊橋技術科学大学）

Shinichi Watari (National Institute of Info. and Com. Tech.)
Masahiro Tokumitsu (Toyohashi University of Technology),
Kentarou Kitamura (Tokuyama College of Technology)
Yoshiteru Ishida (Toyohashi University of Technology)

Abstract

High-energy electron flux at geosynchronous orbit significantly increases associated with high speed solar wind. The high-energy electron cause internal charging of satellites. It is important for satellite operations to forecast increase of the flux. Here, we report a forecast model using neural network with inputs of solar wind data.

１．はじめに

放射線帯は比較的変動が少ないものと考えられてきたが、近年、地磁気嵐などに伴いダイナミックに変動することがわかってきた。通信、放送、気象観測などの衛星で使われている静止軌道は、この放射線帯外帯の外縁にあたる。そのため、放射帯の変動に伴って高エネルギー電子のフラックスが大きく上昇し、内部帯電による衛星障害を発生させることがある[1,2,3,4]。たとえば、1994 年 2 月にリルハンメルオリンピックの日本向けのジャンプ競技の衛星中継が中断された。このとき、米国の気象衛星 GOES で高エネルギー電子フラックスの上昇が観測されていた。

高エネルギー電子は同じエネルギーのイオンに比べて侵入深さが一桁から二桁深いため、宇宙機の外被を通り抜けて宇宙機内部の回路や導体に帯電を起こしたり、宇宙機の外被のケーブルシールドなどの絶縁物に入り込んで帯電を起こしたりする[2]。このような帯電は表面帯電に対して内部帯電と呼ばれている。

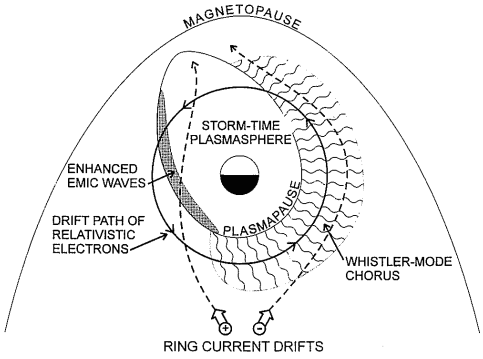

図 1 VLF 波動による高エネルギー電子フラックスの増加メカニズム[1]

高エネルギー電子の増加するメカニズムについては、図 1 に示すように VLF 波動と粒子の相互作用による加速とする説が最近有力になってきているがまだはっきりとはしていない[5,6,7]。また、VLF 波動の直接観測データをリアルタイムで入手するのは現状では困難である。これまでの研究から高エネルギー電子のフラックスは、地磁気嵐の発達に伴って減少し、地磁気嵐の回復期に増加するということがわかっている。また、図 2 に示すように大きな地磁気嵐の後に高速な太陽風が続くと高エネルギー電子フラックスの大きな上昇が起こることが知られている[8,9,10]。

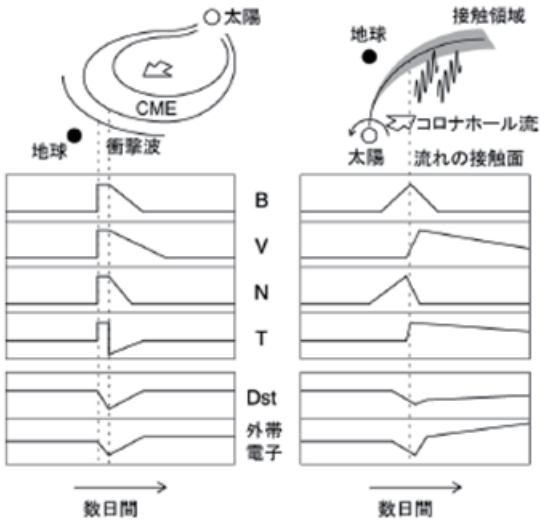

図 2 太陽風の変動(B：磁場、V：速度、N：密度、T：温度)と高エネルギー電子の増加[10]

高エネルギー電子フラックスが危険なレベルに達することをあらかじめ知って衛星の運用を安全に行うためには、高エネルギー電子の増加についての正確な予測が必要となる。そこで、ACE 衛星からの準リアルタイムで入手することができる太陽風データを入力としたニューラルネット[11]による高エネルギー電子の予測について検討を行ったので報告する。

２．ニューラルネットによる予測

２－１予測誤差の評価方法について

予測モデルの検討を行う際には、その予測誤差の評価が必要であり、相関係数(CC: Correlation Coefficient)、二乗誤差（MSE: Mean Square Error、式（1）参照)、予測効率（PE: Prediction Efficiency、式（4）参照）を用いて評価を行った。以下の式で N は予測値の数、f_i は予測値、x_i は予測値に対応する観測値を表す。

$$MSE = \frac{1}{N}\sum_{i=1}^{N}(f_i - x_i)^2 \qquad (1)$$

$$VAR = \frac{1}{N}\sum_{i=1}^{N}(x_i - \bar{x})^2 \qquad (2)$$

$$\bar{x} = \frac{1}{N}\sum_{i=1}^{N} x_i \qquad (3)$$

$$PE = 1 - \frac{MSE}{VAR} \qquad (4)$$

２－２　ニューラルネットへの入力データについて

米国の気象衛星 GOES で観測された 2MeV 以上のエネルギーを持つ電子のフラックス変動、対応する太陽風速度、惑星間空間磁場の南北成分、過去 72 時間のイプシロンの積分値、時刻（UT）の 5 つの入力パラメータにより、24 時間先の電子フラックスの変動を予測することにした。データに関して、太陽風の速度、惑星間空間磁場の南北成分は NASA/NSSDC の OMNI2 データベースからの 1 時間平均値、高エネルギー電子フラックスに関しては NOAA/NGDC のデータベース SPIDR から GOES10 衛星によって観測された 2MeV 以上の電子フラックスの 1 時間平均値を用いた。イプシロンは、以下の式であらわされる赤祖父[12]によって考えられた太陽風から磁気圏へのエネルギーフラックスの指標である。ここで、V は太陽風の速度、B は惑星間空間磁場の大きさ、By は惑星間空間磁場の東西成分の大きさ、Bz は惑星間空間磁場の南北成分の大きさをそれぞれ表す。

$$\varepsilon \propto VB^2 \sin^4\left(\frac{\theta}{2}\right) \qquad (5)$$

$$\theta > B_z \text{ のとき} \quad \theta = \tan^{-1}\left(\frac{|B_y|}{|B_z|}\right) \qquad (6)$$

$$\theta < B_z \text{ のとき} \quad \theta = 180 - \tan^{-1}\left(\frac{|B_y|}{|B_z|}\right) \qquad (7)$$

２－３ニューラルネットについて

ニューラルネットワークを用いた予測モデルを構築する際には、予測誤差や計算時間を考慮して中間層の数及び中間層のニューロンの数を決める必要がある。そこで、まず、中間層のニューロンの数を 10 個に固定して、中間層の数を 1 から 5 まで増やして予測誤差を調べた。その結果、中間層の数を増加させても予測誤差はほとんど変わらないことから、中間層の数を 1 にすることにした。次に中間層の数を 1 に固定して、中間層のニューロンの数を 5 から 25 まで増やして予測誤差を調べた。ニューロン数が 10 個あたりで予測誤差がほとんど改善されなくなることから中間層のニューロン数を 10 とした。

入力データ及び上記の検討から図 3 に示す予測モデルを作成し、1998 年から 2006 年までのデータを使って学習させ、2003 年 1 年間を内挿で予測させた。図 4 にこのモデルによる予測値とそれに対応する観測値の散布図を示す。予測値と観測値を比較した結果、高エネルギー電子フラックスの予測値は磁気嵐主相での急激な減少には追随できないものの、

日変化及び回復相におけるフラックスの増大は予測値と観測値でよい一致が得られることがわかった。

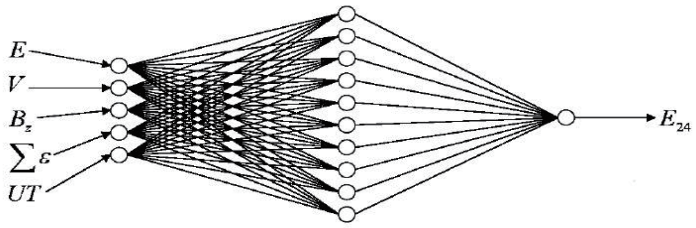

図 3 ニューラルネットワークによる予測モデル

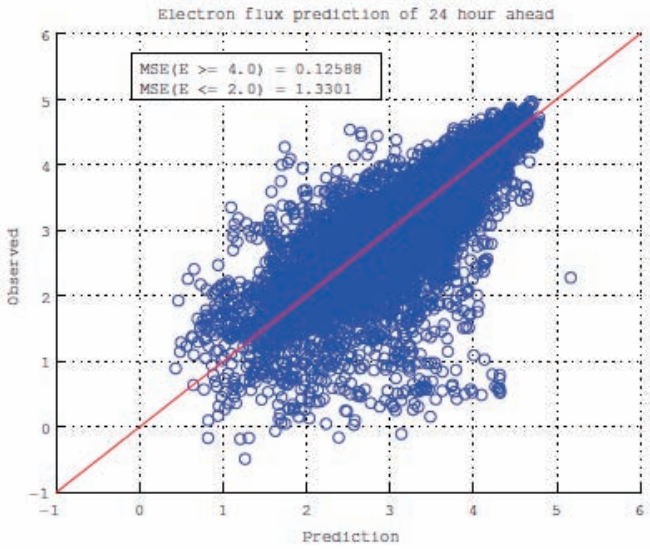

図 4 モデルによる予測値とそれに対応する観測値の散布図

２－４入力データ依存性について

入力データ依存性を調べるため、5 つの入力データから 1 つだけデータを外して 4 つの入力データで学習、予測させて 5 つの入力データによる予測誤差と比較を行った。その結果、現在の高エネルギー電子フラックス値の予測誤差に対する寄与がかなり大きいことがわかった。

３．まとめ

情報通信研究機構では、これまで米国の気象衛星 GOES による高エネルギー電子フラックスのリアルタイムデータをモニターし、2 機以上の GOES 衛星で、そのフラックスが 10,000 を超えた場合に臨時情報を出して衛星運用者に注意を促してきた。また、フラックスレベルを自動判定し、そのフラックスが 1,000 以下であれば「緑」、1,000 を越え 10,000 以下であれば「黄」、10,000 を超えた場合は「赤」という基準で、図 5 に示すような web page のレベルメータによる準リアルタイムの情報配信を行ってきた。

図 5 web page による NICT 宇宙天気情報の提供（http://swc.nict.go.jp/）

これらに加えて、今回報告した太陽風の準リアルタイムデータを入力とするニューラルネットワークによる高エネルギー電子フラックス予測システムを開発した。この予測システムを用いて 2007 年のなかば頃より試験的に図 6 に示すような web page による情報提供を開始した。現在は、3 日先までの予測情報を提供している。

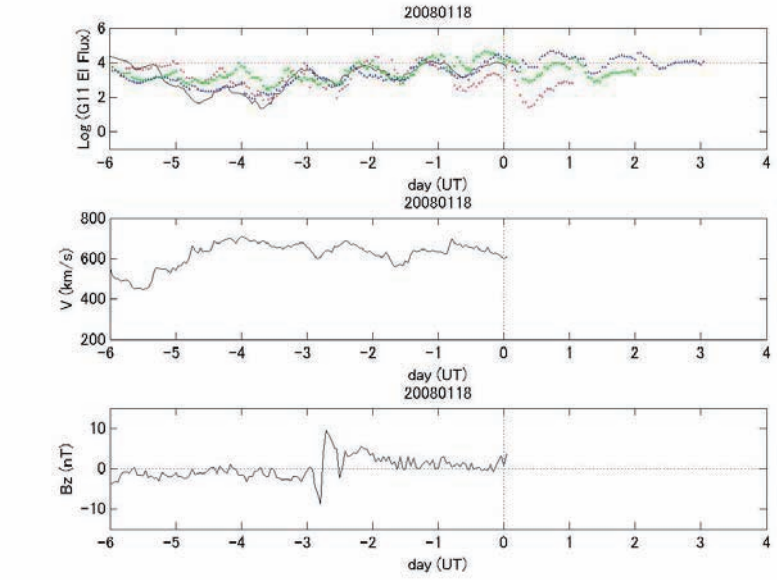

図 6 ニューラルネットワークによる高エネルギー電子フラックスの予測
（http://www2.nict.go.jp/y/y223/sept/swcenter/elforecast.html）

参考文献

1 D.N. Baker, S. Kanekal, J.B. Blake, B. Klecker, and G. Rostoker, “Satellite Anomalies Linked to Electron Increase in the Magnetosphere,” EOS, Trans. Am. Geophys. Union, vol.75, pp.401-405, 1994.

2 趙孟佑, 藤井治久, “宇宙環境での帯電・放電現象についての研究動向と将来課題 第 1 回宇宙環境と宇宙機の帯電電位,” 日本航空宇宙学会誌, vol.51, no.591, pp.109-117, Apr. 2003.

3 亘 慎一, “宇宙天気予報,” 日本航空宇宙学会誌, vol.51, no.598, pp.274-281, Nov. 2003.

4 亘 慎一, “宇宙天気予報小特集 2.宇宙環境擾乱による障害と宇宙天気予報,” プラズマ核融合学会誌, vol.82, no.11, pp.739-744, Nov. 2006.

5 D. Summers, R.M. Thorne, and F. Xiao, Relativistic theory of wave-particle resonant diffusion with application to electron acceleration in magnetosphere,” J. Geophys. Res., vol.109, A03213, 2004

6 R.B. Horne, R.M. Thorne, “Potential waves for relativistic electron scattering and stochastic acceleration during magnetic storms,” Geophys. Res. Lett., vol.25, no.15, pp.3011-3014, Aug. 1998.

7 Y. Chen, D.G. Reeves, and R.H.W. Friedel, “The energization of relativistic electrons in the outer Van Allen radiation belt,” nature physics, doi:10.1038/nphys655, Jul. 2007.

8 D.N. Baker, R.L. McPherron, T.E. Cayton, and R. Klebesadel, Liner Prediction Filter Analysis of Relativistic Electron Properties at 6.6 Re, JGR, vol.95, no.A9, pp.15133-15140, 1990.

9 R. Kataoka, and Y. Miyoshi, “Flux enhancement of radiation belt energetic electron during geomagnetic storms driven by coronal mass ejections and corotating interaction regions,” Space Weather, vol.4, S09004, doi:10.1029/2005SW000211, 2006.

10 片岡龍峰, 三好由純,“放射線帯の宇宙天気予報,”天文月報, Vol.99, no.12, pp.675-681, Dec. 2006.

11 松本隆, , “II 非線形ダイナミカルシステムの再構成と予測,” 階層ベイズモデルとその周辺 時系列・画像・認知への応用, 石黒真木夫, 乾敏郎, 松本隆, 田邉國士編, pp.89-170, 岩波書店, 東京, 2004.

12 S.-I. Akasofu, “Energy Coupling Between the Solar Wind and the Magnetosphere,” Space Sci. Rev., vol.28, pp.121-190, 1981.

帯電・放電

Charging & Discharging

THRESHOLD MEASUREMENT OF SECONDARY ARC ON SOLAR ARRAYS FOR JAPANESE SPACECRAFT CHARGING GUIDELINE

Kazuhiro Toyoda, Takayuki Ose, Hirokazu Masui, and Mengu Cho

Laboratory of Space Environment Interaction Engineering, Kyushu Institute of Technology

1-1Sensui Tobata-ku Kitakyushu 804-8550, Japan

ABSTRACT : *In this paper, we report about the test results on coupons made for Working Group 1(WG1), which was established to make a Japanese guideline for spacecraft charging design. Laboratory tests were carried out with an external circuit simulating a spacecraft power system. The solar array coupon panels simulating the hot and return ends of a string circuit were tested under various combinations of string voltage and string current. We revealed that the threshold conditions for sustained arc were different in string voltage.*

1 - INTRODUCTION

Recently, the discharge phenomenon on solar array has become problem. The satellite potential depends on a surrounding plasma environment, the sunshine condition, and the surface physical properties. In GEO, when a satellite encounters substorm environment, its potential can become extremely negative due to high-energy electrons flowing into the satellite. The potential difference appears between the spacecraft ground and insulator structures like coverglass due to the difference of secondary emission yield. This cover glass potential can be higher than that of the interconnector that is close to the spacecraft ground. This is called inverted potential gradient. The cross-sectional view of spacecraft solar array is shown in figure 1.

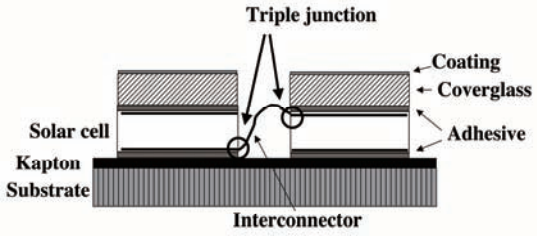

Figure 1 - Schematic of solar cell

An electric field is generated between the coverglass and the conductor, and the electric field is enhanced near the triple junction, which is the boundary of conductor, dielectric and plasma. The field enhancement at the triple junction induces an discharge. The single discharge called the primary arc causes considerable problems, such as electromagnetic interference and destruction of solar array circuit. The primary arc can cause short-circuit between adjacent cells having high voltage potential. This phenomenon is called the secondary arc. The short-circuit current of secondary arc is supplied by solar cells generating electric power. When the secondary arc occurs, the output power of the circuit is lost. This can cause the destruction of the solar array circuit at the worst case. The troubles of destruction of the solar array circuit due to secondary arc are reported[1,2].

The secondary arc is classified into several steps whether short circuit phenomenon is temporary or not. Figure 2 shows the definition of the discharge current waveform. The time that first falls to below 10% of peak value (I_{peak}) on the trailing edge of the primary arc waveform is defined as T_{end}. The time duration, which the current over 90% of peak current value flows from T_{end}, is defined as time duration of the arc. We defined that the secondary arc with time duration less than and more than 2μs were Non Sustained Arc (NSA) and Temporary Sustained Arc (TSA), respectively. If the arc current flows permanently, the

secondary arc is defined as Permanent Sustained Arc (PSA). It is suggested that the occurrence of the secondary arc depends on the voltage between adjacent cells in the solar array (V_{ST}), the power generation current (I_{ST}), the gap length between adjacent cells, and the energy of the primary arc[3-5].

The Working Group 1 was organized to prepare a Japanese spacecraft charging guideline in order to mitigate spacecraft failure due to charging and discharging. In the guideline, the threshold measurement of secondary arc inception was needed to understand the voltage, the current, and the gap length that cause the secondary arcs. We have performed the secondary arc threshold measurement so far[4-5]. In this paper, the test results of secondary arc are reported mainly for the Triple-Junction solar array coupon.

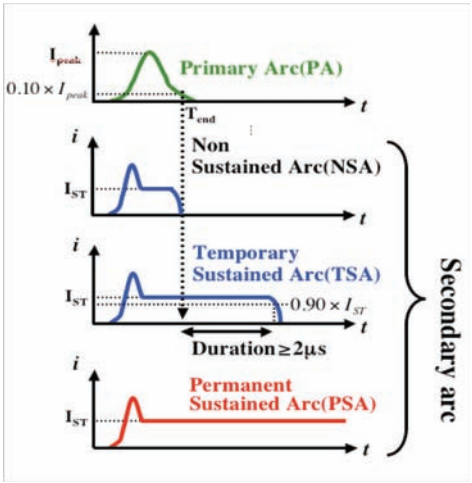

Figure 2 - Definition of primary arc and secondary arc.

2 - EXPERIMENT

9 Triple-Junction (TJ) cell coupons and a Silicone (Si) cell coupon were prepared for the threshold measurement. The gap lengths of TJ coupons were 0.5mm, 0.8mm, 1.0mm, and 2.0mm. The coupons with and without RTV grouting in gap were prepared for the gaps of 0.5mm and 1.0mm. The Si coupon had 0.5mm gap length. Figure 3 shows a example photograph of the coupon used in the experiment. The substrate was made of aluminum honeycomb covered with Carbon Fiber Reinforced Plastic (CFRP). The top of the substrate was covered with the Kapton® film. This solar array coupon consisted of 24 TJ solar cells (76mm×37mm). All solar cells were glued on the Kapton® film by RTV silicone adhesive. Two solar cells were connected in series via the inter-connectors. We used four cells formed two strings with two cells with facing as a treat sample. This coupon was composed of three strings named R, B, and G. The electrodes connected to both ends of the series connection are called bus bar. All bus bars are covered with RTV silicon in order to suppress arc inception there.

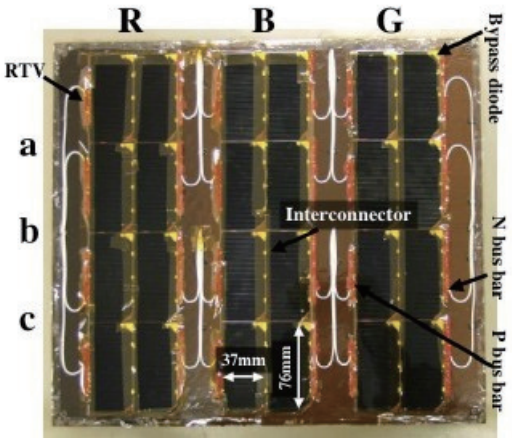

Figure 3 - Picture of solar array coupon.

The sketch of the measurement system is shown in figure 4. The experiments were performed in a vacuum chamber. The GEO environment was simulated by an electron beam gun. All waveforms of the array potential and the discharge current were acquired by a high-speed data acquisition system. During the experiments, the video image of the coupon was recorded in a hard disk drive connected to a PC as a digital video image.

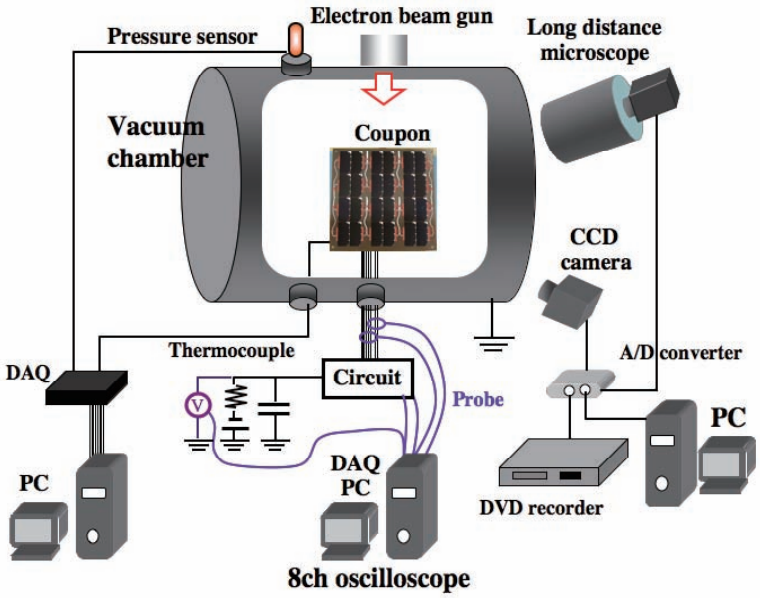

Figure 4 - Experimental setup

The external circuit used in the secondary arc experiments is shown in figure 5. Direct current source V1 is a power supply imitated output of solar array generating electricity. This power supply is demanded to follow the phenomenon of several microseconds like the primary arc[6]. Therefore, we used DC power supply composed of the current regulative diode parallel in this experiment. This power supply has the low output capacitance lower than 5nF and the recovery time of about 0.5μs. RL is pseudo-load.

The C1～C3 is corresponding to the capacitance of one series circuit which 50 TJ cells are connected on a substrate. V_{bias} and C_{ext} imitate the potential and capacitance of the satellite respectively. The primary arc energy is supplied by this capacitance. In the primary arc, the electron charged in C_{ext} flows from arc site to the chamber wall through plasma. This current is called a blow off current. We measured the blow off current with a current probe, CP3. Solar strings having higher potential only a due to RL potential is called HOT line and the other side is called RTN line.

At first, the current usually flow the route of V1-HOT-RL-RTN –V1 by V1 power supply. This route shows the current supplied by the electric power to the load. In normal operation, the V2 cannot usually output because the voltage of V2 is set less than voltage of RL. If arc plasma makes short-circuit between cells of HOT and RTN line, the voltage between strings decrease less than the voltage of V2. Here, all current flows from V1 to arc site. This is a current loop of the secondary arc. The secondary arc inception is judged by measuring the current with current probe (CP1, CP2). The difference between CP1 and CP2 is arc current that actually flows between cells as secondary arc. V_{ST} during steady-state is called string voltage. The bypass capacitance C_{BP} was also connected to simulate a bus capacitance. A LCR circuit controlled a primary arc waveform in order to simulate a flashover current.

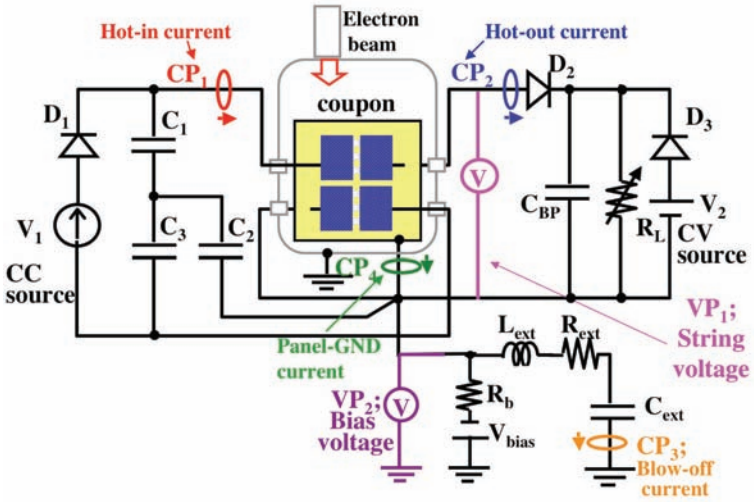

Figure 5 - Experimental circuit.

The test procedure is as follow;

1. Measure TSA threshold at a fixed V_{st} with L_{ext}= R_{ext} = 0 and C_{ext}= 5nF. If a TSA occurs, move to PSA test. If not within 20 arcs, increase current and continue TSA test.
2. Move to a virgin gap and measure PSA threshold from the current of TSA threshold. If a PSA does not occur within 10 TSA, increase current.

After every test case, microscopic pictures were taken by a long distance microscope to check the health of test gaps.

3 - RESULTS AND DISCUSSIONS

Figure 6 shows the threshold test results of secondary arc. The cells in figures were classified by color. The numbers in cells show the average of secondary arc durations except that PSA occurred as 1st secondary arc. The numbers in parentheses show the current value flowing during secondary arc actually.

In every coupon, no secondary arc occurred in the Vst of 30V. The TJ coupon with 2.0mm gap and Si coupon with 0.5mm gap showed higher threshold value of 50V. The threshold current for PSA was 1.5A except for 2.0A in TJ coupon with 2.0mm.

Figure 7 shows the relation between secondary arc duration and current. These durations were average values. As shown in this figure, the secondary arc duration increased with increasing current. The duration of 1ms corresponded to the current from 1A to 2A, resulting in PSA in all coupons. This means the secondary arc duration over 1ms can cause PSA.

V_{st}, V	I_{st}, A			
	0.5	1.0	1.5	2.0
30	No secondary arc up to 4A			
50	7μs (0.7A)	28μs	4534μs (1.7A)	
70	4μs (0.6A)	250μs (1.2A)	7747μs (1.8A)	
90	54μs (0.5A)	231μs (1.2A)		
110	5μs (0.6A)	552μs (1.2A)	2750μs (1.6A)	

PA　NSA　TSA　PSA

(a) TJ 0.5mm

V_{st}, V	I_{st}, A			
	0.5	1.0	1.5	2.0
30	No secondary arc up to 4A			
50		47μs	4086μs (1.7A)	
70	7μs (0.7A)	209μs (1.2A)		
90	4μs	41μs (1.2A)	4384μs (1.8A)	
110	3μs (0.6A)	179μs (1.2A)	7408μs (1.8A)	

PA　NSA　TSA　PSA

(b) TJ 0.8mm

V_{st}, V	I_{st}, A			
	0.5	1.0	1.5	2.0
30	No secondary arc up to 4A			
50		12μs	1126μs	4433μs
70	3μs	25μs	1225μs	
90	3μs	7μs (0.9A)	415μs (1.3A)	
110	4μs	42μs	943μs	

PA NSA TSA PSA

(c) TJ 1.0mm

V_{st}, V	I_{st}, A			
	0.5	1.0	1.5	2.0
50	No secondary arc up to 4A			
70	7μs			
110	2μs	140μs	1400μs	3900μs
200	3μs (0.7A)	110μs (1.1A)	60μs (1.3A)	
300	5μs (0.6A)	25μs (1.3A)	370μs (1.4A)	

PA NSA TSA PSA

(d) TJ 2.0mm

V_{st}, V	I_{st}, A			
	0.5	1.0	1.5	2.0
30				
50	PA	PA	PA	PA
70	3μs (0.6A)	88μs (1.2A)	1098μs (1.7A)	
90				
110	4μs (0.6A)	233μs (1.2A)	727μs (1.7A)	

PA NSA TSA PSA

(e) Si 0.5mm

Figure 6 - Threshold measurement test results of secondary arc.

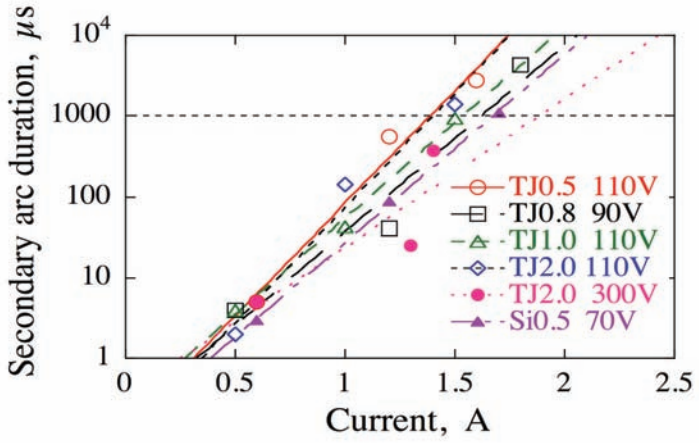

Figure 7 - Relation between secondary arc duration and current.

4 - SUMMARY

The threshold value of secondary arc was acquired for TJ cell and Si cell coupons. The ESD testing method for secondary arc was also established. The results were summarized in figure 8. The threshold value was different in gap and cell type. The safe condition was classified by 4 categories, as follows.

- Safe: no secondary arc can occur.
- Caution: TSA can occur, however PSA cannot occur.
- Danger: PSA may occur.
- Prohibition: PSA can occur.

In the case of TJ cell coupon with the gap length from 0.5mm to 1.0mm, the safe zone was below 30V. The secondary arc duration depended on current, and however showed the independent on voltage. The coupons with these gaps had PSA over 1.5A.

The TJ cell coupon with a 2.0mm gap had the safe zone below 50V. The prohibition zone was over 2.0A.

The Safe and prohibition zone of the Si 0.5mm coupon were below 50V and over 1.5A, respectively.

These test results were included in the Japanese spacecraft charging design guideline.

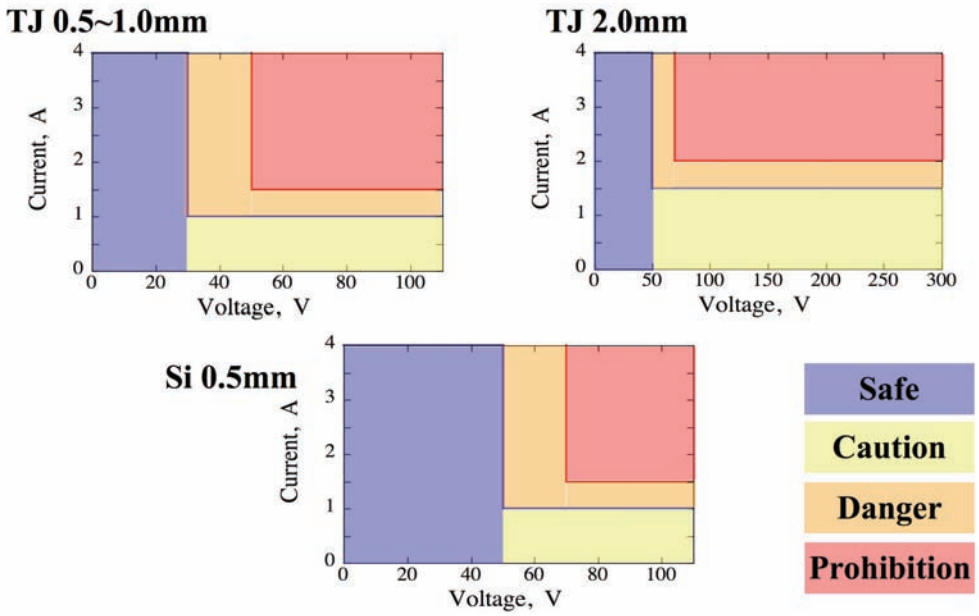

Figure 8 - Safe conditions for secondary arc.

REFERENCES

[1] I. Katz, V.A. Davis, and D.B. Snyder, "Mechanism for Spacecraft Charging Initiated Destruction of Solar Arrays in GEO", AIAA paper 98-1002, 36th Aerospace Science Meeting, Reno, Jnuary1998

[2] M. Cho, and H. Fujii, "Review on Charging and Discharging Phenomena in Space Environment: Arcing on High Voltage Solar Array and Future Issues", Aeronautical and Space Sciences Japan, Vol.51, pp.139-145, 2003

[3] S. Aso, M. Cho ; Threshold for Secondary Arc Formation on Solar Array in Low Earth Orbit Plasma Environment、Transactions of the Japan Society for Aeronautical and Space ,53, 2005, pp.516-523

[4] T. Kitamura, H. Masui, K. Toyoda, M. Cho, "Secondary arc tests on solar arrays for international standardization of ESD test and Japanese spacecraft charging guideline", 10th Spacecraft Charging Technology Conference, Biarritz, France, June 18-21, 2007

[5] H. Masui, T. Ose, K. Toyoda, and M. Cho, "Research of Sustained Arc Threshold for Design Guideline of Satellite Solar Array Panel", Proceedings of 51th Space Sciences and Technology Conference, Hokkaido, JAPAN, November 2007 (in Japanese).

[6] D. Payan, "Risks of low voltage arcs sustained by the photovoltaic power of a satellite solar array during an electrostatic discharge. Solar Arrays Dynamic Simulator", Proceedings of 8th SCTC, 2001

Metal halide lamps - Simulation of power generating solar arrays for secondary arc investigation

Andreas Kroier[1,2], Teppei Okumura[1], Kazuhiro Toyoda[1], Mengu Cho[1], Erich Leitgeb[2]
[1]Kyushu Institute of Technology, Department of Electrical Engineering, Japan
[2]Graz University of Technology, Institute for Broadband Communications, Austria

Abstract

A new method to simulate power generating solar arrays of spacecraft is presented. By combining a multijunction solar array, InGaP-GaAs-Ge, and a metal halide lamp (MHL) secondary arcs were generated. The aim was that the arcs should be comparable to those generated by the currently used methods, which are the solar array simulator (SAS) or a power supply combined with a current regulating diode (CRD) circuit.
The results of the experiment showed a successful generation of secondary arcs, especially of temporary sustained arcs. The arc duration is similar for all three simulation methods. The conclusion therefore is that the MHL method can be used in the same way the SAS or CRD method can be used, as it generates the same results.

1. Introduction

Currently two possibilities are available to simulate the power generating solar array on spacecraft in ground experiments. Those are the solar array simulation method and the so-called current regulating diode method. First these two possibilities will be introduced, followed by the presentation of a new method to simulate the solar arrays on spacecraft. Subsequently a discussion of the gained results, including a comparison of the three methods in terms of the arc duration and the characteristics of the arc waveforms, is done.

2. Solar Array Simulator

The solar array simulator (SAS) is a direct current power supply with the impedance characteristics of a solar array. The inner circuit of the simulator is confidential and therefore no changes to this circuit are possible. The SAS is basically a current source with very low output capacitance of 50nF [5]. To simulate different solar arrays the I-V curve of different arrays under different conditions can be programmed into the simulator. To simulate different internal capacitances of a real solar array, an external capacitance circuit is necessary.

3. Current Regulating Diode Circuit

The current regulating diode (CRD), also often referred to as the current limiting diode or constant current diode, circuit can be attached to any suitable power supply. For the discussed experiments the CRD circuit is combined with the solar array simulator. The internal capacitance of the CRD circuit is around 135pF, one CRD has a capacitance of around 1pF [4]. The CRD function is a limitation or regulation of the current value over a specific voltage range. A detailed CRD circuit description can be found in [2].

4. Simulation Circuit

The circuit in Figure 1 can be split in four parts.

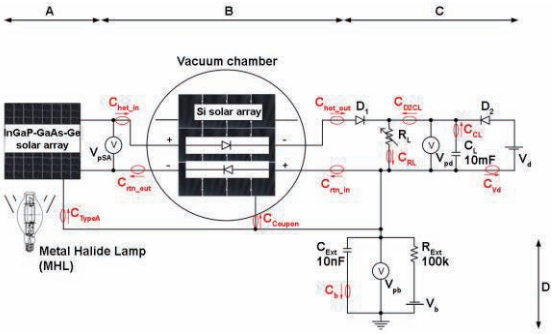

Figure 1 MHL - system circuit

Part A, the left most part, is representing the power generating solar array simulation method. In case of the MHL method this would be the InGaP-GaAs-Ge solar array and the metal halide lamp. In the other cases either the solar array simulator or the SAS and CRD combination. Part B, the middle part of the circuit, is the vacuum chamber representing the space environment to which the solar arrays are exposed and electrostatic discharge (ESD) mechanisms are investigated. The pressure in the chamber was $5x10^{-3}$Pa and the electron temperature was around 0.2eV. The ECR plasma source generated a plasma density of $1x10^{12}m^{-3}$ and the Xenon gas flow rate was 0.4sccm. The chamber size is 1m in diameter and 1.2m in length.
Part C, the right most part, simulates the bus from the solar array to the spacecraft and protection devices of a spacecraft against ESD. Part D, the lower right part, is used to bias the solar arrays to different potentials.
The array inside the vacuum chamber consists of single-junction silicon solar cells. The used coupon contains 12 silicon solar cells. Four cells in a row are connected by interconnectors forming a string. The strings electrical equivalent is a diode due to the p-n-junction nature of the single solar cells which are combined to the string. For the spotlight experiments two strings of the silicon solar array are used. In the following explanation they are referred to as hot-string and return-string. The names are resulting from the direction of the current flowing out of the power generating solar array into

the coupon (hot) or out of the coupon back into the power generating array (return). The current probes measuring these currents are designated as $C_{hot\text{-}in}$ and $C_{rtn\text{-}out}$ in part A of the circuit and $C_{hot\text{-}out}$ and $C_{rtn\text{-}in}$ in part C of the circuit. The substrate of the silicon solar array is biased to the output voltage of the power supply determined as V_b in part D of the simulation circuit. This is necessary as in its real environment the solar array substrate would have the same potential as the surrounding plasma. Also the two used strings of the solar array are biased to the same potential, as this would again be the case on a solar array in its real environment in space. The substrate of the solar array is covered with Kapton® tape on the backside to prevent arcing everywhere other than on the solar cells and their interconnectors. Part C of the simulation circuit contains two diodes, D_1 and D_2. D_1 protects the solar array in part B from any occurring arc current. Having the same functionality, D_2 protects the power supply referred to as V_d. Both diodes are legitimate in terms of realistic simulation as both of them exist on a real system in space. The capacitance C_L of part C of the simulation circuit represents the capacitance of the bus between the solar array and the spacecraft. In the ground experiment it also stabilizes the output of the power supply referred to as V_d. The variable resistance R_L allows for variegating the output power of any of the simulation methods of the power generating solar array. The remaining part D of the simulation circuit biases the solar array inside the vacuum chamber as well as the multijunction solar array or the capacitances of the SAS and CRD method to a certain potential.

5. MHL system

The idea for this new method is based on the fact that it is the intention of the solar array simulator and the CRD method to simulate a power generating solar array as realistically as possible. Therefore taking a real solar array and a light source and comparing the results of all three methods seemed very interesting.

The spectrum of the multi-junction solar array, Figure 2, shows it can operate in a range of electromagnetic radiation with wavelengths reaching from 300nm to 1,600nm. A metal halide lamp best fits the electromagnetic radiation spectrum. Its radiated wavelength lies within a range of 400nm to 1,200nm. The graph in Figure 2 does not include the Ge part of the spectrum as it plays a minor role in terms of the solar arrays efficiency and a more sophisticated spectrometer would be necessary to measure this part of the spectrum.

A test done by JAXA showed the multijunction solar array can survive 140°C during 168h [3]. To ensure the temperature does not exceed the allowed maximum value it is controlled with an infrared temperature sensor. For safety issues it was chosen to shadow the solar array in case no measurements were taken. Therefore a shutter is placed in between the MHL and the solar array. The shadowing is done because switching the MHL on and off within a short time frame would reduce the lifetime of the lamp significantly. To allow cooling of the lamp while it's covered, the shutter leaves room to preserve air circulation. The circulation provided by fans generates enough cooling for the illuminated solar array that its surface temperature hardly exceeds 100°C when the distance between the MHL and the solar array is about 25cm. In this temperature region the proper function of the solar array is guaranteed.

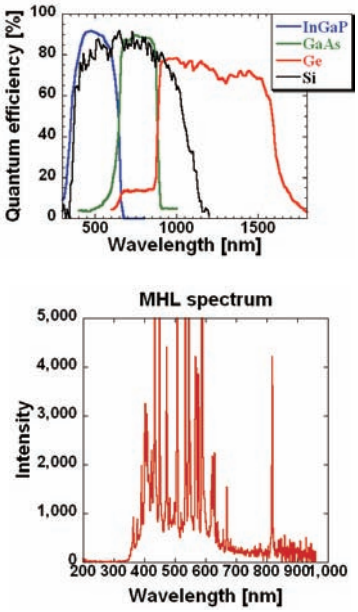

Figure 2 Multijunction solar array spectrum (top), MHL spectrum (bottom)

Taking the IV-curve of the solar array, the output power is adjusted by the variation of the variable resistance value in part B of the simulation circuit and by the amount of light illuminating the solar array. The output power is measured using a differential voltage probe labeled V_{SA}.

To be able to direct the light onto the solar array, a reflector on the backside and two wing reflectors are used (Figure 3). The reflection angles of the two wings can be changed to control the amount of light to which the solar array is exposed to. A top and bottom reflector are not necessary because the light of the metal halide lamp is radiated horizontally, centered on the center illumination point. The color temperature of the metal halide lamp can be controlled with the supply voltage provided through a controller. The color temperature, for MHLs in general, reaches from 2,700K to 20,000K. The color temperature range of the metal halide lamp used for the experiment reaches from 3,900K to

4,800K. During the experiments the color temperature was set to 4,700K. With this color temperature and the mentioned distance to the solar array, an output voltage of 90V and a current of 500mA could be generated. The system includes one metal halide lamp with 3,000W.

6. Metal Halide Lamp

The working principle of a metal halide lamp can be described in four steps. First, the metal atoms move away from the hot arc, which occurs between the two electrodes on the top and bottom of the arc tube and toward to the wall of the arc tube, which has a lower temperature than the arc. The center between the two electrons is what is called the center illumination point and marks where the highest amount of electromagnetic radiation is emitted. On the tube wall the metal atoms combine with the halides and generate a stable molecule. Reaching the hot arc, the molecule breaks and the metal atoms become energized and generate light.

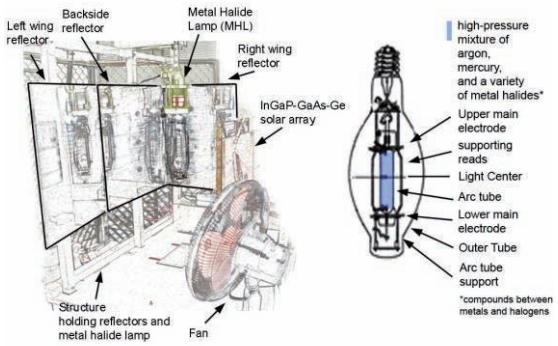

Figure 3 MHL mounting (left); MHL sketch (right)

The halides then move back to the tube wall. In case a metal atom does not combine with a halide it can diffuse through the tube wall. The MHL lifetime ends if the number of diffused metal atoms exceeds a certain limit. In case of the used metal halide lamp the lifetime is stated to be at least 3,600h of operation.

7. Analysis

To analyze the discharges, the solar arrays electric equivalent, the discharge sources and the target point where the discharge occurs are of interest. The solar array simulator and the circuit referred to as the current regulating diode circuit are including capacitances which simulate those of a solar array. These capacitances play a critical role for the discharge waveform and therefore the effects that the discharges have on solar arrays.

The waveforms in Figure 4 are showing temporary sustained arcs. These waveforms are chosen as representative waveforms because the temporary sustained arc is the most interesting type of discharge in terms of potential hazard to a solar array. Of course the sustained arc is the one which definitely destroys the affected strings but this type of discharge is not simulated. One of the aims of the metal halide lamp experiment is to generate temporary sustained arcs and compare them to those generated by the solar array simulator method and the CRD method.

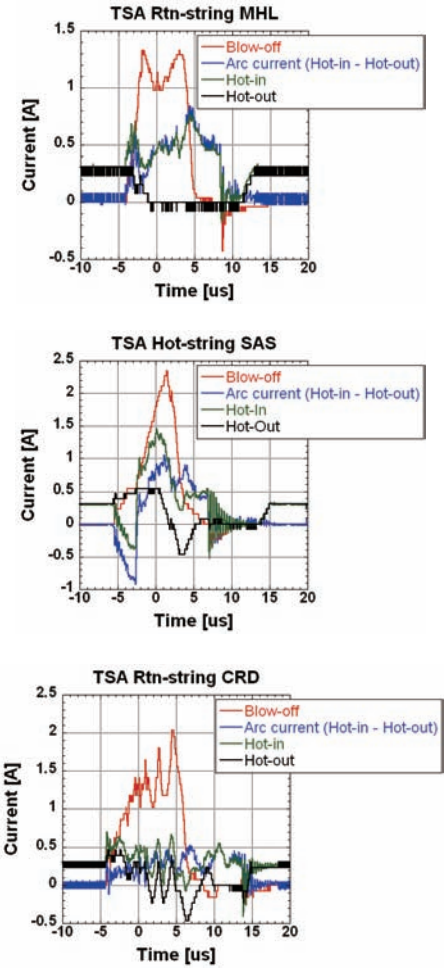

Figure 4 TSA MHL (top), SAS (middle), CRD (bottom)

As can be seen in the waveforms, temporary sustained arcs [1] occurred with all three methods. There is no difference in the arc duration or other arc specifics whether the arc occurs on the hot or the return string. The arc duration is equal or similar for all three methods as shown in Table 1.

	Arc duration [µs]	Standard deviation σ
MHL	4.19	1.733
SAS	4.50	1.553
CRD	4.50	1.412

Table 1 Arc duration comparison

Analyzing the arc path, seen in Figure 5, results in the following observation. First, in this case, the arc occurred on the hot-string of the silicon solar array.

A secondary arc is initiated which transforms into a temporary sustained arc (TSA). A phenomenon which could be observed in the MHL, the solar array simulator and the CRD case is the loss of output current at the end of an arcing event. Figure 5 shows the beginning of the loss at around 8µs and it last until 13µs. The current loss is because of the charging of the internal capacitance of the multijunction solar array, in the case of the MHL method. In the case of the other two methods the internal capacitance of the solar array simulator or the CRD circuit and the external capacitances are consuming the output current. For the current regulating diode method the duration of the output current loss is shorter than the other cases (Figure 4 bottom). This is due to the mode of operation of the CRD which stabilizes the output current over a certain voltage range.

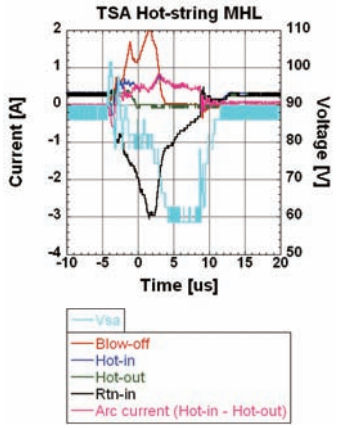

Figure 5 TSA hot-string, MHL method

Considering the multijunction solar array consists of 50 single solar cells which are connected in series, where each cell has a capacity of around 600nF, the whole array has an internal capacitance of 12nF. The output voltage of the solar array is set to 90V and drops to around 60V during an arcing event. The charge of the output current loss is around 900pC which means that a capacitance with a value of around 30pF is discharged.

8. Summary

The conclusion of the MHL experiment is that the arcs are similar to those generated by the solar array simulator and the CRD method. The MHL method has no major disadvantages as it requires no special safety precautions and the overall effort which was necessary to set the system up is not considerably higher than for the SAS or CRD method. The MHL method therefore can be called a third method to simulate power generating solar arrays in ground experiments, without any essential advantages or disadvantages.

References

[1] Mengu Cho, Jeongho Kim, Satoshi Hosoda, Yukishige Nozaki, Takeshi Miura, Takanori Iwata, “Electrostatic Discharge Ground Test of a Polar Orbit Satellite Solar Panel”, IEEE Transaction on Plasma Science, vol.34, pp.2011-2030, 2006

[2] Kazuhiro Toyoda, Seiji Aso, Tokuro Kyoku, Tomoki Kitamura, Mengu Cho, “Proposal of a Current Regulative Diode for Power Supply in Sustained Arc Test”, IEEE Transactions on Plasma Science, vol. 34, No. 5, pp.1967-1972, October 2006

[3] Jaxa: Solar cells, compound semiconductor, triple-junction, high reliability, space use, detail specification; NASDA-QTS-2130-501, 2003.

[4] Agilent: Operating guide for solar array simulator, Agilent models E4350B, E4351B; p.15, Agilent Part No. 5962-8206, 2004.

[5] Semitec – Ishitsuka Electronics Corporation, CRD, p.4, Cat.No.113B, 1998

ESD TEST FOR TRIPLE-JUNCTION SOLAR CELLS WITH MONOLITHIC DIODE

Yukishige NOZAKI[(1)], Hirokazu MASUI[(2)] , Kazuhiro TOYODA[(2)] , and Mengu CHO[(2)]

[(1)]NEC TOSHIBA Space Systems, Ltd. 10, Nisshin-Cho, Fuchu, Tokyo, 183-8551, JAPAN,
E-mail:nozaki.yukishige@ntspace.jp
[(2)]Kyushu Institute of Technology, 1-1, Sensui-cho, Tobata-ku, Kitakyushu-shi, 820-8550, JAPAN,

ABSTRACT

Recently many spacecraft use triple-junction (TJ) solar cells as their primary electrical power source because of their excellent efficiency. However it is also known that triple-junction solar cells are easy to be broken by a low reverse bias voltage. Therefore a discrete by-pass diode should be connected to every solar cell in parallel for the shadow protection. Under these circumstances, TJ solar cells with integrate monolithic diode (MD) have been introduced to market recently.

In the CICing of TJ solar cell with MD, cell-to-cell interconnector is connected on MD pad. The interconnector region forms triple-junction in orbit, making primary arc inception easy. Therefore, it is necessary to study the behavior of arcs on MD solar cell array.

The result of the ESD test for MD solar array revealed that the degradation of MD solar cell is caused by not only large current but also total energy of the discharge. The waveform seems to be affected by the impedance of the solar array circuit.

This paper presents the recent results of ESD test for MD solar array and proposes further investigation based on the test results.

1. Triple Junction Solar Cell with Monolithic Diode

Recently highly efficient triple junction solar cells are mostly used as the primary power source of spacecraft. The power density of the cell is almost double in comparison with crystal Silicon solar cell, a big benefit in the light of the weight and area of the solar array. However, triple junction solar cell is weaker than Silicon solar cell under the reverse bias condition. Therefore by-pass diode connected to each solar cell is required as its shadow protection.

To add the by-pass diode to the TJ solar cell, a discrete Silicon diode is connected by the in-plane inter-connector. But recently TJ solar cell with integrated by-pass function has become available for space solar array. One monolithic diode is grown around the edge of the solar cell in this design and the solar array manufactures can reduce the welding of the inter-connector between by-pass diode and solar cell. Figure-1 shows the typical example of MD solar cell.

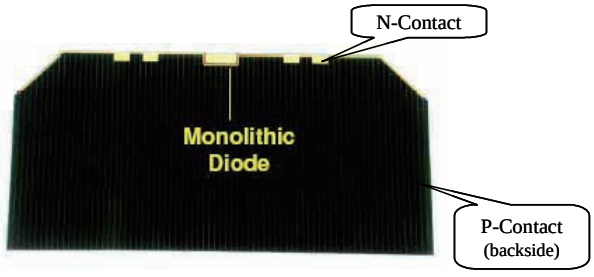

Figure-1 Typical MD solar cell configuration

2. ESD test for MD solar cell array

As shown in Figure-2, the discharges around the interconnector could be observed so often. But cell-to-cell interconnector is usually connected on the MD pad for MD cell as shown in Figure-3. Therefore there is possibility that discharge may occur near or on MD. This is the reason why the ESD test for MD solar cell array was planed.

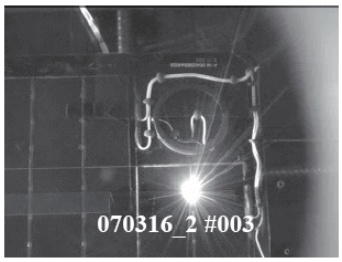

Figure-2 Image of the typical discharge on solar array

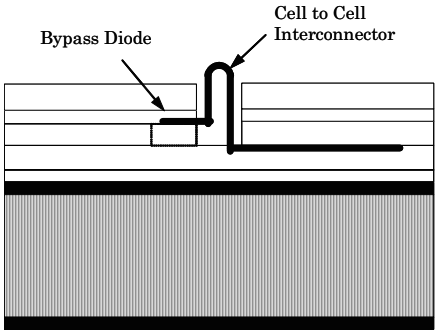

Figure-3 Cross-section of solar array panel

3. MD design for ESD Test and test coupon panel

Two types of MD solar cell were available for our ESD test. Figure-4 shows their schematics.

MD in Design-A is categorized as a Schottky diode. By-pass function is applied between the Top-junction and Middle junction solar cells only.

On the other hand, three junctions are protected by P/N junction diode in Design-B. The MD is grown on the triple junctions shunted by metal layer. The forward voltage drop of this function is slightly higher than the Vf of MD in Design-A.

Same silver interconnector and same cover-glass (CMG-100 with AR coating) are assembled on both types of MD cells. The sizes of both cells are the same. To see the difference between them, they are bonded on the same coupon substrate. The coupon panel for ESD test is a shown in Figure-5. The right module is Design-A CICs and the left CICs are Design-B.

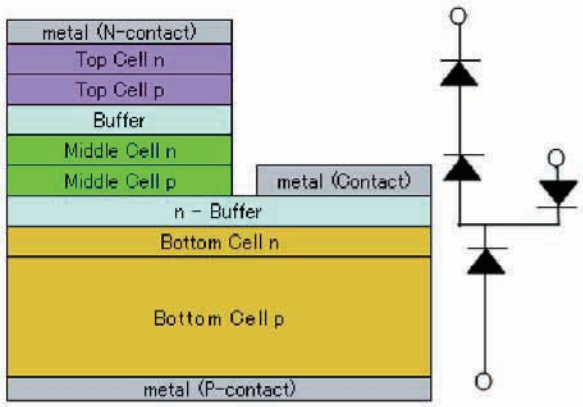

MD function in Design-A

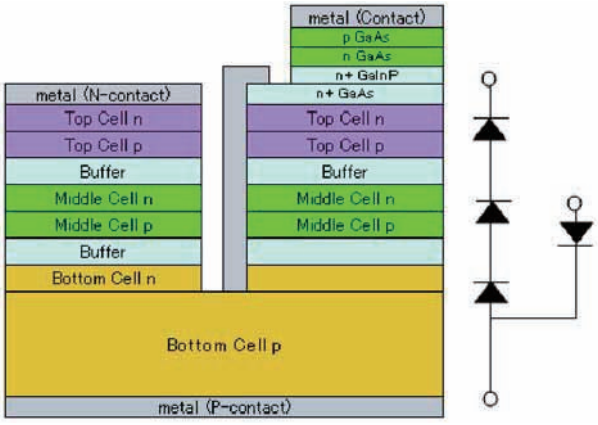

MD function in Design-B

Figure-4 Two types of design of MD for ESD Test

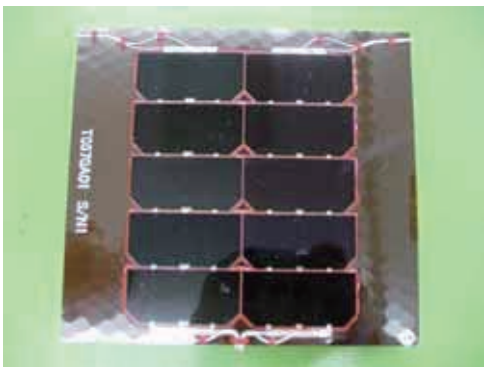

Figure-5 Coupon panel for ESD Test

4. ESD Test for MD cell coupon

Test coupon was set in a space chamber as shown in the Figure-6. The length and diameter of the test are 1.2m and 1.0m. An electron gun, mounted on top of the chamber, irradiate the test coupon with the electron beam. An infrared camera is set in front of the upper window to monitor discharges on the coupon.

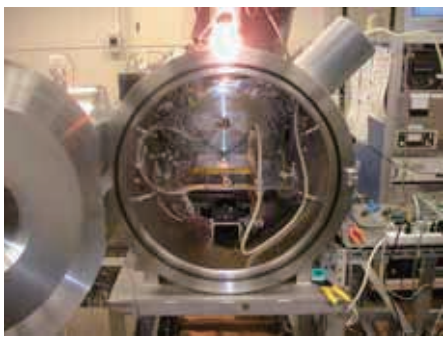

Figure-6 MD cell array coupon in the test chamber

Figure-7 shows the electrical connection in the ESD test. Two solar arrays were connected together and were negatively biased at -4.7kV by DC power supply during the test to simulate the inverted potential gradient conditions. Coupon substrate was insulated from the chamber and was also negatively biased along with the solar cells. This is a typical ESD test configuration of solar array coupon for GEO environment. [1]

C_{ext} in Figure-6 can control the level of the discharge energy. At first, 2 μ F with resistor and inductance was connected, but it became difficult to record the waveform of discharge because of it's complex waveform. So C_{ext} was changed from 2 μ F to 160nF without resistor and inductance.

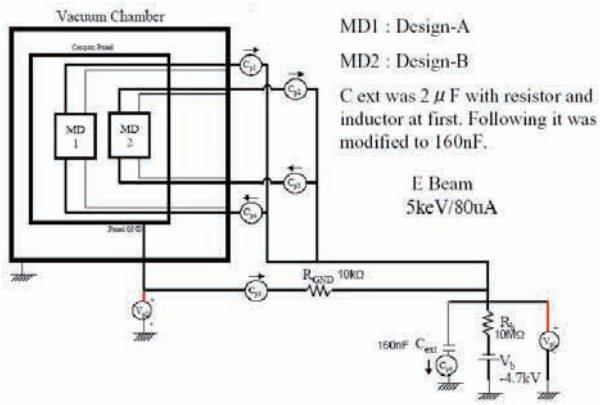

Figure-7 ESD Test Configurations

5. The first ESD test result

The electron beam had been applied on both MD1 and MD2 solar arrays on the coupon panel under the inverted potential gradient condition for 20 hours. V-I curves of each solar array were measured by solar simulator using Xenon lamp before and after ESD test to estimate the degradation of electrical performance of the MD solar arrays precisely.

During the test, 74 discharges were observed. 31 discharges occurred on MD1 solar array and 43 discharges occurred on MD2. Typical discharge images are shown in Fgiure-8.

The V-I curve of MD2 measured by solar simulator estimation after ESD test was degraded so much. The maximum discharge current was more than 60 Ampere. Both by-pass function and solar array junctions were damaged.

On the other hand, the electrical performance of MD1 array didn't change. The maximum discharge current was less than 30 Ampere. The discharge current of MD1 was smaller probably because of the higher impedance of series connected Ge. Therefore, the degradation of electrical performance was prevented.

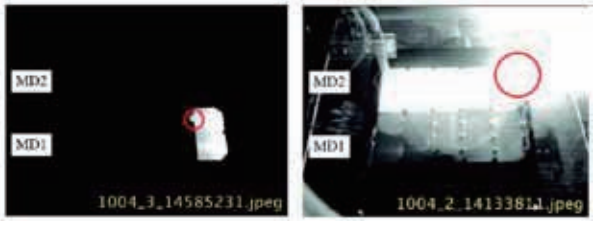

Figure-8 Typical discharge of MD1

6. The second ESD test and the result

To identify the threshold discharge energy to affect the by-pass function, one more coupon panel was prepared. Because MD2 solar cells degraded during the first test, MD1 solar array was covered with Mylar sheet, exposing only MD2 to the electron beam. To control the direction of the discharge current, two diodes were added on array harness as shown in Figure-9.

Electron beam (4keV / 40～100 μA) was applied on the surface of the coverglass of MD2 solar array. Coupon panel was kept at -4kV to generate inverted potential gradient condition on the solar array. C_{ext} was increased from 10nF till when the cell dark V-I curve was changed.

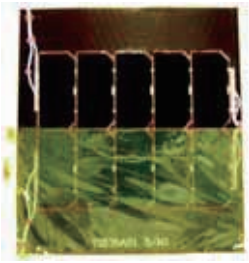

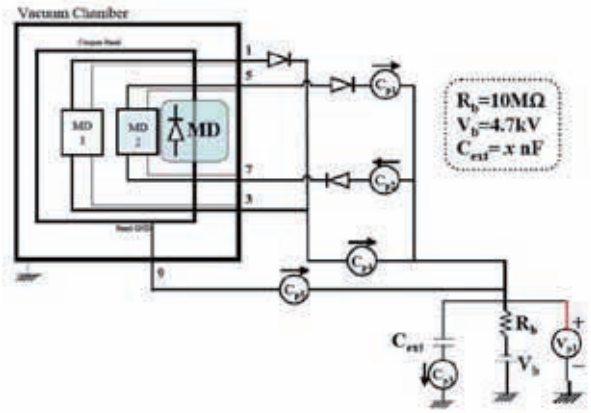

Figure-9 2nd ESD test configuration

Figure-10 shows an image of typical discharge of MD2 observed during the second ESD test. Due to the extra diodes at the positive and negative lines of the solar array, discharge current flew through by-pass function only.

Up to Cext of 60.3nF, dark V-I curve measured after every discharge of the array circuit had not been changed. Five discharges were generated in the case of Cext=60.3nF and the maximum discharge current was 50.3A. There is no change in dark V-I curves. However, when Cext was raised to 73.7nF, the dark V-I curve was changed by the third discharge. The primary arc at the third cell from positive end of the string was observed as shown in Figure-10.

The peak discharge current was 37.5A as shown in Figure-11. The duration was for 30 μsec and discharge energy was 0.8J (350 μC).

Dark I-V curve measured before and the discharge changed as shown in Figure-12. It was clear that the solar array was damaged by the discharge whose waveform is shown in Figure-11.

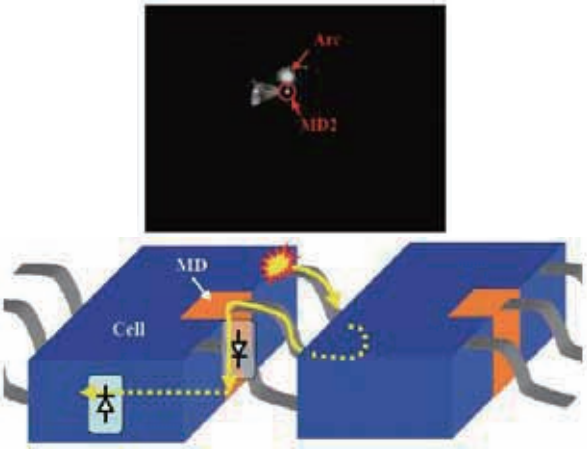

Figure-10 Typical discharge on MD2 solar array

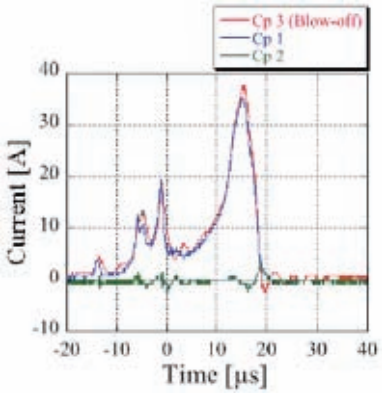

Figure-11 Waveform of the third discharge
Cext = 73.7nF

The coupon panel was removed form the test chamber. The V-I curves of solar array and MD function measured separately indicate that MD function was damaged. Therefore, 0.8J could be considered as the threshold of discharge energy for the by-pass function of MD2 solar cell.

It is interesting that MD2 solar array didn't degrade by 50.3Ampere discharge but 37.5Ampere discharge could affect the performance. This means the energy of the discharge is important when we consider the damage caused by ESD on solar array

7. Discussion and further investigation

Following two things could be pointed out from the above tests.

(1) Discharge current of MD1 was lower than MD2 solar array.
(2) MD2 was healthy to 50A surge current but it was damaged by 38A discharge current (for about 30 μ sec).

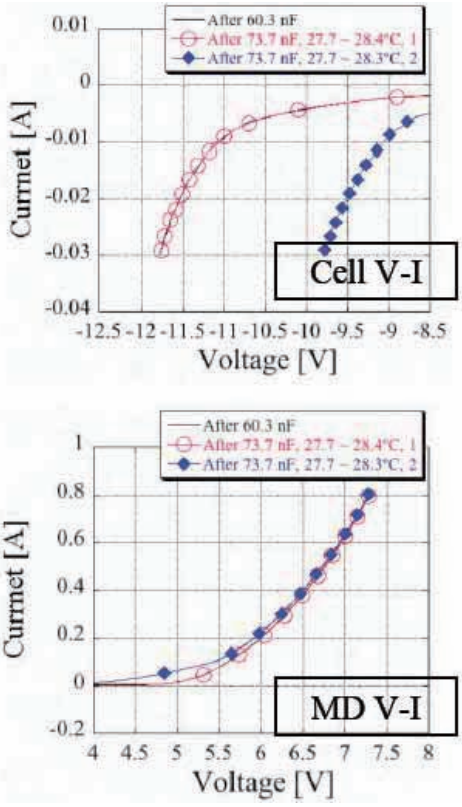

Figure-12 Cell V-I and MD V-I before and after the discharge shown in Figure-11

Related to (1), the discharge current (and/or wave form) might be affected by the circuit impedance. Therefore we should investigate the relationship between the circuit impedance and the discharge current (or waveform).

Based on (2), not only discharge current but also total energy of discharge should be considered in the light of the degradation of by-pass function. This might be the same for MD1, so we would like to do ESD test for MD1 to identify the threshold energy for degradation of MD of Type-A.

8. REFERENCE

1. Toyoda K, et al. Power reduction of solar arrays by arcing under simulate GEO environment, Journal of Spacecraft and Rockets, Vol. 41, No. 5, September-October 2004.

PRELIMINALY STUDY OF THE INFLUENCE OF SOLAR CELL DEGRADATION DUE TO ESD ON SOLAR ARRAY POWER GENERATION

Teppei Okumura[1], Kazuhiro Toyoda[1], Shirou Kawakita[2], Mitsuru Imaizumi[2], Mengu Cho[1]
1. Department of Electrical Engineering
Kyushu Institute of Technology, 1-1 Sensui, Tobataku, Kitakyushu 804-8550, Japan
2. Japan Aerospace Exploration Agency

ABSTRACT

In space, an electrostatic discharge (ESD) can occur on a solar array due to the plasma interaction. One of the issues of ESD is the degradation of solar cell electric performance. To establish the power degradation estimation method due to ESD in solar arrays, light current-voltage characteristics are evaluated in the current value at maximum power. From the results of the calculation, InGaP/GaAs/Ge solar arrays potentially suffer more serious power degradation than Si solar array.

1. Introduction

The electrostatic discharge, the so-called primary arc, occurs on solar arrays because of the plasma interaction. The detail phenomenon about primary arcs is described in Ref. 1. In order to establish an international standard for solar array primary arc tests, the collaboration research is carrying out in France, USA and Japan[2]. Because one of the issues of primary arcs is the degradation of solar cell electric performance[3][4], the primary arc test on Silicon with integrated bypass function solar cell (Si w/IBF cell), Silicon solar cell (Si w/o IBF cell) and InGaP/GaAs/Ge solar cell (3J cell) have been carried out[5].

Originally, only the radiation particles have been considered as the cause of solar cell degradation. Therefore, the solar cell degradation due to primary arcs should be combined with the estimation method for solar array power generation in satellite life. The solar array power degradation due to primary arcs is examined as a preliminary study in this paper.

2. Experiment

The 3J cell, Si w/IBF cell and Si w/o IBF cell are shown in Fig. 1. The solar cell performance is flight quality. The size of the cell is about 40mm×80mm. The solar cell is attached to an aluminum plate which was covered with a polyimide sheet using a silicone adhesive (RTV-S691). The thickness of the coverglass was 100μm. The bus bar was insulated with a silicone adhesive as in the real solar array design.

Fig.2 shows the light current-voltage characteristics (Light IV) and the light power-voltage characteristics (Light PV) of a 3J cell. Because the solar array is operated under constant voltage, the current value at maximum power (I_{mp}) is defined as the characteristic value of the light IV. The change in I_{mp} by one primary arc is defined as dI_{mp} obtained from eq.1.

$$dI_{mp} = \frac{(I_{mp\_before} - I_{mp\_after})}{I_{mp\_before} \times N_{arc}} \times 100, \% \quad (1)$$

The discharge circuit is shown in Fig.3. The primary arc experiment has been carried out under plasma conditions (LEO environment) and high energy electron beam conditions (GEO environment). The detail of the experiment condition is described in Ref.5.

A typical current waveform is a pulse whose duration is approximately 10μsec. We can adjust the peak value of the primary arc current and the primary arc energy by changing C_{ext}. The primary arc energy is obtained from two calculation methods. Under LEO environment, the primary arc energy (W_{arc_LEO}) is obtained from eq.2 where T_{ini} and T_{end} are the beginning and the end time of the primary arc current. Because of the malfunction of the voltage probe in a GEO environment, the arc energy (W_{arc_GEO}) is obtained from eq.3. Q_{arc} is the charge value of the primary arc[5].

$$W_{arc\_LEO} = \int_{T_{ini}}^{T_{end}} I(t) \times V(t)\, dt, J \quad (2)$$

$$W_{arc\_GEO} = Q_{arc}^2 \Big/ 2 \times C_{ext}, J \quad (3)$$

3. Results and Discussion

Fig.4 shows the relationship between dI_{mp} and W_{arc} of a 3J cell. dI_{mp} increases with an increasing value of W_{arc}. The maximum dI_{mp} is 14% at 30mJ of W_{arc_LEO}. The minimum dI_{mp} is 0.05% at 0.8mJ of W_{arc_GEO}. Fig.5 shows the relationship between dI_{mp} and W_{arc} on a Si w/IBF cell and on a Si w/o IBF cell. The minimum W_{arc} for the degradation is 30mJ of W_{arc_LEO}; dI_{mp} is 0.2%. The maximum dI_{mp} is 1.5% at 280mJ of W_{arc_GEO}. Because the silicon solar cell is more robust than the 3J cell as reported in ref.5, dI_{mp} of the Si cell is much smaller than that of the 3J cell under the same W_{arc}.

In general, the solar array is operated under a constant voltage. Therefore the output voltage of each solar cell is briefly determined by the number of solar cells and the output voltage of the solar array. In the case of the 3J solar array (output voltage; 60V, output current; 0.45A, output power; 27W, number of 3J cell;

30), the decrease of the output current by 14% in one 3J cell causes a decrease of 0.7% in output power.

4. Summary and Future work

In order to establish the estimation method for solar array power degradation due to primary arcs in solar arrays, the preliminary study was carried out. Because the solar array is operated under constant voltage, the light IV characteristic is evaluated at the current value at maximum power.

From the results of the examination, the decrease value of the current output is increasing with arc energy in the case of the 3J cell. In the worst case, the 3J cell loses around 10% of its output current from a single arc. In the case of the Silicon cell, the decrease value of the current output does not have a strong relationship with the arc energy. In the worst case, the Silicon cell loses around 1% of its output current from a single arc.

Acknowledgement

This research is being carried out as International Joint Research Program (05IS084) supported by the New Energy Industrial Comprehensive Development Organization (NEDO) of Japan.

REFERENCES

[1] D, Hastings., H, Garrett.: Spacecraft-Environment Interactions, Cambridge University Press, 1st edition, 2000.

[2] Cho, M., Goka, T.: Issues Associated with Standardization of Ground Test Methods of Electrostatic Discharge Phenomena on Spacecraft Surface, 56th International Astronautical Congress, Fukuoka, October 2005

[3] K, Toyoda., T, Okumura., S, Hosoda., M, Cho.: Degradation of High Voltage Solar Array due to Arcing in LEO plasma Environment, 2005, Journal of Spacecraft and Rockets, Vol.42, No.5, pp.947-953.

[4] T, Okumura., H, Masui., K, Toyoda., M, Cho.: Degradation of Electric performance due to Electrostatic Discharge on Silicon solar cell for Space, 2007, J. Japan Soc. Aero. Space Sci., Vol. 55, No.647, pp.590-596.

[5] T, Okumura., S, Ninomiya., H, Masui., K, Toyoda., M, Imaizumi., M, Cho.: Solar cell degradation due to ESD for international standardization of solar array ESD test, 10th Spacecraft Charging Technology Conference, Biarritz France, June 2007.

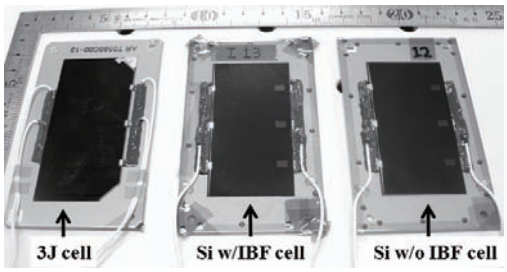

Fig.1 3J cell, Si w/IBF cell and Si w/o IBF cell

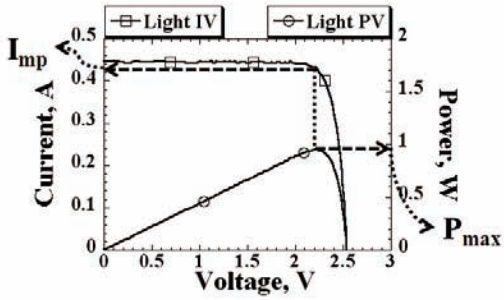

Fig.2 Light current-voltage characteristics and light power-voltage characteristics of a 3J cell

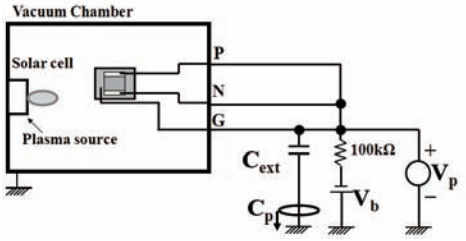

Fig.3 Discharge circuit

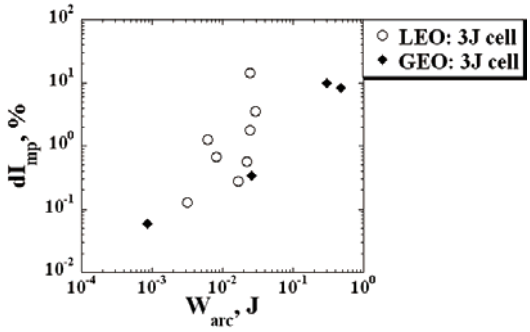

Fig.4 Relationship between dI_{mp} and W_{arc} on a 3J cell

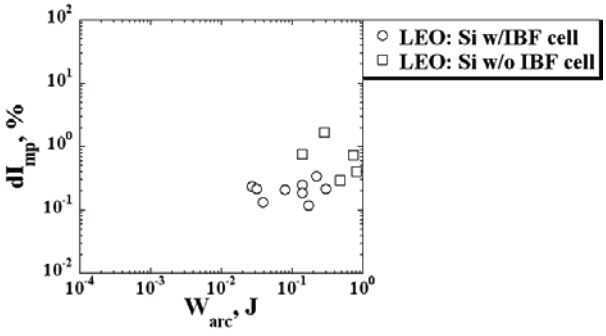

Fig.5 Relationship between dI_{mp} and W_{arc} on a Si w/IBF cell and on a Si w/o IBF cell

Measurement of Photoelectron Emission by Vacuum Ultraviolet Ray Irradiation

Shugo Okamura, Toru Iwao, Motoshige Yumoto (Musashi Institute of Technology),
Hiroaki Miyake, Kumi Nitta (JAXA)

Abstract

Recently, the satellite plays many roles depending on the purpose, including communication, weather observation, astronomy observation and space development. The satellite is requisitioned long life and high reliability in such situation. However, around an altitude of several 100 km, there is Atomic Oxygen (AO) which is a main ingredient agents. AO has high reactivity and its density is about 10^{15} atoms/m^3. Because the satellite collides with AO, surface materials of the satellite are deteriorated. As a result, it leads unevenness and oxidation. Accordingly, it is necessary to monitor the surface condition.

In this study, photoemission characteristics of several materials, such as metals, glasses and polymers are measured by use of the deuterium lamp and the band path filters. From the measurement the threshold energy for photoemission and the quantum efficiency was evaluated. As a result, the thresholds of samples are 4.9 to 5.7 eV. The quantum efficiency of metals is about 100 times higher than other samples. The quantum efficiency of PS which includes benzene ring is several times higher compared with PP and PTFE. From these results, it is deduced that deteriorated materials may emit large amount of photoelectron.

Key words : photoelectron emission, vacuum ultraviolet ray, polymer, threshold energy for photoemission, quantum efficiency

1. Introduction

Recently, the satellite is requisitioned the long life and high reliability. By the way, there is Atomic Oxygen (AO) which is a main ingredient agents in LEO (low-earth orbit). An altitude of several 100 km (about 10^{-3} Pa) AO is the main constituent of the atmosphere in LEO. It is formed by dissociation of O_2 by ultraviolet irradiation from the sun. AO has high reactivity and its density is about 10^{15} atoms/m^3. Because the satellite collides with AO, surface materials of the satellite are deteriorated [(1)]. Therefore it is necessary to monitor the surface materials of the satellite. The authors thought that the change of the deteriorated situation of surface materials might be detected by the measurement of the photoemission characteristic by the sun. Therefore, it is necessary to summarize the fundamental data concerned with photoemission characteristics related to the surface condition of materials. On the other hand, analysis of the surface condition by AO irradiation is important. Compared with these results, it might be effective for the monitoring of the deteriorated situation. In this report, results of preliminary experiment are summarized.

2. Experimental setup

The experimental setup is shown in Fig.1. The deuterium lamp of 200 W and band pass filters (BPF) are used for a source of VUV (vacuum ultraviolet) ray. The VUV ray is reflected by an aluminum vapor deposition mirror made by the vacuum evaporation method on the optical flat glass and is irradiated on the sample. Photoelectrons are collected by the semi-spherical electrode and are measured at the electrode placed the sample. Here, the radiation wavelength range of the deuterium lamp is 115-400 nm. The transmittance of BPF has 15-20 % at the peak wavelength and the half bandwidth is about 20 nm with each filters. Negative bias voltage around 7 V is applied to the sample side, to prevent the pull back electrons that were emitted from the sample and the electrons emitted at the surface of chamber. Additionally, irradiated flux of VUV ray is measured by using a photomultiplier for each wavelength to evaluate the quantum efficiency for the photoemission. The measurement is performed by pressure less than 10^{-2} Pa. The measured samples are metals, glasses, films, paints and polymers.

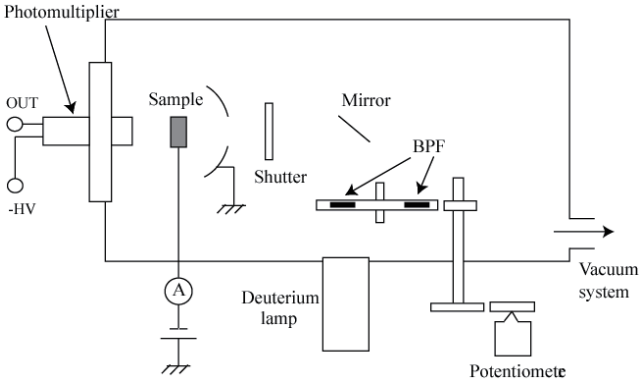

Fig.1 Experimental setup.

3. Results and discussion

3･1 Threshold energy

The square root of the magnitude of photoemission current value corrected by the irradiated VUV ray intensity is shown at the axis of ordinates and energy of the irradiated VUV ray is the axis of abscissas, which is so called Fowler plots is shown in Fig.2. From the graph, the threshold energy for photoemission is evaluated. The results are summarized in Table 1. The metals have the same magnitude as the reported one [(2)]. Now, the dispersion of evaluated value was about ±0.2 eV. The other samples have 5.4-5.7 eV. In the case of polymer, it is reported that the bandgap of polymer has about 9 eV [(3)]. On the other hand, it is reported that the surface level exists around 4-5 eV in the case of polymer [(4)]. Therefore, the reason why the threshold of about 5 eV was obtained is existing a lot of the surface level around 5 eV. The surface depth to emit photoelectrons are extremely shallow, accordingly the results obtained by the measurement may be influenced by these surface level.

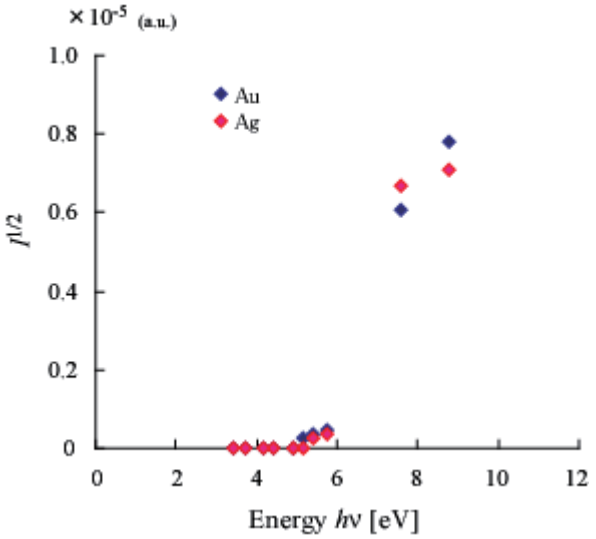

Fig. 2　Fowler plots.

3･2 Quantum efficiency

Quantum efficiency for photoemission was calculated by using the flux of VUV ray irradiated on the sample for each BPF and magnitude of the photoemission current. The flux of VUV ray irradiated on the sample was corrected by the transmittance of each BPF by using the sensitivity of the photomultiplier and was converted into the intensity at the central wavelength of each one. The results are shown in Figs.3-7. The samples with relatively high conductivity tend to emit electrons easily from the figures. For example, It is clear that volume resistively of metals have about 10^{-8} Ω・m and that of polymers have about 10^{15} Ω・m. In the case of paint, samples of conductivity have 10^{5}～10^{6} Ω・m. As well the samples that conductivity is small were not seen in the tendency that photoemission currents decreased with time.

Table 1　Threshold energy for photoelectron emission of each samples.

Materials		Characteristics	Threshold energy (eV)
Au		Metal	4.9
Ag			5.1
Glass A		Glass	5.4
Glass A(deteriorated)			5.7
Glass B			5.7
Glass B(ITO-coated)			5.7
Film A		Film	5.7
Film B			5.4
Film C			5.7
Paint A	Conductive	Paint	5.4
Paint B			5.4
Paint C	Non-Conductive		5.7
Paint D			5.7
Paint E			5.7
PP		Polymer	5.7
PTFE			5.7
PS			5.4

For example, the quantum efficiency of film A from Fig.4 is about 10^{-5} at the photon energy of 7 eV. It is necessary to irradiate photons about 10^{5} with energy of about 7 eV for one electron. The exposure dose of the photon of about 7 eV by the sun in space is measured with about 10^{11}/ m^{2} per second. Accordingly, many electrons might be emitted.

Here in polymers, PS which includes the benzene ring in its chemical structure emits more electrons in each wavelength than PP and PTFE which does not include the benzene ring. Therefore, it is thought that having benzene ring may contribute to photoemission. When polymers are irradiated by AO, it is expected that many polar bonds including oxygen are formed at the surface. It is expected in particular that a lot of double bonds such as a carbonyl group, the carboxyl group and so on are generated. In other words, quantum efficiency of the materials which is deteriorated by AO irradiation might increase, because photoemission quantity of PS having a benzene ring including a lot of double bond increased. On the other hand, unevenness of surface is generated by AO irradiation [(5)]. In figure, quantum efficiency of the deteriorated glass decreased. It is necessary to clarify effect which is dominant for photoemission, one is the introduction of double bonds and the other is the formation of unevenness at the surface. Samples introduced double bonds and

formed unevenness will be prepared and its quantum efficiency will be measured in future. In addition, data between 170-210 nm will be measured in future, because quantum efficiency is looked like discontinuity.

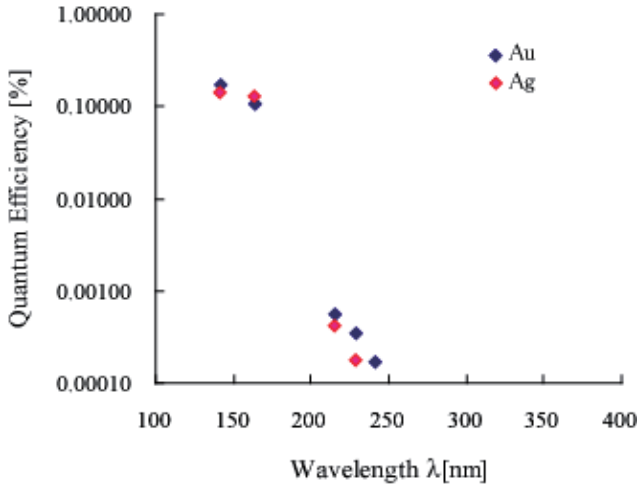

Fig. 3　Quantum efficiency of metals.

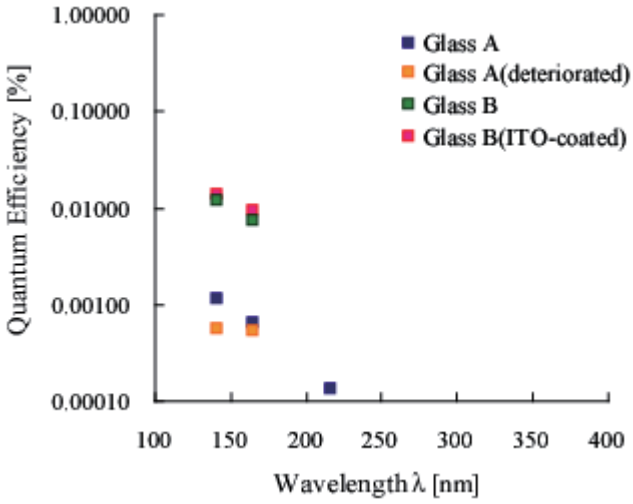

Fig. 4　Quantum efficiency of glasses.

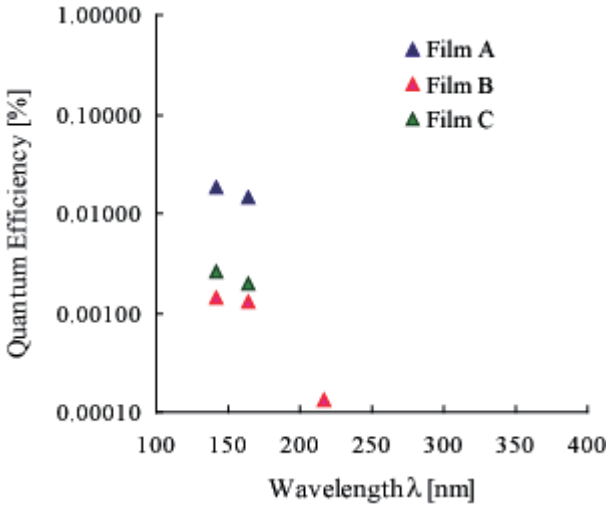

Fig. 5　Quantum efficiency of films.

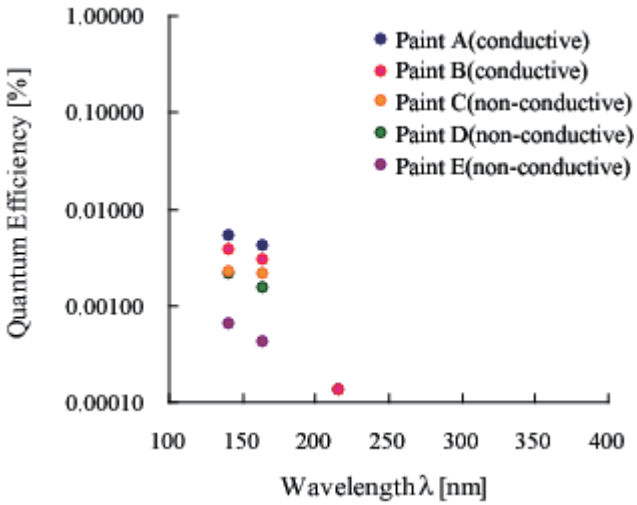

Fig. 6　Quantum efficiency of paints.

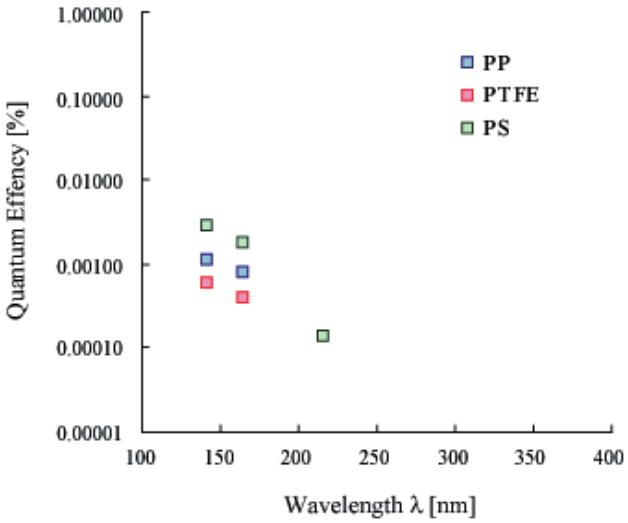

Fig. 7　Quantum efficiency of polymers.

3･2　Magnitude of photoelectron current irradiated by the sun

Comparing with the intensity irradiated by the test and the intensity of the sun, magnitude of photoelectron current from the sample irradiated by the sun was calculated. The results are shown in table 2. More than 10^{-6} A/m^2 is estimated for each sample including the insulator, and more than 10^{-4} A/m^2 is obtained in case of conduction one.

Table 2　Estimated photoelectron current by the sun irradiation of each samples.

Materials		Photoelectron current (A/m^2)
Au		3.6×10^{-3}
Ag		3.2×10^{-3}
Glass A		2.8×10^{-4}
Glass A(deteriorated)		9.7×10^{-6}
Glass B		1.3×10^{-4}
Glass B(ITO-coated)		1.6×10^{-4}
Film A		2.5×10^{-4}
Film B		2.9×10^{-4}
Film C		3.4×10^{-4}
Paint A	Conductive	3.4×10^{-4}
Paint B		3.2×10^{-4}
Paint C	Non-Conductive	3.6×10^{-5}
Paint D		2.6×10^{-5}
Paint E		9.3×10^{-6}
PP		1.4×10^{-5}
PTFE		6.9×10^{-6}
PS		3.0×10^{-4}

4.　Conclusion

The photoemission characteristics from many materials were measured. The result is as follows;

- The threshold energy of metals were similar magnitude to the reported wok function.
- The threshold energy of other samples have 5.4-5.7 eV.
- The samples with small magnitude of volume specific resistance tend to be easy to emit electrons. As the results, the quantum efficiency is high.
- It is deduced that samples with double bonds emit photoelectron easily.

We are planning to clarify the relation between the photoemission characteristics and the deterioration by formation of unevenness by introduction of double bonds.

References

(1) H. Fujii, K. Sonoda and H. Nishimoto: “Spacecraft charging and material degradation in space enviroment”, Trans. IEEJ, Vol.113-A, No.9, pp.609-617 (1993)

(2) V. S. Fomenko., G. V. Samsonov: “Handbook of Thermionic Properties”, New York, Plenum Press Data Division, pp.39-41, pp.60-62 (1966)

(3) T. Tanaka: “Optical absorption and electrical conduction in polyethylene”, *J. Appl, Phys.*, Vol.44, No.5, pp.2430-2432 (1973)

(4) D. K. Davis: “Charge generation on dielectric surfaces”, *J. Phys. D* : *Appl. Phys*., Vol.2, pp.1533-1537(1969)

(5) Eitan Grossman, Y. Lifshitz : “In situ study of Kapton using novel hyperthermal oxygen atom source”, *J. Spacecraft Rockets*, Vol.36, No.1, pp.75-78(1999)

Estimation of Volume Resistivity of Dielectric Films under Electron Irradiation

Rikio Watanabe (Musashi Inst. of Tech),
Hiroaki Miyake and Kumi Nitta (JAXA)

ABSTRACT

A new measurement method for volume resistivity of dielectric material has been tested and compared to the standard ASTM “capacitor method”. This is intended for obtaining resistivity values of highly insulated material for spacecraft surface under realistic condition which simulates vacuum and electron beam irradiation. The resistivity value is calculated from exponential decay time constant of surface potential after electron beam irradiation ceased. The results show that the resistivity value from present method is 10^3 times larger than that obtained from capacitor method. This indicates that charged dielectrics need much longer field relaxation time which would cause reconsideration of current spacecraft design guideline and charge analysis.

1. はじめに

誘電体の体積抵抗率は，誘電体中の電荷移動のしにくさを示す指標であり，抵抗率が高いほど導電率が低く，絶縁性能が高いといえる．しかし，宇宙機に使用する誘電体フィルムについていえば，絶縁性・断熱性の高い材料ほど表面及び内部に蓄積した電荷の移動度が低いことから，一度帯電した場合に，蓄積電荷によって誘起される電界の緩和時間が数日から数ヶ月に及ぶこともある．そのため，特に周期的に荷電粒子帯を通過するような人工衛星等においては，適切な体積抵抗率を有する誘電体材料を使用する必要がある．このように，体積抵抗率は人工衛星設計における誘電体材料選定時の重要なパラメータであるだけでなく，帯電解析を行う数値シミュレーションソフトにとっても重要な入力パラメータの一つとなっている．

体積抵抗率値の計測に関しては，ASTM[1)]や JIS[2)]によって規定された標準的な計測法が存在し，現在でも誘電体体積抵抗率の標準値として利用されている．この方法は「コンデンサ法」とも呼ばれ，誘電体試料を電極で挟み，高電圧（500V）を印加し，数分後の電流値によってオームの法則から抵抗値を算出し，体積抵抗率に変換するものである．人工衛星における誘電体材料の使用形態からすると，コンデンサ法は直流電圧印加であるため，宇宙機が遭遇する真空中での電子線照射環境を模擬していない．また，直流印加後数分では，未だ誘電体材料中には分極電流が主流であり，十分時間が経過した後の暗電流による抵抗計測が誘電体本来の物性を表している．

これらに対し，Frederickson や Dennison らは，真空チャンバ内で誘電体試料に電子線を照射し，蓄積電荷によって誘起される表面電位の時間履歴を計測し，その時間変化から体積抵抗率を計測する手法を考案した[3)4)]．以降これを電荷蓄積法(Charge Storage Method)と呼ぶ．電荷蓄積法によって計測された体積抵抗率の値はコンデンサ法による値より 10^2～10^4 程度大きくなるとの報告もある．もし，より大きな体積抵抗率を人工衛星の設計や帯電解析に用いたとすると，帯電により誘起された電界の緩和時間もより長くなるため，これまでの設計に大幅な改定が必要になってくる．そこで，本研究では，人工衛星によく用いられているポリイミド系フィルムの体積抵抗率を電荷蓄積法により求め，計測値の妥当性を検討する．

2. 電荷蓄積法

2.1 計測装置

Figure 1 に電荷蓄積法による体積抵抗率計測システムの概念図を示す．真空チャンバ内に設置された誘電体試料の開放面に電子線が照射され，表面に電荷が蓄積し，電位を生ずる．その表面電位を表面電位計（Trek, Model 341B, 20kV）で計測する．なお，表面電位計のプローブは真空チャンバ内に設置されており，電子線照射時はチャンバ壁面へ待避しており，電子線照射終了に合わせて試料上面に移動する．計測値はオシロスコープ(Tektronix, 1GHz)でサンプリング・データ蓄積される．試料背面は電極を通して試料を通過する微小電流を計測している．

2.2 表面電荷減衰と体積抵抗率

得られた表面電位の履歴から体積抵抗率を求める．最

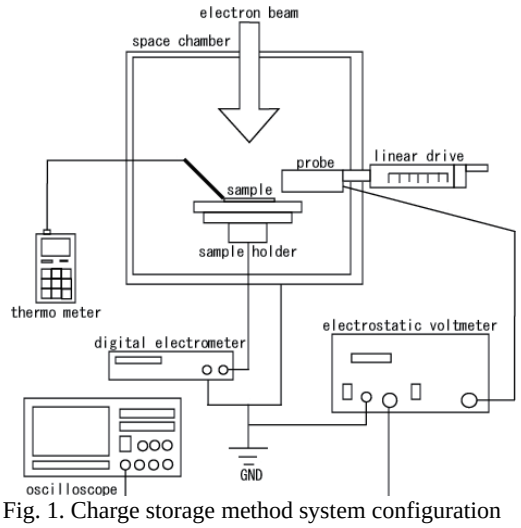

Fig. 1. Charge storage method system configuration

も簡単な表面電位減衰のモデルは，指数減衰モデルである．これは，指数減衰する電位$V(t)$ V に対して，その減衰時定数τ_d s を求めるものである．初期電位をV_0 V とすると，電位の時間変化は式（１）であらわされる．

$$V(t)=V_0 e^{-t/\tau_d} \qquad (1)$$

測定された時定数と誘電率ε F/m から，体積抵抗率ρ Ωm は式（２）によって算出される．

$$\rho=\frac{\tau_d}{\varepsilon} \qquad (2)$$

この指数減衰モデルは電荷が誘電体内をドリフトする，いわゆる暗電流が流れる場合を想定しており，電子線照射直後の分極電流が支配的な状態では適用できない．従って，表面電位の計測は最低でも 1 週間程続ける必要がある．帯電した誘電体表面電位の減衰に関する詳細な物理モデルについては，文献(4)等を参照されたい．現状では，電位の時間履歴を両対数グラフにおいて確認し，指数減衰モデルが適用可能な時間帯における計測点から式（１）を構築し，減衰時定数を求めている．

3. 結果及び考察

3.1　試験条件

対象試料はポリイミド系フィルム 25μm であり，電子エネルギは 10keV，電流は 5.5μA/cm² とした．真空度 2.6×10⁻⁴Pa において 2 分間の電子線照射を行った後，表面電位の計測を開始した．

3.2　表面電位の時間履歴

Figure 2(a)(b)に表面電位の時間履歴を示す．Figure 2 (a)は両軸共に線形，同(b)は両対数で表記している．また，十分時間が経過し，指数減衰モデルによる近似曲線も図中に示した．

計測開始時点における表面電位は 5,010V であるが，3 分ほどで 3kV 台に減衰している．電位の急激な減衰は約 1 日(86，400s)程続き，その後は緩やかに減少している．両対数グラフを見ると，3,000s までの領域，3,000-200,000s までの領域，200,000s 以降の領域と 3 つの領域にわけることができる．最後の 200,000s 以降の領域が暗電流領域であり，この時間帯における表面電位値から指数減衰の式(1)を近似すると，図中の近似曲線$V(t)=1211e^{-9.44\times10^{-7}t}$ となる．試料の比誘電率は 3.4 であるため，体積抵抗率を計算すると，3.1×10^{20}Ωcm となる．コンデンサ法(ASTM)による該当試料の体積抵抗率は1.5×10^{17}Ωcm であるから，電荷蓄積法の結果はコンデンサ法の結果より，約 10^3 倍大きくなったことになる．Dennison らの報告によれば，誘電体試料においては 10^2～10^4 程度大きくなるとのことで，本試験の結果はオーダー的に Dennison らの報告と一致する．

では，千倍も大きくなった体積抵抗率をどう利用するかということであるが，もしこの値を人工衛星設計や帯電解析ソフトに利用した場合，帯電緩和時間が大幅に延長

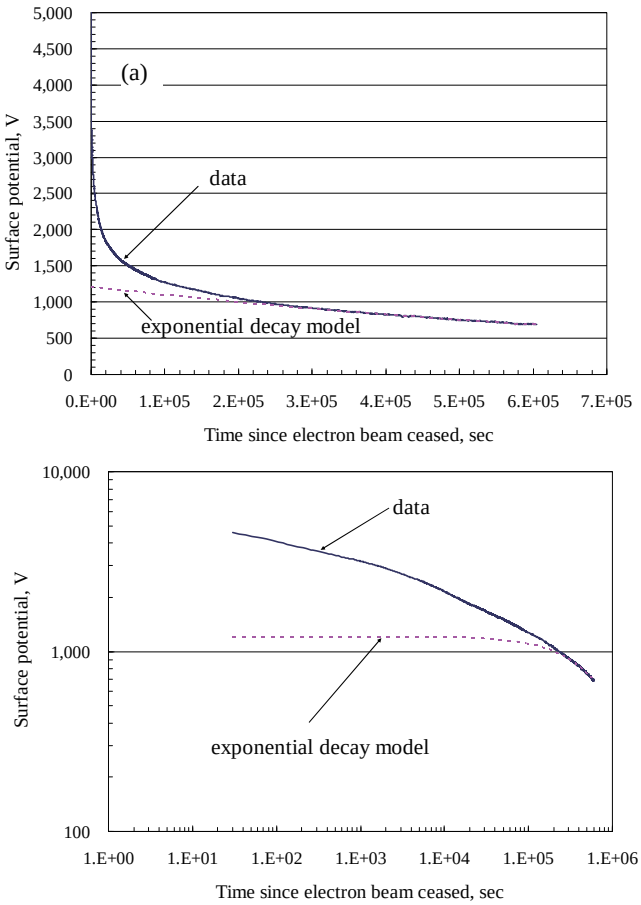

Fig. 2. Time history of surface potential. (a)linear plot, (b)double log plot

され，これまでの設計・解析手法の大幅な見直しが必要になってくる．ポリイミド系フィルムは現在人工衛星用に多用されている材料であり，これらの材料の使用に対して適切な根拠を与える必要がある．

4. まとめ

現在宇宙機用に多用されているポリイミド系フィルムの体積抵抗率に関して，従来のコンデンサ法に代わる電荷蓄積法によって，測定を行った．その結果，コンデンサ法に対して 1,000 倍大きい体積抵抗率を得た．電荷蓄積法による結果をどう扱うかは，今後議論の余地があり，さらなる測定結果が必要となる．

なお，この研究は「JAXA 宇宙機設計標準　電気系分科会　帯電・放電ワーキンググループ（WG1)」の調査事項の一部として行われた．

5. 参考文献

(1)ASTM D-257-99，1999.
(2)JIS K6911
(3)A.R. Frederickson and J.R. Dennison, IEEE Trans. on Nucl. Sci., Vol. 50, No. 6, 2003.
(4)J.R. Dennison, et. al., IEEE Trans. on Plasma Sci., Vol. 34, No. 5, 2006.

Experimental measurement of secondary arc plasma parameter on solar array

Takayuki Ose, Hirokazu Masui, Kazuhiro Toyoda, Mengu Cho

Department of Electrical Engineering, Kyushu Institute of Technology
1-1 Sensui Tobata-ku Kitakyushu 804-8550 JAPAN
Tel&fax : +81-93-884-3229
E-Mail : f346407t@tobata.isc.kyutech.ac.jp

Abstract As the power level of geostationary satellites increases, discharge phenomena on solar array are becoming serious threat to safe operation. Arcs on solar array can short-circuit the satellite circuit, decrease the satellite power, and then cause the satellite permanent failure. To prevent the failure caused by charging and arcing, it is necessary to investigate the mechanism of satellite charging and arcing phenomenon. The purpose of this paper is to investigate the occurrence condition of a secondary arc by measuring arc plasma characteristics in ground test. We measured the arc plasma temperature and identified the materials emitted using spectrometer at arbitrary time during arc occurring. We investigated the difference of secondary arcs occurrence condition during secondary arcs. From the spectroscopic measurement results, we found that it was necessary for shifting to the secondary arc that the metallic vapor same as the cathode material was emitted. In case of PA dimension changes, the probability of secondary arc and TSA occurrence became high. And plasma temperature was not affected by PA dimension. However, the metallic vapor emission of silver was greatly affected. Thus, secondary arc occurrence greatly depends on metallic vapor emission from cathode.

1. Introduction

In geostationary earth orbit (GEO), thin hydrogen plasma exists at density of $10^6 m^{-3}$. Substorm phenomenon sometimes occurs due to earth magnetic field disturbance according to the change of the solar wind. High energy electron flux of tens of keV flows into the satellite when the substorm occurs. In such an environment, arcs occur on the solar array and threaten the safe operation, as the bus power level of satellite increases. The arcs due to interaction between space plasma environment and solar array are serious problem for satellites [1]. Therefore, it is important to investigate the mechanism of the charging and arcing phenomena of the satellite.

When the satellite is charged, the coverglass potential can be higher than the interconnector potential which is equal to the spacecraft ground because of the difference in secondary emission yield. This is called the inverted potential gradient condition. When the inverted potential gradient is formed, the high electric fields are formed at the triple junctions. The electrons are emitted from the surface of the metal by the electron field emission. The secondary electron is emitted there by collide with side edge of the cover glass. Then, the electric field near the triple junction is enhanced further. As the field emission current increases, the gas desorption increases at side edge of the cover glass and forms the gas layer. The arc occurs by ionization in the gas [2]. This arc phenomenon is called primary arc. In addition, the solar array cell can be short-circuited with cell of adjacent strings through the arc plasma formed by primary arc and the arc causes short-circuit between adjacent strings with operational voltage (Fig.1). This arc phenomenon is generally called secondary arc. If secondary arc occurs, the power cannot be supplied to the onboard instrument of satellite because the output power of the solar array circuit is lost by short-circuit between a positive electrode and a negative electrode.

The kind of arc is classified by the current waveforms flowing between adjacent strings as shown in Fig.2. Primary arc is an arc phenomenon that the charge stored on the cover glass flows into the arc spot through the arc plasma. This current that flows into electrode is called as a blow-off current. If there is no secondary arc after a blow-off current finishes, the arc is called the non-sustained arc (NSA). The temporary sustained arc (TSA) and the permanent sustained arc (PSA) are the arc phenomena

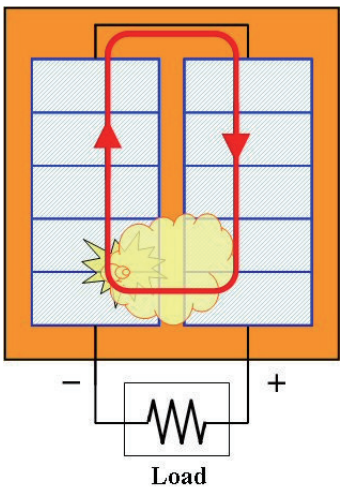

Fig.1 Current path of secondary arc.

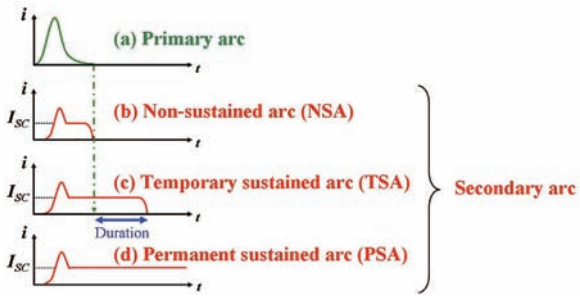

Fig.2　Definition of arc type based on current waveform.

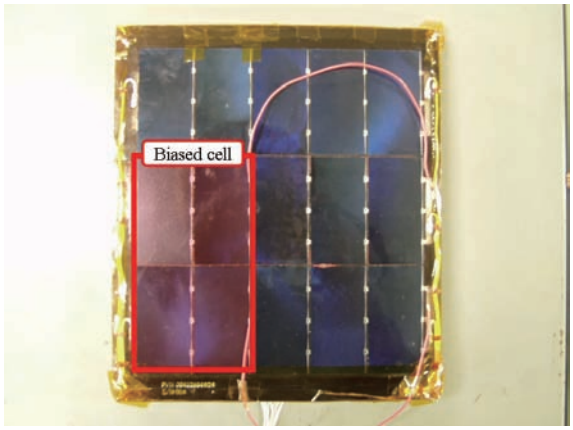

Fig.3　Overview of test coupon.

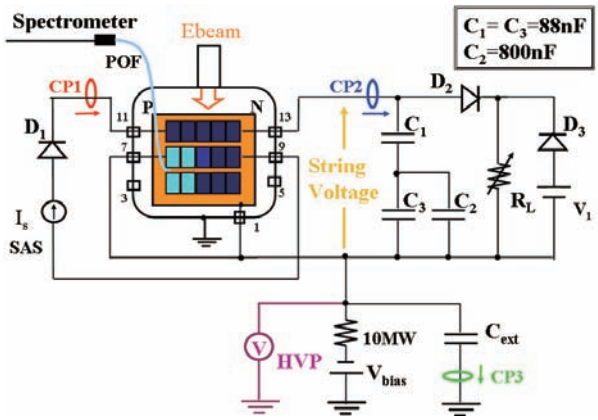

Fig.4　Experimental circuit.

that the current generated by solar cells flows into cells of adjacent strings through the arc plasma and is maintained even after blow-off current ends. This current flowing into the cells of adjacent strings is called as an arc current. Thus, arc plasma might be maintained or not even if the primary arcs are same. However, it is not yet well-known condition of maintained arc plasma which is occurrence condition of secondary arc.

Our purpose of this study is to find the occurrence condition of secondary arcs caused satellite failure by measuring the plasma temperature and the emission metallic vapors by spectroscopy. In this paper, we measured the emission spectrum of arc discharge in arbitrary timing. We calculated the arc plasma temperature associated with arc plasma conductivity, and identified the kind of material emitted from solar array due to arcs. We considered the difference in the property of the arc plasma between NSA and TSA during the secondary arc.

2. Experimental Setup

2.1 Solar Array Coupons

We used solar array coupons designed for Japanese satellite ETS-VIII [3], and composed of Si cells (70x35 mm). This coupon is for measurement it when arcs short-circuit between cells of adjacent strings (Fig.3).

Test coupon has no scar on the surface. We biased 4 cells of adjacent strings (masked cells in Fig.3), and examined the arc phenomena where arc occurs at between the different potential strings.

2.2 Experimental Setup

All experiments were performed in a vacuum chamber, which has 600mm in diameter and 900mm in length. The pressure in the chamber was less than $2x10^{-4}$Pa during experiment. Figure 4 shows the experimental circuit to simulate charging and arcing on orbit. The electron beam gun (acceleration voltage 0~30kV, electronic current densities 0~200μA) (ULVAC: RHEED) simulates the high energy electron that flows into the satellite at the substorm. Moreover, high voltage power supply V_{bias} (0~60kV, 0~10mA) (Glassman: EW60R10) was used to simulate the potential of satellite sinking negatively during the substorm. In addition, a solar array simulator SAS (Agilent: E4351B) was used to simulate the power generation of solar array and supplied to the resistance R_L that simulated the load of the satellite. The voltage between strings was operational voltage of satellite. The C_{ext} that simulated the charge stored in other cover glass because the solar array of an actual size could not be put in the chamber.

When an arc occurs, electrons are emitted from C_{ext} and flow through the solar array, and then reach to the chamber wall through the arc plasma, and flow to the ground. In this case, the current measured at CP3 in the experiment circuit is called a blow-off current. In the case of NSA, the SAS keeps supplying the current to R_L after the blow-off current finished flowing. In the case of TSA, the current flows into the substrate and cannot flow to R_L because R_L is supplied with a voltage of V_1 which simulates generated voltage by other solar array.

2.3 Emission spectroscopy

In this experiment, the spectroscopy was carried out using a spectrometer (Hamamatsu Photonics: PMA11 C8808-01). It has the measurement range of wavelength of 200nm~860nm, the minimum time

resolution of 10ns, the wavelength resolution of 3.0nm. Moreover, a plastic optical fiber POF (Edmund: 53833-G) was attached to the detector to raise intensity from arc discharge.

The oscilloscope outputs the trigger signal to a delay pulse generator DPG (Stanford Research: DG-535) detecting a rising edge of a blow-off current when the arc occurs. The trigger signal is sent to the DPG and makes a TTL and an ECL signal to the spectrometer. The emission spectrum from arc is taken by the detector at time that ECL signal rise. Spectrum acquisition in arbitrary timing after the arc becomes possible by changing delay time (Delay) and pulse width (Gate) of the ECL signal.

The data base of NIST [4] was used to identify of the measured spectrum. C_2 swan band spectrum (420nm~530nm) with high reproducibility was used to calculate of the temperature of plasma. C_2 swan spectrum at from 2,000K to 7,000K is open to the public in BESP [5]. Figure 5 shows C_2 swan spectrum at 6,000K. We paid attention to the area ratio of the first mountain to the second mountain. The correlation with the temperature and the area ratio is shown in Figure 6. It was found that the temperature was represented by the area ratio using the regression curve of exponential.

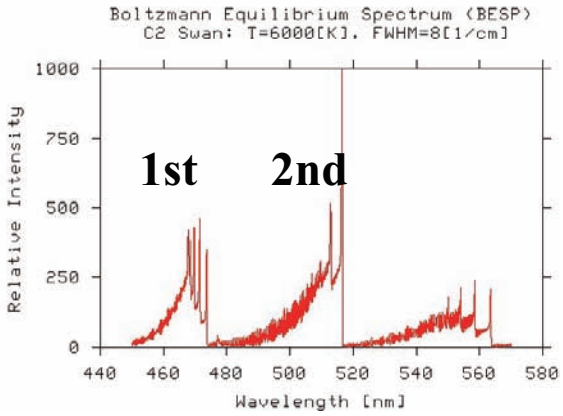

Fig.5 C_2 swan Spectrum in 6,000K (BESP).

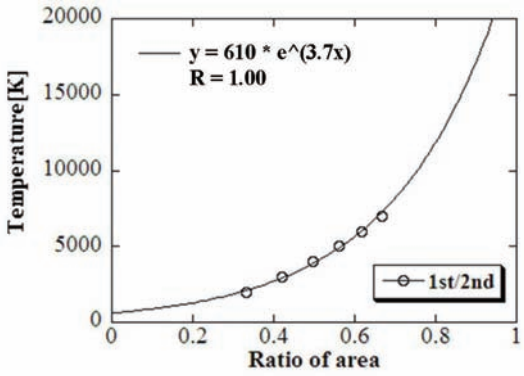

Fig.6 Relation between ratio and temperature of area.

3. Experimental result and discussion

Table 1 shows the experimental parameter used in this experiment. The experiments was performed at about 2~8x10^{-4}Pa. The string voltage is potential difference between two adjacent solar array strings. The I_s is the current supplied from SAS.

3.1 Experiment of arcs at string gap

Time variation of arc plasma temperature for PA and TSA

This experiment was carried out by the parameter in Table1 excluding the following parameters (I_s=1.2A, Gate: 2.5μsec). Table 2 lists the number of arcs measured during this experiment. There was no NSA in this experiment. There are two types of TSA, TSA-Hot is that t arcs occur at the high potential cell's electrode, TSA-Rtn is that arcs occur at the low potential cell's electrode.

Figure 7 shows plasma temperature distribution to time variation for PA and TSA. The time in a blow off current ending is defined as 0μsec (Time=0μsec). As shown in Fig.7, there is no difference in temperature distribution while a blow off current is flowing in PA and TSA.

Table 1 Experimental parameter

Back Pressure		$2x10^{-4}$Pa ~ $2x10^{-3}$Pa
C_{ext}		20nF, 30nF, 45nF, 65nF
V_s		70V, 90V, 105V
I_s		0.05A, 0.1A, 0.2A, 0.5A, 1.2A
V_{bias}		-7kV
Electron Beam		7.2keV ~ 8keV, 100μA
Spectrometer	Gate	1μsec, 2.5μsec
	Delay	0 ~ 30μsec
	Gain	6 or 8

Table 2 Number of arcs at string gap

Is [A]	Arcs at gap	PA	TSA-Hot	TSA-Rtn
1.2	10	9	18	22

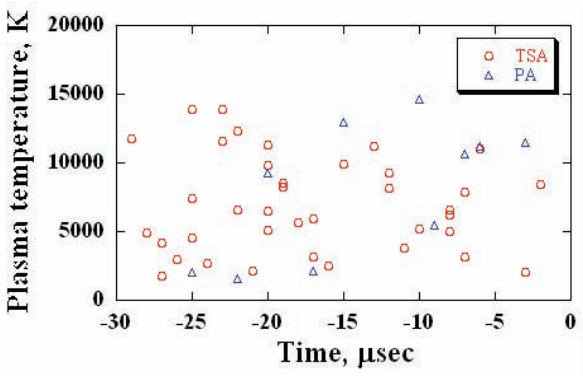

Fig.7 Plasma temperature distribution to time variation for PA and TSA.

Relation between arc plasma temperature and TSA duration

Figure 8 shows that relation between arc plasma temperature and TSA duration before primary arc finished. As shown in Fig.8, the TSA duration did not depend on the plasma temperature. If the plasma temperature rises up to some degree, it might be unrelated to TSA duration.

Identification of material that is emitted from solar array coupon

We examined the relative intensity of silver that was composing the cell's electrode. Figure 9 and 10 show the spectrum of PA and TSA. We found that silver metallic vapor (masked area in Fig.) was emitted much in case of TSA than that in case of PA.

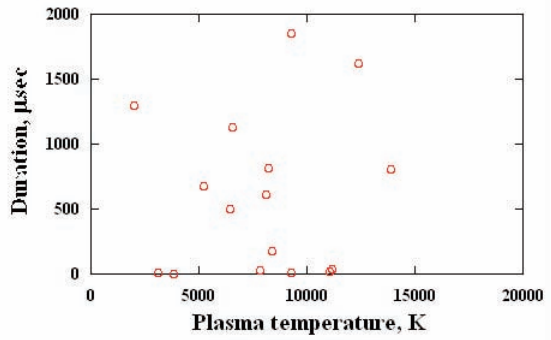

Fig.8　Relation between arc plasma temperature and TSA duration.

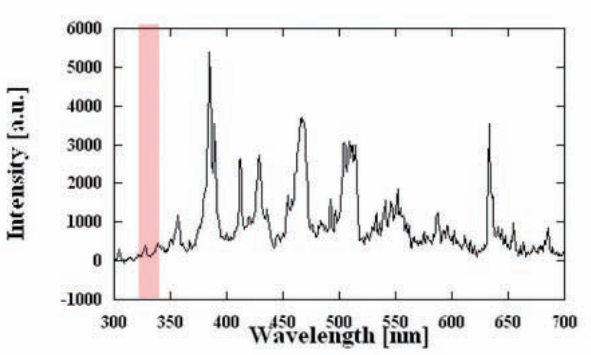

Fig.9　Arc spectrum of PA.

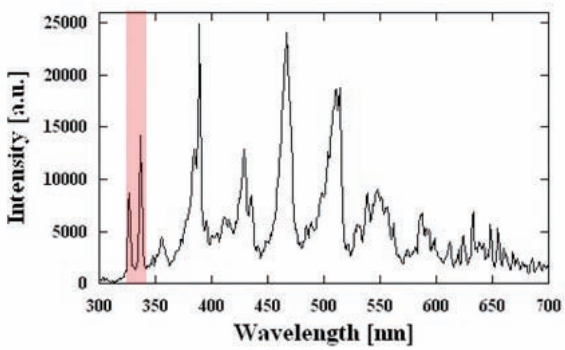

Fig.10　Arc spectrum of TSA.

Relation between emitted metallic vapor and probability of TSA transition

The condition of shifting from PA to TSA was considered by focusing on relative intensity of spectrum of Ag I. Figure 11 shows the relation between probability of shifting to TSA and relative intensity of Ag I and first peak of C_2 molecular. C_2 molecular was measured reproducible at each spectrum. This figure shows that the probability of arc shifting to TSA was high if the amount of silver metallic vapor which composes the cell's electrode was emitted much.

Relation between emitted metallic vapor and TSA duration

Figure 12 shows that relation between relative metallic vapor emission of silver and TSA duration before primary arc finished. As shown in Fig.12, the TSA duration became long if the emitted metallic vapor was much before arc shifting to TSA. The duration of TSA is proportional to amount of emitted metallic vapor.

Relation between metallic vapor emission and arc current

We focused on the source of the metallic

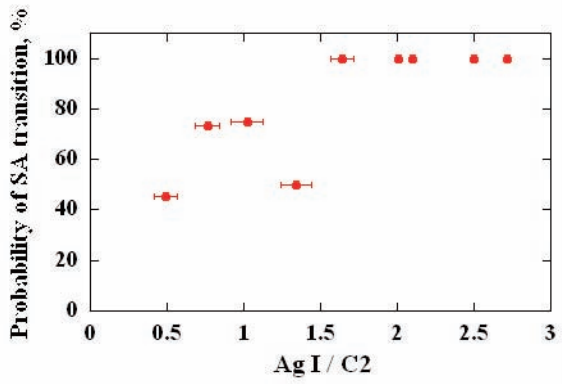

Fig.11　Probability of shifted to TSA for arcs at string gap.

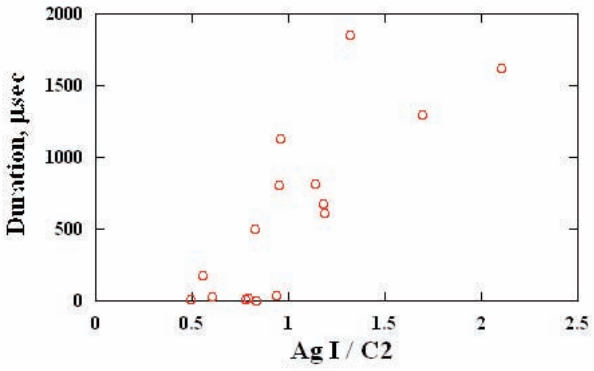

Fig.12　Relation between relative intensity of metallic vapor emission and TSA duration.

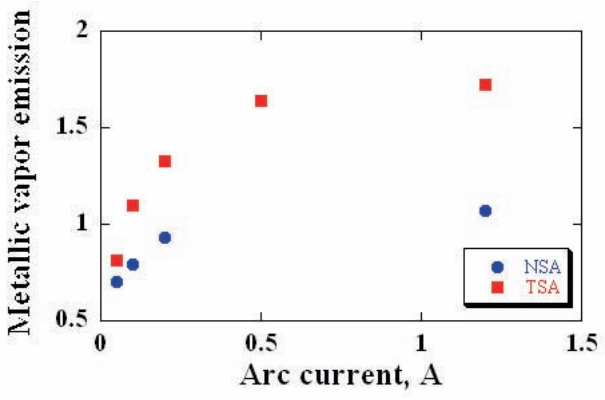

Fig.13　Relation between arc current and amount of emitted metallic vapor.

Table3　PA parameter

Vst [V]	Ist [A]	Cext [nF]	Blow-off current		
			Peak [A]	Pulse width [μsec]	Charge [μC]
70	0.2	30	20.4	18.5	150.3
		45	31.2	19.8	218.1
		65	45.6	17.8	307.3

Table4　Number of arcs

Vst [V]	Ist [A]	Cext [nF]	Number of arcs			
			Total	PA	NSA	TSA
70	0.2	30	20	14	5	1
		45	20	11	5	4
		65	11	4	2	5

vapor emission of silver. In case of generally arcs, metallic vapor is emitted from cathode because the arc current flow into there. Fig.13 shows that relation between metallic vapor emission and arc current.

We found that there is strong relation between secondary arc occurrence condition and metallic vapor emission of silver.

3.2 The effect of PA dimension

We considered the primary arc energy due to external capacitance. Table 3 lists the parameter of PA during this experiment. We carried out the low string current experiment to observe only the effect of PA dimension. In this experiment, we investigate the effect of PA dimension against plasma condition at gap in detail.

SA&TSA probability for external capacitance

First, we investigated whether probability of secondary arc occurrence changes by PA dimension (the value of external capacitance, C_{ext}) Table 4 shows the experimental result of C_{ext} experiment. This is result of number of arcs at gap. From this result, we calculated the probability of secondary arc (SA) and

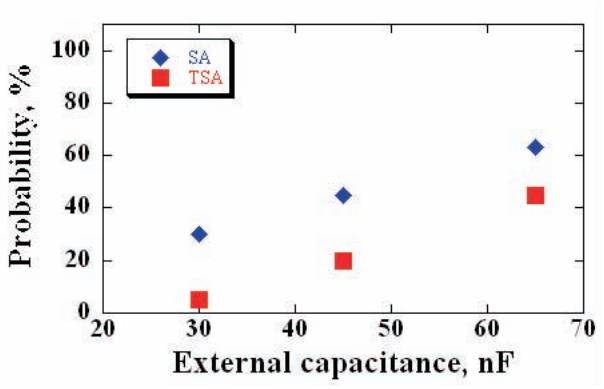

Fig.14　SA＆TSA probability for external capacitance.

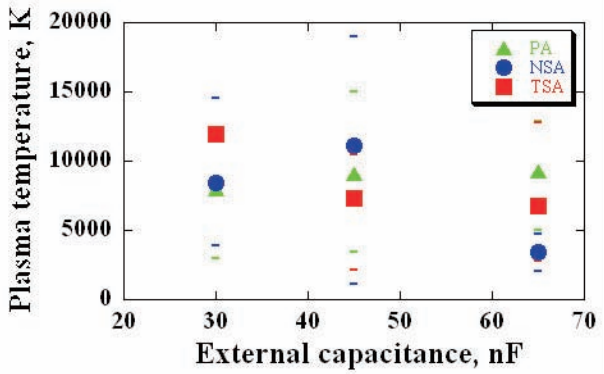

Fig.15　Plasma temperature for external capacitance.

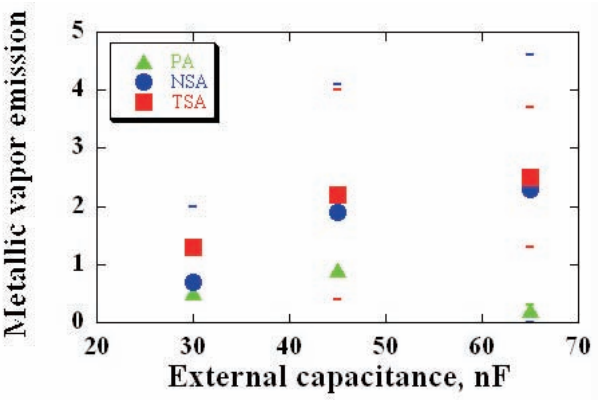

Fig.16　Metallic vapor emission for external capacitance.

temporary sustained arc (TSA) occurrence. Fig.14 shows the calculation result. We found that the bigger PA dimension become, the higher probability of SA and TSA occurrence become.

Plasma temperature during PA

We investigated whether plasma temperature at gap during PA changes by PA dimension. Fig.15 shows the plasma temperature for PA dimension. The error bar means the minimum and maximum value of plasma temperature. We could not determine that the plasma temperature depended on the PA dimension.

Metallic vapor emission during PA

We investigated whether metallic vapor emission of silver at gap during PA changes by PA dimension. The relation of metallic vapor emission and PA dimension is shown in Fig.16. The error bar means the minimum and maximum value of metallic vapor emission of silver. This figure shows that the metallic vapor emission depended on PA dimension.

4. Summary

In this paper, we identified the material emitted by arc and calculated the arc plasma temperature by means of applying spectroscopy on arc discharge.

We investigated the difference of secondary arcs occurrence condition during secondary arcs. From the spectroscopy results, we found that it was necessary for shifting to the secondary arc that the metallic vapor same as the cathode material was emitted. And, TSA duration depends on metallic vapor emission. In case of PA dimension changes, the bigger PA dimension become, the higher probability of SA and TSA occurrence become. And, the metallic vapor emission of silver was greatly affected by PA dimension. However, plasma temperature was not affected by PA dimension. Thus, secondary arc occurrence greatly depends on metallic vapor emission from cathode.

We could investigate the plasma condition due to secondary arcs occurrence. In the future, we must investigate it more detail, and we must consider that the effect of point and shape of cathode spot on secondary arc occurrence. Then, we must investigate the countermeasures method against secondary arcs.

References

[1] Katz, I., Davis V.A; and Snyder, D.B, “Mechanism for Spacecraft Charging Initiated Destruction of Solar Arrays in GEO”, AIAA 98-1002, 36th Aerospace Sciences Meeting & Exhibit, Reno, January, 1998

[2] Cho, M., and Fujii, H., “Review on Charging and Discharging Phenomena in Space Environment: Arcing on High Voltage Solar Array and Future Issues”, Aeronautical and Space Sciences Japan, Vol.51, pp.139-145, 2003

[3] M.Takahashi, H.Nishimoto, S.Kawakita, M.Cho, Y.Nozaki, H.Fujii, Y.Murakami, T.Ozaki, N.Onodera, “ETS-VIII Solar PDL Plasma Interaction Problem Approach”, 7th Spacecraft Charging Technology Conference, Noordwijk, Netherlands, April, 2001

[4] NIST Atomic Spectra Database http://physics.nist.gov/cgi-bin/AtData/lines_form

[5] Boltzmann Equilibrium Spectrum Program http://view.utsi.edu/besp/

[6] Jeongho Kim, Seiji Aso, Satoshi Hosoda, Mengu Cho, “Threshold Conditions to Induce the Sustained Arc on the Solar Array Panel of LEO Satellite”, 9th Spacecraft Charging Technology Conference, Tsukuba, Japan, April, 2005

Plasma and solar array arcing caused by space debris impact

Shinya FUKUSHIGE[1], Yasuhiro AKAHOSHI[1], Keiko WATANABE[2],
Toshikazu NAGASAKI[1], Kenshou SUGAWARA[1],
Takao KOURA[1], Mengu CHO[1]

1.Department of Mechanical Engineering, Faculty of EngineeringKyushu Institute of Technology
1-1, Sensui-cho, Tobata-ku, Kitakyushu, Fukuoka, 804-8550, Japan
Phone & Fax: +81-93-884-3151
E-mail: e584102s@tobata.isc.kyutech.ac.jp
2. Osaka University

Abstract

There is high possibility that space debris impacts to a solar array paddle in spacecraft parts, because the solar array paddle has large area. Space debris impact to the solar array causes not only mechanical damage but also electrical damage such as arcing on the solar array through local high density plasma created by hypervelocity impact. In the worst case, Joule heating of this arcing carbonizes insulation layer and permanent short-circuit path is created. This is permanent sustained arc. However, no permanent sustained arc caused by space debris impact in orbit has been reported. Purpose of this study is evaluation of possibility of permanent sustained arc through the plasma created by debris impact. Hypervelocity impact tests to solar array coupons in the condition of pseudo power generation were conducted. We ascertained that space debris impact can lead to permanent sustained arc on the solar array due to plasma created by hypervelocity impact

Key Words: Space Debris, Solar Array, Plasma, Discharge

1. INTRODUCTION

In recent years, a solar array of a spacecraft has become larger with the voltage higher because a spacecraft has a large amount of power in requests from an advanced mission. Therefore the risk of a space debris impact and discharge on the solar array is increasing. Space debris impact to the solar array causes not only mechanical damage such as destruction of a solar cell and insulation layer but also generation of local high density plasma due to impact energy[1]. This plasma can lead to arcing between solar cells or cell and substrate on the solar array[2]. In the worst case of this event, Joule heating of this arcing can carbonize insulation layer and create permanent short-circuit path. This is permanent sustained arc (PSA). Purpose of this study is evaluation of possibility of PSA through the plasma created by debris impact. It is considered that micro debris which has high probability of impact cannot trigger PSA because no PSA caused by hypervelocity impact on the actual solar array of spacecraft in orbit has been reported. Therefore we conducted hypervelocity impact tests using comparatively large size projectile which was 3 [mm] Al sphere. Target was solar array coupon in the condition of pseudo power generation. Temperature and density of plasma created by hypervelocity impact as well as current and voltage of external circuit which connected to the solar array coupon were measured. We ascertained that space debris impact can lead to permanent sustained arc on the solar array due to plasma created by hypervelocity impact.

2. EXPERIMENTAL SETUP

The hypervelocity impact tests were carried out using the two-stage light gas gun, installed at Laboratory of Spacecraft Environmental Interaction Engineering (La SEINE) in Kyushu Institute of Technology. The experimental setup is shown in Fig. 1. The projectile was Al2017 sphere which was 3 [mm] in diameter. This projectile is accelerated in a launch tube with sabot. The sabot separation section and the test chamber are partitioned out by the polyester film which is 25 [μm] in thickness. The ambient pressure of sabot separation section is 10 [kPa] and that of the test chamber is 4×10^{-2} [Pa] because the separation of projectile from sabot needs air drag. The magnet detector, which consists of a permanent magnet and a pick up coil, was set up in the blast tank, and the signal of the projectile was used as oscilloscope trigger to record data.

Solar array coupon is shown in Fig. 2. The solar cell is silicon cell. The cell and coverglass are 100 [μm] in thickness. The substrate is CFRP Al honeycomb sandwich.

Solar array coupon can simulate the condition of power generation with connection to the external circuit, which is shown in Fig. 3. The external circuit consisted of quick response constant current (CC) power supply, resistor and constant voltage (CV) power supply[3]. The resistor simulates load resistance of a spacecraft. The output of CC power supply simulates that of a string of solar array. The CV power supply simulates the voltage which maintained by the other strings of solar array when discharge occurs on the string. The voltage of the CV power supply was set 1 [V] lower than that of CC power supply. CRD power supply which consisted constant current regulation diodes and voltage source was used as quick response CC power supply. The current probe 1 (Cp_1) measured current of circuit which

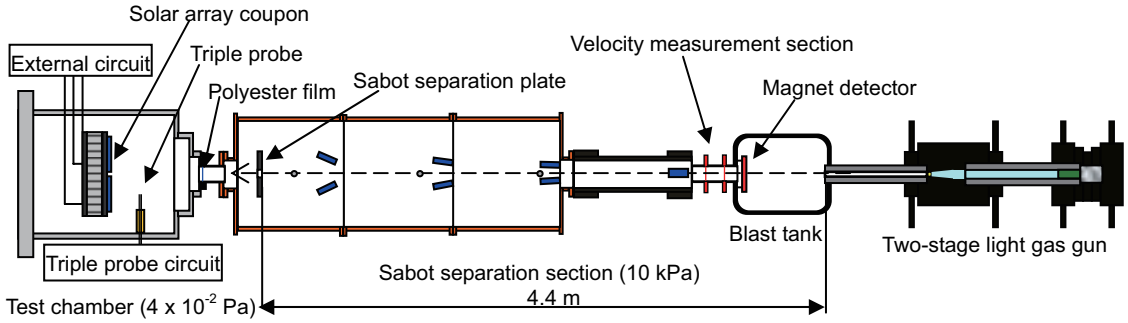

Fig. 1 Experimental setup of hypervelocity impact test

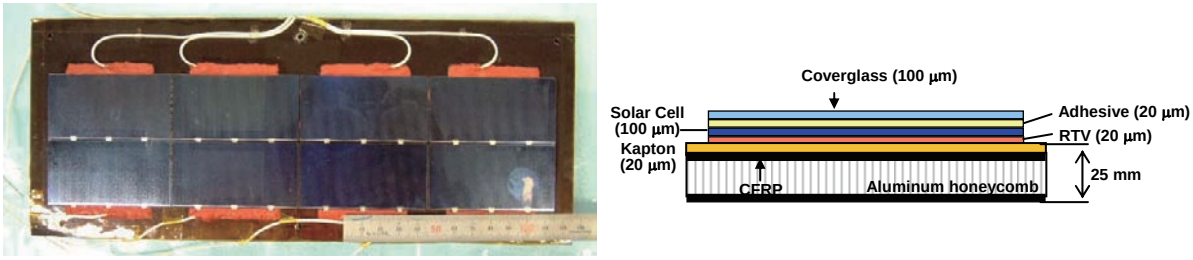

(a) Front view　　(b) Cross section

Fig. 2 Solar array coupon

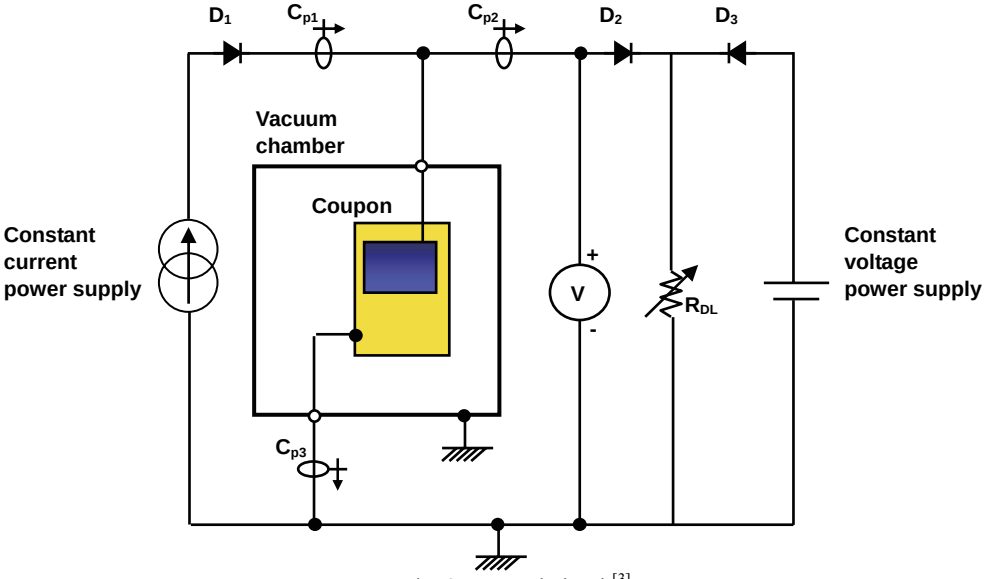

Fig. 3 External circuit[3]

simulate the output of a string of the solar array. The current probe 2 (Cp_2) measured current which flow to resistance. The current probe 3 (Cp_3) measured discharge current between the cell and substrate. The voltage probe measured string voltage.

Triple probe[4] was set at a distance of 100 [mm] from the front of the solar array coupon to measure electron temperature and density of plasma created by hypervelocity impact. The configuration of the triple probe is shown in Fig. 4. The probe was made of coated copper wire. The diameter was 2 [mm] and the exposure length was 20 [mm]. The near part of the tip of the probe was insulated by Kapton tape. The electron temperature Te [eV] and density N_e [m^{-3}] can be calculated by V_2, V_3 and following equations. The electron temperature is obtained from equations (1) and (2);

$$\frac{I_1 + I_2}{I_1 + I_3} = \frac{1 - \exp(-\phi_{d2})}{1 - \exp(-\phi_{d3})} \quad (1)$$

$$I_1 = I_2 + I_3 \quad (2)$$

where $\phi_{d2} = eV_{d2}/\kappa Te$, $\phi_{d3} = eV_{d3}/\kappa Te$, e is elementary electric charge and κ is Boltzmann constant. Finally, electron density can be calculated by following equations.

$$I_i = \frac{I_3 - I_2 \exp(-\phi_{\Delta V})}{1 - \exp(-\phi_{\Delta V})} \quad (3)$$

$$N_e = [(M)^{1/2} / S\,]\, I_i\, f_1(V_{d2}) \quad (4)$$

$$f_1(V_{d2}) = 1.05 \times 10^{15} (Te)^{-1/2} [\exp(\phi_{d2}) - 1]^{-1} \quad (5)$$

Here M [g] is ion mass, S [mm^2] is surface area of the probe and I_i [μA] is ion current. In this study, V_{d2} = 3 [V], V_{d3} = 18 [V] and the resistance was 0.25 ~ 10 [kΩ].

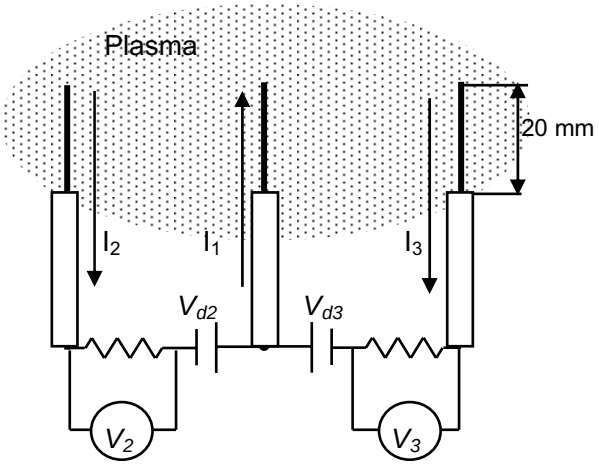

Fig. 4 Triple probe circuit

The measurement results of electron density and temperature depend on measurement point and time because plasma created by impact diffuses from impact point. Therefore, the solution of the advection-diffusion equation was defined as fitting curve to time history of electron density at the measurement point on the assumption that plasma diffusion can be represented by that solution, which is following formula.

$$N_e = \frac{n_e}{(4\pi Dt)^{3/2}} \exp\left(-\frac{(r-Ut)^2}{4Dt}\right) \qquad (6)$$

where t is elapsed time since impact, N_e is electron density, and r is distance from impact point to measurement point of the triple probe. The fitting parameters, which are electron number n_e, diffusion coefficient D, and advection velocity U can be obtained by the curve fitting.

The electron temperature at the time when the electron density is maximum value on the fitting curve is adopted as a representative value of electron temperature because diffusion into vacuum is isothermal expansion.

3. TEST RESULTS

Test results about discharge are distinguished by the following definitions. Primary arc (PA) is discharge just after impact. Temporary sustained arc (TSA) is discharge that discharge current measured by C_{p3} equals to circuit current measured by C_{p1} for over 2 [μsec]. Permanent sustained arc (PSA) is that there is permanent short-circuit path after hypervelocity impact test. Hypervelocity impact test were conducted in the impact velocity of mainly approximately 4 [km/s] and several different velocity. The test results are shown in Table 1. The results of discharge which are arranged on voltage and current condition of external circuit are shown in Fig. 5. The results of a longer duration of discharge are shown in Fig. 1, where there are various results in the same condition of voltage and current setting.

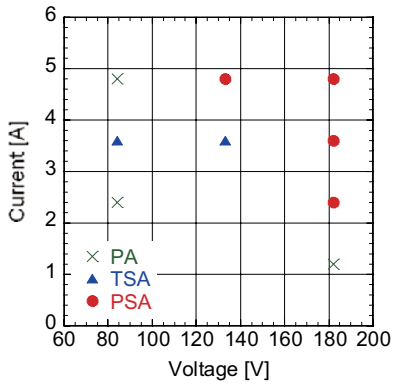

Fig. 5 Test results about discharge

These results confirm hypervelocity impact causes PSA on a solar array. In the case that impact velocity was around 4 [km/s], PSA occurred under the conditions that voltage was 182 [V] and current was 2.4 [A] and more. In the other impact velocity, although there were few tests conditions of voltage and current, PSA occurred under 133 [V] – 4.8 [A] and 182 [V] – 4.8 [A] with the impact velocity of about 2.1 [km/s] and under 182 [V] – 4.8 [A] with the impact velocity of around 4.7 [km/s].

The typical example of the voltage and current waveforms of the external circuit is shown in Fig. 6. Applied voltage and

Table 1 Test results of hypervelocity impact test

Voltage [V]	Current [A]	Impact velocity [km/s]	Discharge	Electron number x10^{13}[electrons]	Electron temperature [eV]	Diffusion coefficient [m^2/s]	Advection velocity [km/s]
84	2.4	3.78	PA	180	1.74	64.7	5.81
	3.6	3.68	TSA	45.4	2.63	15.9	4.14
	4.8	3.52	PA	163	1.77	54.1	4.74
133	3.6	3.72	TSA	194	1.71	53.9	5.50
		4.02	TSA	295	2.07	58.3	4.52
	4.8	2.08	PSA	3.74	1.04	6.18	2.12
		2.85	PA	30.8	1.06	27.2	3.63
		3.74	TSA	350	1.85	74.2	4.14
		3.85	TSA	154	1.46	57.8	5.52
		4.82	PA	892	2.86	104	6.14
182	1.2	3.95	PA	259	2.10	54.7	5.46
	2.4	3.81	PSA	129	1.50	42.3	5.78
	3.6	3.74	PSA	185	2.37	39.0	4.55
	4.8	2.14	PSA	3.08	1.37	5.15	1.95
		3.76	PSA	233	1.76	51.3	5.72
		4.65	PSA	643	2.93	95.3	6.23

current were 133 [V] and 3.6 [A], respectively, and impact velocity was 4.02 [km/s].

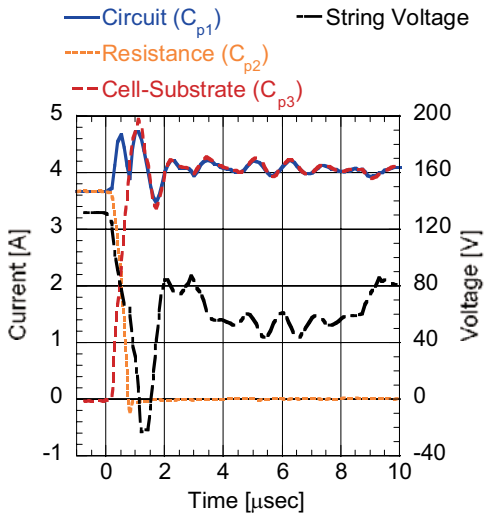

Fig. 6 Current and voltage of onset of arcing

The contact between the cell and substrate through the Al sphere cause short circuit, in the penetration process of the Al sphere into the solar array coupon. The time at the voltage drop due to short-circuit between the cell and substrate was set to 0 [sec] in Fig. 6. It took the circumference of largest dimension of the Al sphere approximately 400 [μsec] to pass through the cell. The plasma created by hypervelocity impact sustained discharge between the cell and substrate after the perforation. Collision of ions into substrate, which is cathode, generates neutral gas and secondary electrons while plasma diffuses. Thermionic emission occurs due to local temperature rise of the substrate caused by ion collision depending on conditions. The electrons generated by those processes ionize the neutral gas and the arcing can be sustained by the new ions and electrons after diffusion of plasma created by impact. If the arcing stops before insulation layer is carbonized by Joule heating, this arcing is TSA, if not, PSA occurs. Therefore, ion current density which is collected by the substrate at the impact point plays a vital role in the occurrence of TSA or PSA. This ion current density can be calculated by equation (6) and (7) using the number of electrons, electron temperature, diffusion coefficient and advection velocity, which were shown in Table 1.

$$i_i = \exp\left(\frac{1}{2}\right) eN_e \sqrt{\frac{\kappa Te}{m_i}} \qquad (7)$$

Here i_i is ion current density and m_i is ion mass. The calculation results at 1 [nsec] after impact are plotted on Fig. 7 as a function of impact velocity. These results can be fitted by power law with index of 2.0. Therefore, the ion current density is proportional to kinetic energy of the projectile. In the tests, the impact velocities were low in comparison with that of debris in low earth orbit, which is 10 [km/s] on an average. However, because the ion current density which is collected by the substrate at the impact point is proportional to kinetic energy, it is considered that higher velocity impact can trigger PSA.

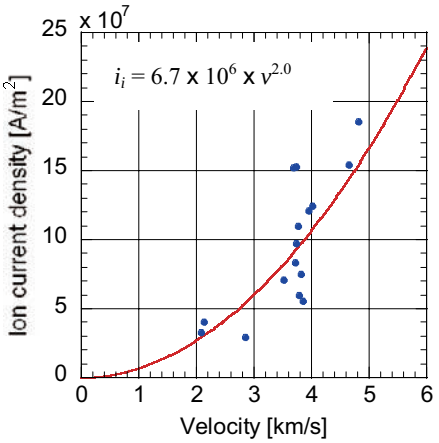

Fig. 7 Ion current density at impact point

4. CONCLUSION

In this study, hypervelocity impact tests using comparatively large size projectile which was 3 [mm] Al sphere were conducted to evaluate possibility of PSA due to the plasma created by debris impact. As a result, we concluded that hypervelocity impact can lead to PSA on a solar array. The plasma created by hypervelocity impact was measured by triple probe and the electron number, electron temperature, diffusion coefficient and advection velocity were obtained using the solution of the advection-diffusion equation. The ion current density which is collected by the substrate at the impact point can be calculated from these parameters. The calculation results shows that the ion current density is proportional to kinetic energy of projectile.

ACKNOWLEDGMENTS

This work was supported by two organizations including 38th Kurata bounty sponsored by the Kurata Memorial Hitachi Science and Technology Foundation and Grant-in-Aid for Young Scientists (B), No. 18760608, sponsored by the Japan Society for the Promotion of Science.

REFERENCES

[1] Gerhard Drolshagen, “Hypervelocity Impact Effects on Spacecraft”, Proceedings of the Meteoroids 2001 Conference, ESA Publication Division, pp.533-544, 2001

[2] S. Fukushige, Y. Akahoshi, K. Watanabe, T. Harano, Y. Machida, N. Furusawa, T. Koura, S. Hosoda, M. Cho, and S. Harada, “Hypervelocity Impact Test to Solar Array for Evaluation of Possibility of Sustained Arc”, Proceedings of the 25th International Symposium on Space Technology and Science, pp.1356-1361, 2006

[3] Payan, D., Schwander, D. and Catani, J. P.: Risks of Low Voltage Arcs Sustained by the Photovoltaic Power of a Satellite Solar Array during an Electrostatic Discharge, Solar Array Dynamic Simulator, 7th Spacecraft Charging Technology Conference, 2001

[4] S. Chen and T. Sekiguchi, “Instantaneous Direct- Display System of Plasma Parameters by Means of Triple Probe”, Journal of Applied Physics, pp.2363-2375, August 1965

4th Space Environment Symposium, Tokyo, 2008

Preliminary ESD Ground Tests on Meter-Class Solar Panels in Simulated GEO Environments

Hideto Mashidori[1], Minoru Iwasa[1], Atsushi Wada[1], Kumi Nitta[1], Masayuki Nomura[2] and Kazuhiro Toyoda[2]
1. Japan Aerospace Exploration Agency, 2-1-1 Sengen, Tsukuba, Ibaraki 305-8505, Japan
2. Kyushu Institute of Technology, 1-1 Sensuicho, Tobata, Kitakyushu 804-8550, Japan

Abstract

Preliminary ESD ground tests with two meter-class solar panels were conducted in a simulated GEO environment. The results indicated that the plasma propagation velocity was approximately 10^4 m/s, and the plasma propagation length was greater than 2.8 m. The neutralization current decreased with an increase in the distance from the arc spot.

1. Introduction

In recent years, satellite losses have occurred because of power system failures resulting from spacecraft charging/discharging phenomena [1]–[3]. Hence, electrostatic discharge (ESD) in solar array panels is an important issue related to satellites.

A so-called primary arc might occur at a triple junction on a solar panel if the electric potential of the cell coverglass is higher than that of the spacecraft ground [1]. The plasma generated by the primary arc propagates throughout the solar array and neutralizes the charge stored on the coverglass. Therefore, plasma propagation length and velocity are important for estimating the discharge current waveforms on the solar arrays. ESD ground tests have been conducted in several research institutes to investigate the plasma propagation velocity [4]–[6]. However, the plasma propagation length has not been fully understood. Although the plasma propagation length has been estimated as 3–4 m [7], it has not been confirmed through laboratory experiments because it is difficult to use a large-scale solar panel.

The space plasma chamber used in these experiments is located at the Institute of Space and Astronautical Sciences (ISAS) of the Japan Aerospace Exploration Agency (JAXA). Figure 1 illustrates the space plasma chamber used in this study. The chamber has a diameter of 2.5 m and length of 4 m. Accordingly, the chamber enables us to perform the ESD ground tests with a large solar array panel with a surface area larger than 1 m^2.

Preliminary ESD ground tests using two meter-class solar array panels were conducted in a simulated geosynchronous-earth-orbit (GEO) environment. The tests were designed to investigate the plasma propagation length and velocity. The results of the tests are described herein.

2. Experimental Setup

Figure 2 presents a photograph of the two meter-class solar array panel used in this study. This

Fig. 1. A photograph of the space-plasma chamber in ISAS/JAXA.

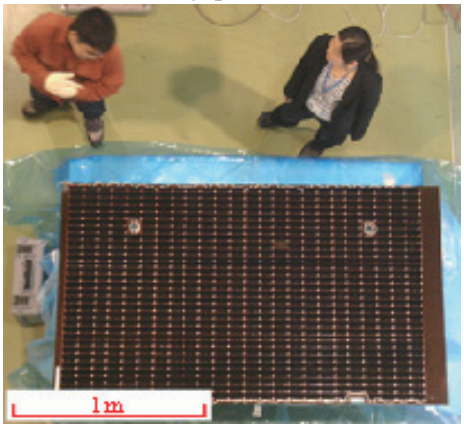

Fig. 2. A photograph of a solar array panel used in this study.

panel consisted of more than 700 solar cells arranged in 24 strings. There were 30–31 cells in a string, which were connected in series by inter-connectors. The panel was 1.77 m long and 1.10 m wide. The solar cell was a triple junction (TJ) cell with a bypass diode. The surface area of the cell was 37 mm × 76 mm. The coverglass thickness was 0.1 mm.

Figure 3 depicts the experimental apparatus. The two panels were placed in a vacuum chamber. Two electron beam guns were mounted at the chamber. These guns were used to simulate GEO environment. These can generate 50 keV electron beams with a maximum current of 200 μA. Two aluminum foils were used to expand the irradiation area of the electron beam. The thickness of the aluminum foils was 100 nm.

Figure 4 illustrates the experimental circuit. The circuit was connected to the solar array via a high voltage feedthrough. A high-voltage power supply biased the panels to a negative potential. The P- and N-electrodes of all the solar cell strings were mutually connected. The current probes were attached to six independent strings among the 48 strings on the panels. These independent strings have been referred to as ST1, ST2, ST3, ST4, ST5, and ST6. Strings ST1 and ST6 were located at both ends of the panels. The distance between the respective strings is indicated in Fig. 4. In addition to ST1–ST6, other strings were bundled together. They have been collectively referred to as ST7. Another current probe was attached to ST7. The current arc that occurred on a string has been referred to as the “arc current.” Negative current flows in other strings have been referred to as the “neutralization currents.” The bias voltage of the panel was measured using a voltage probe.

Table 1 presents the experimental conditions. The pressure in the vacuum chamber was maintained at 4.0×10^{-4} Pa. The two solar array panels were biased at –5 kV by a high-voltage supply. The acceleration voltage of the electron guns was fixed at 8.5 kV.

3. Results and Discussion

The confirmed plasma propagation length and velocity based on the neutralization currents

Figure 5 presents the typical current waveforms. The abscissa axis depicts the time; the ordinate axis depicts the current. The time at which the arc discharge started was defined as the null time. Figure 5 depicts the case wherein an arc occurred at ST5. The arc current passing through ST5 lasted approximately 400 μs. The neutralization currents passed through strings ST1–4, and these currents decreased with an increase in the distance from the arc spot. It is noteworthy that the neutralization current passed through ST1 even though ST1 was located as far away as 2.83 m from ST5. The result indicates that the plasma propagation length is inferred to be longer than 2.8 m.

The plasma propagation velocity was calculated based on the test result obtained from Fig. 5. The calculation result is presented in Table 2. The velocity was approximately 10^4 m/s, and it was approximately equal to other research results obtained with small coupon panels [4]–[6].

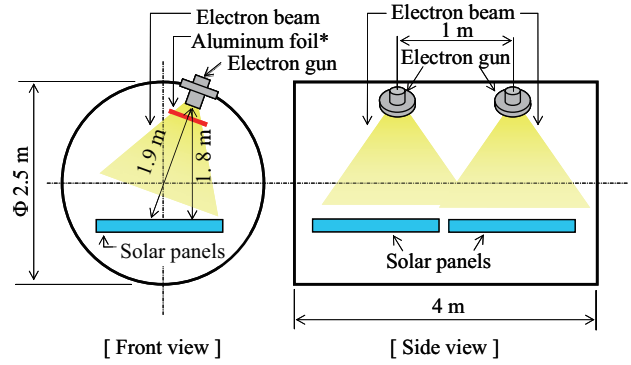

* Al foil was used to expand the irradiation area of electron beam.

The experimental setup.

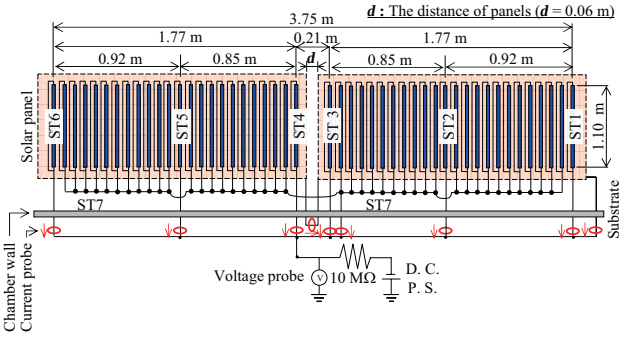

Fig. 4. The experimental circuit used in this study.

Table 1 Experimental conditions.

Pressure	4.0×10^{-4} Pa
Panel bias voltage	-5 kV
The acceleration voltage of electron guns	8.5 kV

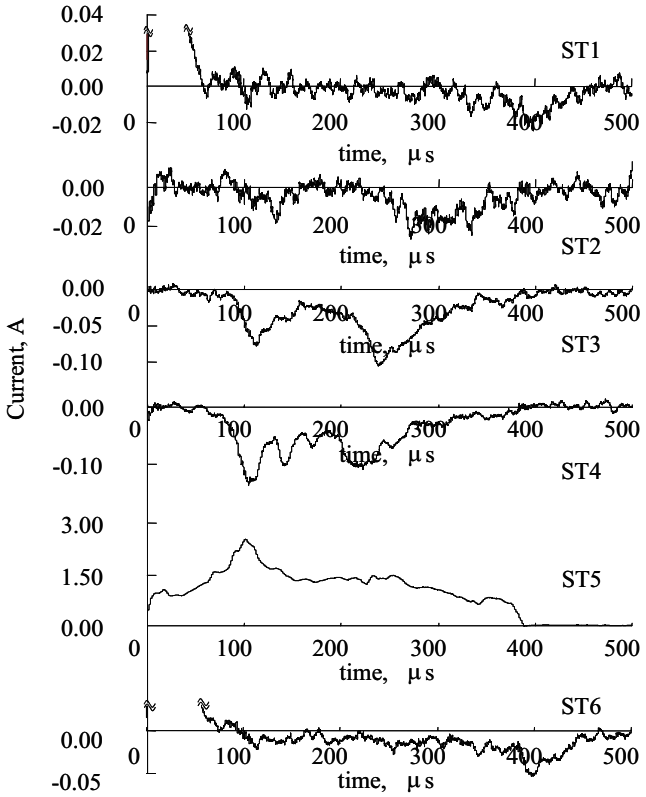

Fig. 5. The typical current waveforms for the arc that occurred at ST5.

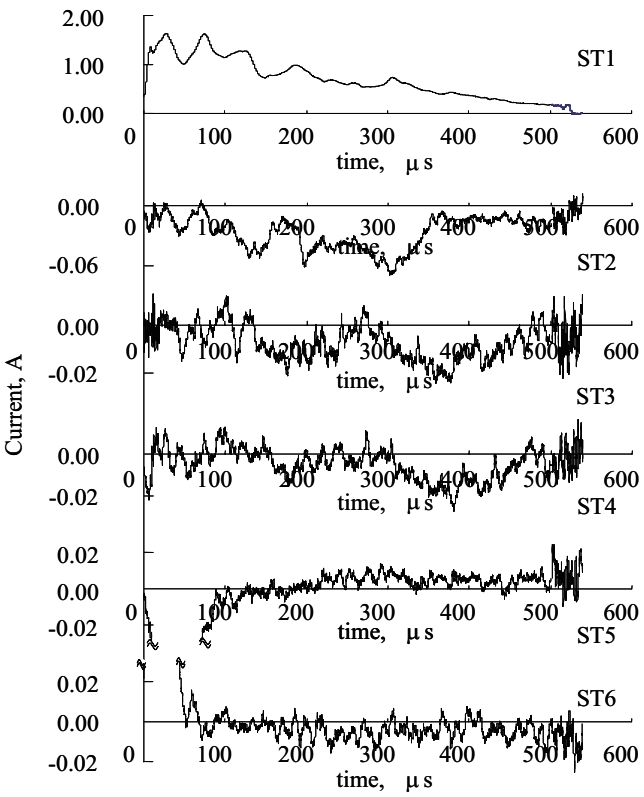

Fig. 6. The typical current waveforms for the arc that occurred at ST1.

Table 2　Plasma propagation velocity.
(Calculated based on the result shown in Fig. 5.)

String	Time of current start*	Distance to ST5+	Plasma propagation velocity
ST3	80 μs	1.06 m	1.3×10^4 m/s
ST4	50 μs	0.85 m	1.7×10^4 m/s

* Time origin is defined as the occurrence of the arc on the panel.
+ This is the case where an arc occurred at the ST5.

Table 3　Plasma propagation velocity.
(Calculated based on the result shown in Fig. 6.)

String	Time of current start*	Distance to ST1+	Plasma propagation velocity
ST2	60 μs	0.92 m	1.5×10^4 m/s
ST3	130 μs	1.77 m	1.4×10^4 m/s

* Time origin is defined as the occurrence of the arc on the panel.
+ This is the case where an arc occurred at the ST1.

The presumed plasma propagation length based on the arc current and plasma propagation velocity

Figure 6 depicts other typical current waveforms for an arc that occurred at ST1. Table 3 shows the plasma propagation velocity calculated based on the result illustrated in Fig. 6. The plasma propagation velocity was approximately 10^4 m/s, and it was equal to the result presented in Table 2. Additionally, the arc current passing through ST1 lasted approximately 500 μs. This result indicates the possibility that the plasma had reached ST6. (ST6 was located as far away as 3.75 m from ST1.)

To further clearly research the plasma propagation length, we plan to measure the solar panel surface electric potential before and after discharge.

4. Summary

Preliminary ESD ground tests with two meter-class solar array panels were conducted in a simulated GEO environment. The tests were performed to investigate the plasma propagation length and velocity.

The following is a summary of this study.

1. The plasma propagation velocity was approximately 10^4 m/s.
2. The plasma propagation length was inferred to be over 2.8 m.
3. The neutralization current decreased with the increase in the distance from the arc spot.
4. When an arc occurred on the strings at the edges of the solar panels, the arc current lasted 500 μs. The result indicates the possibility that the plasma propagated through all the panels.

References

[1] M. Cho and H. Fujii, “Review on charging and discharging phenomena in space environment: arcing on high voltage solar array and future issues,” Aeronautical and Space Sciences Japan, Vol.51, 2003, pp.139–145.

[2] I. Katz, V. A. Davis and D. B. Snyder, “Mechanism for spacecraft charging initiated destruction of solar arrays in GEO,” 36th Aerospace Sciences Meeting & Exhibit, Reno, NV, AIAA 98–1002, Jan. 1998.

[3] S. Hosoda, J. Kim, M. Cho, K. Toyoda, S. Kawakita, M. Kusawake, M. Takahashi and H. Maejima, “Ground investigation of sustained arc phenomena in power cables on ADEOS-□□ satellite,” Journal of the Japan Society for Aeronautical and Space Sciences, Vol.54, 2006, pp.427–433.

[4] P. Leung, “Plasma phenomena associated with solar array discharges and their role in scaling coupon test results to a full panel,” 40th Aerospace Sciences Meeting & Exhibit, Reno, NV, AIAA 2002–0628, Jan. 2002.

[5] E. Amorim, D. Payan, R. Reulet and D. Sarrail, “Electrostatic discharges on a 1 m2 solar array coupon influence of the energy stored on coverglass on flashover current,” 9th Spacecraft Charging Technology Conference, Tsukuba, Apr. 2005.

[6] T. Kawasaki, Y. Shikata, S. Hosoda, J. Kim and M. Cho, “Influence of coverglass on arcing phenomena on GEO satellite solar array,” 24th International Symposium on Space Technology and Science, ISTS 2004-S-07, Miyazaki, June 2004.

[7] M. Cho, R. Ramasamy, M. Hikita, K. Tanaka and S. Sasaki, “Plasma response to arcing in ionospheric plasma environment: Laboratory experiment,” Journal of Spacecraft and Rockets, Vol.39, No. 3, 2002, pp.392–399.

材料物性

Material properties

Erosion properties of polyimide as a monitoring material of atomic oxygen environment in space (3): Synergistic effect of atomic oxygen and ultraviolet

Graduate School of Engineering, Kobe University
Masahito Tagawa and Kumiko Yokota

Erosion property of polyimide was studied through the ground-based synergistic studies. Hyperthermal atomic oxygen and 172nm VUV exposed to polyimide and polyethylene in various conditions. *In-situ* mass loss measurement of polymers during the atomic oxygen and/or VUV exposures was achieved with a quartz crystal microbalance. The effect of simultaneous ultraviolet exposure on the atomic oxygen-induced erosion was observed at the ultraviolet intensity of 0.5-2.6 x 10^{-15} mJ/atom for polyethylene. In contrast, the similar effect was observed in polyimide at the relative ultraviolet intensities one order greater than that of polyethylene. It was also found that the effect of 172 nm ultraviolet was different in polyimide and polyethylene; i.e., photo-induced erosion was observed only for polyethylene. It was concluded that polyimide is less sensitive to the simultaneous ultraviolet exposure during atomic oxygen bombardment, and thus evaluated as a better material for measuring atomic oxygen fluence in space.

1. Introduction

There exist many environmental factors in low Earth orbit (LEO) such as microgravity, thermal cycling, plasma, ultraviolet, radiation, neutral gas and space debris. In particular, one of the most important factors that gives serious damages to many polymeric materials used at the exterior surfaces of spacecraft is atomic oxygen, which is a dominant neutral species in LEO. Due to the difficulty to simulate atomic oxygen environment in laboratory, details of the erosion properties are still not understood deeply. Many polymeric materials are exposed to real space environment as well as simulated atomic oxygen environment to study their survivability. Since the absolute fluence of atomic oxygen in material exposure test is difficult to determine, Kapton equivalent fluence is widely accepted as a method to measure atomic oxygen fluence. In this method, the material erosion of a targeted polymer is compared with that of Kapton-H whose erosion rate is assumed to be 3.0 x 10^{-24} cm^3/atom. However, it is natural to consider that the material response with hyperthermal atomic oxygen collision depends on a material. It is thus emphasized that the erosion properties of Kapton-H (PMDA-ODA polyimide) in various exposure conditions have to be well-understood as a reference material for material erosion tests. Not only PMDA-ODA polyimide, but also polyethylene and fluorinated polymer should be studied in the same manner since ASTM-E2089, which describes standard method of atomic oxygen testing, requires the measurement of the erosion rate of these polymers as standard materials [1]. One of the key points on erosion properties is the synergistic effect of atomic oxygen and ultraviolet. Among three standard materials, it is recognized that fluorinated polymer is sensitive to ultraviolet. For atomic oxygen measurement, a material insensitive to ultraviolet should be selected.

In this paper, polyethylene and polyimide were compared as an atomic oxygen fluence monitoring material under the bombardment of hyperthermal atomic oxygen and 172 nm ultraviolet radiation. The effect of simultaneous ultraviolet exposure on the atomic oxygen-induced erosion of polyethylene and polyimide was discussed based on the ground-based experimental results.

2. Experimental details

The samples used in this experiment were low-density polyethylene (LDPE) and pyromelliticdianhydride-oxydianiline (PMDA-ODA) polyimide films. Both of the films were spin-coated on QCM sensor crystals. The polyethylene solution containing 0.3 g of LDPE (average molecular weight: 6500) in 40 ml xylene was prepared for polyethylene film. Precursor of PMDA-ODA polyimide was spin-coated on a QCM sensor crystal and then annealed at 150 °C 1h and at 300 °C 1h.

A space environment simulation facility at Kobe University was used in this study. This facility equipped a laser detonation atomic oxygen beam source, which was originally designed by Physical Sciences Inc., as a hyperthermal atomic oxygen source. An excimer light source with a wavelength of 172 nm was used as an ultraviolet source in this study. Axes of the atomic oxygen beam and the ultraviolet crossed 90° and the sample was rotatable with the axis perpendicular both to atomic oxygen and ultraviolet. In this configuration, the effective atomic oxygen and

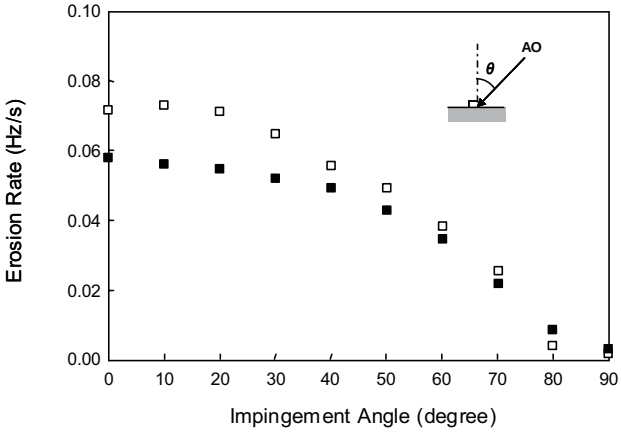

Figure 1 Erosion rates of the polyethylene and the polyimide during atomic oxygen exposures measured from the resonant frequency of the QCM. ■:polyethylene (AO Flux: 6.0 x 10^{14} atoms/cm^2/s), □: polyimide (6.8 x 10^{14} atoms/cm^2/s).

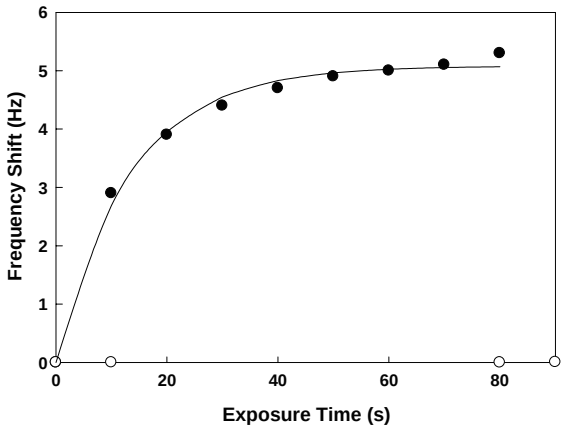

Figure 2 Frequency shift of the polyimide-QCM during ultraviolet exposures (4.5 mW/cm^2 at normal incidence). ●: pre-exposed to atomic oxygen (2.3 x 10^{18} atoms/cm^2), ○: without pre-exposure to atomic oxygen. Note that atomic oxygen was not exposed during the measurements. Solid line is the best-fit curve using equation 1.

ultraviolet fluxes can be changed by rotating the sample [2]. The maximum atomic oxygen flux and ultraviolet flux at the sample position were 6.0 – 14.0 x 10^{14} atoms/cm^2/s and 0.55 mW/cm^2, respectively. The erosion rate of polymer film was calculated from the resonant frequency of QCM during the atomic oxygen beam and/or ultraviolet exposures. The sample temperature was kept at 311 K during the experiment by the temperature-controlled circulating water system.

3. Results and discussion

3.1 Atomic oxygen-induced polymer erosion

In the experiment reported herein, the relative intensity of atomic oxygen and ultraviolet was adjusted by rotating the QCM sample along with the axis, which is perpendicular to the axes both to atomic oxygen and ultraviolet. However, in this experimental configuration, the incident angle of atomic oxygen at polymer surface is changed when relative atomic oxygen/ultraviolet intensity is adjusted. Therefore, it is necessary to investigate the effect of incident angle of atomic oxygen and ultraviolet on the polymer erosion prior to the quantitative analysis of synergistic effect of atomic oxygen and ultraviolet.

From the previous result regarding the incident angle dependence of atomic oxygen on the erosion of polyimide-coated QCM, it was observed that the erosion rate is linear with time in every incident angle and the erosion rate decreased with increasing incident angle with following a cosine distribution [3]. The experimental result on the incident angle dependence of atomic oxygen-induced erosion of polyethylene showed a similar tendency with those reported on polyimide film as shown in Figure 1 [4]. However, it is not a simple cosine distribution ($\cos^{0.87}\theta$) compared with polyimide ($\cos^{1.0}\theta$). The fact that the incident angle dependence of the erosion rate follows closely to a cosine law indicates that the erosion rates of polyethylene and polyimide are both basically proportional to the effective flux of atomic oxygen. It was thus concluded that the reaction yield of atomic oxygen with these polymers is identical to the incident angle.

It was observed from atomic force microscopy that the surfaces of polymers were roughened by atomic oxygen exposure. Therefore, an actual incident angle of oxygen atom to a surface moiety is not directly related to macroscopic incident angle because surface is not atomically flat due to the presence of microscale roughness. Thus, the macroscopic erosion rate of polymer is simply reflected the effective fluence of atomic oxygen which follows cosine law with the macroscopic incident angle.

3.2 Ultraviolet-induced polymer erosion

Effect of incident angle of ultraviolet radiation on polyethylene and polyimide erosion was also studied [2]. Figure 2 shows the frequency shift of the polyimide-coated QCM after ultraviolet exposures at normal incidence (solid circle). The flux of 172 nm ultraviolet radiation was 4.5 mW/cm^2 at normal incidence. Note that the sample surface was exposed to atomic oxygen (2.3 x 10^{18} atoms/cm^2) prior to ultraviolet irradiation in order to avoid the non-linear phenomena. As shown in Figure 2, resonant frequency of the QCM was increased when ultraviolet

starts irradiating due to desorption of the adsorbed gaseous molecules. However, the slope of the curve gradually decreases with time. It has been analyzed that the curve can be fit in the form of

$$\Delta f = A[1-\exp(-ct)] \qquad (1),$$

where Δf is the frequency shift of QCM, A and c are the constant, and t is the exposure time of ultraviolet radiation. The fact that the experimental data was fit by the equation (1) suggests that the surface oxidizing species (CO or CO_2) are desorbed by ultraviolet exposure (photo-induced desorption). This is confirmed by the fact that the no mass loss was detected by the ultraviolet exposure without pre-oxidation process (open circle in Figure 2). The incident angle dependence of ultraviolet radiation was also examined. By increasing the incident angle of ultraviolet radiation, desorption rate of the oxidized species is decreased. This is explained by the decrease in effective photon flux of ultraviolet radiation.

In contrast, polyethylene showed a different tendency of mass change with ultraviolet exposure. Figure 3 showed a typical mass change of polyethylene under 172 nm ultraviolet exposure (4.5 mW/cm^2). Mass of the polyethylene shows a decrease with exposure time. Unlike polyimide, the saturation of mass loss is not obvious in polyethylene. The absolute mass lost by the ultraviolet exposure was much greater than that of polyimide. This mass loss property suggests that not only the adsorbed gaseous molecules, but also the polyethylene structure is decomposed by the 172 nm ultraviolet exposure.

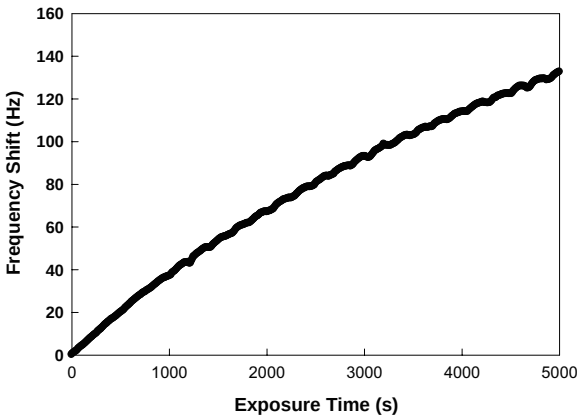

Figure 3 Frequency shift of the polyethylene- QCM during ultraviolet exposures. Ultraviolet intensity: 4.5 mW/cm^2. The sample surface was oxidized by atomic oxygen prior to the ultraviolet exposure (5.9 x 10^{17} atoms/cm^2).

3.3 Synergistic effect of atomic oxygen and ultraviolet

Atomic oxygen and ultraviolet beams irradiated polymer-coated QCM simultaneously and the erosion rate was recorded by the resonant frequency of QCM. The maximum atomic oxygen flux and ultraviolet flux at the sample position were 6.8 x 10^{14} atoms/cm^2/s and 0.55 mW/cm^2, respectively. Figure 4 (a) and (b) show the erosion rates of polyimide and polyethylene under simultaneous atomic oxygen and ultraviolet exposure condition as a function of incident angle of atomic oxygen. The abscissa is the incident angle of

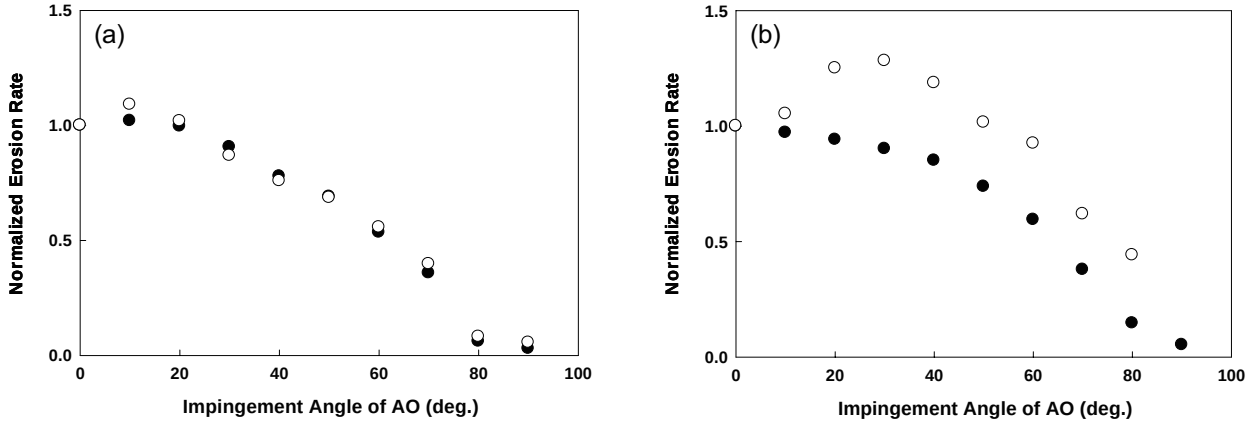

Figure 4 Normalized erosion rates of polyimide and polyethylene during atomic oxygen exposure (●) and simultaneous atomic oxygen and ultraviolet exposure (○). (a): polyimide, atomic oxygen flux: 6.8 x 10^{14} atoms/cm^2/s, ultraviolet flux: 0.40 mW/cm^2, (b): polyethylene, atomic oxygen flux: 6.0 x 10^{14} atoms/cm^2/s, ultraviolet flux: 0.55 mW/cm^2.

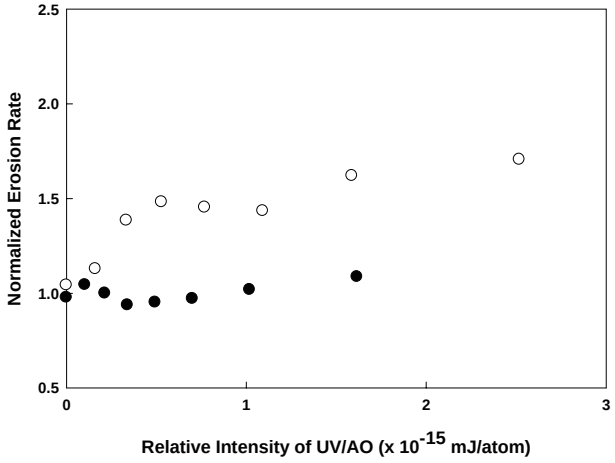

Figure 5 The relationship between the relative intensity of UV/AO and the normalized erosion rate. (○): polyethylene, (●): polyimide.

atomic oxygen; i.e., the incident angle of 0° means 100 % atomic oxygen and 0 % ultraviolet, and the incident angle of 90° means 0 % atomic oxygen and 100 % ultraviolet. The longitude is the normalized erosion rate. If no ultraviolet effect was observed, the data points with ultraviolet exposure (open circle) should follow the cosine function. This is the case for polyimide (Figure 4 (a)). In contrast, the erosion rates with ultraviolet exposure (open circle) do not follow cosine function and are 30 to 100 % greater than those without ultraviolet exposures (solid circle) in the case of polyethylene (Figure 4 (b)). It was clear that simultaneous ultraviolet exposure affects the atomic oxygen-induced erosion of polyethylene. The relationship between the relative intensities of ultraviolet per atomic oxygen (UV/AO ratio) and the normalized erosion rate was replotted in Figure 5. The erosion rate of atomic oxygen-induced polyethylene was enhanced 30-80 % at the relatively low UV intensities at UV/AO ratio of 0.5-2.6 x 10^{-15} mJ/atom, where polyimide does not show any enhancement of mass loss with ultraviolet exposure. As reported elsewhere [2], the synergistic effect of atomic oxygen and 172 nm ultraviolet on polyimide was obvious when ultraviolet intensity is higher than 1 x 10^{-14} mJ/atom. However, it was not obvious in the UV/AO ratio lower than 10^{-15} mJ/atom, as demonstrated in Figure 5. In contrast, polyethylene shows a clear synergistic effect of ultraviolet irradiation even in the UV/AO ratio lower than 10^{-15} mJ/atom.

4. Conclusion

Synergistic effects on atomic oxygen-induced erosion of polyimide and polyethylene with 172 nm ultraviolet were investigated using QCM. In order to change the relative intensity of atomic oxygen and ultraviolet, the polymer sample on QCM was rotated with an axis perpendicular both to the axes of atomic oxygen and ultraviolet. It was found that no ultraviolet-induced erosion was observed for polyimide without atomic oxygen exposure. In contrast, a clear mass loss was obvious when polyethylene was exposed to 172 nm ultraviolet even without atomic oxygen. It was observed that the atomic oxygen-induced erosion of polyethylene increased 30-80 % by a simultaneous ultraviolet exposure in the UV/AO ratio of 10^{-15} mJ/atom. The increase in mass-loss was considered due to the photo-induced decomposition of carboxyl group and C-C backbone of polyethylene. Since the synergistic effect for polyethylene was obvious at the ultraviolet intensities one order lower than that for polyimide, it was concluded that polyimide is a better material as a witness sample for measuring atomic oxygen fluence in LEO from the viewpoint of the synergistic effect with vacuum ultraviolet [5].

Acknowledgments

This study was partially supported by the Grant-in-Aid for Scientific Research from the Ministry of Education, Culture, Sports, Science and Technology, Japan and the Space Utilization Promotion from the Japan Space Forum. Financial support from Kawanishi Memorial Shinmaywa Education Foundation is also acknowledged.

References

[1] “Standard practices for ground laboratory atomic oxygen interaction evaluation of materials for space applications”, ASTM Designation: E2089-00.

[2] Yokota, K., Ohmae, N. and Tagawa, M., “Effect of relative intensity of 5 eV atomic oxygen and 172 nm vacuum ultraviolet in the synergism of polyimide erosion.” High Performance Polymers, Vol.16, pp.221-234, 2004.

[3] Yokota, K., Tagawa, M., and Ohmae, N., “Impingement Angle Dependence of Erosion Rate of Polyimide in Atomic Oxygen Exposures,” Journal of Spacecraft and Rockets, Vol.39, No.1, pp.155-156, 2002.

[4] Tagawa M., Yokota K., Ohmae N., "Synergistic study on atomic oxygen-induced erosion of polyethylene with 172 nm vacuum ultraviolet," Journal of Spacecraft and Rockets, Vol.41, No.3, pp.345-349, 2004.

[5] Yokota K. and Tagawa M., "Comparison of polyethylene and polyimide as a fluence monitor of atomic oxygen" Journal of Spacecraft and Rockets, Vol.44, No.2 (2007) pp.434-438

衛星用表面材料の光電子放出電流分布の測定

岡野　拓哉，山納　康，小林　信一（埼玉大学）
仁田　工美（JAXA）

Measurement of distribution of photoemission current of surface materials used for satellite

Takuya Okano (Saitama University), Kumi Nitta (JAXA), Yasushi Yamano, Shinichi Kobayashi (Saitama University)

Some kinds of film and paint-type coating materials are used as a thermal control material for the artificial satellite. It is necessary to survey the characteristics of the thermal, optical, mechanical and electrical properties about them. This report describes results of measurement of the photoemission current from the film and paint-type coating materials excited by ultraviolet-light.

The used film samples were four kinds of materials (germanium coating, ITO coating, nonconductive) and the used coating samples were seven kinds of white paint materials (inorganic conductive, inorganic nonconductive, silicon based conductive, silicon based nonconductive) which are used for the artificial satellite. The following measurement results were obtained. Photoemission sites on each sample were distributed into active area and inactive area. Photoemission currents value of conductive samples are larger than those of nonconductive samples except for white paint B. Photoemission currents of Ge-coated films are uniformly distributed all over the sample. The current values are less than those of ITO-coated film. Photoemission currents value of silicon based samples were smaller than those of inorganic samples. Distributions of active area and inactive area about photoemission sites on white paint materials is greater than those of film samples.

キーワード：放出型電子顕微鏡、光電子放出、電子電流
Keywords: Electron emission microscope, Photoelectron emission, electron current

１．　まえがき

現在、人工衛星の表面材料に太陽からの電磁波や高エネルギー粒子が入射することにより帯電・放電が生じ、それらが材料の劣化や機器の故障を引き起こしていることが報告されている。そのため、宇宙環境下での衛星の電位解析のために、様々な材料における光電子放出特性を調べる必要がある。本報告では衛星用表面の熱制御材料として用いられる導電性・非導電性フィルムと白色系塗料について、紫外線照射時の光電子放出電流値の分布を測定した結果について述べる。

２．　実験装置および実験方法

図１に、今回使用した放出型電子顕微鏡が装備された実験装置の概略図を示す。実験用真空容器内の圧力はイオンポンプにより常に 10^{-6}Pa 台に維持されている。試料台は、真空容器外部に設けられたパルスモータにより放出型電子顕微鏡の対物レンズ前面を走査することができるようになっており、試料表面上の電子放出点の拡大像を観測しながら電子放出点の分布を調べることができる。また、蛍光板を動作させる高電圧電源と接地の間には電流計が接続されており、蛍光板に入射する電子電流を測定することができる。この電子電流を測定しながら、試料を走査することにより、試料表面の電子放出特性の分布を調べることが可能である。

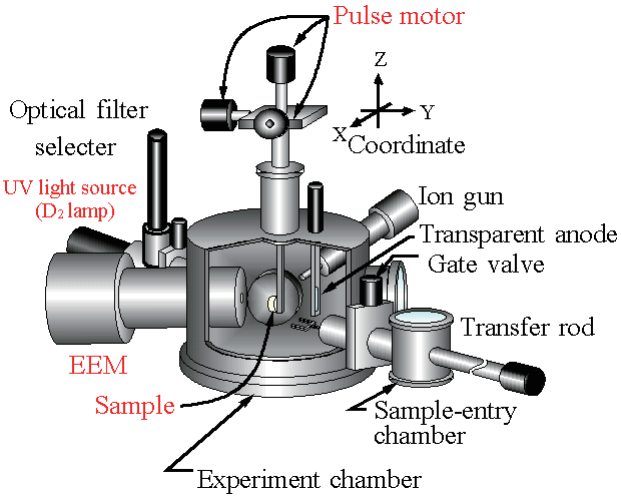

図１　実験装置概略図

図２に、放出型電子顕微鏡の概略図を示す。この顕微鏡は、文献[1],[2]に基づき当研究室で設計し製作したものである。図に示されるように、本顕微鏡は三つのユニポテンシャルレンズ、MCP、および蛍光板からなる。試料の電子放出点は、試料と対物レンズの孔とで構成される界浸レンズにより対物レンズ内に結像し、その像を後段のレンズで拡大し、MCP 上に結像させる。MCP で電子増倍の後蛍光板に投影された像を真空容器外部からビデオカメラにより観測する。

真空紫外光源は 浜松ホトニクス　L1835　出力 150W を用いており、波長 115～400nm の UV 域に連続スペクトルを有している。図３に光源のスペクトル強度を示す。真空紫外光は、光源から放射される光の発散を軽減するために LiF 製のレンズによりビーム化した後、顕微鏡の対物レンズに設けられた孔を通して、試料に照射される。真空紫外光源には、MgF_2 の窓が用いられており、また、光路に LiF のレンズが使用されていることから、照射光のエネルギーの最大値は約 10.8eV である。この光路中には光学フィルターも設けられており、照射（波長）エネルギーを選択することができる。今回の実験ではフィルターを用いていないので、10.8eV 以下のスペクトルの光が試料に入射している。

今回使用した試料を表１に示す。試料はそれぞれ非導電性と導電性に分かれており、塗料系の試料はさらに無機系と Si 系に分かれている。これらの試料はそれぞれ図４に示すように金が試料表面 6mm 角の部分を除き蒸着されている。金を蒸着したのは、金を参照電極として用いることにより、より正確な測定を行うことができるようにするためである。ただし、非導電性の試料および塗料系の試料については金蒸着を行っていない。これらの試料は背後電極上にカーボンテープと導電性の接着剤を用いて固定し使用している。

次に、実験の手順について示す。測定する場所は、図５のように試料中央の 6mm 角の部分である。放出型電子顕微鏡の三つのユニポテンシャルレンズには試料表面を約 250 倍に拡大することができるような電圧がそれぞれ印加されており、蛍光板上には試料表面の 0.12mm の部分の像が投影されている。試料を 0.2mm ステップで x － z 方向にラスタースキャンしながら蛍光板に接続されている微小電流計によってそれぞれのサンプルで電流値の測定を行い、実験結果とする。

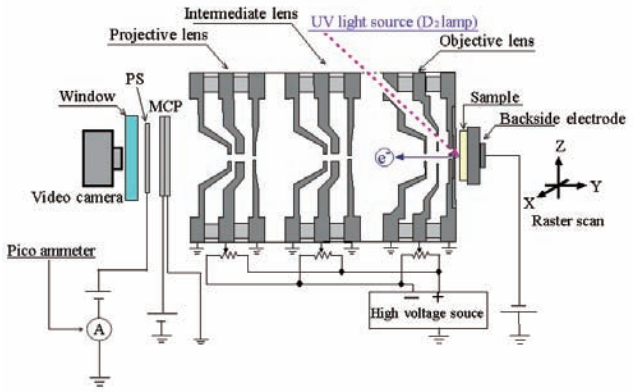

図２　放出型電子顕微鏡概略図

３．　実験結果

各試料の光電子電流の分布を表したものが図６である。横軸が x 方向、縦軸が z 方向である。各セルの色により電流値の大小を表している。それぞれの試料は、中央の 3mm 角の部分を除き、表面に金が蒸着されているため、中央の ±1.5mm の部分が、それぞれの試料からの光電子放出電流を測定した部分であり、周りの部分は、金からの光電子放出電流を測定した部分となる。

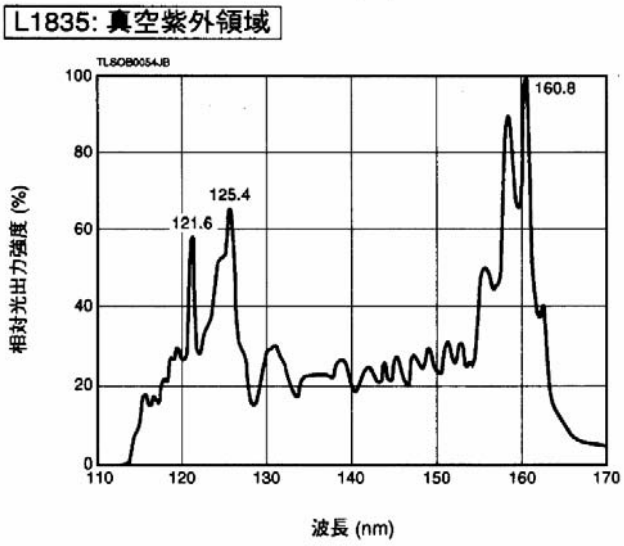

図３　放射スペクトル分布（カタログより参照）

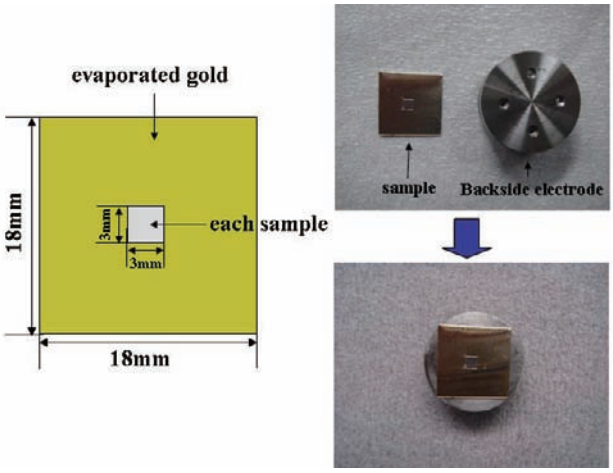

図４　試料の概略図

表１　実験で使用した試料

名称		導電性	体積抵抗率[Ωm]	特徴
熱制御剤 白色塗料	White paint A	非導電	≒10^{10}	無機系白色塗料
	White paint B		≒10^{6}	
	White paint C		≒10^{11}	Si 系白色塗料
	White paint D	導電	ー	無機系白色塗料
	White paint E		≒10^{6}	
	White paint F		≒10^{6}	
	White paint G		ー	Si 系白色塗料
熱制御フィルム	Film A (Ge-coated)		0.46(Ge)*	ポリイミドフィルム上にコーティング剤を塗布
	Film B (Ge-coated)			
	Film C (ITO-coated)		2～10×10^{3}(ITO)* (表面抵抗率)	フッ化樹脂フィルム上にコーティング剤を塗布
	Film D	非導電	ー	フッ化樹脂
シリコンA		導電	2.0×10^{-4}*	n型半導体
シリコンB			10	n型半導体
銅			1.6×10^{-8}*	純度：99.96%
鉄			8.7×10^{-8}*	純度：99.998%
チタン			4.2×10^{-8}*	純度：99.5%
アルミニウム			2.5×10^{-8}*	純度：99.999%
ニッケル			6.6×10^{-8}*	純度：99%
銀			1.5×10^{-8}*	純度：99.98%
金			2.0×10^{-8}*	-

*金属便覧および製品カタログ値参照、それ以外の材料の抵抗率は実測値[3],[4]

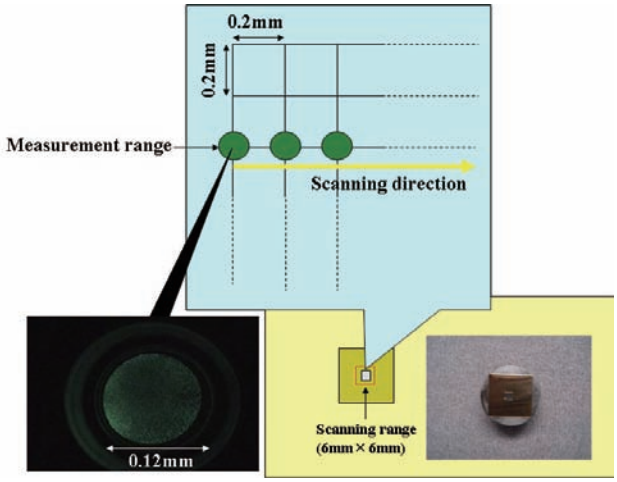

図５　測定範囲

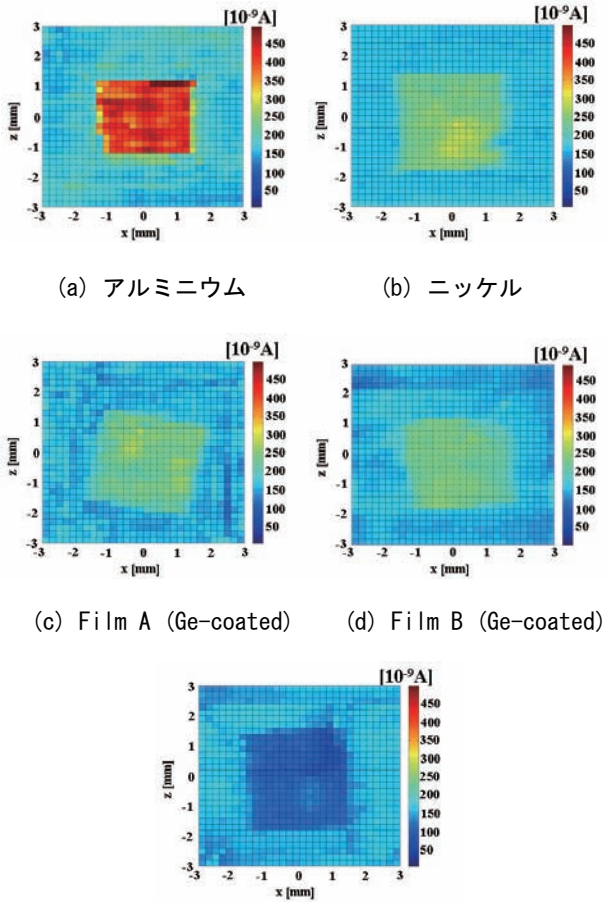

(a) アルミニウム　(b) ニッケル

(c) Film A (Ge-coated)　(d) Film B (Ge-coated)

(e) Film C (ITO-coated)

図６　各試料における電子電流値の分布

また、測定した電流値の平均値、標準偏差を試料ごとにまとめたものを表２に示す。

図６を見ると、衛星用表面材料、金属材料において、共に同一の材料を測定しているにもかかわらず光電子放出電流値は場所により違いが生じている。次に表２の光電子電流の平均値を見ると、導電性の試料のほうが非導電性の試料より電流値が大きく測定されていることが確認される（非導電性試料である White paint B を除く）。導電性フィルムにおける光電子電流値は表面がゲルマニウムコーティングされた試料を用いた Film A と Film B においてほぼ同じ値となっている。また、標準偏差は導電性フィルムにおいてゲルマニウムがコーティングされた試料よりも ITO がコーティングされた試料の方が電子が放出されやすい場所とされにくい場所の差が大きくなっている。これは、ITO コーティングが表面に一様にされていないか、酸化の程度が場所によって分布している可能性がある。

白色系塗料においては Si 系の試料は導電・非導電にかかわらず測定された電流が非常に小さく、無機系試料の光電子電流値よりも小さい値であるということが確認された。

また、白色系塗料と導電性フィルムの標準偏差は、白色系塗料の方が導電性フィルムよりも電子が放出されやすい場所とされにくい場所の差が大きくなっている。白色系塗料の場合、標準偏差が大きくなるのは試料の凹凸などが大きく関係しているためと考えられる。また、白色系塗料はその多くが体積抵抗率 $10^6\Omega$m 以上の試料であり、試料によっては場所により帯電が生じて、これが光電子放出特性に影響している可能性がある。

表２　各試料における光電子電流の測定値

名称	導電性	特徴	平均値[nA]	標準偏差[%]
White paint A	非導電	無機系	0.162	98.3
White paint B			26.4	38.5
White paint C		Si 系	0.070	110.6
White paint D	導電	無機系	49.4	40.7
White paint E			47.9	67.0
White paint F			8.28	48.5
White paint G		Si 系	0.334	16.6
Film A (Ge-coated)		―	234	6.1
Film B (Ge-coated)			230	5.8
Film C (ITO-coated)			100	12.3
Film D	非導電		0.484	46.2
シリコンA	導電		246	7.4
シリコンB			284	4.9
アルミニウム			419	8.6
銅			203	7.1
鉄			198	9.2
チタン			113	11.5
ニッケル			248	7.0
銀			170	4.1
金			158	4.3

４．　まとめ

・衛星用表面材料、金属材料において、共に同一の材料を測定しているにもかかわらず光電子放出電流値は場所により違いがあるということが確認された
・非導電性試料よりも導電性試料のほうが、非導電性試料 White paint B を除いて、光電子電流が大きく測定された
・導電性フィルムにおける光電子電流値は表面がゲルマニウムコーティングされた試料を用いた Film A と Film B においてほぼ同じ値となった
・導電性フィルムにおいてゲルマニウムがコーティングされた試料よりも ITO がコーティングされた試料の方が電子が放出されやすい場所とされにくい場所の差が大きい
・白色系塗料において、Si 系試料の光電子電流値は、無機系試料の光電子電流値よりも小さい
・白色系塗料の方が導電性フィルムよりも電子が放出されやすい場所とされにくい場所の差が大きい

謝辞

本研究を進めるにあたりまして、独立行政法人情報通信研究機構から白色塗料の提供を受けましたことを、深く感謝いたします。

文献

[1]A. D. Archer, “Spectroscopic Studies of Field-Induced Electron Emission from Isolated Microstructures”, PhD Thesis, Aston University, 1992

[2]Rod V Latham, “High Voltage Vacuum Insulation; Basic Concepts and Technological Practice”, pp.82-84, Academic Press, London, 1995

[3] 日本金属学会:「金属便覧」,丸善,pp.2-5 (1960)

[4] 高橋，山納，仁田，小林:「GPM/DPR プロジェクトで使用される熱制御材料の表面抵抗率・体積抵抗率の測定」,第 3 回宇宙環境シンポジウム講演論文集,pp.147-150 (2006)

衛星用絶縁材料の真空中における表面抵抗率・体積抵抗率測定

小宮山 丈行(埼玉大学)，仁田 工美(JAXA)，山納 康(埼玉大学)，小林 信一(埼玉大学)

Measurement of surface and volume resistivity of insulator materials for satellites in vacuum condition

Takeyuki Komiyama (Saitama University), Kumi Nitta (JAXA) ,
Yasushi Yamano (Saitama University), Shinichi Kobayashi (Saitama University)

This paper investigates surface and volume resistivity of insulator materials used for the artificial satellites. Measurements were carried out under vacuum and atmospheric conditions respectively. The measured materials are two kinds of white paints which are used for the antena portion of satellites, two kinds of glasseswhich are used for the cover glass of solar panel and a polyimide film which are used for the thermal control material on the satellite. It was confirmed that the surface resistivity for almost all of the insulator materials except for polyimide film under vacuum condition was higher than that under atmospheric condition. Desorption of moisture vapor from the insulator surface is the main cause of the increase of the surface resistivity in vacuum. On the other hand, their volume resistivity except for the white paints had no difference between vacuum and atmospheric conditions. White paints under vacuum condition showed the higher volume resistivity than that of atmospheric condition.

キーワード：真空，表面抵抗率，体積抵抗率
Keywords：Vacuum, Surface resistivity, Volume resistivity

1. はじめに

人工衛星のアンテナ部分に使われる熱制御材料や太陽電池パネルのカバーガラスなど宇宙機の設計に必要な絶縁材料の選定には，機械的特性，熱光学特性，そして電気的特性などの物性値が必要である。

一般的に絶縁材料の表面抵抗率は,その周囲環境によって大きく変動し,特に真空環境下では大気中の値と比べて大きく異なり,材料によりその変動幅も異なることが予想される。

本研究では,アンテナ部に使用される白色塗料および太陽電池パネルのカバーガラスやポリイミドフィルムなどの絶縁材料の表面抵抗率・体積抵抗率を大気中,真空中でそれぞれ測定し,その変化を調査した。

2. 測定試料

測定に使用した試料は，２種類の白色塗料，２種類の石英ガラス,およびポリイミドフィルムで,また,比較として真空中の代表的な絶縁材料であるアルミナセラミックスも用意した。白色塗料の特性を表１に,石英ガラス,ポリイミドフィルム,アルミナセラミックスの特性を表 2 に示す。白色塗料は非導電性で製造メーカーの異なる無機系とシリコン系の 2 種類のもので,石英ガラスもそれぞれ製造メーカーが異なるものである。

表１　白色塗料の特徴

名称	導電性	特性	膜厚[μm]
White paint A	非導電性	無機系白色塗料	144
White paint B	非導電性	Si 系白色塗料	179

表２　各絶縁体の特徴

名称	特性	厚さ[μm]
Glass A	石英ガラス	111
Glass B		106
Polyimide Film	ー	32
Alumina Ceramics HA-95	純度：95%	5000

3. 実験方法・装置

表面抵抗・体積抵抗測定試験は大気圧から 10^{-2}Pa 程度の真空環境下で測定可能な抵抗率測定容器を用いて実験を行った。

本実験では各試料に対して,抵抗率測定用に銀ペーストを用いて電極を作製した(1)。抵抗率測定用の電極の概略図を図１に,各電極の寸法を表3に示す。

測定回路とそれぞれの抵抗率の算出方法は,参考文献(1)を用い,各試料について大気中と真空中で抵抗率の測定を行った。

4. 結果および考察

表 4 に各試料の真空中，大気中の表面抵抗率を示す。ほとんどの試料の表面抵抗率は，上昇幅はさまざまであるが大気中に比べて真空中において大きく増加した。これは真空中では試料表面に吸着している水分が脱離したためと考えられる。ポリイミドフィルムは大気中,真空中で表面抵抗率はほぼ変わらない結果となった。

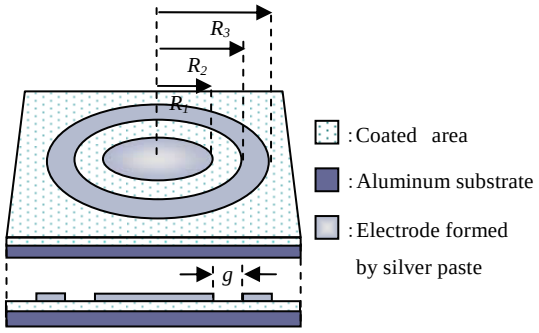

図１　電極作製後の白色塗料の概略図

表３　電極作成後の試料の寸法(単位：[mm])

R_1	R_2	R_3	電極間距離 g
5.0	7.0	10.0	2.0

表 4　各試料の表面抵抗率(単位：[Ω])
(100V 値, ただしアルミナ HA-95 のみ 1000V 値)

測定試料	大気中	真空中
Alumina Ceramics HA-95	2×10^{14}	1×10^{17}
White paint A	4×10^{9}	9×10^{11}
White paint B	5×10^{13}	5×10^{15}
Glass A	5×10^{15}	2×10^{16}
Glass B	2×10^{16}	$>2\times10^{17}$
Polyimide film	2×10^{16}	1×10^{16}

表 5　各試料の体積抵抗率(単位：[Ωm])
(100V 値, ただしアルミナ HA-95 のみ 1000V 値)

測定試料	大気中	真空中
Alumina Ceramics HA-95	1×10^{14}	2×10^{14}
White paint A	5×10^{6}	2×10^{10}
White paint B	2×10^{10}	3×10^{11}
Glass A	2×10^{13}	3×10^{13}
Glass B	1×10^{13}	1×10^{13}
Polyimide film	9×10^{14}	6×10^{14}

表 5 に各試料の真空中, 大気中の体積抵抗率を示す。体積抵抗率は真空中と大気中で白色塗料を除くすべての試料においてほとんど変わらない値となったが, 白色塗料だけは大気中に比べ真空中では大きく増加した。

真空中での表面抵抗率が, 真空容器内の圧力でどのように変化していくのかを調べるため, 次のような実験を行った。試験容器内を大気圧にし, 真空ポンプで 10^{-2}Pa 程度の真空まで排気した後, He ガスを容器内に導入して圧力を大気圧まで戻し, その後容器内を大気曝露した。その間にいくつかのポイントで表面抵抗率測定を行った。このとき試料にはアルミナ HA-95 を用いた。

図 4 に示されるように, 大気圧から 1.0×10^{4}Pa に容器内圧力を低下させていくと, 容器内圧力の低下とともに表面抵抗率が増加した。一方, 容器内圧力を 1.0×10^{4}Pa からさらに下げても, 表面抵抗率は増加することなく, ほぼ一定の値を示した。その後, 排気した状態から大気圧になるまで He ガスを導入すると, 同図に示すように表面抵抗率は減少せず, 真空環境の表面抵抗率と同様の値を示した。さらにその後容器内に大気を導入すると表面抵抗率は低下した。このことから, 大気中の表面抵抗率の値には周囲環境の水蒸気とその吸着量が大きく関わっている可能性があることがわかる。

一方, 表 5 に示すように体積抵抗率は、白色塗料以外は大気中と真空中でほとんど変化が見られなかった。これは, 体積抵抗率が絶縁体内部に流れる電流から求められ, これらは材料固有の値であり, 周囲環境の影響を受けないためである。しかし, 白色塗料だけは, 体積抵抗率の値が真空中と大気中とで大きく異なった。これについて, より詳細に調べるため, 体積抵抗率の容器内圧力依存性を調べた。図 5 に白色塗料 A の場合の容器内圧力と体積抵抗率の関係を示す。最初の大気圧条件下では図の一番右下の点で, 体積抵抗率は $1\times10^{7}\,\Omega$m であった。

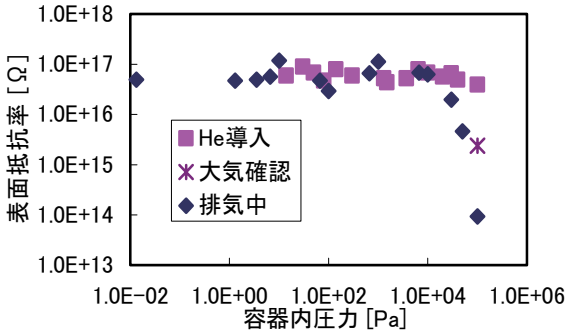

図 4　容器内圧力と表面抵抗率の関係(HA-95)

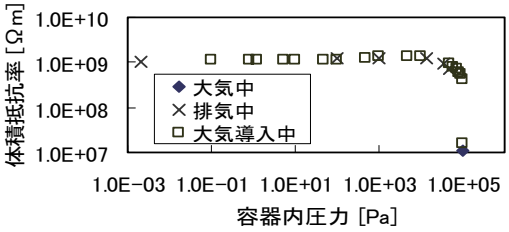

図 5　容器内圧力と表面抵抗率の関係(White paint A)

容器内圧力を 1.3×10^{4}Pa まで低下させると体積抵抗率が $1\times10^{9}\,\Omega$m に増加し, その後さらに容器内圧力を低下させても, 体積抵抗率に変化は無かった。真空環境下では大気圧時に比べ体積抵抗率が 2 桁ほど急増した。その後, 大気を導入して容器内圧力を増加させると, 1×10^{4}Pa 以上から体積抵抗率に減少が見られ, さらに大気圧まで戻したところ, 体積抵抗率は $2\times10^{7}\,\Omega$m となった。このことから白色塗料 A は大気圧に近い圧力で体積抵抗率に変化が起こることが確認された。白色塗料 A は真空中になると塗料内の水分が抜けたことや, 塗料の状態になんらかの変化が起きたことが予想され, 試料周囲の環境の影響を受けやすいことが考えられる。

5. まとめ

真空中の表面抵抗率は, 材料によってその上昇率はさまざまであるが大気中の値よりも増加することが明らかになった。本実験においてはポリイミドフィルムでは, 表面抵抗率が真空中と大気中とで変化が見られなかった。一方、体積抵抗率は, 白色塗料を除くすべての材料で真空中と大気中とで同じ値を示した。白色塗料はその値が真空中で増加することが明らかになった。

謝　辞

本研究を進めるにあたりまして,独立行政法人情報通信研究機構から白色塗料の提供を受けましたことを,深く感謝いたします。

文　献

(1) 日本規格協会編:「JIS ハンドブックセラミックス」, Vol.35, pp.140-207 (2002)

絶縁体への電子線照射効果の各種光学特性による評価

廣川　紫月*　　西川　宏之*　　三宅弘晃**

Optical study on the degradation phenomena of insulators under electron beam irradiation

Shizuki HIROKAWA*, Hiroyuki NISHIKAWA*, Hiroaki MIYAKE**

We studied charging and formation mechanisms of defects in insulators such as glasses and polymers irradiated by 20 keV electron beam. We performed cathodoluminescence (CL) and photoluminescence (PL) studies on insulator to understand the degradation phenomenon of insulators under electron beam irradiation including charging of insulators in outer space.

キーワード：ガラス，高分子材料，電子線，帯電，カソードルミネッセンス
Keywords：glass, polymer, electron-beam, charging, cathodoluminescence

1.　はじめに

宇宙環境下にある宇宙機（人工衛星等）は地球磁気圏の磁場、電場、プラズマ、粒子線（電子線、陽子線、α線、重粒線等）、電磁波（X線、γ線、紫外線、可視光、赤外線、マイクロ波等）、原子状酸素等による複合環境の中、活動を行っている。そのため宇宙機の各部品の劣化や太陽電池にあるカバーガラスの帯電等を引き起こす[(1)(2)]。

本研究の目的は様々な光学的測定法から宇宙機に使用されている材料の劣化現象を解明し、宇宙環境下効果の基礎理解をすることである。そのためまず私たちは電子線に注目をし、宇宙機に使用されているガラスや高分子材料等の絶縁材料に電子線照射し実験を行った。今回、ガラスや高分子材料に電子線を照射するために走査型電子顕微鏡（SEM, Shimadzu, SSX550）を用いた。さらに帯電も含む絶縁体の劣化現象を解明することが可能なカソードルミネッセンス（CL）測定法を用いた。この測定法は試料に電子線照射したことにより発生する光を測定するもので、SEMのチャンバー内で行うことにより大気の影響を受けずにその場測定できるという利点がある。今回はCLスペクトル測定を複数行い、照射量に対するCL発光強度測定も行った。

2.　CLの原理

一般に絶縁物に電子やイオンなどの高エネルギーの粒子が入射すると基底状態から受け取ったエネルギーにより、価電子が励起され励起子および電子・正孔対が発生する。この際生じた励起子および電子・正孔対は、再結合する時に発光を伴うことがある。特に高エネルギーの電子線照射による物質の発光現象をカソードルミネッセンス(Cathodoluminescence, CL)という（図1）。また絶縁体中に欠陥や不純物などの電荷捕獲中心がある場合、励起子や電子・正孔対は再結合せずに捕獲中心に捕獲され、発光を示すことがある。したがって電子線照射下でCLを測定することにより、宇宙空間などの極限環境下での帯電も含む絶縁体の劣化現象を解明することが可能となると考えられる[(3)]。

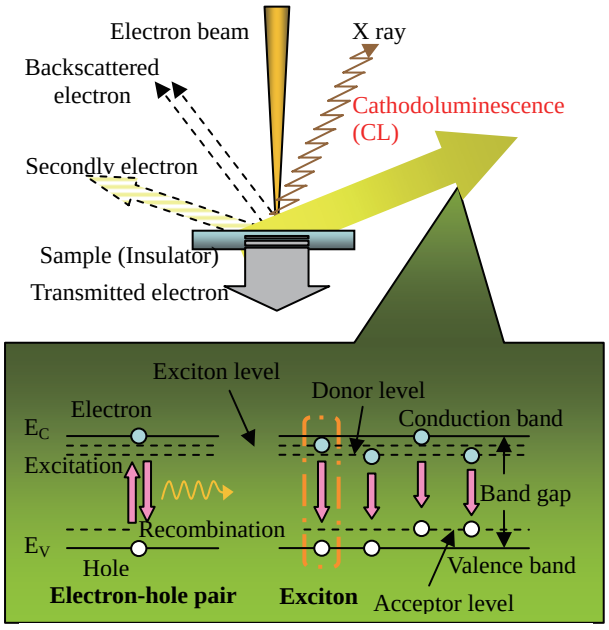

Figure 1.　Mechanism of CL

*　芝浦工業大学工学部電気工学科
〒135-8548　東京都江東区豊洲 3-7-5
Department of Electrical Engineering, Shibaura Institute of Technology, 3-7-5 Toyosu, Koto-ku, Tokyo 135-8548
**　宇宙航空研究開発機構
〒305-8505　茨城県つくば市千現 2-1-1
Japan Aerospace Exploration Agency (JAXA)
2-1-1 Sengen, Tsukuba-shi, Ibaraki 305-8505

Table 1.　Impurity content and size of glasses

	Al	Ca	Ti	Na	OH	Size (mm^3)
ES (ppm)	0.1	0.1	<0.01	0.05	1200	10 x 10 x 1.000
	Al_2O_3		B_2O_3		Na_2O	
Pyrex (%)	2.3		12.7		4.0	10 x 10 x 1.000
CMG	Borosilicate glass, doped with cerium oxide					10 x 10 x 0.150

ES: Synthetic quartz glass (by TOSOH Co., Ltd.), Pyrex: Borosilicate glass (by IWAKI Co., Ltd.), CMG: Borosilicate glass (by Thale)

Table 2.　Structural formula of polymers

	Structural formula	Size (mm^3)
PMMA	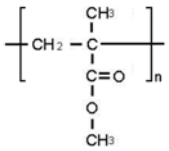	10 x 10 x 1.000
FEP	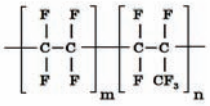	10 x 10 x 0.125
Upilex	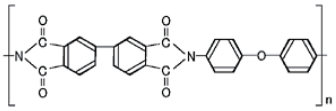	10 x 10 x 0.125

PMMA: Acrylic (by Goodfellow Co., Ltd.), FEP: Fluorine (by Sheldah), Upilex: Polyimide (Ube Industries, Ltd.)

3.　実験方法

カソードルミネッセンス励起源として走査型電子顕微鏡（Shimadzu, SSX550）を用いた。電子線照射時の SEM の加速電圧は 20 kV、倍率 500 倍（150×200 μm^2）にて行った。ビーム電流値はファラデーカップを用いて測定したところ、ガラスでは約-100nA で高分子材料では約-1.33nA であった。CL 測定では図 1 のような SEM に設置した CL 測定用分光器（GATAN-UK, MonoCL3）を使用した。

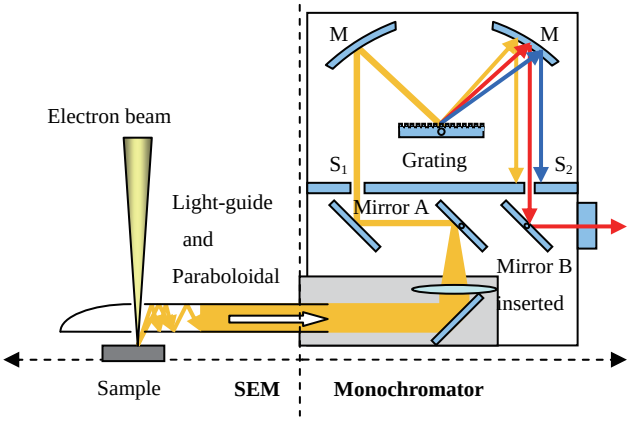

Figure 2.　Experimental setups for electron-beam irradiation and CL measurements

図 2 に CL 測定方法の手順を示す。1 回の CL スペクトル測定には 6 分 36 秒を要し、測定後 Grating が初期位置に戻るまで 1 分 6 秒を要するので、10 回の連続測定により電子線の総照射時間は 76 分 40 秒となる。今回の照射量は①式により 1.53×10^4 C /m^2 となる。

また照射基板に用いたものは大きく分けるとガラスと高分子になる。ガラスの種類はシリカガラスである ES（日本石英製）そしてホウケイ酸ガラスである Pyrex と CMG である。各ガラスの不純物含有量と形状は表 1 に示し、各高分子の組成と形状は表 2 に示した。

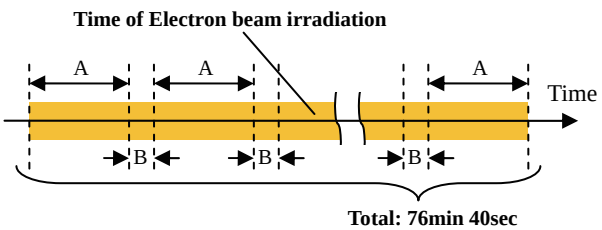

A: CL spectra measurement: 6min 36sec
B: Time interval between each CL measurement: 1min 6sec

Figure 3.　Time sequence of electron beam irradiation

$$照射量(C/m^2)=\frac{ビーム電流(C/\mathrm{sec})\times\quad 照射時間(\mathrm{sec})}{照射面積(m^2)}\cdots(1)$$

4. 実験結果

図 4 に各ガラスの CL スペクトル測定の結果、および図 5 に各照射量に対する CL 発光強度の変化を示す。図 4(a)において試料 ES では 290 nm 帯、460 nm 帯および 650 nm 帯にピークが確認できた。この 290nm 帯と 460nm 帯のピークは式 (2)により生成された酸素欠乏性欠陥(Oxygen Deficient Center: ODC, ≡Si－Si≡)による発光であり、そして 650 nm 帯のピークは式 (3)より不純物 OH から生成された非架橋酸素ラジカル(Non-Bridging Oxygen Hole Center: NBOHC, ≡Si-O˙, ただし“˙”は不対電子)であることが報告されている[4]。図 6(a)および(b)に ODC と NBOHC を図に示した。

$$\equiv Si－O－Si\equiv \rightarrow \equiv Si－Si\equiv + O \quad \cdots\cdots (2)$$

$$\equiv Si－OH \rightarrow \equiv Si\text{-}O˙ + .H \quad \cdots\cdots (3)$$

また図 4(b)において試料 Pyrex では 380nm 帯、410nm 帯、460nm 帯および 745nm 帯にピークが確認できた。この中の 380nm 帯のピークは Pyrex に添加されている Al と Na による発光ではないかと考えられる[5]（図 6(c)）。さらに 460nm 帯ピークが 410nm 帯のピークに埋もれていることが分かる。この 460nm 帯は試料 ES のピークと同じものと考えられる。

図 4(c)において試料 CMG でも 380nm 帯、410nm 帯、460nm 帯および 745nm 帯にピークが確認できた。これらのピークは、同様の borosilicate glass である試料 Pyrex と同じ理由で発光していると考えられる。

さらに図 5 では図 4 で確認したピークが照射量によってどのように変化するかを示した。図 5(a)において ES の 460nm 帯では CL 強度は一度上昇し照射量がある一定まで達した後飽和するという現象を確認できた。試料 ES の 460nm 帯での上昇過程は酸素欠乏性欠陥（ODC）などの欠陥発生過程を反映し、飽和する過程は欠陥発生と欠陥消滅が均衡した平衡状態にあるなったことを示すと考えられる[6]。また図 5(b)において試料 Pyrex の 380nm 帯では CL 発光強度が減衰している。この減衰過程は添加物である Al と Na が電子捕獲し、内部帯電した結果、電子線の試料への入射を妨げるためと考えられる。図 5 (c)において試料 CMG の 410nm 帯と 460nm 帯では、いったん CL 発光強度が減衰するがその後、上昇または飽和に転じる。この電子線照射初期の減衰は支配的な発光ピークである 410nm の減衰が影響しているものだと考えられ、上昇および飽和過程は試料 ES においても観測されている 460nm 帯での上昇と飽和過程が影響していると考えられる。これは 2 つのピークが互いに近接し重畳しているためと考えられ、波形分離により詳細に調べる必要がある。

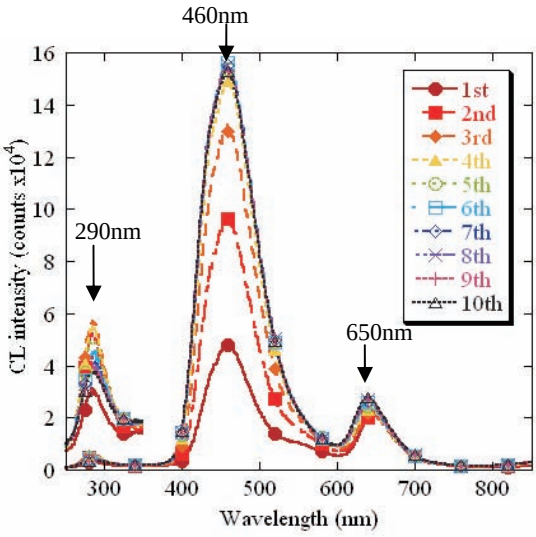

(a) ES glass

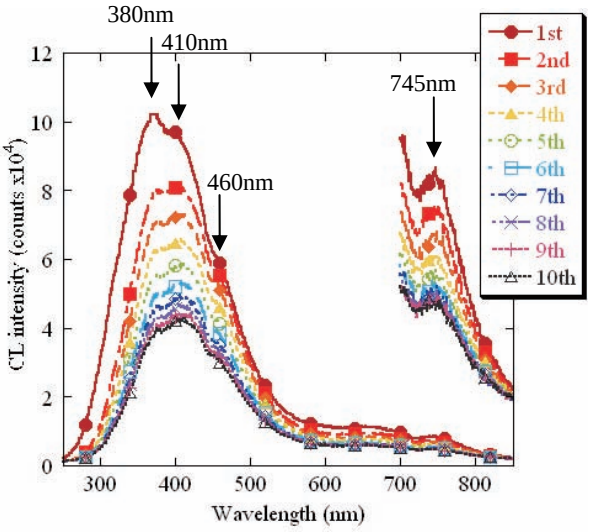

(b) Pyrex glass

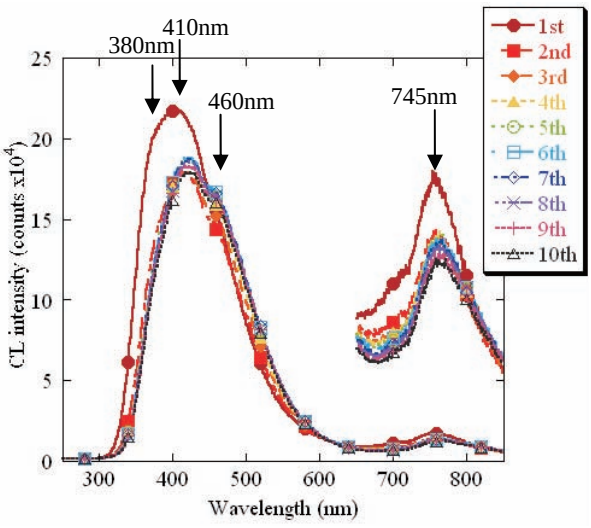

(c) CMG glass

Figure 4. CL spectra obtained for various glasses

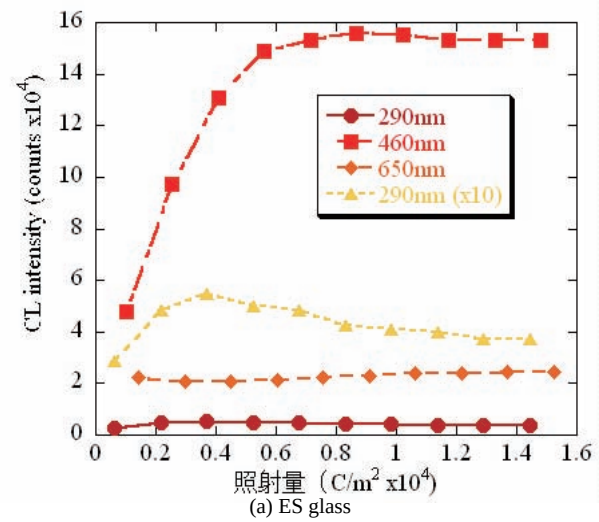

(a) ES glass

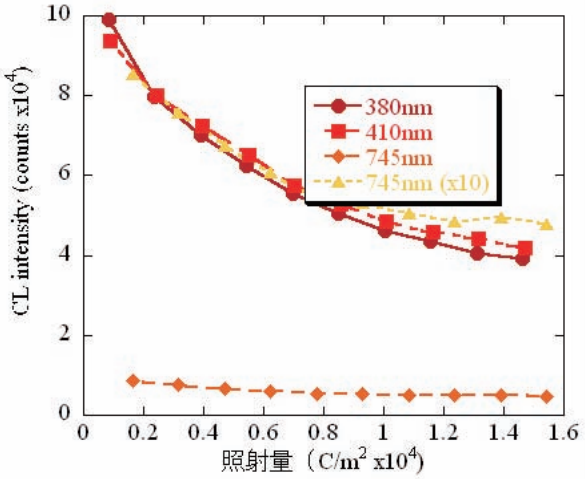

(b) Pyrex glass

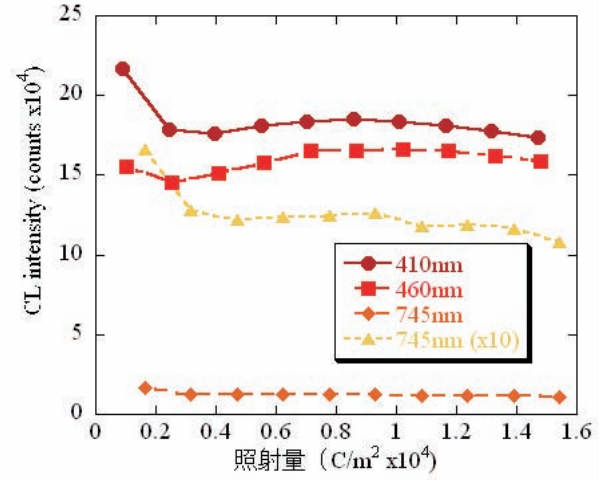

(c) CMG glass

Figure 5.　Dose dependent CL curves observed for various types of glasses

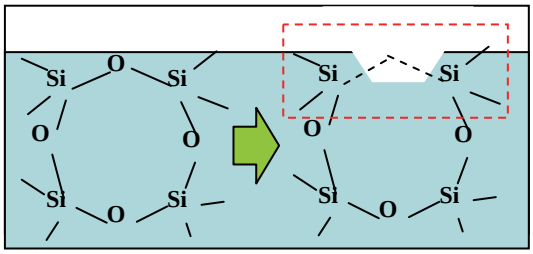

(a) ODC

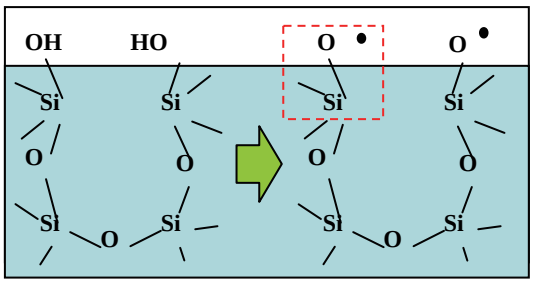

(b) NBOHC

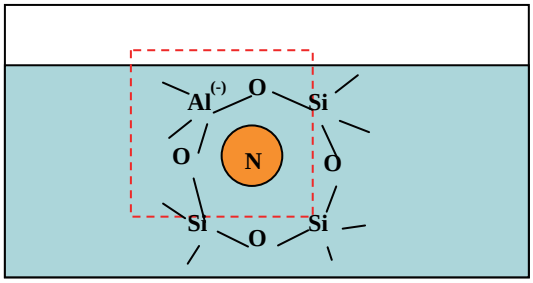

(c) Associated with (AlO_4/Na^+) center

Figure 6.　Defects induced by electron beam irradiation in various types of glasses.

次に図 7 に各高分子による CL スペクトル測定の結果を示す。図 7(a),(b)および(c)より、試料 PMMA では 500 nm 帯で、試料 FEP では 520nm 帯で、試料 Upilex では 510nm 帯で CL ピークが確認できた。各ピークは試料表面で起きた劣化反応や帯電の影響を示していると考えられる。

図 8 にこれらのピークが照射量によってどのように変化するかを示す。図 8(a)において PMMA の 500nm 帯は CL 強度が一度上昇し、照射量がある一定まで達すると飽和するという現象を確認できた。また(b)において試料 FEP の 520nm 帯そして(c)において試料 Upilex の 510nm 帯では CL 強度が減衰している。この原因として試料自体が電子線の熱により劣化したもの、もしくは内部帯電により電子線が入射しにくくなり発光が抑えられたのではないかと考えられる。

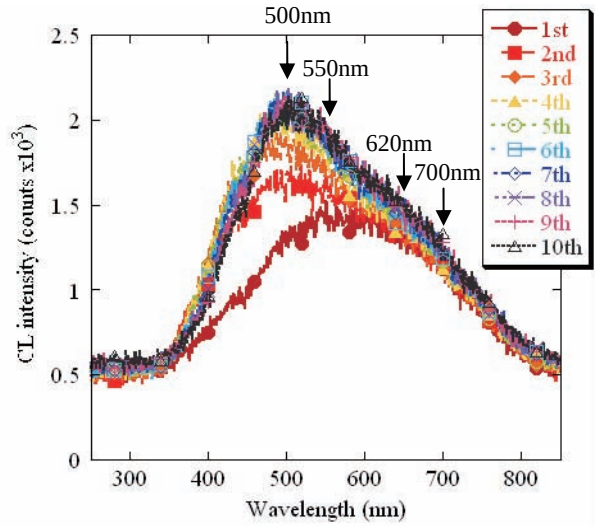

(a) PMMA

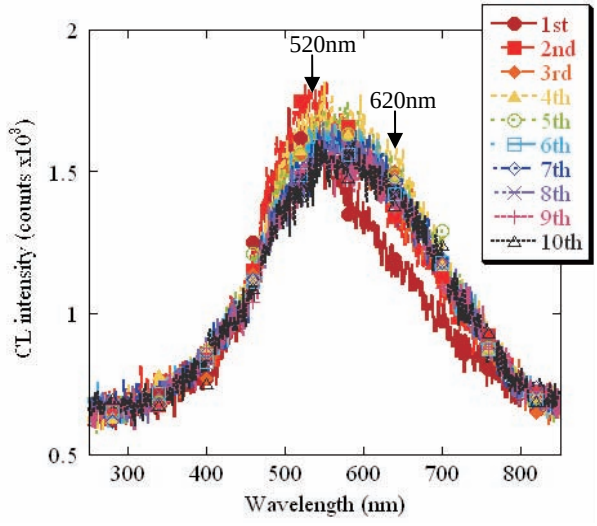

(b) FEP

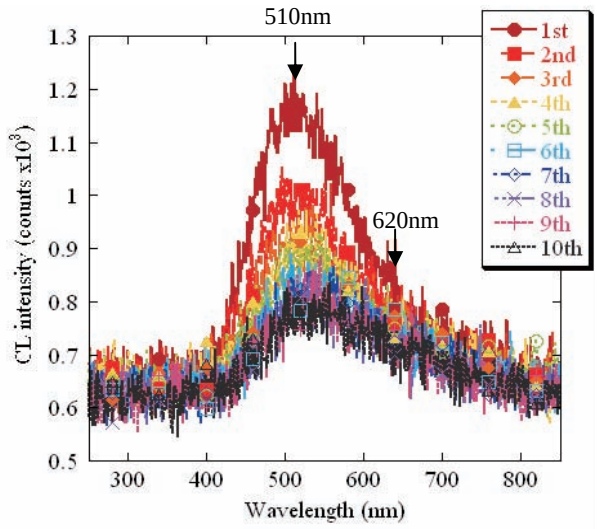

(c) Upilex

Figure 7. CL spectra obtained for various polymers

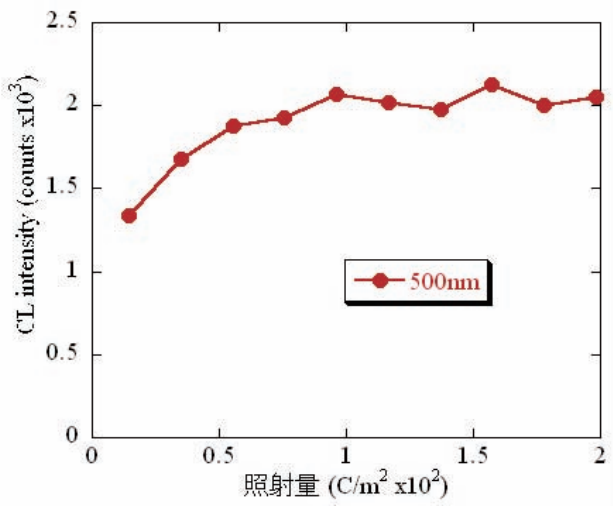

(a) PMMA

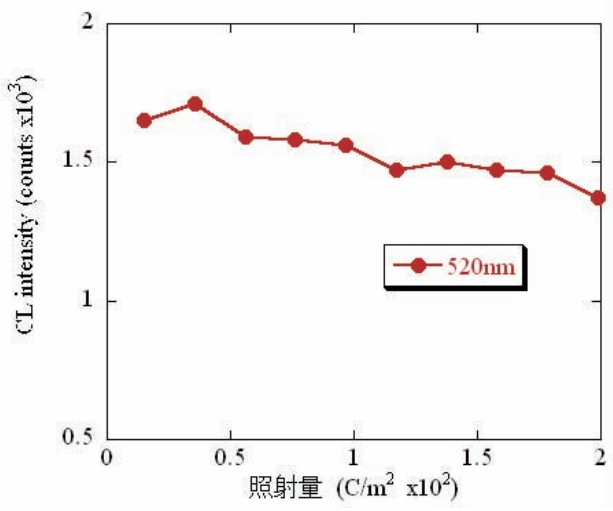

(b) FEP

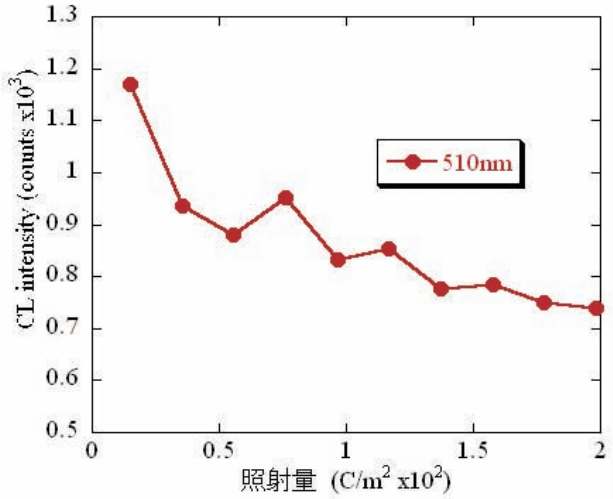

(c) Upilex

Figure 8. Dose dependent CL curves observed for various types of polymers

Table 3.　Summary of the CL peaks observed for various glasses and polymers

glasses	290nm (ODC)	380nm (Al, Na)	410nm	460nm (ODC)	650nm(NBOHC)	745nm
ES	○	—	—	○	○	—
Pyrex	—	○	○	○	—	○
CMG	—	○	○	○	—	○
polymers	500nm	510nm	520nm	550nm	620nm	700nm
PMMA	○	—	—	○	○	○
FEP	—	—	○	—	○	—
Upilex	—	○	—	—	○	—

以上の結果より、各試料の CL 発光強度のピークをまとめたものを表 3 に示す。これによりいずれのガラスにおいても酸素欠乏性欠陥(Oxygen Deficient Center: ODC, ≡Si－Si≡)による 460nm 帯にピークが生じる。また CMG150AR には Pyrex と同じ 380nm 帯にピークが出ることが分かった。これより CMG の不純物として Pyrex と同様に Al や Na の存在が考えられる。一方、高分子材料では 620nm 帯付近でいずれの試料にも共通の CL ピークが確認できた。これにより各高分子材料の表面で帯電や劣化等のような同様の現象が起きていると考えられ、今後、ガラスと同様に検討してゆく。

4. まとめ

本研究では、宇宙機に使われている絶縁体材料に電子線を照射し、その帯電や欠陥生成の機構などを明らかにすることを目的として、走査型電子顕微鏡により組成の異なる 3 種類のガラスと高分子に電子線照射を行い、照射効果を CL 測定により評価した。

これにより宇宙機に使われている CMG ガラスの CL スペクトル測定では試料 Pyrex と同じ 380nm 帯のピークが見られ、CMG ガラスに添加されている不純物の中に Al と Na が含まれている可能性が考えられる。また照射量に対する CL 発光強度では不純物含有量が多い試料 Pyrex のように CL 発光強度で減衰と不純物含有量が少ない試料 ES のような CL 発光強度の上昇と飽和が合わさったような現象が見られた。これにより試料 Pyrex のように帯電しやすいのではないかと考えられる。さらに今回の実験で宇宙機に使われている高分子材料に電子線照射をすると劣化や帯電が起きているのではないかと考えられる各波長でのピークが確認できた。

今後は、より詳細な劣化や帯電のメカニズムを調べるため、ガウシャンを用いた各ピークの CL スペクトルの分解、さらに PL や FT-IR 等の光学的測定法さらに空間電荷測定と CL 測定との相関の検討する必要がある。

文　　献

(1) 趙孟佑：「宇宙機器の高電圧に向けた課題」，第 37 回電気電子絶縁材料システムシンポジウム予稿集，pp.1-9 (2007)

(2) 岩田稔：「宇宙環境技術研究センターにおける材料研究」，第 2 回宇宙環境シンポジウム講演論文集，pp.107-110 (2005)

(3) B. G. Yacabi et al.: “Cathodoluminescence microscopy of inorganic solids”, Lightning source UK Ltd. (1990)

(4) Takuya Harada et al.: “Electron-beam irradiation effects on silica glass studied by cathodoluminescence”, SiO2006 symposium, (2006)

(5) Stevens Kalceff M.A. et al.: “Cathodoluminescence microcharacterization of the defect structure of quartz”, Physical Review B, Vol.52, No.5 pp.3122-3134 (1995)

(6) T.E. Tsai, et al.: ”Mechanism of Intrinsic Si E'-Center Photogeneration in High-Purity Silica”, Physical Review Letters, Vol.61, No.4 pp.444 (1988)

小型表面帯電分布計測システムの開発

籾山　弘行*，鈴木　祥太，田中　康寛，高田　達雄(武蔵工業大学)

Development of a small size measurement system for observing a surface charge

Hiroyuki Momiyama, Shouta Suzuki, Tanaka Yasuhiro, Tatsuo Takada (Musashi Institute of Technology)

ABSTRACT

The purpose of this research work is to develop a small size measurement system to observe the surface charge distribution on insulator in vacuum chamber for space environmental test. Recently, a lot of satellites many purposes like a telecommunication, a weather report are being launched. These satellites are flying in a very severe space environment where the high energy radiations are scattered from the sun. In this environment, electrical charging phenomenon occurs on the insulation of spacecraft surface and electrical discharge or dielectric breakdown occurs by the high electric field. Therefore devices in spacecraft have a risk of failure. So we need to find out a mechanism for the occurrence of surface discharge on insulation and a best insulating materials for space conditions. Until now, my senior at our laboratory has made a measuring system of surface charging on insulation using the BSO crystal has Pockels effect. The measuring system has been used the observation of surface discharging on insulation under conditions of non-destructive and non-contact. However this measuring system is large size and the techniques for setting an optical axis is hard. So it was difficult to apply the measuring system to the space environment simulator of small vacuum chamber. So we need to make a small size measurement system for surface discharging observation. By using a plate type light source of LED and changing a optical type , the system area can be reduced 200×150mm from 1200×700mm. Then we researched surface charging on BSO crystal and Kapton film, by using the small system. Then we researched measuring accuracy of the small system.

Key words: Pockels effect, Surface charging, plate type light source

1. はじめに

宇宙機が飛行する宇宙空間では、太陽から多量のプラズマやイオン、プロトンなどの荷電粒子、γ線などの高エネルギー電磁波が放出されている。この環境下において、宇宙機表面に用いられる絶縁体は帯電し、沿面放電や絶縁破壊が発生する可能性がある。これらの現象は、宇宙機に搭載された機器の誤作動や故障を引き起こすことがあるので、宇宙機システムの高信頼度化、長寿命化のためには、絶縁体表面上で発生する放電発生メカニズムの解明や、沿面放電の絶縁材料依存性を調査する必要がある。そこで、これまで、電気光学効果の一種であるポッケルス効果を示す誘電体結晶を用いて、光学的に沿面放電の２次元分布を計測する装置を開発してきた。この装置を用いて、非破壊、非接触で絶縁体表面の沿面放電進展過程を観測することが可能であるが、光学系の調整に長時間必要とする上、大型であるため、宇宙環境を模擬した真空チャンバー内等の特殊環境下における測定が困難であった。そこで、我々は、特殊環境下での測定を可能とするために、光学調整が簡便な小型装置の開発をすることを目的としている。

2.　ポッケルス効果を用いた表面帯電分布の測定原理

2.1 ポッケルス効果

以下にポッケルス効果による偏光位相差について説明する。

図１に示すポッケルス素子表面に電荷が存在していたとすると、この電荷により、ポッケルス素子のｚ方向に電界が発生し、素子内で誘電率のｘ方向、ｙ方向成分に異方性が生じる。これにより素子内の屈折率がｘ方向とｙ方向で異なるため、ポッケルス素子内を伝播する電磁波のｘ方向、ｙ方向に速度差が発生する。これにより出射光には偏光位相差Δθが発生する。この偏光位相差は、式(1)で表され[1]、Ｚ方向成分の電界を積分することにより、表面電位分布の式として表すことができる。

$$\Delta\theta_{(x,y)} = \frac{2\pi}{\lambda} n_0^3 \gamma_{41} \int_0^d E_z dz = \frac{2\pi}{\lambda} n_0^3 \gamma_{41} V \qquad (1)$$

Δθ: 偏光位相差　　E_z : z 方向成分の電界

n_0 : 常光線屈折率　　λ : 波長

γ_{41} : ポッケルス係数　　d: ポッケルス素子の厚さ

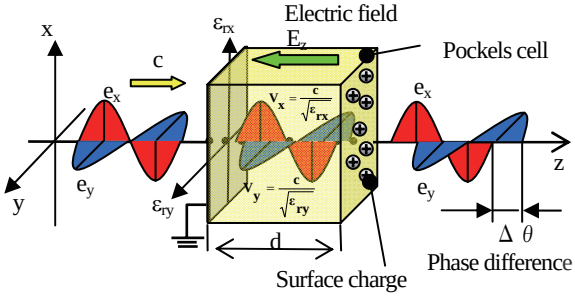

Fig.1 Principle of pockels effect

2.2　表面帯電分布の測定原理

以下に沿面放電観測に用いる光学系と各素子での偏光状態を説明する。図2は偏光子、λ/4板、ポッケルス素子であるBSO結晶、検光子の各素子の配置とそれを透過する光の偏光状態を示している。偏光子を透過する光は直線偏光となり、λ/4板を透過することで円偏光となる。次に、円偏光が表面電荷発生時のBSO結晶を透過することにより位相差が発生するため、円偏光が楕円偏光となる。次に楕円偏光が検光子に入射するという偏光状態となっている。また、この光学系では、ポッケルス効果による偏光位相差Δθと最大光強度I_0、放電発生時光強度Iの関係を式(2)で表すことができる。この式のうち、最大光強度I_0と放電発生の光強度Iおよび、最小光強度I_{off}は測定可能であるので、3つの光強度から偏光位相差Δθを算出することができる。また、位相差分布から愛器(1)により表面電位分布を算出することができる。

$$\frac{I_{(x,y)}-I_{off\,(x,y)}}{I_{0(x,y)}-I_{off\,(x,y)}}=\sin^2\left(\frac{\Delta\theta_{(x,y)}}{2}+\frac{\pi}{4}\right) \quad (2)$$

Δθ: 偏光位相差　　I_0 ： 最大光強度

I：放電発生時の光強度　　I_{off} ： 最小光強度

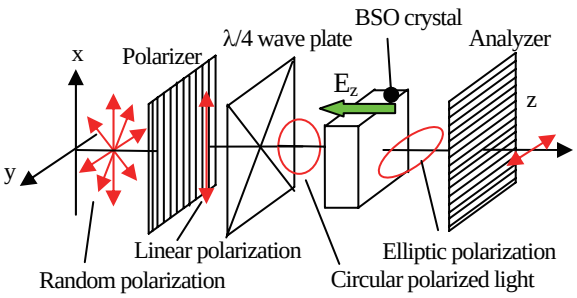

Fig.2 Principle of measurement for surface charge

3.　小型表面帯電計測システムの構成

図3に小型沿面放電測定システムを示す。装置のサイズは、縦60㎜、横53㎜、高さ65㎜である。装置の筐体部分は、アクリルで作製しており、筐体側面に溝を設け、筐体下部にはLED平面光源を設置する。溝にはスライド板にはめ込んだ円偏光フィルム(偏光子－λ/4)、BSO結晶を取り付ける。この装置で、沿面放電発生時の透過光を装置上部に設置したハイスピードビデオカメラで撮影することで、沿面放電の経時変化を可視化することができる。以下に装置の小型化の詳細について述べる。

3.1 平面光源の採用

これまでは、光源にHe-Neレーザー光源を使用していたが、作製した小型沿面放電測定装置では、発光ダイオード(LED)を6×6個を並べたLED平面光源を採用した。その結果、従来の装置で[2]レーザ・ビーム径1mmを50mmに拡大するビーム・エキスパンダーが不要になる。なお、平面光源の波長は651 nmを中心に半値幅50 nmに広がっているが、使用した光学素子等の機能には、ほとんど影響がないことを確認している。この装置の改良により、レーザー本体およびビーム・エキスパンダーで長さ約650mmであった部分が、平面光源により、長さ約9mmにまで小型化できた。

3.2　透過型光学系の採用

装置の小型化のため、沿面放電を観測するセンサー部の改良点について示す。従来は、BSO結晶面の反射光を計測する方式であったが、この従来型では、ミラーや偏光ビームスプリッタなどが必要になり、光路長も長く取る必要があったため、それらの素子が不要で光路長も最短に出来る透過型に変更した。透過型にすることにより、各素子を直線的に配置でき、面積の縮小が可能となった。すなわち、53mm×60mmに収めることができた。ただし、透過光型の採用により、不透明の絶縁材料の沿面放電の計測が困難になることが欠点である。

3.3 円偏光フィルム

円偏光を得るために、λ/4の位相差フィルム付き偏光子(透過光軸φ=0°の偏光子に進相軸がφ=45°の位相板が貼られた円偏光フィルム)を、平面光源とBSO結晶の間に挿入した。従来の装置では、PBSと1/8波長板がこの役割を果たしていたが、この円偏光フィルムを採用したことにより、光路長を短縮することができた。なお、円偏光フィルムは、使用する波長によっては、楕円偏光を出射するが、今回使用した平面光源では、ほぼ円偏光とみなせることを確認した。

3.4 光路長の短縮

上述した改良により、光路長は、平面光源、円偏光フィルム、BSO結晶、針電極、検光子、ハイスピードビデオカメラのレンズまでの101mmである。従来の装置の光路長が約1200mmであったので、光路長をおおよそ1/10程度に短縮できた。

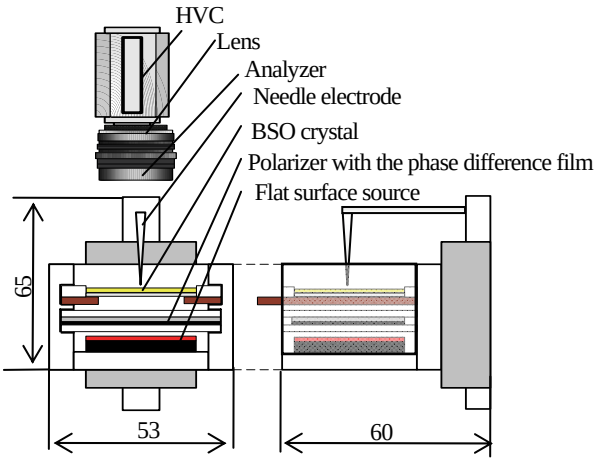

Fig.3 The small size measurement system for surface

3.5　LPF による画像処理

従来のシステムでは、S/N 比を向上させるため画像ロックインアンプの手法を使っていたが、位相変調用の BSO 結晶などが必要であり、装置を小型化するために、この装置では、この手法を用いていない。そこで、取得した画像の S/N 比を向上するために低帯域フィルタ(LPF)により画像の高周波成分を低減させた。具体的には、ハイスピードカメラで計測した光強度から位相差分布を算出した後、LPF をかけることにより、高周波ノイズの除去を行った。ロックインアンプを用いた従来の手法では、数枚を積算して 1 枚の画像を得ていたためにハイスピードカメラの最小の時間分解能で画像を取得することができなかったが、今回の装置では、ハイスピードカメラの最小の時間分解能でのデータ取得が可能となった。

4.　沿面放電観測例

4.1 実験条件、手法

図 4 に実験装置を示す。実験装置は、単発・複発交流波形制御回路、ネオントランス、小型沿面放電測定システムで構成されている。この装置を用いて、大気中において BSO 結晶上、Kapton®上での沿面放電観測実験を行った。実験条件として、BSO 結晶に印加する電圧波形は、図 5 に示す波形であり、振幅 5kV、50Hz の交流を 1 周期分印加した。この電圧印加時の BSO 結晶表面の画像をハイスピードビデオカメラで撮影した。また、信号処理により沿面放電撮影画像を位相差分布表示とするために、沿面放電発生時の光強度 I、最大光強度 I_0、最小光強度 I_{off} の光強度を測定した。

4.2 沿面放電観測結果

以下に BSO 結晶上、Kapton®上(12.5μm)での沿面放電の経時変化の結果を示す。画像は、信号処理を行い、位相差分布表示としている。また、測定範囲は、針電極を中心に 10㎜×10㎜ の範囲である。図 6 は BSO 結晶上での沿面放電の進展結果を示し、図 7 は Kapton®12.5μm 上の沿面放電結果を示す。画像の下部にフレームナンバーを示しており、図 6 の frame と対応した沿面放電の進展画像を示している。また、測定精度の比較のために、図 8 に従来の装置での BSO 結晶上での沿面放電結果、図 9 に Kapton®12.5μm 上での沿面放電進展結果を示す。

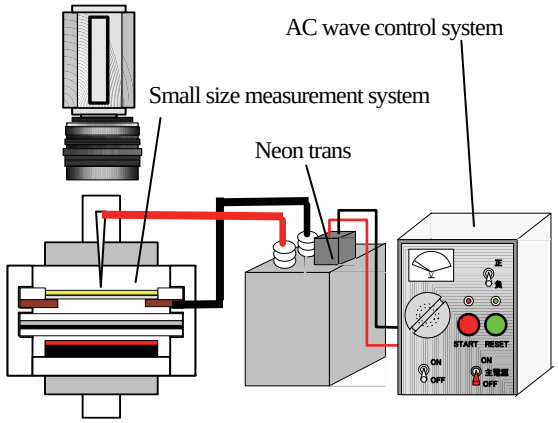

Fig.4　measurement system

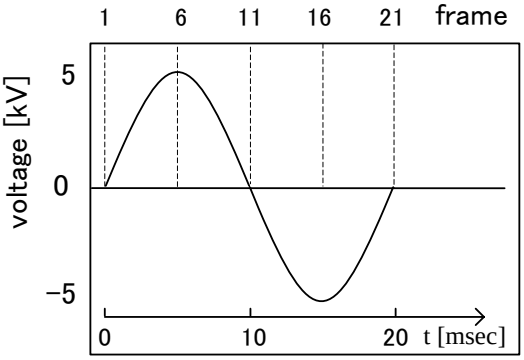

Fig.5　Voltage wave

Table1　measurement sample

試料	Kapton
厚さ(μm)	0(センサ上)
	12.5

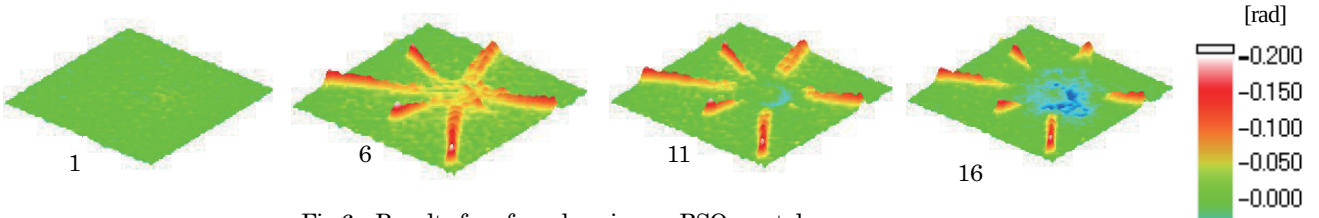

Fig.6　Result of surface charging on BSO crystal

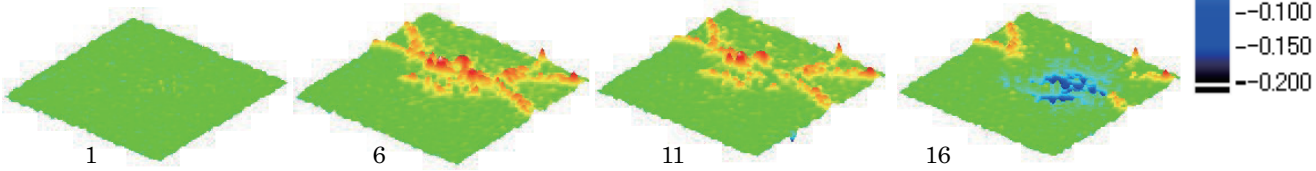

Fig.7　Result of surface charging on Kapton film(12.5μm)

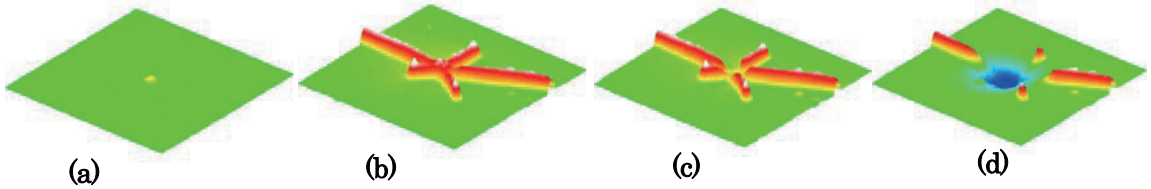

Fig.8　Result of surface charge on BSO crystal by using the existing device

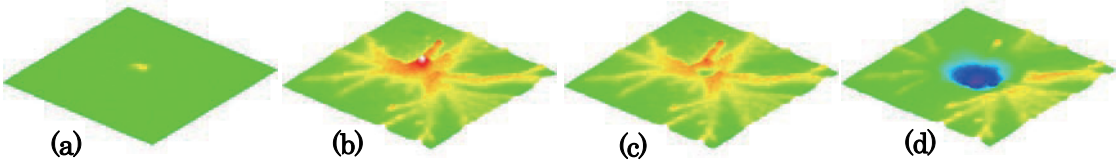

Fig.9　Result of surface charging on Kapton film(12.5 μ m) by using the existing device

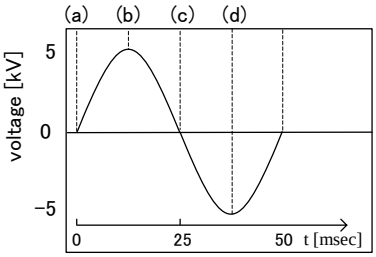

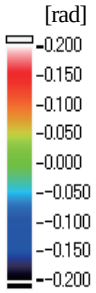

4. 3 印加電圧と沿面放電の進展

図 7 の BSO 結晶上での沿面放電観測結果より、振幅 5kV、50Hz の正弦波電圧を 1 周期印加した結果、印加電圧＋5kV となるフレームナンバー6 では、放射上に伸びる正極性ストリーマが 6 本確認できる。次に、印加電圧－5kV となるフレームナンバー16 では、針電極付近に同心円状の負極性ストリーマが進展していることが確認できる。また、図 8 より kapton®12.5 μ m 上での沿面放電結果では、印加電圧 5kV となるフレームナンバー6 で、樹脂状に進展する正極性ストリーマが観測でき、印加電圧が－5kV となるフレームナンバー16 で、針電極を中心に同心円状に広がる負極性ストリーマが確認できた。

5. 小型化した沿面放電測定システムの性能

将来的に、特殊環境を作り出す小型真空チャンバー内において、沿面放電を観測するために、沿面放電測定装置の小型化を図った結果、小型沿面放電測定システムのサイズは、縦 60㎜、横 53㎜、高さ 65㎜ となった。実験に用いる小型チャンバー内の直径は 250mm であり、小型沿面放電測定装置より大きいため、装置をチャンバー内に収めることが可能であると言える。また、装置をモジュール化したことにより、小型真空チャンバー内で、光学系のセッティングが不要となる装置となった。

次に小型装置の沿面放電測定精度について検討する。図 7、図 8 に示した BSO 結晶上における沿面放電観測結果と Kapton®上における沿面放電結果から、画像に目立つノイズがのることなく、正極性、負極性ストリーマを視認することができた。図 9、図 10 に示す従来の装置での BSO 結晶上、Kapton12.5 μ m 上における沿面放電観測結果と比較すると、小型装置の BSO 結晶における沿面放電結果では、従来と同様のストリーマの進展が確認できる。しかし Kapton(12.5 μ m)上において、従来の装置では、正極性ストリーマの進展の先端部まで詳細に観測することが可能であるが、小型装置での結果では、ストリーマの進展は確認できるが、従来の装置の結果に比べると、画像が粗いため、ストリーマの進展を詳細に観測することができないことが確認できる。このため、作製した小型装置において、Kapton 上での沿面放電を詳細に観測することは困難であることが確認できる。

6. まとめ

透過型の光学系を採用したことで、沿面放電測定システムの小型化に成功した。また、装置をモジュール化することにより、光学系のセッティングが容易となる装置の開発に成功した。小型沿面放電観測装置を用いて、沿面放電観測を行った結果、BSO 結晶上において沿面放電観測が可能であるといえた。しかし、Kapton®上では、ストリーマの進展画像は得られるが、従来と同等の精度を出すことができなかった。

文　献

(1)　川崎俊之・高田達雄：電気光学効果を応用した誘電体表面電荷分布の測定に関する研究：平成 5 年
(2)　安野順介・田中康寛・高田達雄：電気光学効果を用いた絶縁体表面上の 2 次元電位、電界分布光学測定装置の開発：平成 18 年

電子線を照射した各種ポリマーの内部帯電現象

長澤健一郎*, 本城正人, 田中康寛, 渡邉力夫, 高田達雄 （武蔵工業大学）

Internal Charging Phenomenon in Election Beam Irradiated Polymers

Kenichiro Nagasawa, Masato Honjoh, Yasuhiro Tanaka, Rikio Watanabe, Tatsuo Takada (Musashi Institute of Technology)

Abstract:

The spacecraft like a communication or a broadcasting satellite flying in GEO is always exposed to plasma and/or radioactive-rays such as α-, β- and γ-rays. When the dielectric materials, in which the spacecraft is wrapped to keep temperature in it stable, are irradiated by the high energy electron beam, sometimes an unexpected accident due to an electrostatic discharge happens. The accident sometimes causes a serious mission error of the spacecraft. However, there remain many unknown factor about a charge accumulation in dielectric materials by irradiation of electron beam. Therefore, we need to measure the charge distribution in the bulk of dielectric materials. We have been developing a system for measuring such a charge distribution in dielectric materials using pressure wave propagation method.

Using this system, we tried to measure the charge distribution under electron beam irradiated Low Density Polyethylene, Polyethylene Terephthalate, Polycarbonate, Polyethylene Naphthalate in addition to Polyimide and PTFE films which are used as a thermal control layer or a optical solar reflector of spacecrafts. We observed accumulation behavior of charge in each sample, survey relationship with each sample's molecular structure. As a result, It's believed that charging characteristics of insulating material is linked to benzene ring in each sample's molecular structure.

1. はじめに

宇宙機は、温度変化の激しい宇宙環境を飛行するため、機内の温度を一定に保つ必要があり、絶縁材料フィルムを積層したサーマルブランケット(MLI:Multilayer Insulation)が熱制御材料として使用されている。しかし、MLI はプラズマ環境、放射線環境下に曝されることで帯電する。帯電量が大きくなると放電事故が発生し、絶縁材料の劣化や搭載されている機器の誤作動・故障を引き起こすといわれている。そのため、宇宙機の設計には MLI などに使用される絶縁材料等の電気特性が重要な要因になってくる。しかし、現在検討されている宇宙機設計のガイドラインでは、電子線などの高エネルギー粒子線が照射された絶縁材料の電気的特性はほとんど考慮されていない。

そこで本研究では、宇宙機用絶縁材料で生じる内部帯電現象のメカニズムを解明するために、圧電素子誘起圧力波法(PIPWP)法を用いた内部帯電計測装置を開発し[(1)]、電子線照射装置と真空チャンバーを用いて真空環境における高分子絶縁材料内部の空間電荷分布測定を行ってきた。今回は、絶縁材料として実際に宇宙機の熱制御材として使用されているポリイミド(PI)およびポリテトラフルオロエチレン(PTFE)に加え、低密度ポリエチレン(LDPE)、ポリエチレンテレフタレート(PET)、ポリカーボネート(PC)、ポリエチレンナフタレート(PEN)などの代表的な有機高分子材料について電子線照射実験を行ない、各試料の電荷蓄積挙動を観測するとともに、分子構造との関係について調査した。

2. 圧電素子誘起圧力波(PIPWP)法の原理

図 1 に PIPWP 法の原理図を示す。まず、パルス電圧 e(t)をアルミ電極で挟まれた圧電素子に印加すると、パルス圧力波 p(t)が発生する。パルス圧力波 p(t)は接地されたアルミ電極を伝播して、空間電荷 ρ (z)が蓄積している試料を通過する。このとき伝播してきた圧力波によって、試料内の空間電荷 ρ (z)が微小変位し、それにより外部回路に変位電流 i(t)の電気信号が誘起される。この電気信号 i(t)を増幅器で増幅し、オシロスコープで電圧信号として検出する。その後、PC により適切な信号処理を行うことで試料中の空間電荷分布を得ることができる。

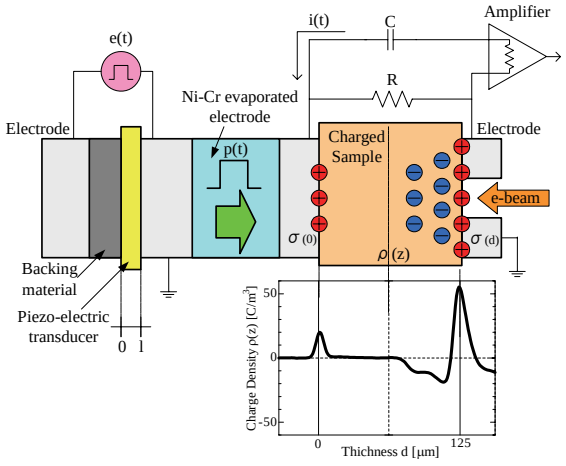

図 1 PWP 法原理図

3. 測定システム

＜3-1. PWP 測定装置＞

図 2 に PWP 測定装置の写真および概略図を示す。本装置には、電子線を試料に照射するための直径 10mm の照射孔が照射側電極に設置され、試料表面に蒸着されたアルミ電極とともに、接地電極を構成している。また、下部電極として石英ガラス上面に Cr-Ni を蒸着して、信号検出電極として用いている。石英ガラスは、信号検出用の電極を接地導体から絶縁するために用いている。なお、真空下で試料と電極の密着性を高めるために、ガラス上面に溝を加工し、試料と電極間の空気を排気する構造にしている。

この測定装置では厚さ 4μm の PVDF(ポリフッ化ビニリデン)に、パルス幅 1nsec、電圧値 200V のパルス電圧を印加することで、幅 1nsec のパルス圧力波を発生させることができる。現在、本測定装置の位置分解能は約 6μm であり、厚さ 50μm 程度以上の試料が測定可能となっている。

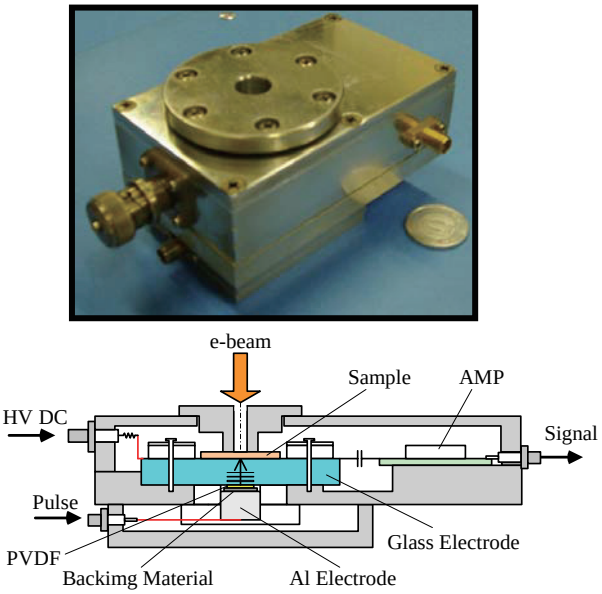

図 2　PWP 測定装置

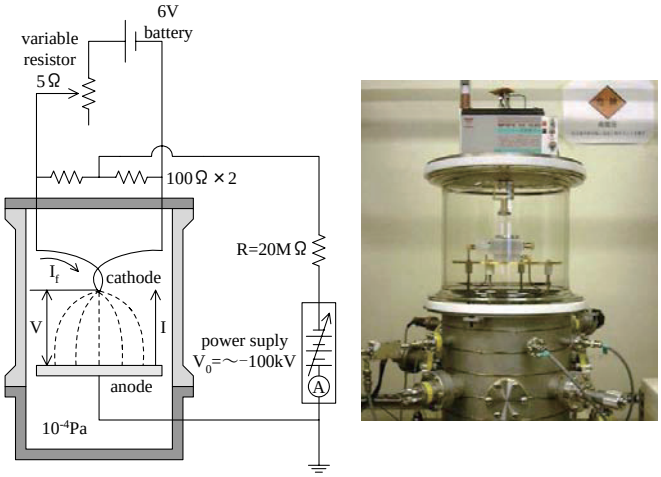

図 3　電子線照射用真空チャンバー

＜3-2. 電子線照射用真空チャンバー＞

図 3 に電子線照射用真空チャンバーの概略図および写真を示す。電子線の照射には電子顕微鏡用のタングステンフィラメントを用い、加速エネルギー100keV までの電子線照射が可能であり、チャンバー内の真空度は約 10^{-5}Pa まで到達可能である。

4. 測定方法

表 1 に、測定に用いた試料の分子構造とその試料厚さを示す。照射した電子線の加速エネルギーは 40 および 60keV であり、電流密度を 70nA/cm^2 一定として真空チャンバー内の真空度 6.0×10^{-4}Pa 以下において空間電荷分布を測定し、電荷分布を積分することにより試料内部に蓄積している電荷量を算出した。また、測定時間は PET, PC, PEN, PI, LDPE においては照射中、照射後ともに 20 分間の測定を 30 秒間隔で行った。なお、PTFE 以外の試料では照射時間とともに、電荷の蓄積挙動が明確になるが、PTFE に関しては、照射時間が 20 分間では電荷の蓄積挙動が明確にならないために、照射時間 80 分で行っている。

表 1 測定試料と分子構造

ベンゼン環有り	ベンゼン環無し
PET(125μm) 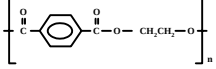	LDPE(100μm) 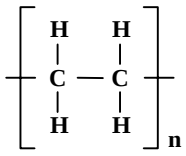
PC(145μm) 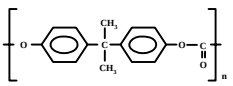	
PEN(125μm) 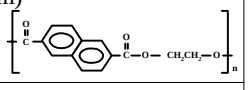	PTFE(100μm) 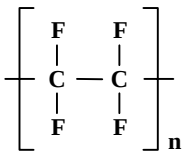
PI(125μm) 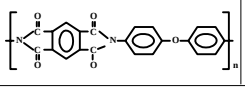	

5. 実験結果及び考察

<5-1 各種ポリマーにおける電荷蓄積挙動観測>

電流密度 70nA/cm^2 一定として、加速エネルギー40 および 60keV において電子線照射実験を行った。図 4,5-(a)~(f)に 40 および 60keV における各試料の空間電荷分布図を示す。このとき、電子線は図中右側から照射したように表示してあり、照射面側から矢印で示されている破線の位置は(1)式に示すフェーザの式から求めた電子の最大飛程の位置である。(1)式での T は照射する加速エネルギー[MeV]、R が面積密度[mg/cm^3]であり、R を透過する物質の密度で除すことにより、最大飛程を求めることができる。また、図 6,7-(a)(b)に加速エネルギー40 および 60keV における蓄積電荷量の経時変化(電子線照射時間 20 および 80 分)を示す。

$$R=407\times T^{1.38} \qquad \cdots\cdots(1)$$

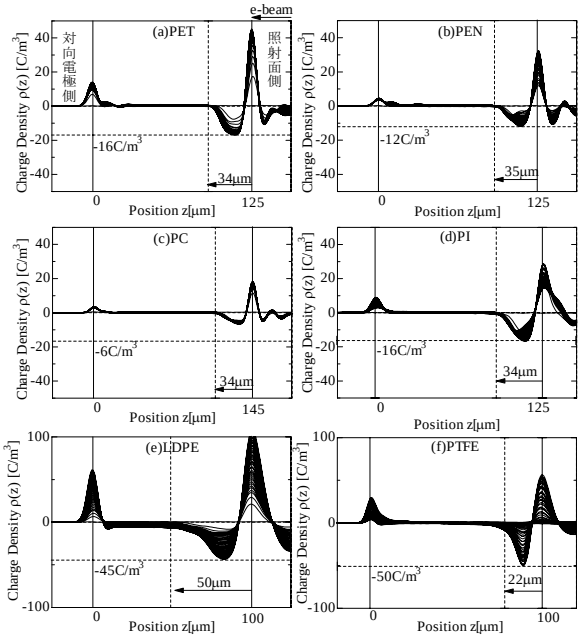

図 4 空間電荷分布図(加速エネルギー40keV)

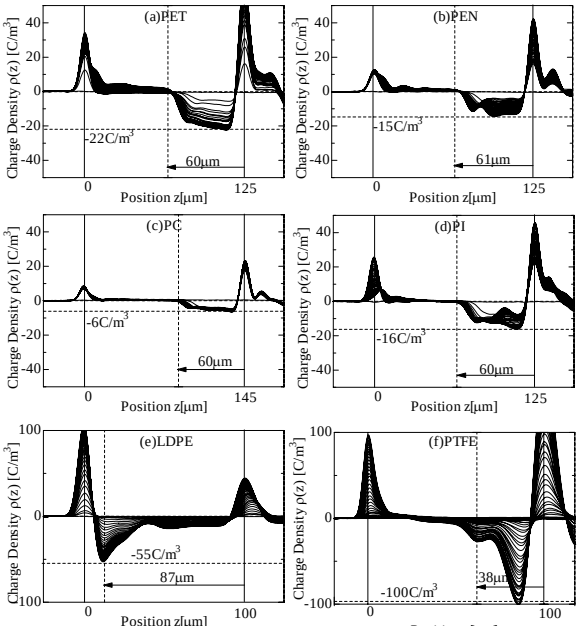

図 5 空間電荷分布図(加速エネルギー60keV)

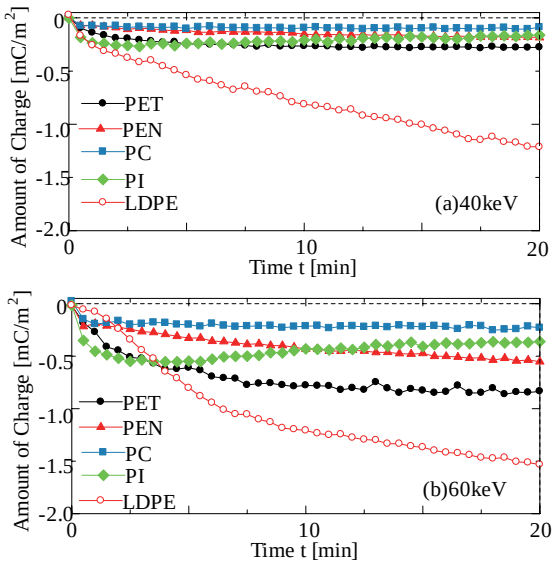

図 6 各種試料における蓄積電荷量の経時変化(照射時間 20 分)

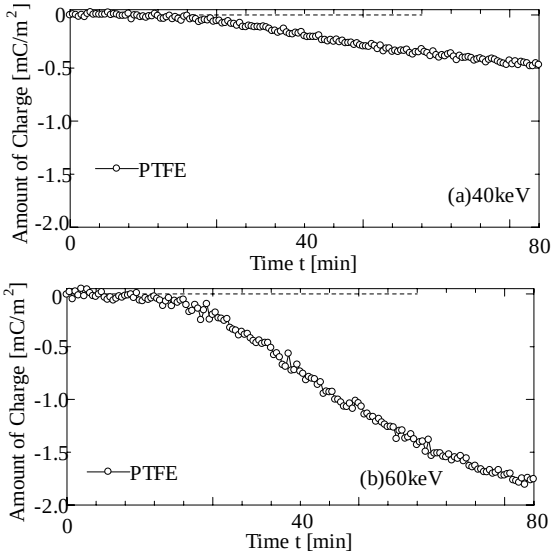

図 7 PTFE における蓄積電荷量の経時変化(照射時間 80 分)

まず、図 4 の加速エネルギー40keV における電荷分布図を見ると、LDPE および PTFE では、蓄積する電荷量が増加すると、負電荷が電子の最大飛程の位置を越えて対向電極側方向に移動していることがわかる。特に LDPE においては、試料全体にわたって負電荷が分布しているといえる。計算によって求められた最大飛程までの領域に分布する電子は、試料中に注入された電子が、エネルギーを失ってトラップに捕獲されたものと考えられるが、LDPE の場合は明らかに最大飛程を越えて電子が分布している。これは蓄積した電子によって形成された電界により、一旦停止した電子が対向電極側に移動したためであると考えられ、多量に電荷が蓄積する試料において発生する傾向があると考えられる。

る。一方、PET, PEN, PC, PI においては、そのような電子の移動は見られず、最大飛程の位置で電子の侵入は完全にとどまっている。また、図 5 から、この電荷分布の傾向は加速エネルギーを 60keV にあげた場合も同様であるが、加速エネルギーをあげたことで電子の最大飛程も大きくなったため、LDPE では負電荷の多くが対向電極の極めて近傍に蓄積している。さらに、PEN, PI, PTFE においては 2 つのピークをもつ分布になっていることもわかる。

次に図 6,7-(a)(b)を見ると、すべての試料において加速エネルギーを増加させたことによって蓄積する電荷量が増加する傾向が見られたが、試料ごとに電荷蓄積挙動や蓄積する電荷量に違いが見られた。PI においては電子線照射開始

直後から電荷が蓄積し、その後は電子線照射中にもかかわらず、蓄積電荷量が減少に転じる傾向が見られた。PET や PC においては、電子線照射中に蓄積電荷量はほぼ飽和状態となったが、PET に比べて、PC では蓄積する電荷量が小さいことがわかる。また、PEN, LDPE, PTFE においては電子線照射中、蓄積電荷量は増加し続けている。特に PTFE においては、電子線照射開始直後には電荷が蓄積せず、ある程度時間が経過した後、蓄積する電荷量が増大するという傾向が見られた。また、PEN に比べて、LDPE, PTFE では蓄積する電荷量が非常に大きい。これは、図 4,5-(e)(f)の空間電荷分布図で示したように、電子の最大飛程の位置を越えて対向電極側まで侵入してきた電荷によるものであると考えられる。

<5-2 各種ポリマーの分子構造と電荷蓄積挙動の関係性>

今回測定を行った 6 種類のポリマーを、分子構造で大きく分類すると、表 1 のようにベンゼン環を含んでいる試料(PET, PEN, PC,PI)と、ベンゼン環を含んでいない試料(LDPE, PTFE)に分類できる。本節では、各種ポリマーの分子構造と前節までに示した各試料における電子線照射中における電荷蓄積挙動との関係性について示す。

前節でも述べたように、分子構造にベンゼン環を含んでいる PET, PC, PI は電子線照射中において蓄積電荷量が飽和状態になり、PI においては、電子線照射中にもかかわらず蓄積電荷量が減少に転じた。また、分子構造にベンゼン環を含んでいる PEN においては電子線照射中、蓄積電荷量は増加し続けているが、分子構造にベンゼン環を含まない LDPE, PTFE に比べて蓄積する電荷量は非常に小さいことがわかる。さらに、PTFE においては、電子線照射開始直後には電荷は蓄積しないが、ある程度時間が経過した後、電荷が蓄積し始め、電子線照射中、蓄積する電荷量は増加し続けるという傾向を示した。これらのことから、ベンゼン環を含んでいない試料(LDPE, PTFE)に関してはベンゼン環を含んでいる試料(PET, PEN, PC, PI)に比べて蓄積する電荷量は非常に大きく、電子線を長時間照射した場合にも蓄積する電荷量が飽和する傾向にはないと考えられる。また、図 8 に各試料における加速エネルギーと電子線照射中における蓄積電荷量の最大値の関係を示す。

図 8 からベンゼン環を含んでいる試料（PET, PEN, PC, PI）とベンゼン環を含んでいない試料(LDPE, PTFE)とでは蓄積電荷量の最大値に大きな差があることがわかる。さらに、ベンゼン環を含んでいない試料(LDPE, PTFE)は、電子線照射中において蓄積電荷量が増加し続けており、飽和状態に達するとは考えられないため、ベンゼン環を含んでいる試料（PET, PEN, PC, PI）との差はさらに大きくなると考えられる。これらのことから、分子構造にベンゼン環を含んでいる試料（PET, PEN, PC, PI）のほうがベンゼン環を含んでいない試料(LDPE, PTFE)に比べて電荷の蓄積を抑制する特性があることわかり、絶縁材料の帯電特性にベンゼン環の有無が影響を与えていると考えられる。なお、一般にベンゼン環の大電子は高エネルギー電子などのエネルギーを吸収すると言われており、放射線環境下で使用される高分子材料にはベンゼン環を含む材料が多い。今回の実験では、ベンゼン環を含む材料で、電荷蓄積の増加が抑制されているが、これは、ベンゼン環を含む材料では、注入された電子がベンゼン環にエネルギーを吸収されるために電荷が蓄積できるような物理的欠陥を発生させないのに対して、ベンゼン環を含まない試料では高エネルギー電子が分子鎖を切るなどして、電荷が蓄積するトラップを多く発生させているためであるかも知れない。これらの原因の詳細について今後検討する予定である。

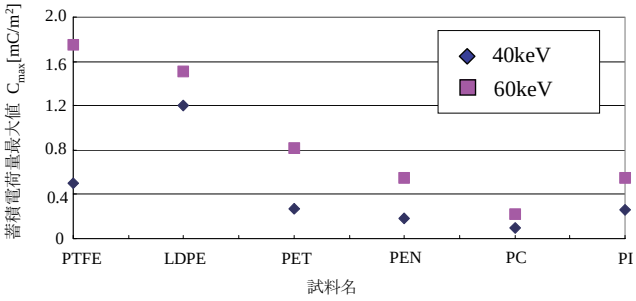

図 8 各試料の蓄積電荷量最大値

6. まとめ

6 種類のポリマーを用いて電子線照射実験を行い、各試料の電子線照射中における電荷蓄積挙動とその分子構造との関連性について検討を行った。その結果、今回測定に使用した試料の電荷蓄積挙動は大きく分けて 2 つに分類できることがわかった。1 つ目は電子線照射中に電荷の蓄積が飽和状態に達する傾向を示すものであり、2 つ目は電子線照射中に電荷が蓄積し続けていく傾向を示すものである。電子線照射中に電荷の蓄積が飽和状態に達する試料は PET, PC, PI であり、3 種類とも分子構造にベンゼン環を含む試料である。特に PI においては図 6-(a)(b)からもわかるように、一度飽和状態に達した後、電子線照射中にもかかわらず蓄積電荷量が減少に転じるという傾向を示した。次に電子線照射中に電荷が蓄積し続けていく傾向を示す試料は PEN, LDPE, PTFE であり、特に PTFE においては電子線照射開始直後には電荷の蓄積が見られず、ある程度時間が経過したあとに電荷の蓄積が増大する傾向を示した。しかし、図 9 からもわかるように、この 3 種類の試料の中で唯一分子構造にベンゼン環を含む PEN の蓄積電荷量が LDPE, PTFE に比べて非常に小さい。これらのことからベンゼン環を含む試料(PET, PEN, PC, PI)はベンゼン環を含まない試料(LDPE, PTFE)に比べて電荷の蓄積が抑制されていることがわかり、分子構造中に含まれるベンゼン環が絶縁材料の帯電特性に影響を与えていると考えられる。

文　献

(1)　田中ほか：電学論 A, Vol.121, No.2 pp143～148 (2001)

軌道上観測結果・シミュレーション

Measurement on orbit & Simulation

静止軌道上帯電データ解析・評価の状況

古賀清一、上田裕子、五家建夫（JAXA）
八田真児、金正浩（MUSE）

１．概要

近年、衛星の帯電・放電に関連すると考えられる事故が国内外で多数、報告されることから、設計段階から帯電・放電の観点に立った検討を正しく行う必要性が認識されている。JAXA では静止衛星についてはこれまで、米国で 70 年代に開発され世界のデファクトスタンダードとしての地位を確立していた NASCAP/GEO と呼ばれる解析ツールを利用してきた。しかしその後、機能拡張、改良され、低軌道衛星、極軌道衛星にも対応可能となったツールは、輸出規制のために日本で使用することはできない。そこで 2004 年 11 月から衛星帯電解析ソフトウェア MUSCAT(Multi-Utility Spacecraft Charging Analysis Tool)の開発に着手し、2007 年 3 月に完成した。

本発表は、この MUSCAT による解析結果を実際の衛星（ETS-V）で取得したデータと比較し報告する。ETS-V は、静止軌道上で１０年間の帯電データを取得しており、ほぼ太陽活動周期１回分のデータが得られている。このデータを MUSCAT の解析結果と比較することにより、衛星電位と帯電サンプルとの電位差について検証することが可能であり、成果を帯電設計基準等に反映することができる。

また、MUSCAT にユーザ要求による機能の追加を行ったため、これについても報告する。

２．静止軌道での帯電計測

ETS-V は、１９８７年８月２７日に打ち上げられ、１１月から技術データ取得装置（TEDA）の計測を開始した。ETS-V に搭載されている TEDA の内、帯電計測装置（POM）[1]の概要を以下に示す。

取り付け衛星構体面	：＋Y 面（南面）
サンプル	：銀蒸着テフロン、アルミ蒸着カプトン、OSR
計測範囲	：＋１ｋV～－１０ｋV
サンプリング	：１分
データ取得期間	：1987.11.26～1997.09.12

図１に ETS-V での約１０年間の計測結果を示す。

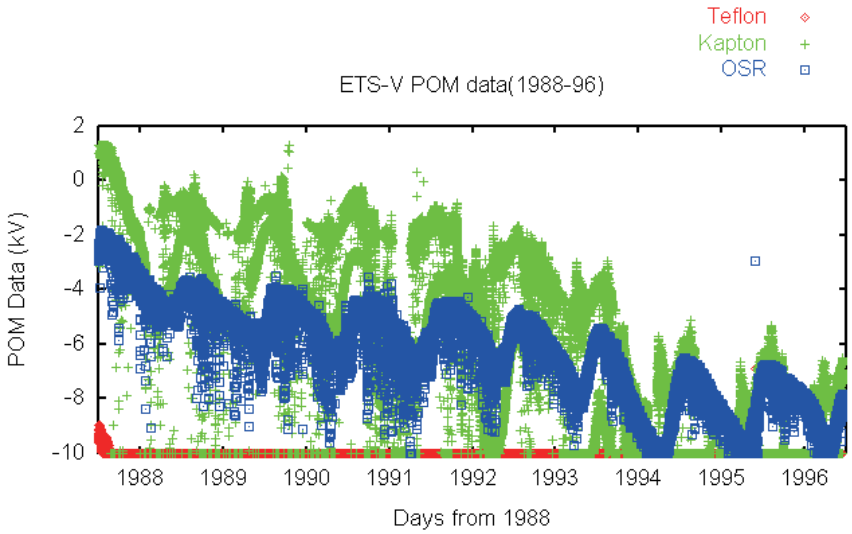

図１　ETS-V の約１０年間の計測データ

データは、１年に１回周期的に変化している。これは、POM が衛星の南面パネルに搭載されているため、１年間で日陰と日照が起こるためと考えられる。また全体的な電位の変化は、表面の特性の経年変化によるものと考えられる。

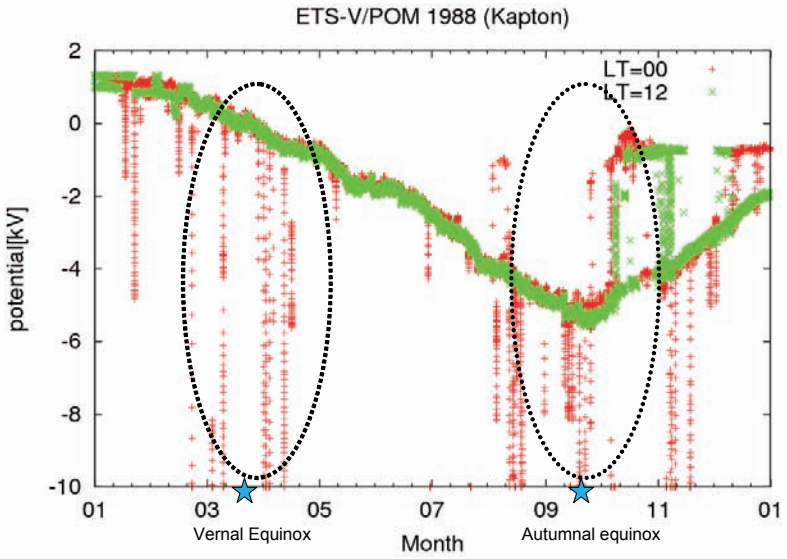

図２　１９８８年、１年間の Kapton のデータ

図２に１９８８年の１年間の Kapton のデータを示す。LT＝0 時のデータ（赤）と LT=12 時（緑）のデータをプロットしている。急激に帯電しているのは LT=0 時の方であり、一般的に言われている夜側のサブストームによる帯電に対応している。また、急激な帯電は春分点と秋分点付近に多く見られ、これも R-M 効果による磁気嵐やサブストームの増加に対応している。

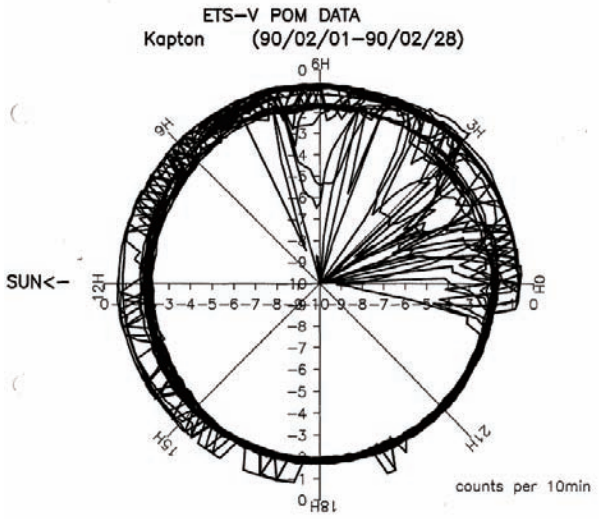

図３　１９９０年２月の Kapton のデータの帯電電位地方時依存性

図３に１９９０年２月の Kapton のデータの帯電電位地方時依存性を示す。これも SCHATHA の観測例と同様に、サブストーム時の粒子の流入が多いと言われている真夜中から夜明けの間に大きな帯電が集中している。

３．MUSCAT による解析結果との比較

図４に MUSCAT 解析に使用した ETS-V の形状モデルを示す。

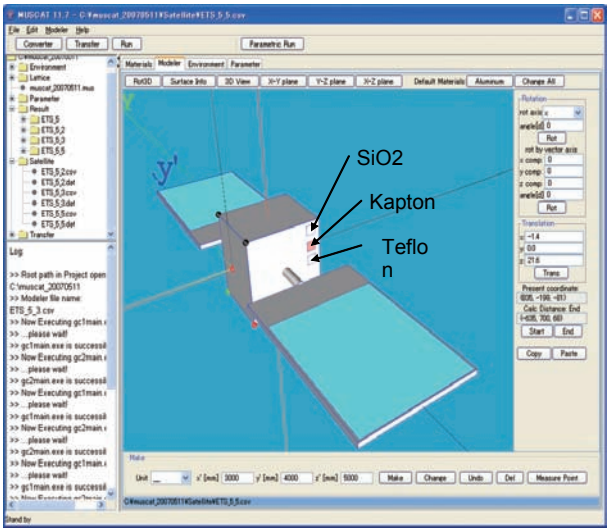

図４　ETS-V 形状データ

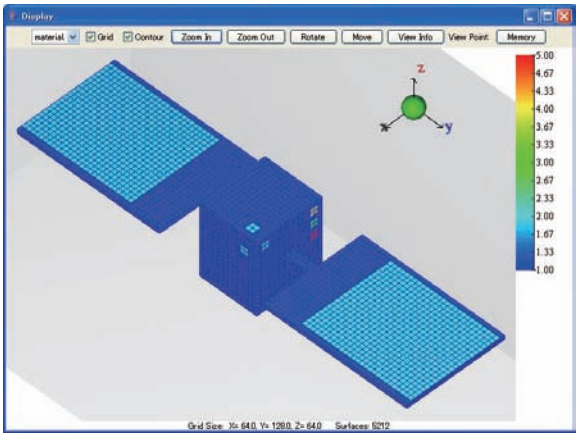

図５　ETS-V グリッドモデル

衛星の大きさは、パドルの両翼が約 9.7m、幅が 2.3m、衛星構造体が約 1.5m 四方である。実際には地球指向面にアンテナがあるが今回は省略している。

解析におけるグリッド・モデルを図５に示す。グリッドサイズは、１０ｃｍであり、解析空間のグリッド数は、64×128×64 なので、解析空間の大きさは、6.4×12.8×6.4m となっている。

POM の実際のサンプルの大きさは、4cm×4cm であるが、グリッドの関係で 20cm×20cm で模擬している。コーナーのパッチは、太陽光の影響を見るために配置している。

図６に計算結果の１例を示す。解析を行った外部環境の条件は、表６の通りである。

表６　外部環境パラメータ

		密度[m-3]	温度[eV]
低エネルギ一粒子	電子	0.9E6	600
	陽子	1.0E6	350
高エネルギ一粒子	電子	1.65E6	25600
	陽子	1.65E6	25150
太陽方向	＋Z 軸方向		

上記の条件は、NASA の静止軌道衛星の設計ガイドライン NASA-TP-2316［2］の SCATHA 衛星観測による典型的な最悪ケース（Mullen，et.al.,1982）[3]にあたる。それぞれのサンプルと衛星構体との電位差を以下に示す。

SiO2　　：　-2186V
カプトン：　-2454V
テフロン：　-4035V

この計算結果は、衛星構体に光があたり、POM が日陰の状態にあたり、実際の計測データではさらに電位が下がっていることもあり、より詳細な外部環境との比較が必要である。ETS-V には残念ながらプラズマ環境の計測機器が搭載されていないため、今後は、実際の LANL 等の実測値等を用いて詳細解析を行う予定である。また、材料特性の経年変化についても、放射線による試験等の２次電子や光電子放出の変化などのデータも考慮に入れながら解析を行う必要がある。

４．１９年度の MUSCAT の機能追加について

MUSCAT の開発時に行ったユーザレビュー会において要求が多かった GUI やクライアント-サーバシステムについて以下の機能追加を行った。

（１）衛星を構成する部材のグループ化機能
（２）衛星の軌道パラメータに対応する宇宙環境パラメータ及びそれらの変動範囲等をユーザに示す機能
（３）パラメトリック・ランの結果から表面電位がある閾値を越える条件を解析可能なファイルとして出力する
（４）クライアントソフトの速度、メモリ使用量等の改良
（５）クライアントーサーバ接続プログラムの表示等の改良

（１）については、グループ指定中の部材を半透明化して表示（図７）、多重グループ化、パドルなど、同一形状のコピー/ペーストおよび回転、並行移動などの機能を追加している。（２）に関しては、GEO 解析時にはローカルタイム別に外部環境を示す機能や、LEO 解析時には軌道デー

タを入力し、指定した期間での外部環境の変化のグラフを示す機能等を追加した。（３）に関しては、パラメトリック・ランの結果を Excel 形式で出力し、ETS-Ⅷや WINDS 等で使用した放電閾値を超える確率を計算するワークシートに渡し、チャンバー等での実験条件が算出可能にした。

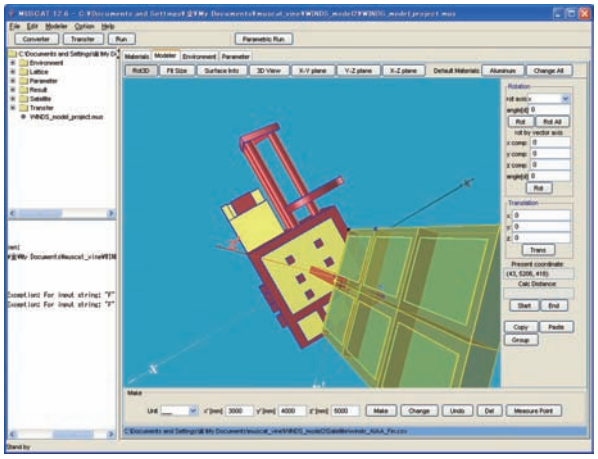

図７　太陽電池パドルのグループ化の例

５．今後の予定

MUSCAT 解析に関し、ETS-V 観測期間の環境データ（LANL 等）を取得し、実際の外部環境を用いた解析と POM 実測の詳細な比較、材料パラメータの変更による差、衛星へ入射する光の角度や、POM のアンテナの影等を考慮した詳細解析等を行う予定である。

また、MUSCAT に関しても、随時ユーザ要求を取り入れた機能追加を行ってゆく予定である。

参考文献

[1]廣三壽　他、「静止軌道宇宙環境における熱制御用絶縁性材料の帯電観測」、電学論 A、118 巻 7/8 号、p759-766、平成１０年

[2]Purvis, C.K. et. al., Design Guideline for Assessing and Controlling Spacecraft Charging Effects, NASA Technical Paper 2361, NASA, 1984

[3]Mullen, E.G. and Gussenhoven, M.G., SCATHA Environmental Atlas, AFGL-TR-83-0002, Air Force Geophysics Lab., 1983.(AD-A131456)

宇宙機環境プラズマシミュレータによる「れいめい」電流モニタの校正

上田裕子、村中崇信(JAXA)
臼井英之(京大)、篠原育(JAXA)
岡田雅樹(NIPR)

目的

- 宇宙機環境シミュレータの機能実証
  - 3D Full-PIC Electrostatic Code
  - プラズマと内部導体等の相互影響を精密に計算
  - PEO環境を実パラメータでシミュレーション可能
- れいめい電流モニタ(CRM:Current Monitor)の特性評価
  - 高時間、空間分解能　→プラズマパラメータの統計的データとして活用
  - 校正のための地上実験データが不足

Outline

1. れいめいCRMによる観測
2. シミュレーション・モデル
3. 解析状況
4. まとめと今後の予定

1. れいめいCRMによる観測

- 軌道：太陽同期、極軌道、高度620-670km
- CRM: 衛星側面に取り付けられたパッチ型ラングミュア　プローブ(1 single probe, 2 double probes)、320ms/sweep
- 背景プラズマパラメータ推定に対する衛星構体の影響評価が必要
  - 構体によるシース
  - 衛星ドリフトによるWake
  - 光電子

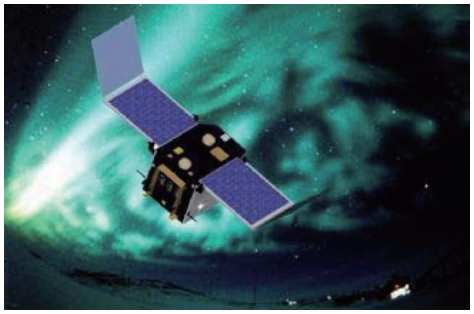

観測データの例

2006年9月2日　UT09:00-09:04

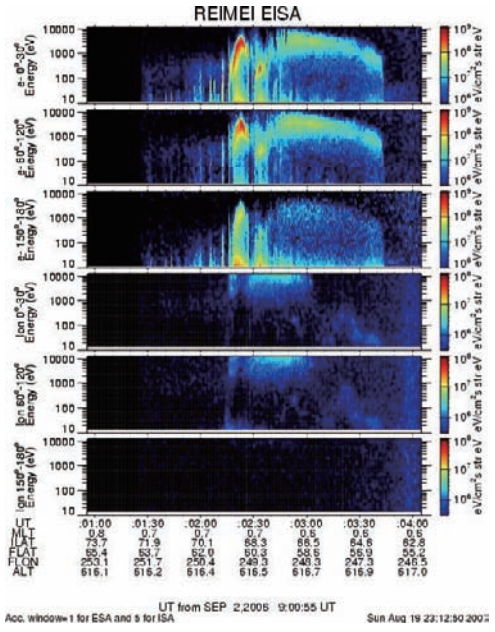

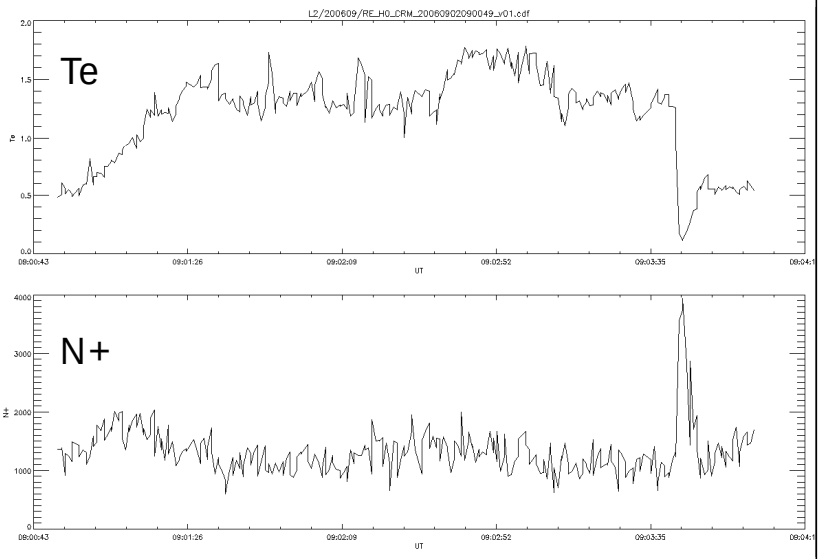

CRMデータからの推定値

2．シミュレーション・モデル

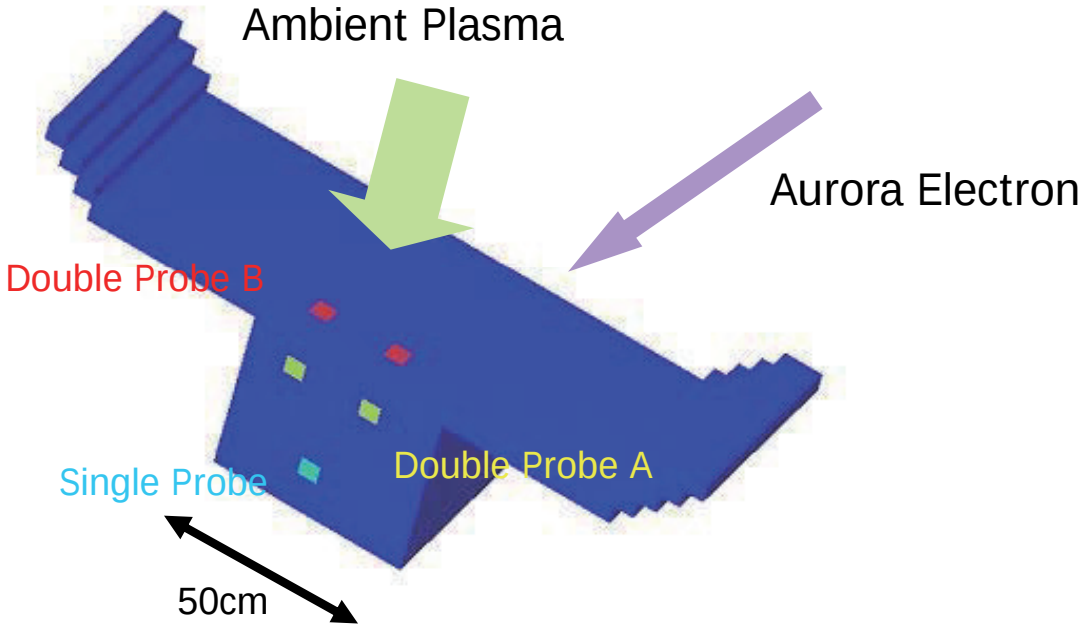

パラメータ

Background Plasma	Density	2.0e9 [m^{-3}]
	Temp.	0.20 [eV]
High Energy Electron	Density	7.8e6 [m^{-3}]
	Temp.	750 [keV]
	Drift Energy	7.5 [keV]
Satellite Drift Velocity		8.0 [km/s]
Simulation System	Number of Grids nx*ny*nz	128*128*128
	dx=dy=dz	0.05 [m] = ½ Debye Length
	dt	5.0e^{-8} [s]

3. 解析状況

3.1 衛星構体によるシースの影響評価

- Thermal プラズマ中（ドリフト無し）
- 構体によるシースの影響を受けないTest ProbeとCRM Single Probeを同時に挿引(構体浮動電位に対してバイアス)

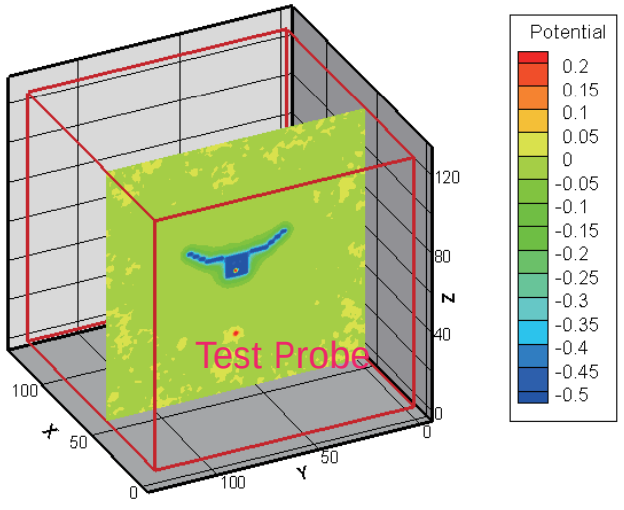

電位分布

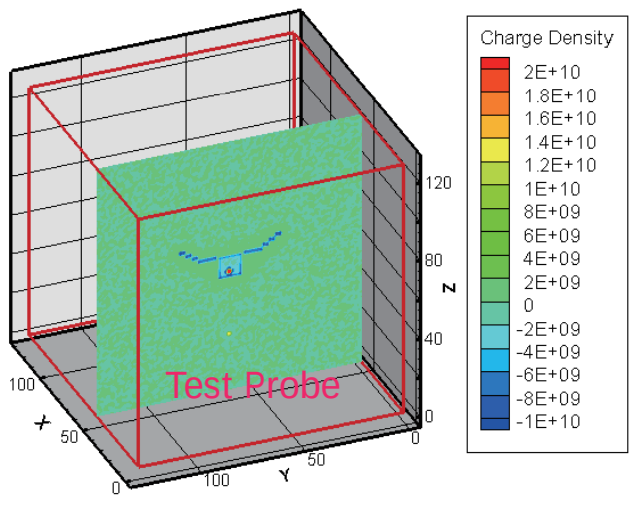

電荷密度分布

3.1　衛星構体によるシースの影響評価

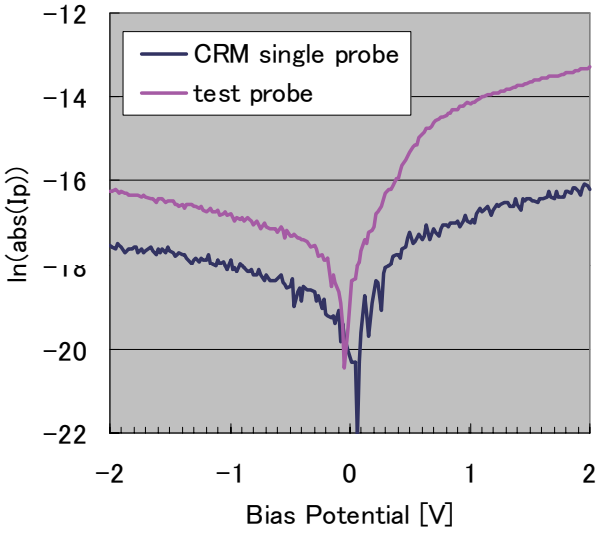

プローブ電流－電圧特性

	理論値	Test Probe	CRM Single
電子温度 [eV]	0.20	0.21	0.34
電子密度 [m^{-3}]	$2.0e^9$	$2.3e^9$	$1.9e^9$

電子温度推定値は構体によるシースにより本来の値より高く見積もられる

密度推定には電子温度推定値を用いるためその誤差が伝播する

3.2　衛星ドリフトの影響評価

- ドリフト速度はイオン熱速度と同程度
- Single Probe面はドリフト方向と垂直

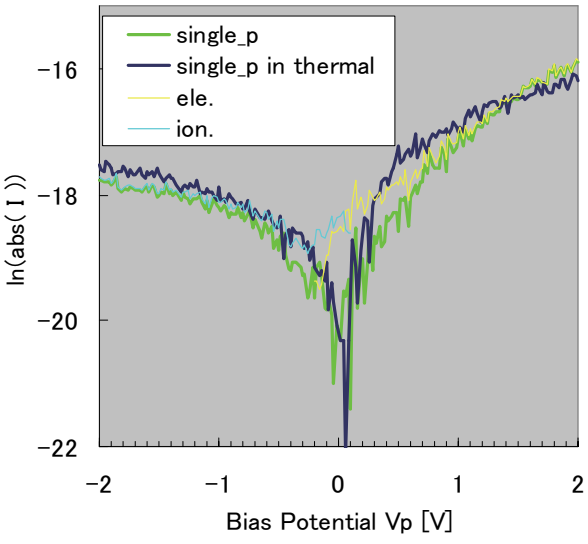

プローブ電流－電圧特性

	理論値	Thermal	Drift
電子温度 [eV]	0.20	0.34	0.38

3.2 衛星ドリフトの影響評価

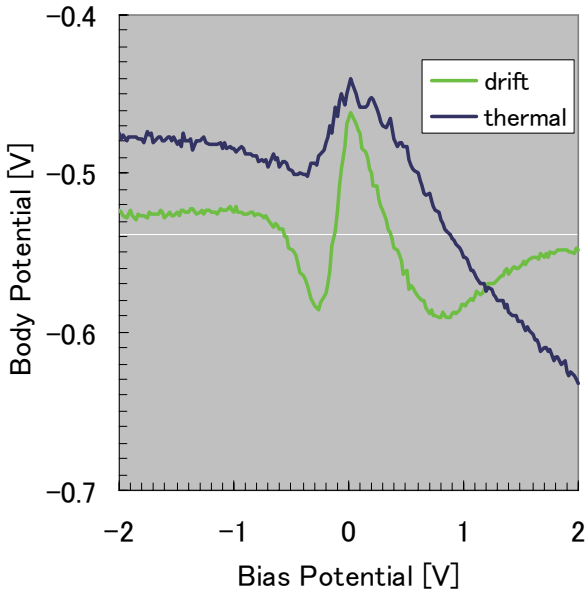

プローブ電圧による衛星浮動電位の変化

Vp>0側でイオンドリフト電流のため構体電位が負になりにくい

↓

電子温度推定に影響が大

まとめ

- Full-PICシミュレーションで「れいめい」CRMの特性を再現することが可能
- 衛星構体によるシース中での測定では、本来より高い電子温度推定値を示す
- 衛星ドリフトにより、電子温度推定値はさらに高い推定値を示す

今後の予定

- オーロラ環境でのCRMの特性確認
- 誘電体面（太陽電池カバーガラス）を考慮
- 光電子放出を考慮
- CRM推定値校正のためのデータ蓄積

だいち衛星(ALOS)軌道に於ける宇宙放射線環境評価
- 計測結果と太陽活動極小期宇宙放射線環境モデルの比較 -

丸山 健太*[1]、越石英樹[2]、松本晴久[2]、五家建夫[2]

[1] 鹿児島大学、 [2] 宇宙航空研究開発機構

Evaluation of the space radiation environment in the orbit of the DAICHI satellite (ALOS)
- Comparison of the measurement results with the space radiation environment models during the solar activity minimum period -

Kenta Maruyama* [1], Hideki Koshiishi [2], Haruhisa Matsumoto [2], Tateo Goka [2]

[1] Kagoshima Univ., [2] Japan Aerospace Exploration Agency

概要

今現在、地球周りの放射線環境を模擬したモデルが多数存在している。放射線帯に捕捉されている陽子線や電子線に関しては AP-8, AE-8 モデル、太陽陽子線に関しては JPL-1991, SOLPRO モデル、銀河宇宙線に関しては CREME モデルなどである。しかし、これらの放射線モデルはどれも 1990 年代よりも昔のデータに基づいて作成されており、データの精度があまり良くないという問題点がある。また、モデルによる計算結果が実際の放射線環境とはズレが生じていることがわかってきており、さまざまな問題点や改良すべき点が報告されている。それらの問題点や改善点を考慮した新しい放射線モデル作成の提案が出ているが、まだまだ議論や観測データが必要とされている。

そこで本研究では、新しい放射線モデル作成に有益な情報を得ることを目的として、だいち衛星によって観測されたデータとこれらのモデルの計算結果を用いることで、だいち衛星の軌道に於いてという限られた範囲ではあるが、既存モデルと実際の放射線環境との比較を行った。

1. イントロダクション

地球周りの放射線環境は大きく分けると、捕捉粒子線、太陽陽子線、銀河宇宙線に分けられる。

捕捉粒子線とは放射線内帯に捕捉されている電子線、陽子線のことであり、それぞれに関して AE-8[(1)]、AP-8[(2)]という放射線モデルが存在する。また、太陽陽子線とは太陽フレアなどに伴い太陽から飛来してくる陽子線で、これに関しては JPL-1991[(3)]、SOLPRO[(4)]という放射線モデルが存在する。銀河宇宙線とは太陽系外から飛来してくる粒子線で、これに関しては CREME[(5)]というモデルにより計算される。

なぜこのような放射線モデルが必要なのだろうか。近年、宇宙機に搭載されるような半導体素子はより高性能で小型化されてきているが、それに伴い放射線に対する感受性が高くなり、トータルドーズやシングルイベントと呼ばれる劣化や誤動作を衛星に引き起こすことがある。従って、これらのモデルを用いて軌道上での放射線環境を予測するということが重要となってくる。

しかし、これらのモデルはどれも 1990 年代よりも前の観測データに基づいて作成されているためにデータの精度が悪いという問題点がある。また、各国の衛星による観測データとつき合わせてみると、実際の放射線環境とはズレが生じているという報告が多数されている。

そこで本研究では、だいち衛星によって観測されたデータとモデルによる計算結果を用いることで、だいち衛星の運用されている軌道に於いてという限られた範囲ではあるが、既存モデルと実際の放射線環境との比較を行う。

2. 観測装置

本研究で使用した観測データはだいち衛星（ALOS）に搭載された技術データ取得装置（TEDA: Technical Data Acquisition equipment）により観測された。だいち衛星は 2006 年 1 月 24 日に種子島宇宙センターより打ち上げられた地球観測衛星であり、赤道上高度：691.65km、軌道傾斜角：98.16°の太陽同期準回帰軌道で運用されている。技術データ取得装置は衛星周りの放射線環境を知る目的で搭載されており、軽粒子観測装置（LPT: Light Particle Telescope）、重イオン観測装置（HIT: Heavy Ion Telescope）から構成される。本研究では LPT により観測された電子、陽子のデータを用いて解析を行った。LPT の主要緒元を表 1.に示す。

表 1.　軽粒子観測装置（LPT）の主要緒元

観測粒子	観測エネルギー範囲（MeV）
電子	0.100 – 4.122
陽子	5.9 – 25.7
He3	20.7 – 94.0
He4	23.5 – 96.0

3. 観測結果

図 1、図 2 にだいち衛星により観測された陽子、電子フラックスの地理的分布を示す。

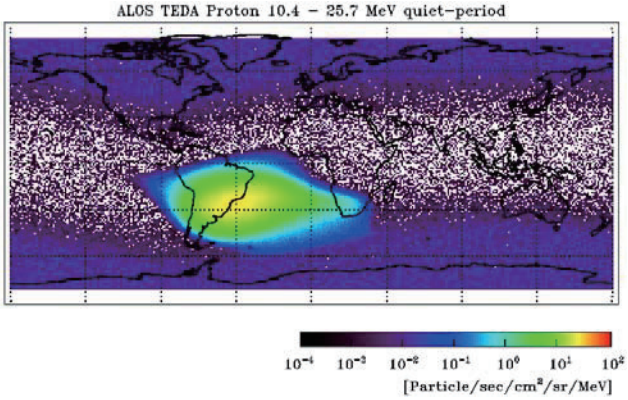

図 1. 陽子フラックスの地理的分布（静穏期）

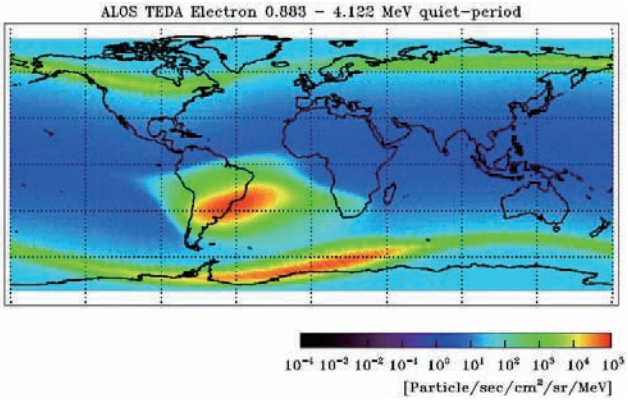

図 2. 電子フラックスの地理的分布（静穏期）

今後、だいち衛星により観測されたデータと既存モデルの計算結果とを比較するために、観測データを平均したモデルを作成する。ここで問題となってくるのは SAA（South Atlantic Anomaly）領域と呼ばれる放射線内帯の一部が低軌道に入り込んでいる領域（図 1、2 のブラジル上空に見られる粒子フラックスの値の大きい領域）が存在することである。SAA 領域とそれ以外の領域とでは放射線環境が大きく異なるため、観測データの平均モデルを作成する際にはこれらを分けて考える必要がある。また電子については放射線外帯の一部が低軌道に入り込んでいる Horn 領域（図 2 の高緯度域で見られる粒子フラックスの値の大きい領域）も分けて考える必要がある。

したがって、陽子については SAA 領域とそれ以外、電子については SAA 領域と Horn 領域とそれ以外の領域でそれぞれ平均モデルを作成していく。

図 3、図 4 に太陽活動の比較的静かな静穏期に於ける SAA 領域についての陽子、電子フラックスの地理的分布と IGRF モデル[6]により計算された磁場との関係を示す。

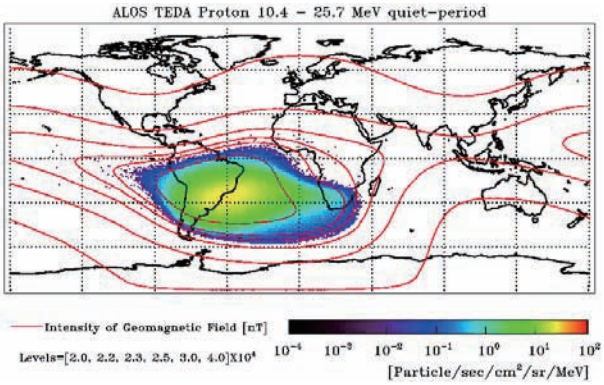

図 3. 陽子フラックスの地理的分布（SAA 領域）

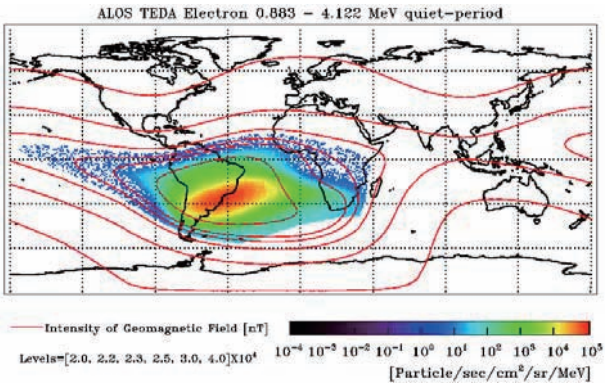

図 4. 電子フラックスの地理的分布（SAA 領域）

SAA 領域に於いては、陽子、電子の粒子フラックスは磁場に沿って分布している。よって SAA 領域に於ける平均モデルを作成する際には、粒子フラックスと磁場の相関関係を利用することにする。

同様に SAA 領域以外に於いては、粒子フラックスと Geomagnetic Cut-Off Rigidity の相関関係を利用し、Horn 領域に於いては粒子フラックスと経度の相関関係を利用してそれぞれの領域に於いて陽子と電子の平均モデルを作成する。

また、だいち衛星の運用期間は太陽活動極小期にあたるために太陽活動は比較的静穏なのだが、2006 年 12 月に太陽フレア/CME (Coronal Mass Ejection)が多数発生している。したがって、太陽フレアなどの太陽活動が活発な時期をフレア期、それ以外の時期を静穏期として分けて解析を行った。

4. 作成した平均モデルについて

図 5、図 6 に SAA 領域に於ける陽子、電子フラックスと磁場の関係を示す。図の横軸は磁場の強さ、縦軸は粒子フラックスで表されており、黒色は静穏期、赤色はフレア期のデータであることを示している。また、エラーバーによりその点のデータがどれほどのバラつきを持ったデータの平均値なのかということを示している。

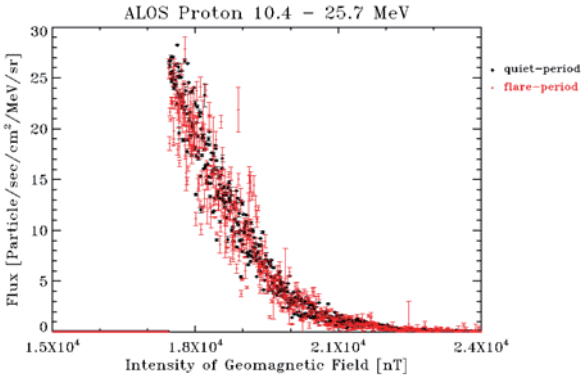

図 5. 陽子フラックスと磁場の関係（SAA 領域）

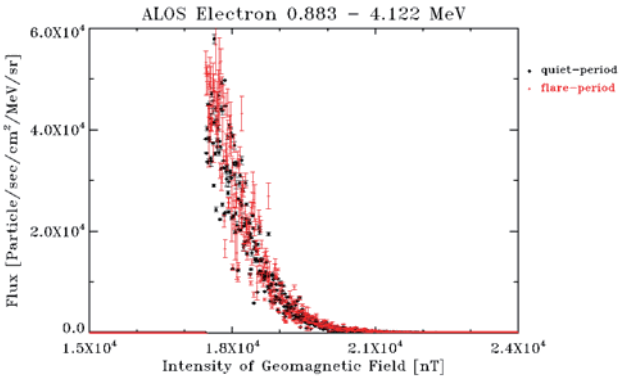

図 6. 電子フラックスと磁場の関係（SAA 領域）

陽子、電子ともに粒子フラックスと磁場に良い相関関係が見られる。静穏期とフレア期のデータを比べるとあまり大差ないように見える。これは SAA 領域に捕捉されている粒子が放射線内帯の粒子であり、放射線内帯は太陽フレアなどの影響を受けにくい安定な領域であるためと考えられる。しかし、データのバラつきを見てみるとフレア期のデータのバラつきが大きいため、太陽フレアなどの影響をいくらかは受けているようである。

図 5、図 6 を多項式でフィッティングしたものを図 7、図 8 に示し、これを SAA 領域に於ける平均モデルとする。

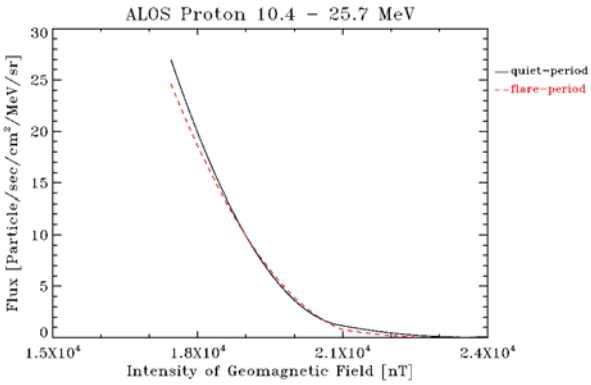

図 7. 平均モデル（SAA 領域、陽子）

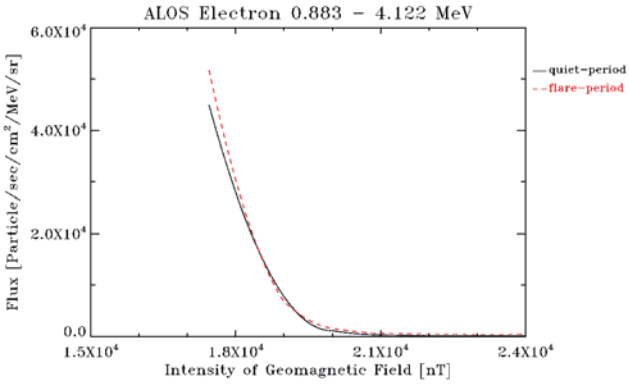

図 8. 平均モデル（SAA 領域、電子）

同様にして作成した SAA 領域以外に於ける平均モデルを図 9、図 10 に示す。フレア期のデータで Rigidity が小さい領域、つまり極域で粒子フラックスの値が大きいのは、磁力線の開いた極域に太陽フレアなどに伴う粒子が降り込んできているためであると考えられる。電子のデータが一部除かれているのは、Horn 領域の定義として Rigidity が 0.1 – 3 GV という定義をしているためである。

Horn 領域に於ける静穏期、フレア期の平均モデルを図 11、図 12 に示す。図の青色は北極側の Horn 領域、橙色は南極側の Horn 領域の平均モデルを示している。粒子フラックスの値の違いはあるが、静穏期とフレア期とでは同じような形を持った平均モデルが得られた。

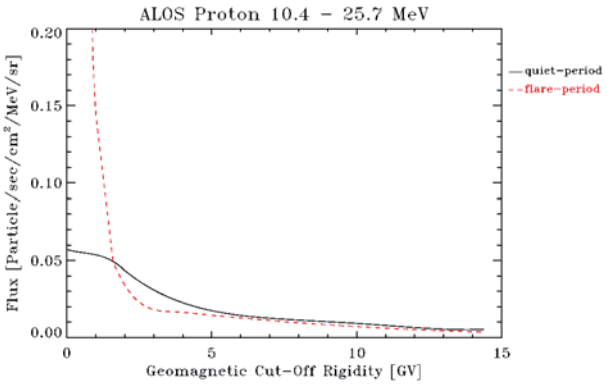

図 9. 平均モデル（SAA 領域以外、陽子）

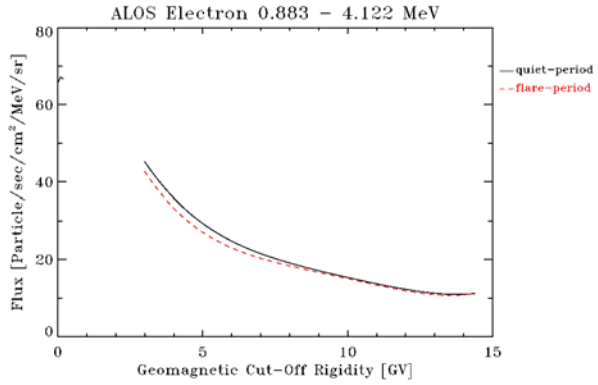

図 10. 平均モデル（SAA 領域以外、電子）

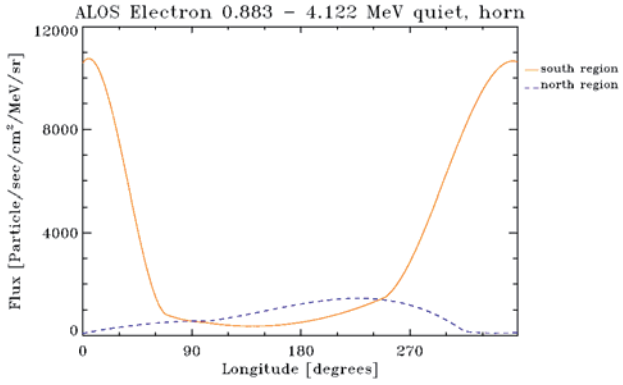

図 11. 平均モデル（Horn 領域、静穏期）

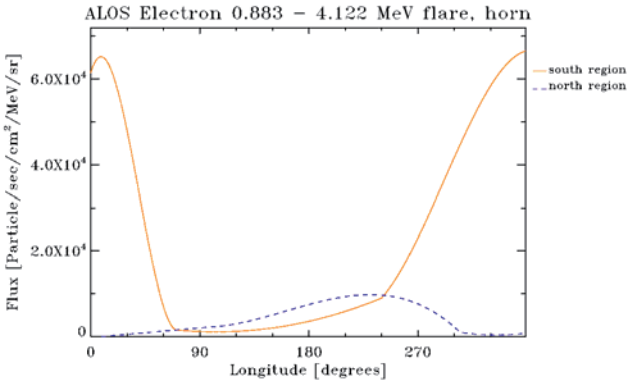

図 12. 平均モデル（Horn 領域、フレア期）

5. 既存モデルとの比較

次に上記のようにして作成した平均モデルと既存モデルによる計算結果とを比較してみる。

図 13、図 14 に SAA 領域に於ける陽子の平均モデルと既存モデルによる計算結果を示し、図 15、図 16 に SAA 領域に於ける電子の平均モデルと既存モデルによる計算結果を示す。ここではそれぞれを比較しやすいように縦軸のスケールを合わせてある。また、だいち衛星の観測データは太陽活動極小期にあたるデータであるため、既存モデルでは太陽活動極小期のモデルである AP8MIN の計算結果を比較対象としている。

陽子、電子についてそれぞれ比較してみると、陽子については既存モデルが平均モデルよりも過大評価、電子については既存モデルが平均モデルよりも過小評価しているという結果になった。

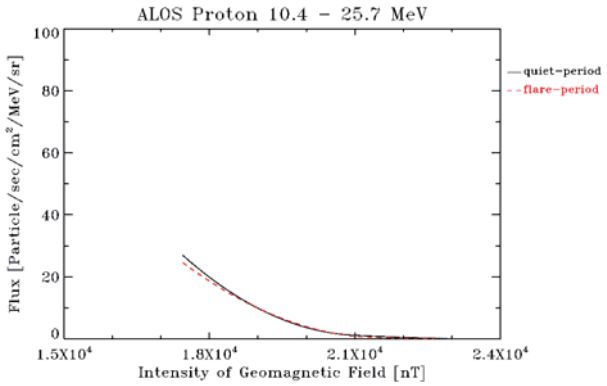

図 13. 平均モデル（SAA 領域、陽子）

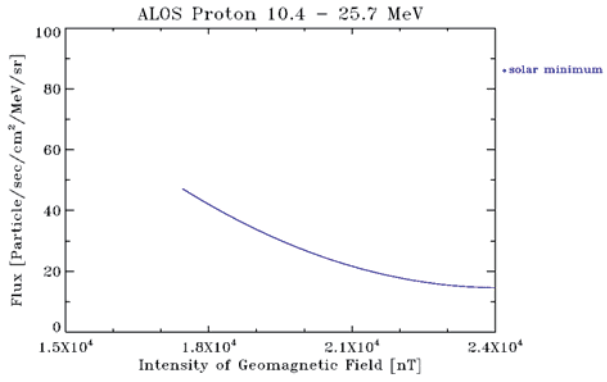

図 14. 既存モデル（SAA 領域、陽子）

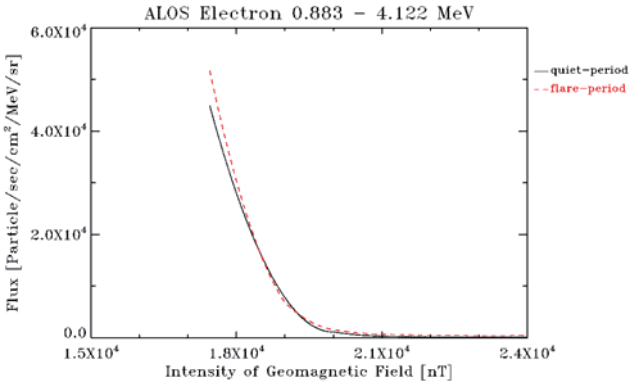

図 15. 平均モデル（SAA 領域、電子）

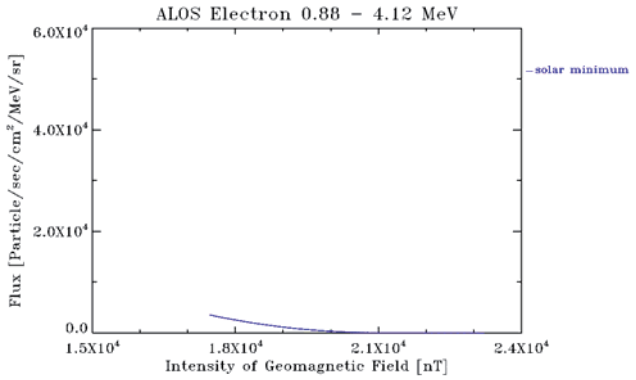

図 16. 既存モデル（SAA 領域、電子）

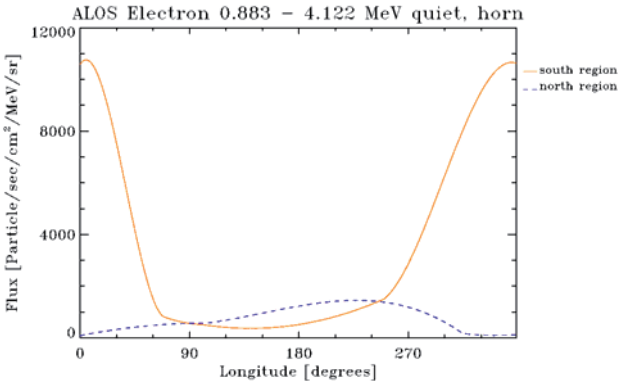

図 17. 平均モデル（Horn 領域、静穏期）

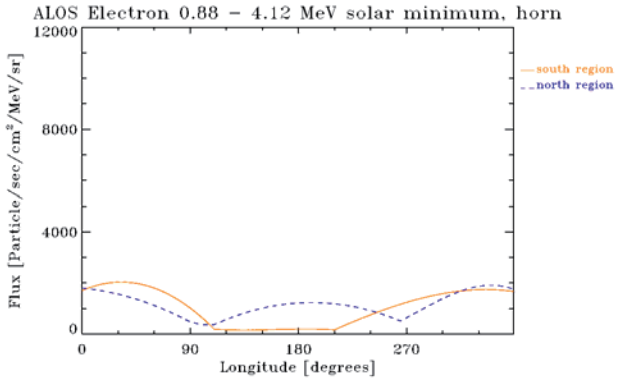

図 18. 既存モデル（Horn 領域、極小期）

SAA 領域以外に於いては、陽子に関してはいくつかの既存モデルが存在するが、電子に関しては存在しない。陽子の既存モデルもだいち衛星のような低軌道に関してはあまり良い計算結果が得られず、観測データと比較するにしても極域のごくわずかな領域でしか比較することができない。また、このような低軌道に於ける放射線環境は SAA 領域による影響が大半を占めており、それ以外の領域による影響は極めて小さい。

そこで本研究では SAA 領域以外に於いては平均モデルと既存モデルとの比較を行わないこととし、既存モデルとしては AP-8、AE-8 モデルを用いて比較を行っていく。

図 17、図 18 に Horn 領域に於ける電子の平均モデル（静穏期）と既存モデルによる計算結果を示す。ここでもそれぞれを比較しやすいように縦軸のスケールを合わせてある。既存モデルとしては太陽活動極小期のモデルである AE8MIN の計算結果を比較対象としている。

比較してみると、北極側ではモデルの形も粒子フラックスの値もほぼ一致していると言えるが、南極側では既存モデルが平均モデルよりも過小評価しているという結果となり、SAA 領域と同様の結果が得られた。

6. 粒子フルエンスの比較

これまでの結果を受け、平均モデル、既存モデルを粒子フルエンスを用いて比較する。

粒子フルエンスというのは粒子フラックスを時間方向に積分したもので、ある軌道に於いてどれだけの放射線環境に曝されてきたのかということを示す値である。実際に衛星の設計などで耐放射線環境を考える際には、設計寿命の間でどれだけの放射線環境に曝されるかということが問題となってくるため、放射線モデルにより粒子フルエンスを計算することは耐放射線環境設計において非常に重要なものである。

図 19、図 20 に 1 年 4 ヶ月分の陽子、電子の粒子フルエンスを示す。黒は平均モデルにより計算された粒子フルエンス、赤は実際にだいち衛星により観測された実測値、青は既存モデルにより計算された粒子フルエンスを示している。既存モデルにより計算された結果には SAA 領域以外の計算結果が含まれていないため、赤と黒の点線により SAA 以外の領域を除いた平均モデルの計算結果、実測値を示している。

また、既存モデルの結果は太陽活動極小期のモデルで計算したものであり、太陽フレア/CME の影響はほとんど含まれていない。一方、平均モデル、実測値では 2006 年 12 月

に複数発生した太陽フレア/CME の影響でその期間において急激に粒子フルエンスが増大している。

陽子について SAA 領域以外を除いた平均モデル、実測値の計算結果（図の点線で表されている結果）、つまり SAA 領域のみでの計算結果では、太陽フレア/CME による影響が見られない。これは陽子が太陽フレア/CME の影響を受けるのは主に極域であることによるものである。

一方、電子について SAA 領域以外を除いた平均モデル、実測値の計算結果では太陽フレア/CME による影響を受けているように見える。これは電子では SAA 領域以外を除いても Horn 領域が含まれているためである。

つまり、陽子では太陽フレア/CME により主に極域で粒子フラックスが増大するが、電子では極域での粒子フラックスの増大よりも、Horn 領域での増大の影響が大きいということになる。

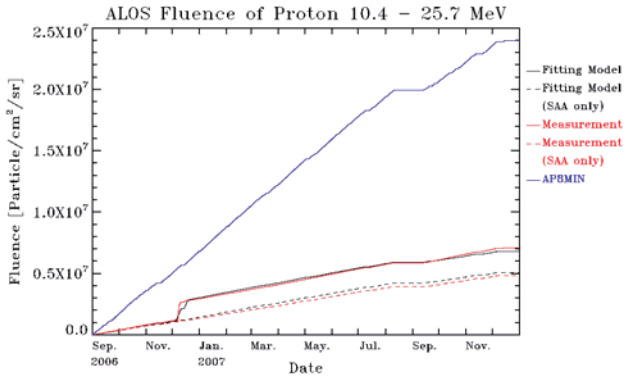

図 19. 陽子の粒子フルエンス

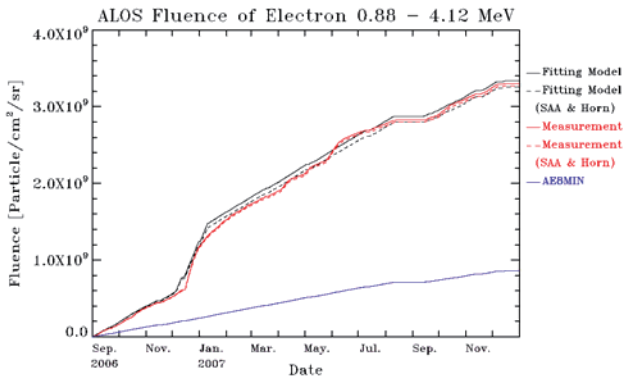

図 20. 電子の粒子フルエンス

陽子について見てみると、既存モデルが実際の放射線環境を 1 年間換算で約 4.6 倍大きく見積もっているという結果になる。

電子については、既存モデルが実際の放射線環境を 1 年間換算で約 1/4 倍小さく見積もっているという結果になる。

7. まとめと課題

地球周りの放射線環境を模擬するモデルが多数存在しているが、どのモデルも 1990 年代よりも昔のデータに基づいて作成されており、データの精度があまり良くないという問題点がある。また、これらのモデルにより計算された結果と実放射線環境との間にズレが生じているという報告もなされており、さまざまな問題や改善点が残されている。そこでこれらの問題や改善点を考慮した新しい放射線環境モデルを作成しようという試みがあるのだが、まだ完成には至っていない。

そこで本研究では、新しい放射線環境モデルが作成されるまでの間に実際の放射線環境を知ることを目的とし、だいち衛星の軌道に於いてという限られた範囲ではあるが、実際に衛星によって取得された観測データと既存モデルで計算された結果との比較を行った。

結果として、太陽活動極小期、高度約 700km の低軌道において、AP8MIN は陽子の放射線環境を 1 年間換算で約 4.6 倍過大評価しており、AE8MIN は電子の放射線環境を 1 年間換算で約 1/4 倍過小評価しているという結果が得られた。

今後の課題として、だいち衛星の観測データのみでは全ピッチ角をカバーしきれていないため、ピッチ角の分布を考慮した解析が必要であるということがある。また、本研究では粒子フルエンスを用いて既存モデルと実放射線環境との比較を行ったが、より実用的な新放射線モデル作成のためにはスペクトルを用いての比較結果が必要となる。

参考文献

(1) D.M. Sawyer, J.I. Vette:"AP-8 trapped proton environment for solar maximum and solar minimum", 1976
(2) J.I. Vette:"The AE-8 trapped electron model environment", 1991
(3) J. Feynman et al.:"Interplanetary proton fluence model - JPL 1991", Journal of Geophysical Research (ISSN 0148-0227), vol. 98, no. A8, p. 13,281-13,294., 1993
(4) E.G. Stassinopoulos:"SOLPRO: A computer code to calculate probabilistic energetic solar proton fluences", 1975
(5) J.H. Adams Jr. et al.:"Cosmic ray effects on microelectronics. Part 1: The near-Earth particle environment", 1981
(6) J. Geomag. Geoelectr.:"International Geomagnetic Reference Field, 1991 Revision", IAGA Division V Working Group 8, 43, 1007-1012, 1991

GEOTAIL衛星より発生した光電子の非対称分布とその原因

下田忠宏 (1)、町田忍 (1)、向井利典 (2)、齋藤義文 (3)、笠羽康正 (4)、早川基 (3)
(1) 京都大・理・地球惑星 (2)JAXA (3)ISAS/JAXA (4) 東北大・理・地球惑星

1　導入

人工衛星の導体表面からは、太陽紫外線の照射により光電子が発生する。地球磁気圏内では衛星の導体表面は背景プラズマに対し数 V から 100V 正に帯電しているため、発生した光電子のうち衛星電位以下のエネルギーのものは衛星表面に引き戻され、プラズマの粒子計測器で観測対象とする自然のプラズマに混入してしまう。従って、粒子計測器で観測された電子の速度空間分布データから光電子の分布を推定することが可能である。本研究では、GEOTAIL 衛星によって観測された光電子の速度分布関数と、その衛星電位依存性について調べた。

2　衛星および観測機器

GEOTAIL[1] は磁気圏探査用衛星として、1992 年 9 月に打ち上げられた。本衛星は、図 1 に示すように本体が直径 2.2m、高さが 1.6m の円柱形であり、その本体からは直交する 50m 長のワイヤーが 2 組 4 本伸びており、また、長さ 6m および 4m の 2 本のマストが対向して設置されている。衛星本体およびマストは導電性の酸化インジウムで覆われており、これらの表面はほぼ等電位となっている。

本研究では、GEOTAIL 衛星に搭載されている観測機のうち、低エネルギー粒子計測器 (LEP-EA)[2]、電場観測プローブ (EFD-P)[3] および磁力計 [4] より得られたデータを用いた。LEP-EA(以下、LEP) は、視野を衛星の回転方向に 16 分割 (Sector 0-15)、仰角方向に 7 分割 (Channel(CH.) 1-7: CH. 番号が大きいほど LEP 視野の仰角は小さくなり、CH. 4 は衛星表面垂直方向から飛行する粒子を観測)、粒子のエネルギー (速度) について 32 分割し、これらを掃引することで、電子・イオンの 3 次元速度空間分布を 12 秒の時間分解能で観測する。この観測器にはエネルギー範囲が異なる 2 つのモード (RAM-A, RAM-B) がある。また、EFD-P は、2 組 4 本のワイヤー (直径 0.45mm) で構成され、先端部以外はポリイミドの絶縁塗装がなされている。2 組のワイヤーは、先端にワイヤーのうち先端に直径 105mm の球プローブがついている 1 組 (PANT) と先端のプローブが無い 1 組 (WANT) からなり、衛星電位は PANT により測定される。PANT では、先端の球プローブと衛星本体間にバイアス電流を流すことで、球表面と背景プラズマをほぼ等電位に保っている。

以下、観測された光電子について、衛星と垂直に入射する場合 (LEP の CH. 4) を中心に述べ、最後に上下方向 (CH. 1, 7) から入射した光電子についての結果を紹介する。

3　光電子分布の 1 例

図 2 は、1995 年 1 月 11 日 1045-1115UT の時間帯に得られた電子カウントを 4 つの飛来方向に分けて求めたエネルギー・時間分布図 (E-t 図)、および衛星電位の時間変化に関するプロットである。このとき衛星は地球中心から $44R_E$ (R_E は地球半径) 離れたほぼ真夜中の領域に位置していた。

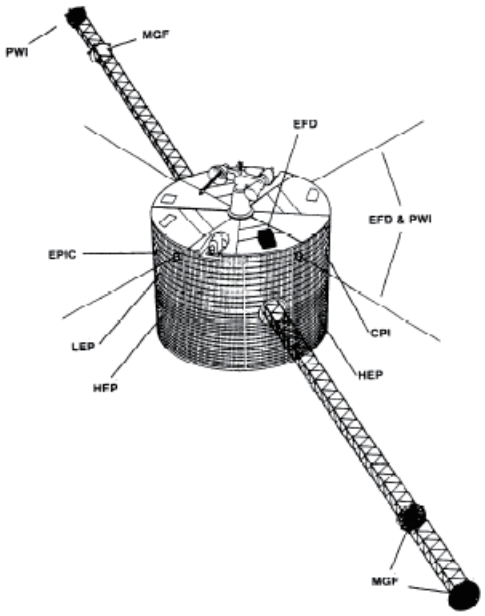

図 1: GEOTAIL 衛星の外観 [1]

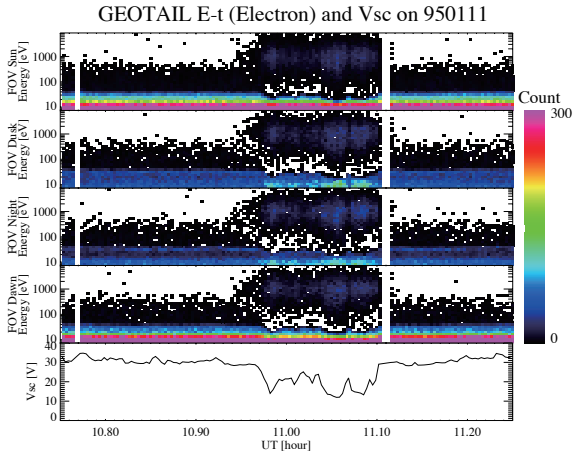

図 2: 1995 年 1 月 11 日 1045-1115UT の期間の電子カウント E-t 図および衛星電位。上から順に、昼側から (夜側へ)、夕方側から、夜側から、朝側から飛行する電子のカウント、衛星電位。上 4 つのパネルについてエネルギーの範囲は 7.4eV - 8.5keV。

30eV より下のエネルギー帯で見られる大きいカウントが光電子によるものであるが、太陽方向と反太陽方向だけではなく、朝側の方向と夕方側の方向についても光電子カウントのエネルギースペクトルに違いが見られ、衛星電位が大きいときに朝夕の非対称性がより明確になる傾向を示している。

4 統計解析

光電子分布の朝夕非対称性と衛星電位の関係を調べるため、以下の統計解析を行った。使用したデータは 1993 年 9 月から 1997 年 6 月までの期間の電子データで、観測モードが RAM-B、衛星が磁気圏内にいてかつ日陰にいないときのデータを選んだ。そのように抽出したデータを衛星電位について 1V 単位でグループ分けした後、それぞれのグループについて電子の微分フラックスの平均値を求めた。衛星の領域判定については、イオンの密度が 0.5 個/cc 以上、イオン速度の反太陽方向成分が 200km/s 以上、イオン温度が 400eV 以下、およびイオン動圧 ($P_d = mnv^2$) が 0.5nPa 以上という 4 つの条件を全て満たすときに、衛星は磁気圏の外 (太陽風中またはマグネトシース) にいると判断して解析より除いた (Nakamura et al., (1997)[5] にて用いられた条件を若干変更)。このデータ抽出より得られた全部で 168,166 個のデータについて、衛星の位置をプロットしたものを図 3 に示す。この図から、磁気圏の広範囲にわたるデータが使用されていることが確認できる。

図 4 に、衛星電位が 12-13V(a)、29-30V(b)、50-51V(c) の時の解析結果を示した。衛星電位よりエネルギーが低い光電子は、衛星電位が高い (c) の場合には、観測器が太陽方向を向いているとき (Sector 13) と反太陽方向を向いているとき (Sector 5) のフラックス比だけでなく、朝側を向いているとき (Sector 9) と夕方側を向いているとき (Sector 1) の比も大きくなる事が分かる。さらに、朝夕のフラックス比は、衛星電位が 12V 台 (a) の時は 8eV(電子の観測下限エネルギー)、同じく 29V 台 (b) では 10eV、50V 台 (c) では 16eV のエネルギーで特に大きく、これらのエネルギーは (b) と (c) の場合、衛星電位の約 1/3 となっている。このことから、光電子分布の偏りは衛星電位そのものよりもむしろ衛星電位に対する光電子のエネルギー (E_0/V_{sc}) に依存していることが推測される。

そこで、上の統計解析で用いられた全てのデータについて、光電子微分フラックスの朝夕比と昼夜比を、衛星電位に対する光電子エネルギー (E_0/V_{sc}) の関数としてプロットした。その結果を図 5 に示す。この図より、光電子フラックスの朝夕比、昼夜比ともに E_0/V_{sc} に強く依存していること

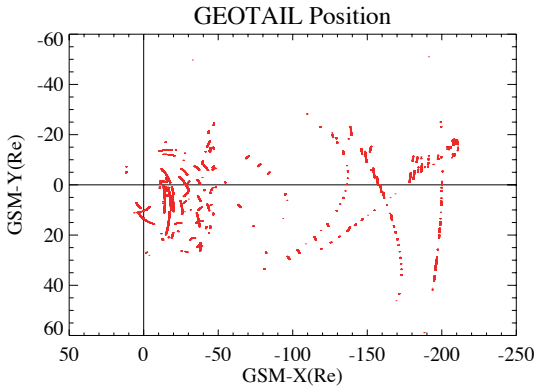

図 3: データ取得期間の衛星位置。GSM-X、GSM-Y の正の向きはそれぞれ地球から見て太陽方向、ほぼ夕方方向。

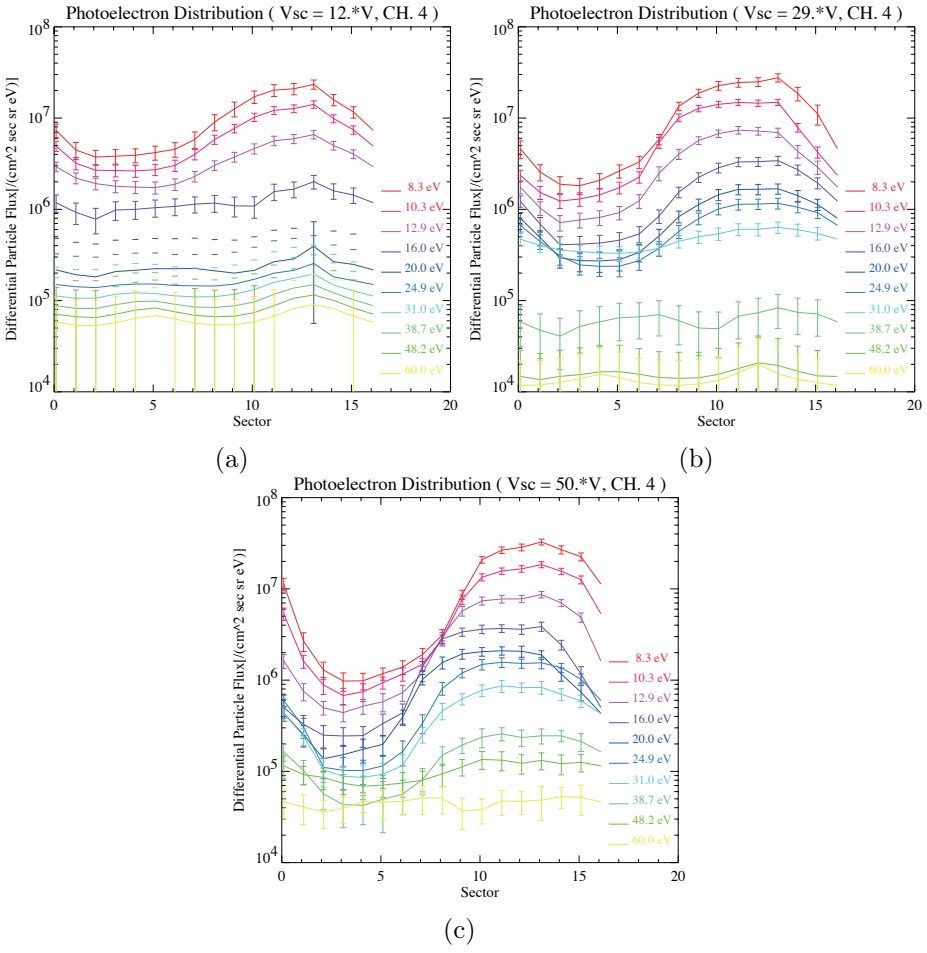

図 4: 3 種類の衛星電位 (V_{sc}) (a) 12V $\leq V_{sc} <$ 13V (データ数 6126) (b) 29V $\leq V_{sc} <$ 30V (同 1182) (c) 50V $\leq V_{sc} <$ 51V (同 36) に関する光電子微分フラックスの衛星スピン軸に直交する面での分布。横軸の Sector 1,5,9,13 はそれぞれ夕方側、夜側、朝側、昼側からの電子が飛来する方向に対応し、エラーバーはそれぞれ平均値からの標準偏差 ($\pm\sigma$)。

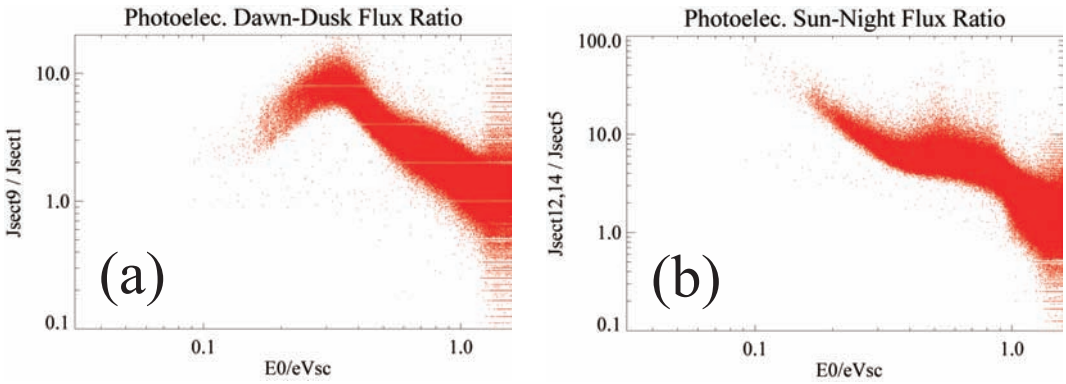

図 5: 統計解析より得られた光電子分布非対称性の E_0/V_{sc} 依存性。(a) 朝側-夕方側から飛来する (光) 電子のフラックス比 ($\frac{J_{sect9}}{J_{sect1}}$) (b) 昼側-夜側から飛来する電子のフラックス比 ($\frac{J_{sect12}+J_{sect14}}{2J_{sect5}}$)。計測器内部に太陽光が直接入り込んでしまう Sector13 のデータは除外。

が分かる。そして、昼夜比は電子のエネルギーが低いほど大きく、朝夕比は衛星電位の約 1/3 のエネルギーで約 10 となり最も大きくなることが分かる。

5 数値計算

統計解析によって明らかになった光電子の非対称性について、数値計算を用いることでその原因を調べた。この数値計算では、3 次元円筒座標系にて電子を LEP の位置から時間を遡ってトレースし、光電子の発生位置を求めている。数値計算における空間領域および衛星の形状を図 6 に示す。計算リソースの都合上、マストの形は扇形とし、PANT, WANT の長さを実物より短くしている。また、PANT, WANT のワイヤー径は数値計算の格子間隔に比べて非常に細いため、これらは動径方向の格子線として与えた。

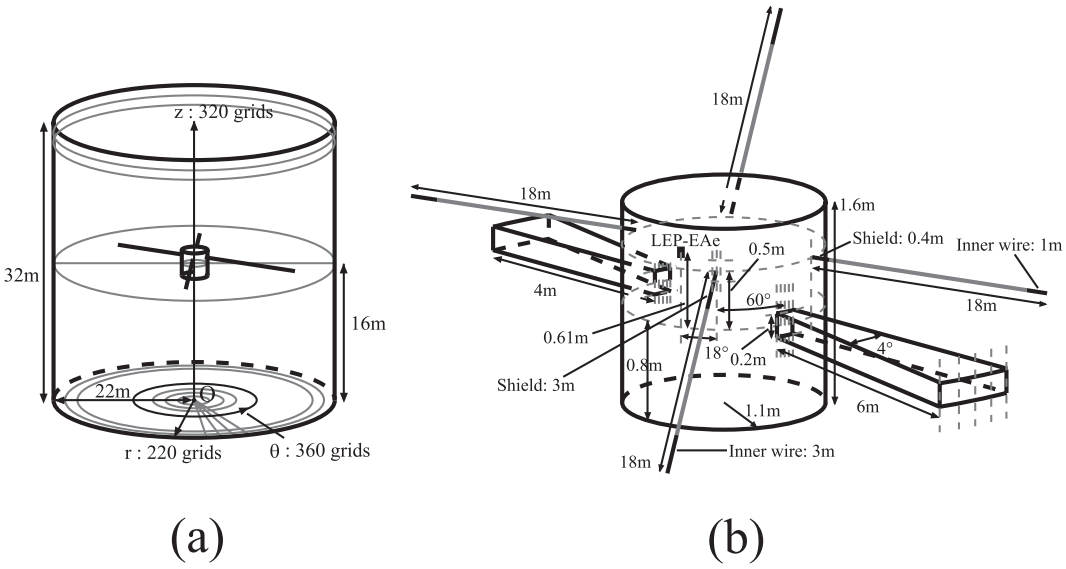

図 6: (a) 数値計算空間および GEOTAIL の配置 (b) 数値計算上での GEOTAIL の形状モデル

上記の系の境界条件としては、衛星電位を 30V、計算領域の外部境界を 0V とした。PANT の先端から 1m の電位は 2V とし、PANT の衛星側、WANT 全体、マストの電位は衛星電位と同一とし

た。また、電場の計算には Laplace 方程式を用いた。衛星周辺の空間には光電子が存在しているにもかかわらず、これらを無視して電場を求めているのは、Cluster 衛星の数値計算 [6] においてこれらの光電子の有無による電位差は高々0.6V 程度となり、衛星電位に比べて無視できるほど小さいためである。

電場を計算した後に、LEP に入射する光電子について LEP 入射時点から時間を遡り、軌道と発生位置を計算した。その際、光電子は全て衛星本体から発生したものと考え、光電子がマストの位置に来たときにはそのまま通り抜けるものとした。

このようにして求めた衛星周辺の電位分布および XY 平面上に投影した光電子軌道は図 7 のようになる。この図では、LEP の視野角内 (仰角 10 度×回転方向角 5 度) で掃引した同一エネルギーの光電子の軌道を全て表示している。WANT や PANT、マストの存在により、衛星周辺の電位分布は 1/r 則に従わず、光電子の軌道はワイヤー周辺の電場の影響を大きく受けている。特に、7eV の電子は LEP から回転方向角正方向の領域から発生し、衛星の表面から数 m の距離まで飛行してから LEP に入射することがわかる。この位置関係は、LEP が朝側 (夕方側) を向いているときに光電子の発生位置が昼側 (夜側) となる。

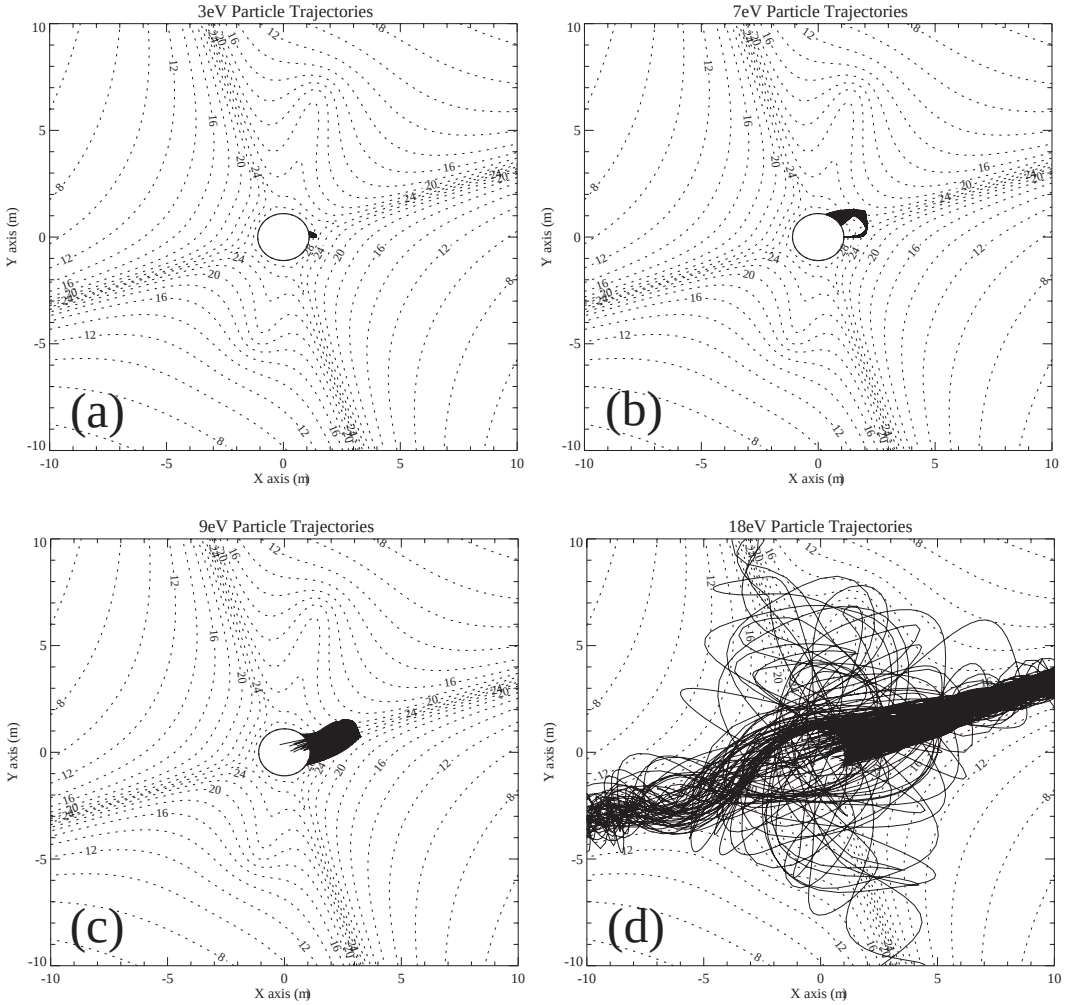

図 7: GEOTAIL 周辺の電位分布および光電子の軌道。 (a)3eV の光電子の場合。 (b) 同 7eV。 (c) 同 9eV。 (d) 同 18eV。

このことを踏まえ、観測データの統計解析と同様、数値計算の結果について光電子のフラックス比を求めた。

LEP の視野の向きを決めることで、図の結果を用いて個々の光電子発生位置の太陽角が一意に決まる。その発生位置の光電子生成量を光電子のフラックスとし、このフラックスを数値計算で扱った全ての光電子についてを足し合わせることで、LEP に入射する光電子フラックスが計算できる。本研究ではその光電子生成量を、太陽光が照射している面では $q_{ph}\cos\theta + q_{iso}$、太陽光が照射していない面 (頂面、底面含む) では q_{iso} として与えた。ここで、q_{ph}, q_{iso}, および θ はそれぞれ光電子生成関数、(2 次電子などの) 等方的に発生する成分、太陽方向を基準とした角度を表す。このようにして求めた光電子のフラックス比を図 8 に示す。

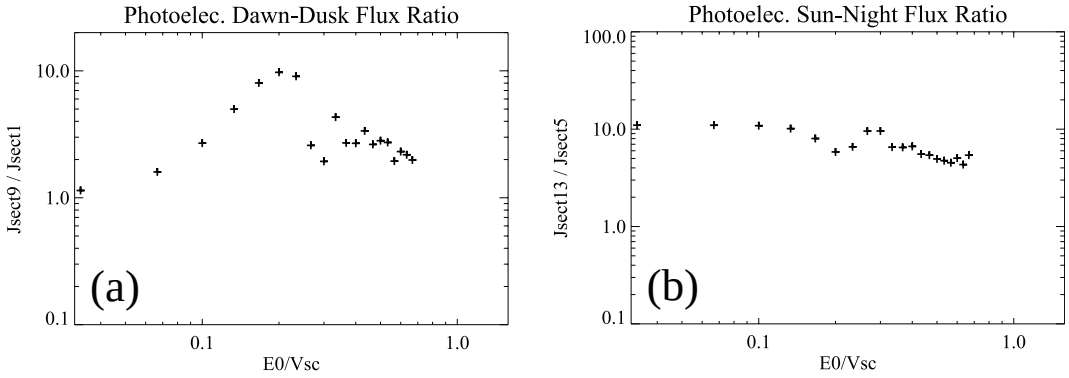

図 8: 数値計算より得られた光電子分布非対称性の E_0/V_{sc} 依存性。(a) 朝側-夕方側から飛来する (光) 電子のフラックス比 ($\frac{J_{sect9}}{J_{sect1}}$) (b) 昼側-夜側から飛来する電子のフラックス比 ($\frac{J_{sect13}}{J_{sect5}}$)。数値計算では太陽光が直接計測器に入射する影響がないため Sector13 のデータを使用。

フラックス比と光電子エネルギーの関係について、エネルギーが観測結果 (図 5) より低い方向にずれているものの、両者は互いによく似た傾向を示している。

6　上下方向から飛来する光電子

これまでは衛星の側面に垂直に入射する (LEP の CH.4) 光電子のみを扱ったが、上方向 (CH.1) および下方向 (CH.7) から飛んでくる光電子についても同様の解析および数値計算を行った。これらについても、観測と数値計算とで非常に近い傾向の曲線が得られたが、その中で特徴的なのは、図 9 に示すように CH.7 において夜側から入射する光電子フラックスが昼側から入射する成分を上回るエネルギーが存在することである。この現象は Cluster 衛星でも観測されているが [7]、今回の数値計算によって得られた軌道を見ると、昼側で発生した多量の光電子の一部が衛星底面の下を通って夜側に回りこみ、LEP に入射していることがわかった。

7　考察とまとめ

GEOTAIL 周辺の光電子分布を解析することで、光電子が昼夜方向のみならず朝夕方向にも非対称分布を持つことがわかった。また、数値計算により、人工衛星本体の太陽面で発生した光電子がワイヤーアンテナ近傍の電場により朝側に運ばれ、それを LEP が観測している様子が明らかになった。さらに、光電子フラックス比についても、観測と同様の傾向が再現された。

光電子フラックス比について観測の統計解析と数値計算を比較すると、比がピークとなる光電子エネルギーがシフトしているものの、フラックス比と光電子エネルギーの関係は両者ともにほとんど同じ傾向を示し、数値計算は観測結果を再現しているといえる。

このことから、光電子の非対称性は、衛星近傍にあるワイヤーによって生じる電場が原因だと結論づけることが出来る。このような非対称性を無くすためには、粒子計測器から見たワイヤーなど

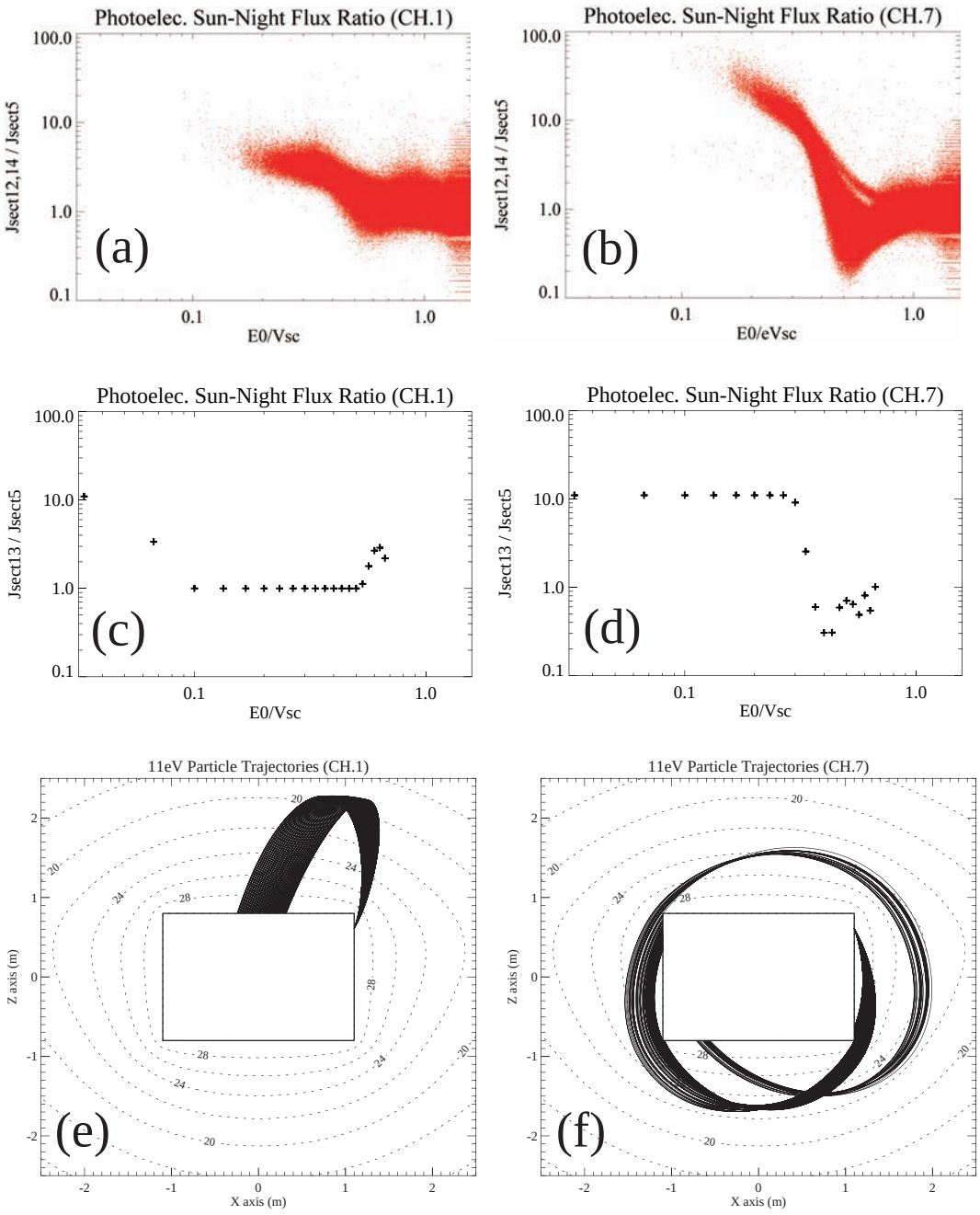

図 9: (a) 観測より得られた CH. 1 での昼側-夜側光電子フラックス比 ($\frac{J_{sect12}+J_{sect14}}{2J_{sect5}}$)。 (b) 同 CH. 7。 (c) 数値計算より得られた CH. 1 での昼側-夜側光電子フラックス比。 (d) 同 CH. 7。 (e)CH. 1 に入射する 11eV の光電子の軌道。 (f) 同 CH. 7。

の構造物が対称に配置されることが必要であり、本研究で得た知見は今後のデータの理解や衛星の構造設計に有効に役立つことが期待される。

参考文献

[1] A. Nishida. The GEOTAIL mission. *Geophys. Res. Lett.*, 21(25):2871–2873, 1994.

[2] T. Mukai, S. Machida, Y. Saito, M. Hirahara, T. Terasawa, N. Kaya, T. Obara, M. Ejiri, and A. Nishida. The low energy particle (LEP) experiment onboard the GEOTAIL satellite. *J. Geomag. Geoelectr.*, 46:669–692, 1994.

[3] K. Tsuruda, H. Hayakawa, M. Nakamura, T. Okada, A. Matsuoka, F. S. Mozer, , and R. Schmidt. Electric field measurements on the GEOTAIL satellite. *J. Geomag. Geoelectr.*, 46:693–711, 1994.

[4] S. Kokubun, T. Yamamoto, M. H. Acun a, K. Hayashi, K. Shiokawa, and H. Kawano. The GEOTAIL magnetic field experiment. *J. Geomag. Geoelectr.*, 46:7–21, 1994.

[5] R. Nakamura, S. Kokubun, T. Mukai, and T. Yamamoto. Changes in the distant tail configuration during geomagnetic storms. *J. Geophys. Res.*, 102(A5):9587–9601, 1997.

[6] C. M. Cully, R. E. Ergun, and A. I. Eriksson. Electrostatic structure around spacecraft in tenuous plasmas. *J. Geophys. Res.*, 112:A09211, doi: 10.1029/2007JA012269, 2007.

[7] S. Szita, A. N. Fazakerley, P. J. Carter, A. M. James, P. Travníček, G. Watson, M. André, A. Eriksson, and K. Torkar. Cluster PEACE observations of electrons of spacecraft origin. *Ann. Geophys.*, 19:1721–1730, 2001.

能動的プラズマ放出による
極域衛星帯電緩和に関するPICシミュレーション

臼井 英之、今里 康二郎（京都大学 生存圏研究所）、國中均（JAXA/ISAS）
E-mail: usui@rish.kyoto-u.ac.jp

1. まえがき

我々は、プラズマ粒子シミュレーション[1)]を応用して、衛星表面の金属-誘電体間に生じる部分帯電の解析、及びその緩和手法の検討を行っている。特に、極軌道衛星に着目しており、オーロラ電流による KeV オーダーの帯電[2)]や、太陽パネル表面のガラス部と衛星金属筐体の間に生じる部分帯電[3)]の緩和プロセスを調べる。帯電緩和の手法はさまざまな方法[4)]が提案されているが、今回は、衛星から人工的にプラズマを放出するプラズマコンタクタ[5)]の利用を想定している。部分帯電では、誘電体に電荷が貯まることにより、金属-誘電体間に電位差が生じる。このため、部分帯電を緩和するには誘電体上の蓄積電荷量を制御する必要がある。衛星表面放電で一番問題となるのは衛星本体より誘電体の電位が高い、いわゆる逆電位勾配と呼ばれる状態では、通常 400V 程度の電位差で放電が起こる。ちなみにその逆の状態である順電位勾配では数 kV 程度までは放電しない。これは、逆電位勾配の時、太陽パネルの構造によりトリプルジャンクションが生じるためである。この部分帯電を緩和するために、衛星の金属部分にプラズマ放出口を設け、人工プラズマを放出する。本研究では、この人工プラズマ放出により太陽パネル上の部分帯電緩和の様子を詳細に解析する。本研究によって得られる結果は、地球観測衛星に代表されるような極軌道衛星搭載用のプラズマコンタクタに必要とされる性能や設置場所、個数を検討する上での基礎資料となる。

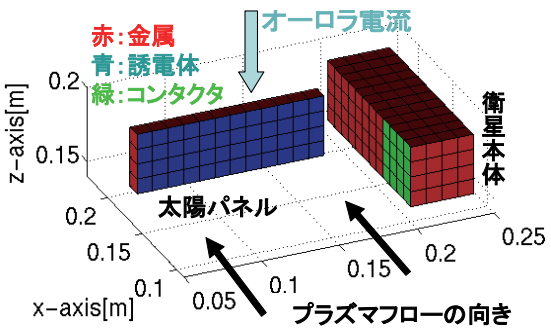

図 1　シミュレーションモデル

2. シミュレーションモデル

極軌道（PEO: Polar Earth Orbit）においてオーロラ電流が存在し、衛星本体が約-50Vまで帯電した場合について、衛星に取り付けたプラズマコンタクタからプラズマ放出を行い衛星の部分帯電の緩和現象について調べた。人工衛星モデルは図 1 に示すように衛星の本体となる直方体と太陽パネルである薄い直方体の羽が 1 枚あり、それらが電気的に繋がっているモデルを用いた。等温プラズマである電離層プラズマの中を衛星が進んでいる状況を想定した。シミュレーションでは衛星から見た系を考え、モデル空間の中心に衛星があり、宇宙プラズマがシミュレーション空間中を移動しているものとした。今回は、計算機資源の節約のため、全体が数十センチの非常に小さな衛星モデルを採用した。図 1 において、赤が金属部分、青が太陽パネルの誘電体部分を示している。誘電体面はプラズマフローのラム側にあり、プラズマコンタクタは衛星本体の側面、緑で示される部分に取り付けてあり、ここから人工プラズマを放出する。また、オーロラ電流は水色で示される通りプラズマフローとも誘電体面とも直交する向きで衛

星方向に流れている。その密度は背景プラズマ密度 $2.5\times10^{10}m^{-3}$ の 1/10 倍とし、温度、ドリフトエネルギーがそれぞれ 20eV、100eV となるように設定した。放出する電子は、背景プラズマと同じ温度 0.5eV を持ち、背景プラズマ密度の 10 倍の密度となるように設定した。また、放出プラズマは衛星内部のプラズマ生成室で生成されているものとした。このモデルを用いて衛星帯電緩和に関するシミュレーションを行った。3-1 節では電子のみを放出する場合を考え、3-2 節では、電子と伴にイオン放出も行う場合を検討した。

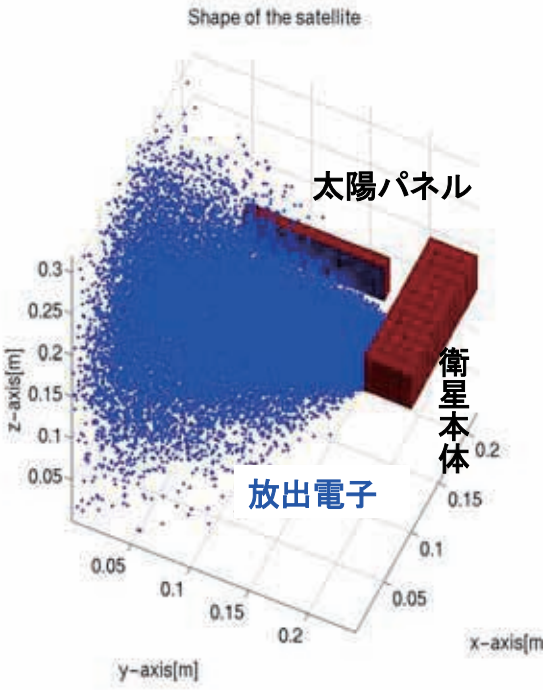

図 2：コンタクタからの放出された電子の様子

3.　部分帯電緩和現象の解析

3-1. プラズマコンタクタからの熱電子放出

上述のモデルを用い、プラズマコンタクタから熱電子が放出される場合について衛星帯電の変化を観測した。本実験では、衛星が浮遊電位に落ち着いている状態（時刻 0）から電子放出を開始し、その後の衛星電位および衛星流入電流の時間変化を調べた。図 2 は、コンタクタから放出される電子の様子を示したものである。

図 3 に衛星電位、衛星の金属部および誘電体部における各プラズマ電流成分の時間変化を示す。図 3-(a)の縦軸の電位は宇宙プラズマの空間電位を基準に 0V とし、赤が金属部の電位、青が太陽パネル上の誘電体部の電位を示している。図 3-(b),(c)にはそれぞれ衛星金属筐体部および太陽パネルの誘電体部に流入する電流量の時間変化を粒子種毎に示す。 図 3-(a)からわかるよ

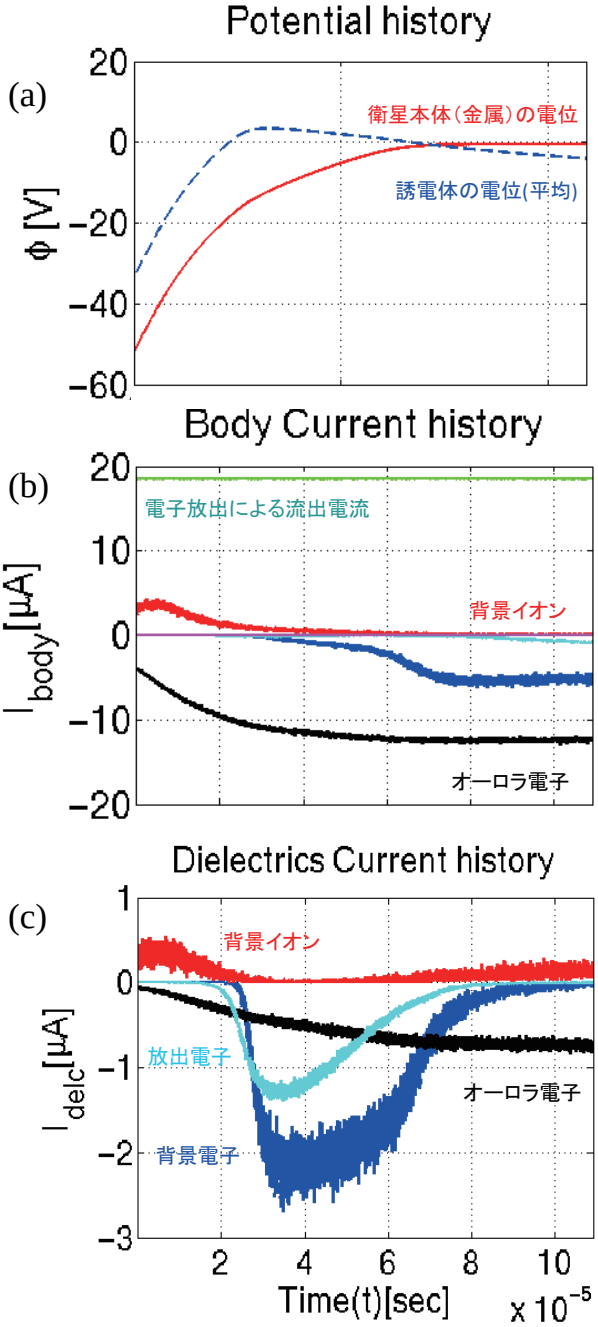

図 3：(a) 衛星電位、(b) 衛星の金属部および(c)誘電体部における各プラズマ電流成分の時間変化

うに、最初、衛星本体および太陽パネルの誘電体面はそれぞれ-50V, -30V 程度に帯電している。まず衛星筐体金属部の電位変化（図 3-(a)の赤線）に着目する。コンタクタからの電子放出（図 3-(b)の緑色の線）により衛星電位が上昇する。この電位上昇に伴い、図 3-(b)に示すように衛星筐体への背景イオン流入（赤線）が減少し、オーロラ電子による電流（黒色）および背景電子（青色）の流入が増大する。最終的には、電子放出による電流量と流入電子による電流量が釣り合って安定電位にむかう。この場合、背景イオン電流の寄与は少ない。

次に、太陽パネル上の誘電体部の電位変化について図 3-(c)の電流図と関連付けて述べる。2×10^{-5}(s)の時間までは、衛星本体に引きずられ誘電体部の電位も上昇するが、一旦、プラズマ電位より上になると、それを緩和するために放出電子、背景電子、オーロラ電子の流入により誘電体電位は再び下がり始める。電位降下によりこれらの電流量は時間と伴に減少していき、図では示されていないが、最終的には、誘電体表面での背景イオン、オーロラ電子の釣り合いによって電位が安定する。すなわち、シミュレーション開始時の電位になる。

まとめると、電子放出によって衛星筐体の電位緩和は可能であるが、部分帯電の原因である誘電体部電位の緩和には寄与できないことがわかった。ただし、本実験では、2 次電子放出を考慮していないため誘電体面では負の電位になるが、2 次電子放出を考慮すると電位の上昇が考えられる。この点については今後の課題とする。

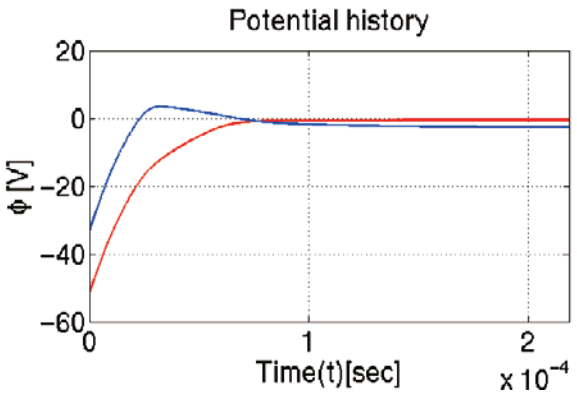

図 4: プラズマ放出時の衛星電位の時間変化。金属部、誘電体部の電位はそれぞれ赤色、青色。

3-2. プラズマコンタクタからのプラズマ放出

プラズマコンタクタでのホローカソードプラズマ生成を仮定し、電子のみならずイオンの熱温度放出も同時に行った。図 4 に衛星筐体金属部および太陽パネル誘電体部の電位の時間変化図をそれぞれ赤色、青色の線で示す。図に示すように、6×10^{-5}(s)の時間までは衛星電位がプラズマ電位より低いため、放出イオンは衛星外部には出ない。そのため、衛星電位変化は、図 3 で示した電子のみ放出の場合とほぼ同じである。しかし、一旦金属部がプラズマ電位に緩和され、誘電体部が元の負電位に戻ろうとする際には、放出イオンのフラックスが誘電体に流入し、図 4 に示されたように、結果としてその電位はプラズマ電位とほぼ同じになる。背景イオンに加え放出イオンがあるために表面電位を決定する電流バランス条件が変化したためである。図 5 は 1×10^{-4}(s)における放出イオンの密度分布を表している。密度は背景プラズマの平均密度 N_0 で規格化されている。図からわかるとおり、放出イオンは太陽パネルの誘電体部に流入しており、これにより誘電体部の電位の低下を回避している。すなわち、本ケースでは部分帯電緩和が実現されている。

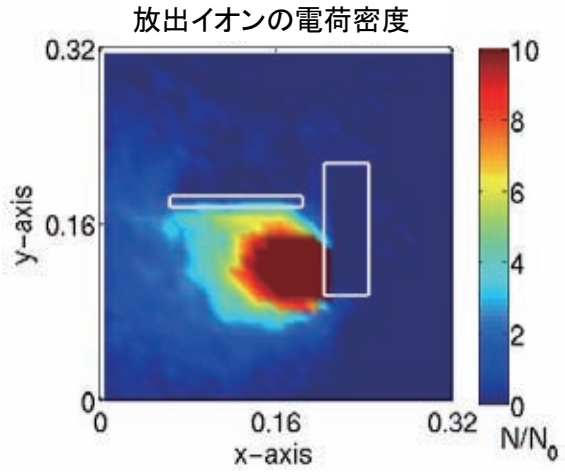

図 5: 太陽パネル上の誘電体部に流れる放出イオン

3-3. 放出プラズマダイナミクスと衛星環境への影響

図２に示したが、負に帯電している衛星本体から電子を放出すると、衛星近傍に形成されたシース内における強い電界により電子は衛星本体から外向きに加速を受ける。この電子加速は衛星の浮遊電位エネルギー程度であり、加速された電子は地球磁場の影響でサイクロトロン運動する。本ケースではそのジャイロ半径が数メータであり、衛星の大きさよりも大きいため、加速電子が衛星に戻ってくる可能性は低いが、実際の数メータオーダーの衛星であれば、放出電子が地球磁場の影響により衛星に戻ってくる可能性がある。ただし、電子の加速方向と地球磁場の方向が垂直でない場合は磁場方向に電子が拡散するため、直接衛星に戻ってくる可能性は少ないと考える。ただし、この場合、磁力線に沿った高速電子流がパルス的に流れるため、それによるビームプラズマ不安定性の可能性があり、それによる衛星近傍での電界擾乱やそれによる２次的な電子加熱などが生じる可能性はある。

4. まとめ

本研究では、極軌道においてオーロラ電流によって人工衛星の電位が大きく下がる状況をシミュレーション空間内に再現し、プラズマコンタクタによる衛星の絶対・部分帯電の緩和現象を調べた。

まず、絶対帯電緩和については、電子放出が有効であることを示した。放出された電子は、衛星近傍のシース領域の電界で加速され衛星からは電子ビームとして離れる。今回示さなかったが、放出電子量が多い場合、帯電緩和はすばやく緩和されることも確認した

また、太陽電池パネル上の誘電体と衛星筐体との間で生じる部分帯電の緩和については、電子放出による絶対帯電緩和が行われる状況のもとでイオン放出による誘電体表面の電荷緩和が有効であることを示した。衛星筐体と違って、誘電体面の電荷は局所的に蓄積されるため、誘電体近傍においてイオン放出を行い、この局所的な電荷の緩和を行う必要がある。

帯電緩和のために放出される電子は、衛星近傍のシース電界によってパルス的に加速を受ける。また、加速電子は地球磁場の影響を受け、サイクロトロン運動のため衛星に戻ってくる可能性がある。また、磁場方向に加速を受けたパルスビームはプラズマ不安定性の原因になる可能性もある。これらの放出プラズマダイナミクスと衛星環境への影響については、今後大規模な計算機シミュレーションにより詳細解析を行う必要がある。

参考文献

[1] H. Matsumoto, and Y. Omura, Computer Space Plasma Physics: Simulation Techniques and Software, Terra Scientific Publishing Co., 1993, chap.2.

[2] Rabin, A.G., Spacecraft charging in the supra-auroral region, Nuclear Science, IEEE Transactions on, Volume 36, Issue 6, Dec 1989 p2015 - 2020

[3] Whipple, E. C., Potential of surfaces in space, Rep. Prog. Phys., 44, p1197-1250, 1981

[4] Lai, Shu T., A Critical Overview on Spacecraft Charging Mitigation Methods, Plasma Science, IEEE Transactions on, Dec. 2003 Volume: 31,Issue: 6, Part 1, p1118- 1124

[5] 竹ヶ原 春貴, 小境 正也, 山極 芳樹, 大西 健夫, 田原 弘一, プラズマコンタクタ, 日本航空宇宙学会誌, 52(602), pp.79-85, 2004

Jason-2搭載
宇宙環境計測装置の開発

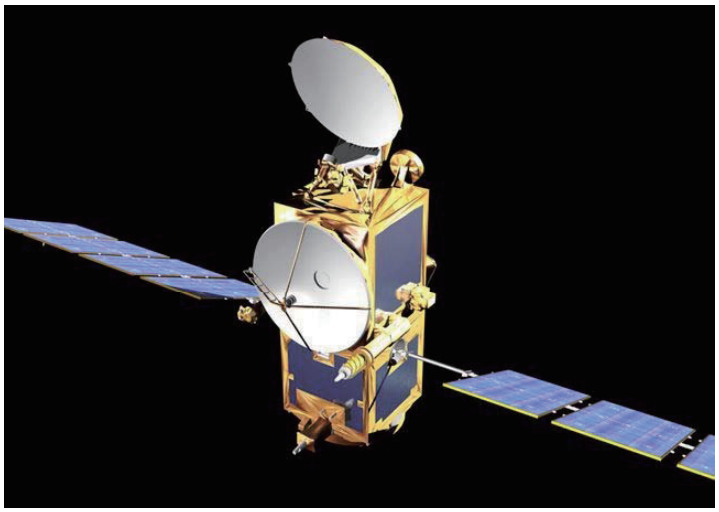

JAXA
総合技術研究本部
環境計測グループ
○込山立人、松本晴久、佐々木康友、五家建夫

2008年1月23日

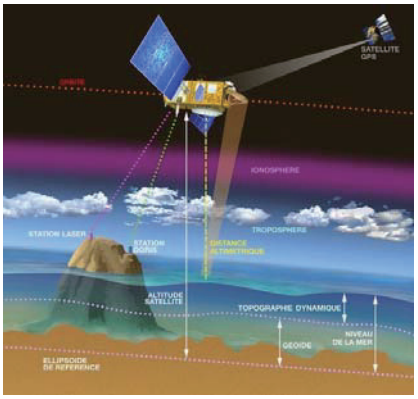

Jason-2の概要

- フランス国立宇宙研究センター（CNES)が開発中の海洋面観測衛星
- CNES、NASA、NOAA、EUMETSATが参加
- 打上げ予定：2008年6月
- 軌道高度：約1300km
- 軌道傾斜角：66°
- ミッション期間：5年

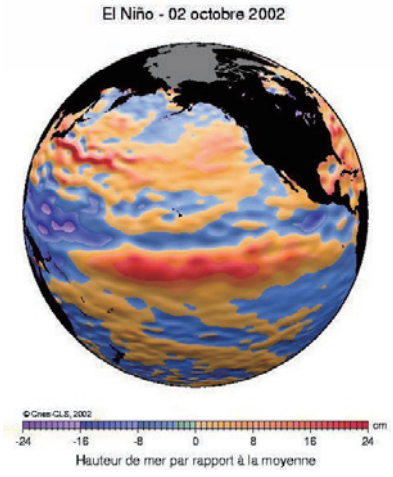

2008年1月23日

Jason-2搭載宇宙環境計測装置（LPT）の目的

- **JAXAは、Jason-2に宇宙環境計測装置(LPT: Light Particle Telescope)を提供。**
- **LPTの目的:**
  - 放射線による出力変動があるミッション機器の校正のため、Jason-2軌道の放射線環境を測定。
  - 宇宙環境データの蓄積。
  - CNES提供の宇宙放射線計測装置（CARMEN2）とのデータ相互交換・相互校正・共同解析によるデータ蓄積。

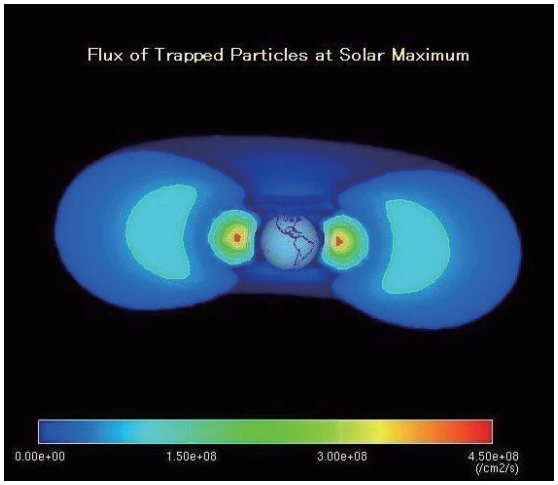

2008年1月23日

Jason-2搭載LPTの目的 (cont.)

宇宙環境データ蓄積・取得計画

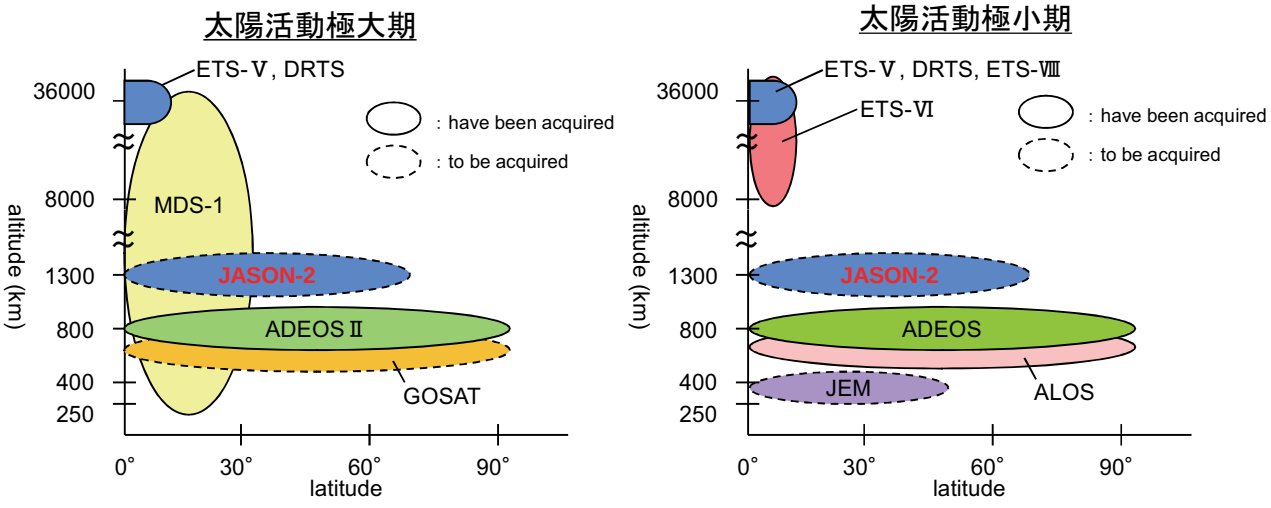

→ これらのデータをもとに宇宙環境モデルを開発し、ISOに提案。

2008年1月23日

Jason-2搭載LPTの開発スケジュール

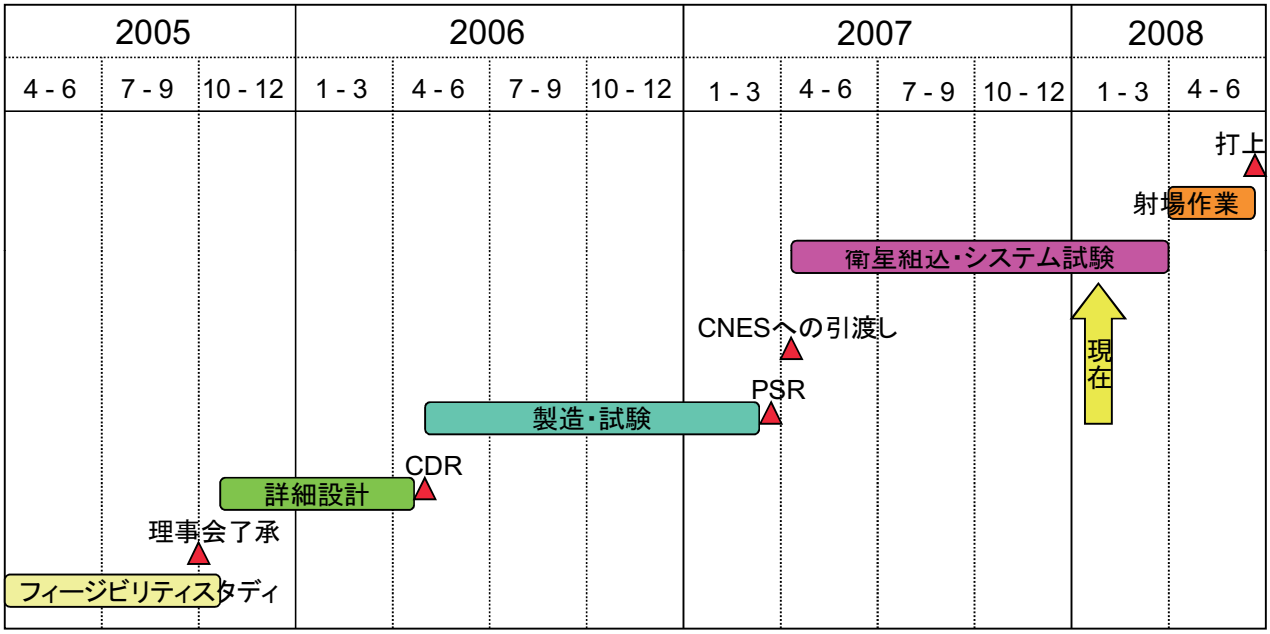

2008年1月23日

Jason-2搭載LPTの状況

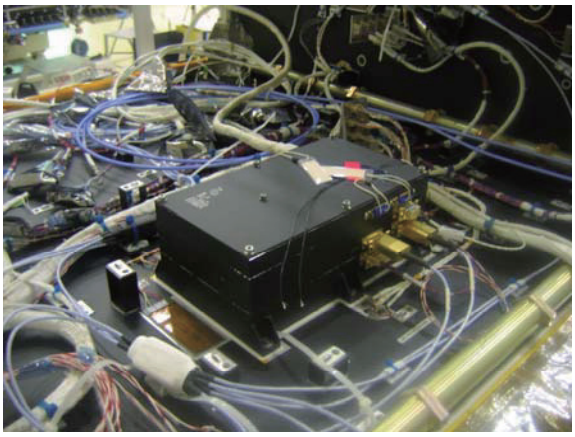

2008年1月23日

Jason-2搭載LPTの概要

LPT-E

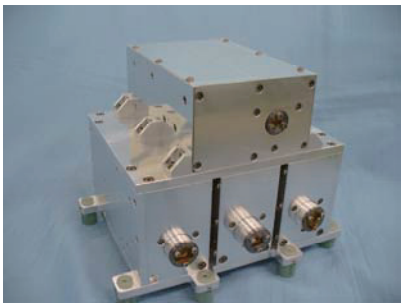

LPT-S

- LPT-E：電気処理部
- LPT-S：センサ部
- 外形寸法：
  - LPT-E：240 ×165 × 93 mm
  - LPT-S：216 × 182 × 175 mm
- 重量：
  - LPT-E：2.86 kg
  - LPT-S：6.19 kg
- 電力： 最大16.5W 通常15.5W
- 電子、陽子、重水素、三重水素、^{3}He、^{4}Heのエネルギー分布を1秒間の時間分解能で取得。

2008年1月23日

Jason-2搭載LPT ブロックダイアグラム

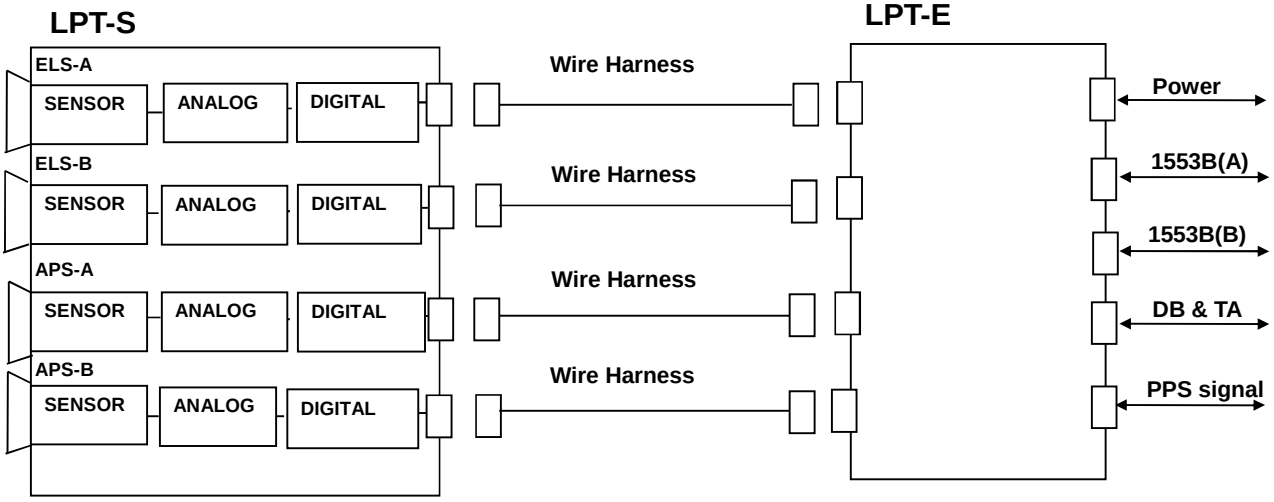

2008年1月23日

Jason-2搭載LPT　計測粒子・エネルギー範囲

計測エネルギー範囲（設計値）

- ELS-A:
  30keV - 1.3MeV　電子
- ELS-B
  0.28MeV - 20MeV 電子
- APS-A
  0.4MeV - 37MeV 陽子
  0.75MeV/n - 40MeV/n ^{4}He
- APS-B
  1.5 MeV - 250MeV 陽子
  2.5 MeV/n - 100MeV/n ^{4}He

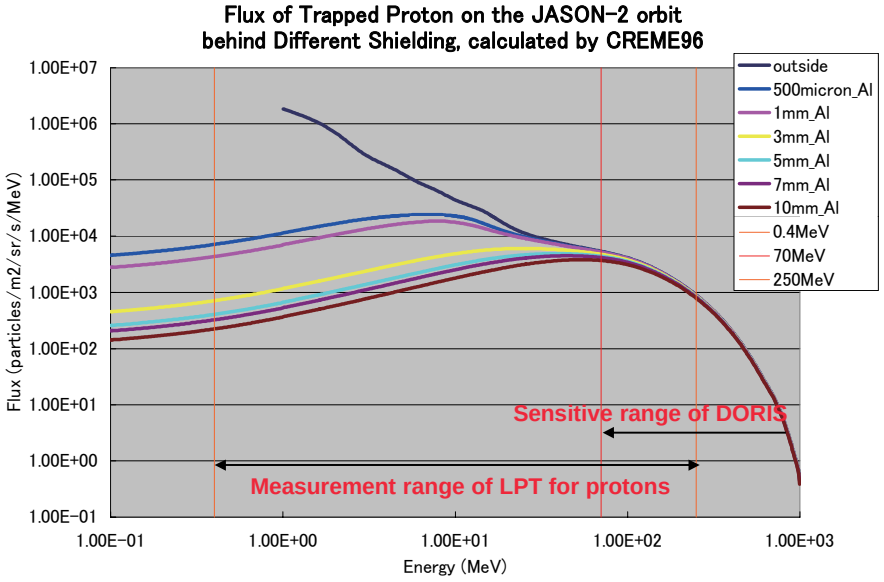

2008年1月23日

Jason-2搭載LPT　センサ機能ブロックダイアグラム

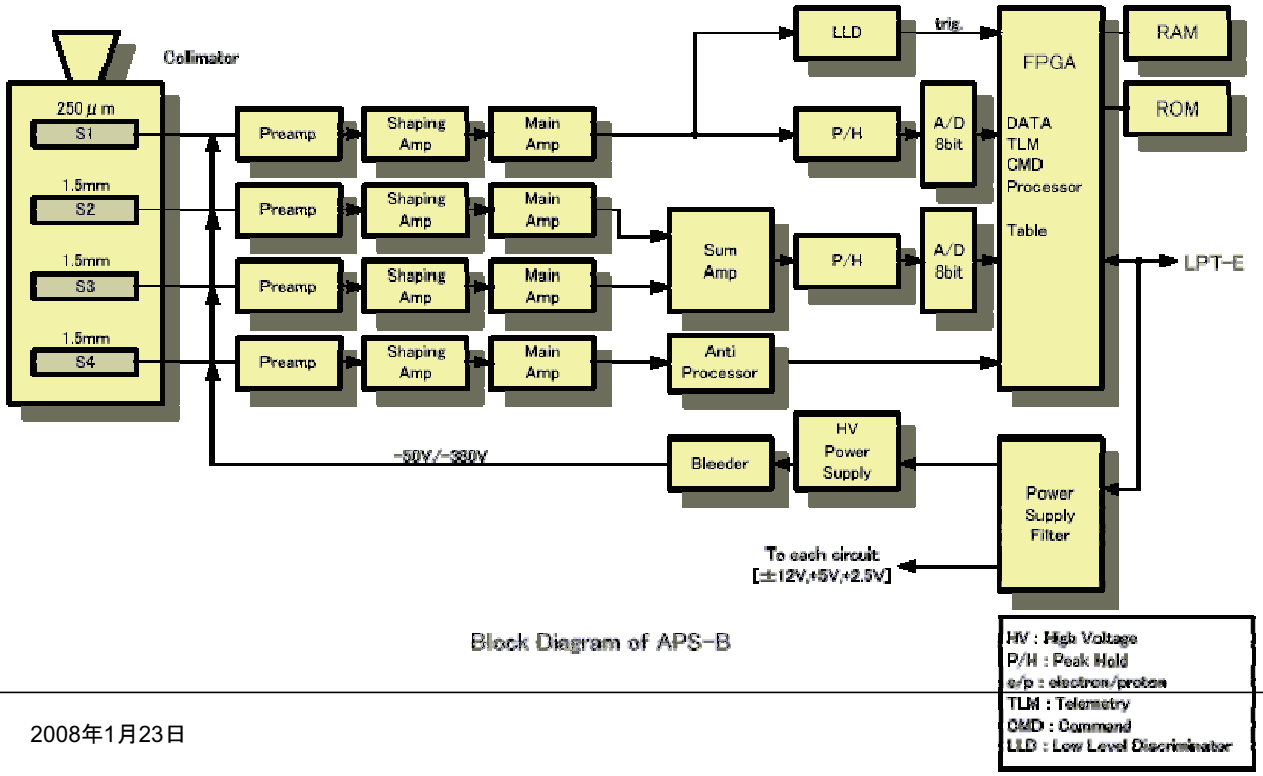

Block Diagram of APS-B

2008年1月23日

Jason-2搭載LPT　粒子計測・弁別原理

APS-B

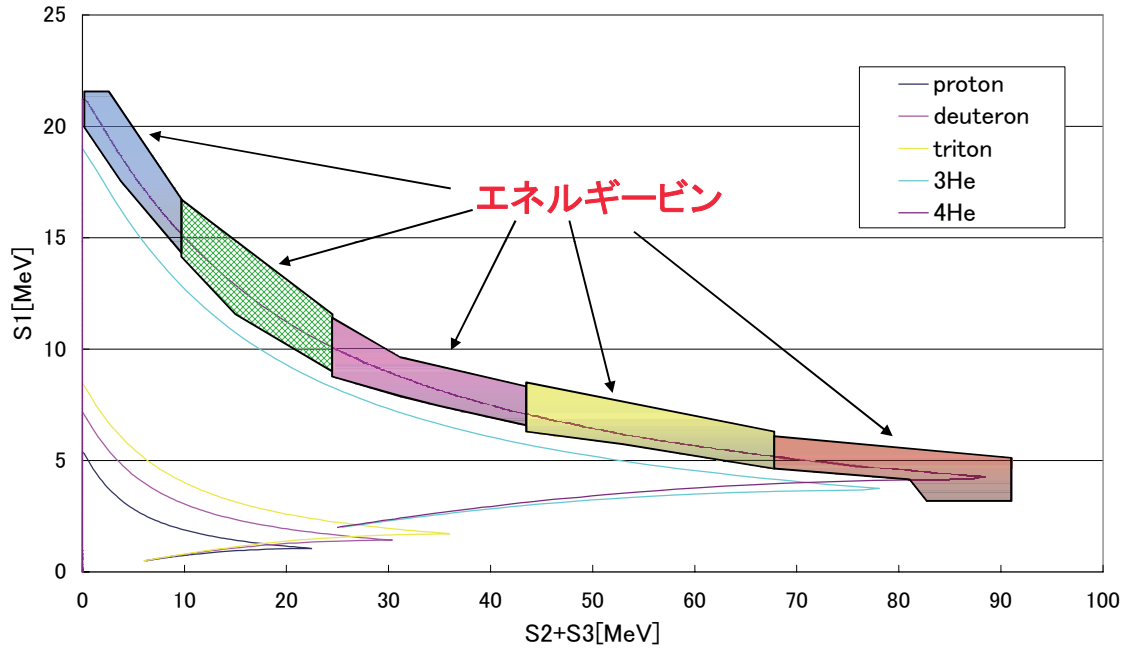

2008年1月23日

Jason-2搭載LPT　各センサのエネルギービン数

Sensor	Particle	No. of Energy BIN
ELS-A	electron	21
ELS-B	electron	14
APS-A	proton	20
	deuteron	5
	triton	3
	^{3}He	4
	^{4}He	16
	上記以外	1
APS-B	proton	12
	deuteron	6
	triton	3
	^{3}He	6
	^{4}He	10
	上記以外	1

2008年1月23日

エネルギービン内の粒子エネルギー分布の推定

- **目的**
  - 各エネルギービンの設定のため。
  - データユーザの詳細解析を可能にするため。
- **次の順序で実施**

① 電気校正試験／照射試験により各検出器の（ADCのチャンネル）対（検出器内に粒子が落としたエネルギー）関係を把握する。

② ①の結果と各センサの幾何形状を用いて、各センサに単一エネルギーの粒子を等方的に入射させたときの検出器応答を計算する。その際入射エネルギーを粒子、センサごとに15～95点程度種々変えて計算する。

③ ②の結果を用いて、各ビンへ入る粒子のスペクトルを計算するとともに、照射試験で取得したスキャッタープロットも併せて考慮することにより、エネルギービンを設定する。

2008年1月23日

エネルギービン内の粒子エネルギー分布の推定　①

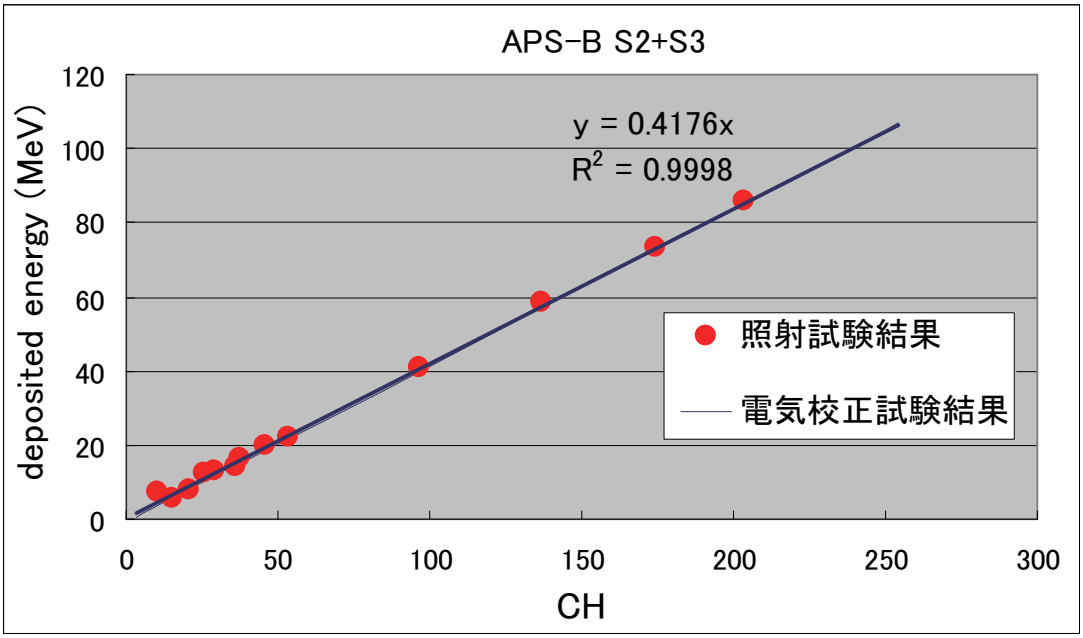

2008年1月23日

エネルギービン内の粒子エネルギー分布の推定

- 次の順序で実施

① 電気校正試験／照射試験により各検出器の（ADCのチャンネル）対（検出器内に粒子が落としたエネルギー）関係を把握する。

② ①の結果と各センサの幾何形状を用いて、各センサに単一エネルギーの粒子を等方的に入射させたときの検出器応答を計算する。その際、入射エネルギーを粒子、センサごとに15～95点程度種々変えて計算する。

③ ②の結果を用いて、各ビンへ入る粒子のスペクトルを計算するとともに、照射試験で取得したスキャッタープロットも併せて考慮することにより、エネルギービンを設定する。

2008年1月23日

エネルギービン内の粒子エネルギー分布の推定②

- **放射線計算シミュレーションコード PHITS**
  - PHITS： Particle and Heavy Ion Transport code System
  - 高度情報科学技術研究機構（RIST)、東北大学、日本原子力研究開発機構（JAEA)が共同で開発。
  - 光子・電子・陽子・中性子から重イオンまで3次元でモンテカルロシミュレーションが行えるコード。
    - NASAの重イオン計算シミュレーションコード（HZETRN）が1次元しか扱えないのに比べ、大きなメリット。

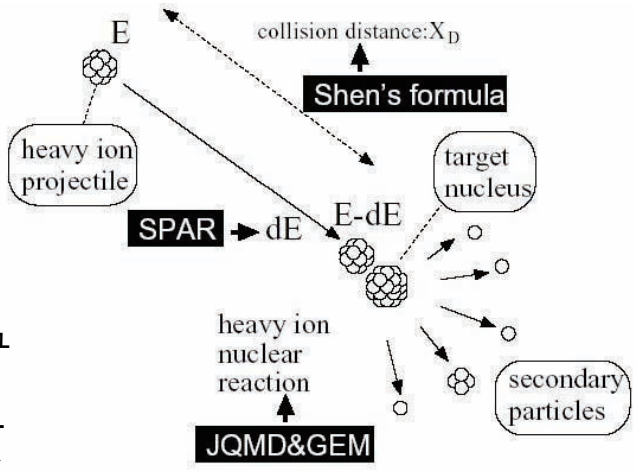

2008年1月23日

エネルギービン内の粒子エネルギー分布の推定②

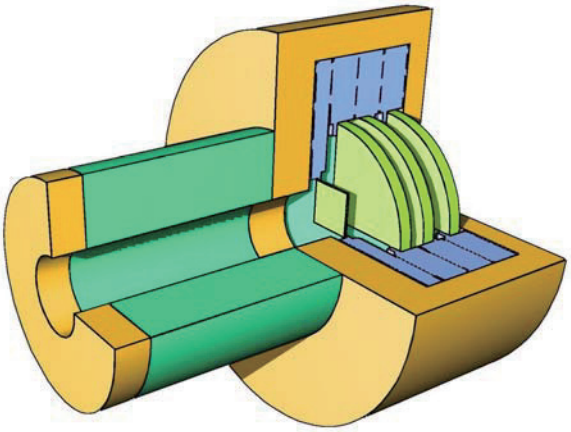

APS-B 計算シミュレーション幾何形状

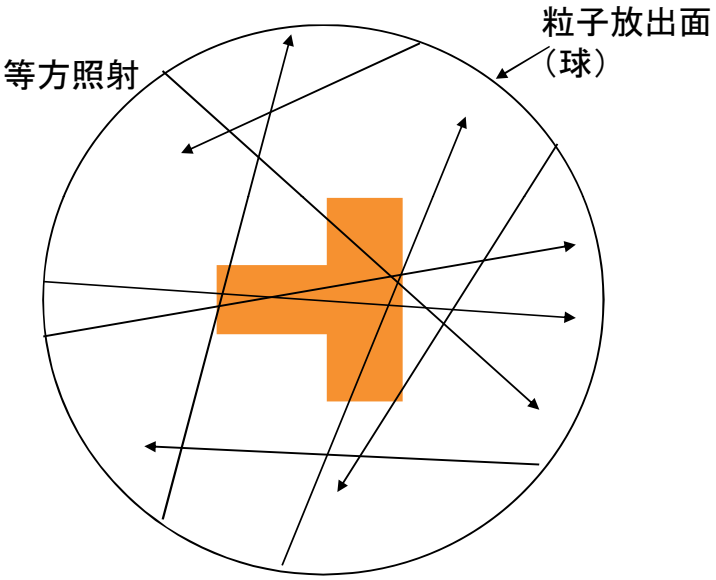

2008年1月23日

エネルギービン内の粒子エネルギー分布の推定②

APS-Bに^{4}He 14.0MeV/nを入射したときの検出器応答

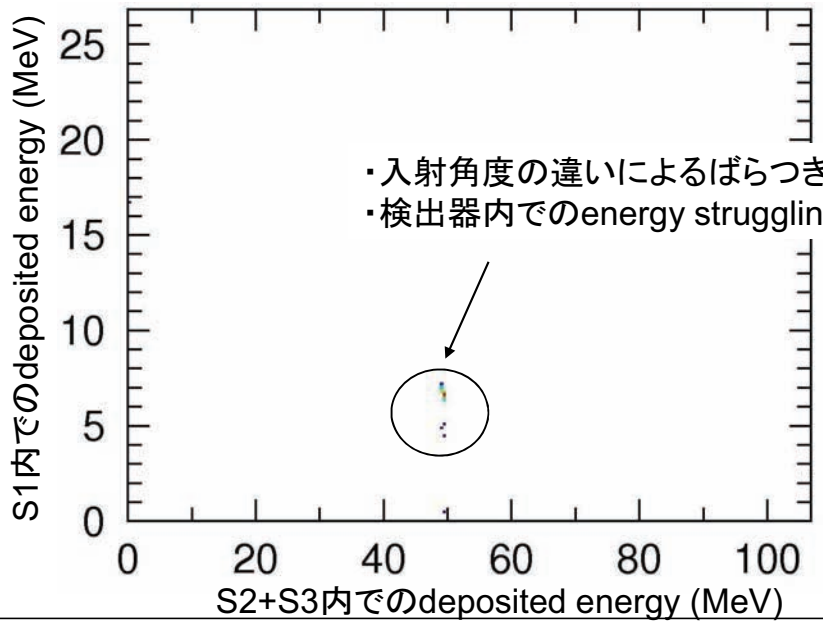

・入射角度の違いによるばらつき
・検出器内でのenergy struggling によるばらつき 等

2008年1月23日

エネルギービン内の粒子エネルギー分布の推定

- 次の順序で実施

① 電気校正試験／照射試験により各検出器の（ADCのチャンネル）対（検出器内に粒子が落としたエネルギー）関係を把握する。

② ①の結果と各センサの幾何形状を用いて、各センサに単一エネルギーの粒子を等方的に入射させたときの検出器応答を計算する。その際、入射エネルギーを粒子、センサごとに15～95点程度種々変えて計算する。

③ ②の結果を用いて、各ビンへ入る粒子のスペクトルを計算するとともに、照射試験で取得したスキャッタープロットも併せて考慮することにより、エネルギービンを設定する。

2008年1月23日

エネルギービン内の粒子エネルギー分布の推定③

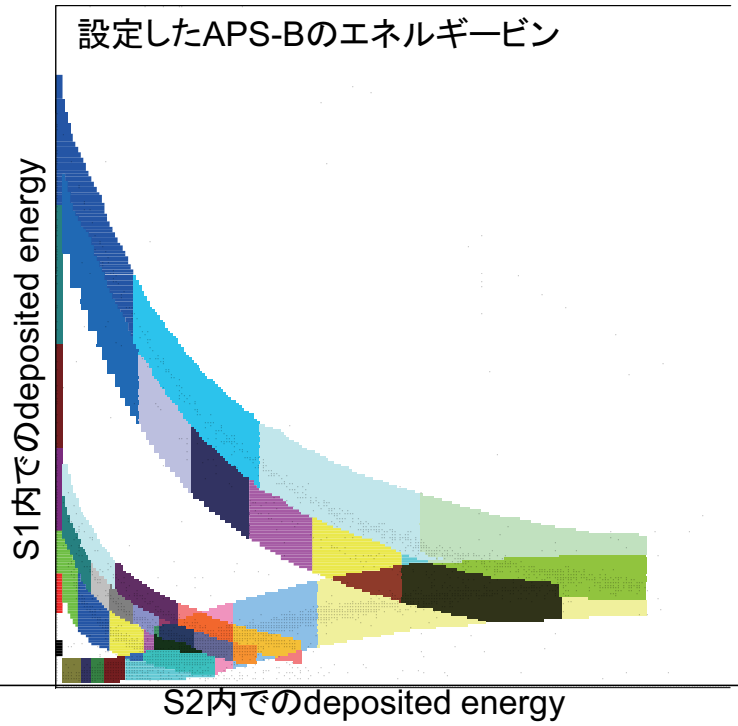

2008年1月23日

エネルギービン内の粒子エネルギー分布の推定③

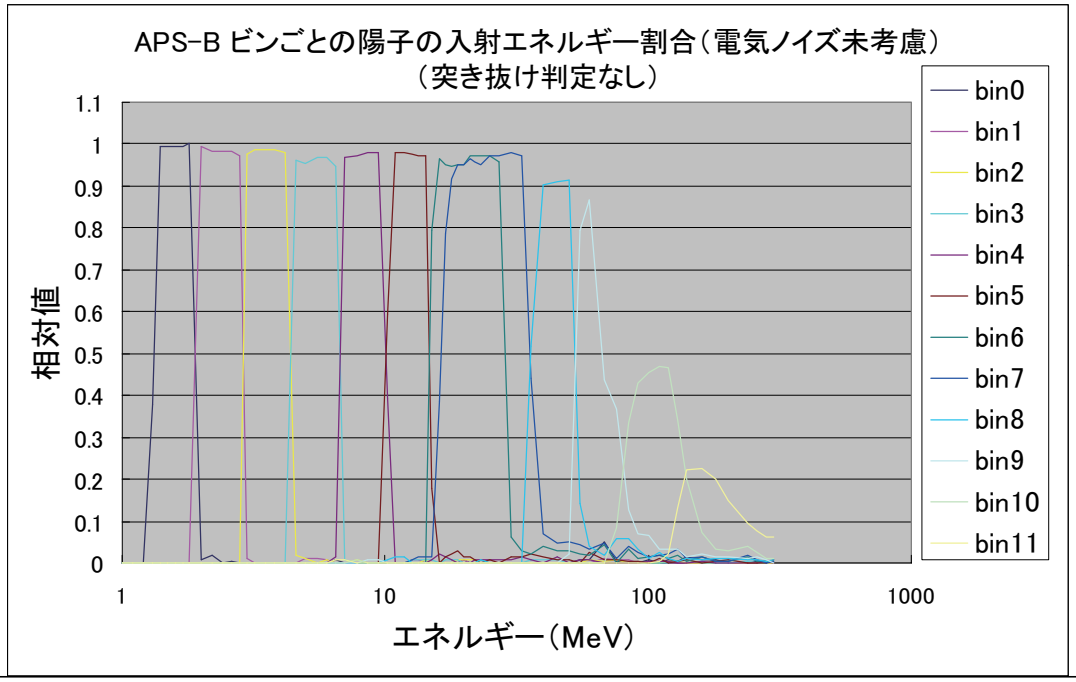

2008年1月23日

まとめ

- **Jason-2搭載用の宇宙環境計測装置（LPT）を開発し、CNESに引渡した。LPTは現在、順調にシステム試験中であり、2008年6月打上げ予定。**
- **エネルギービン設定とデータユーザの詳細解析に資するため、各エネルギービンに入る粒子のエネルギー分布を計算した。今後、電気ノイズ等を考慮し、各ビンに入る粒子のエネルギー分布を精査する。**

2008年1月23日

GOSAT搭載技術データ取得装置の開発

宇宙航空研究開発機構　総合技術研究本部　環境計測グループ
五家　建夫、松本　晴久、○佐々木　康友

第4回　宇宙環境シンポジウム
平成20年1月23日

技術データ取得装置の目的

- 温室効果ガス観測技術衛星(GOSAT)
  - 軌道高度：　666km
  - 軌道傾斜角：　98°
  - ミッション期間：　5年

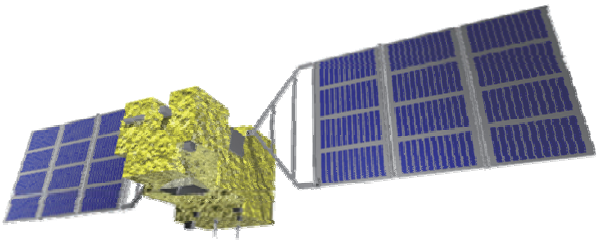

- 技術データ取得装置(TEDA)の目的
  - GOSATに搭載される高速、高機能、大容量半導体デバイスに誤動作や故障が生じた場合に、誤動作や故障の原因が宇宙環境によるものかどうかの切り分けを行うためのデータを取得する。
  - 宇宙機設計に必要な放射線モデルを改良するためのデータを取得する。

開発状況

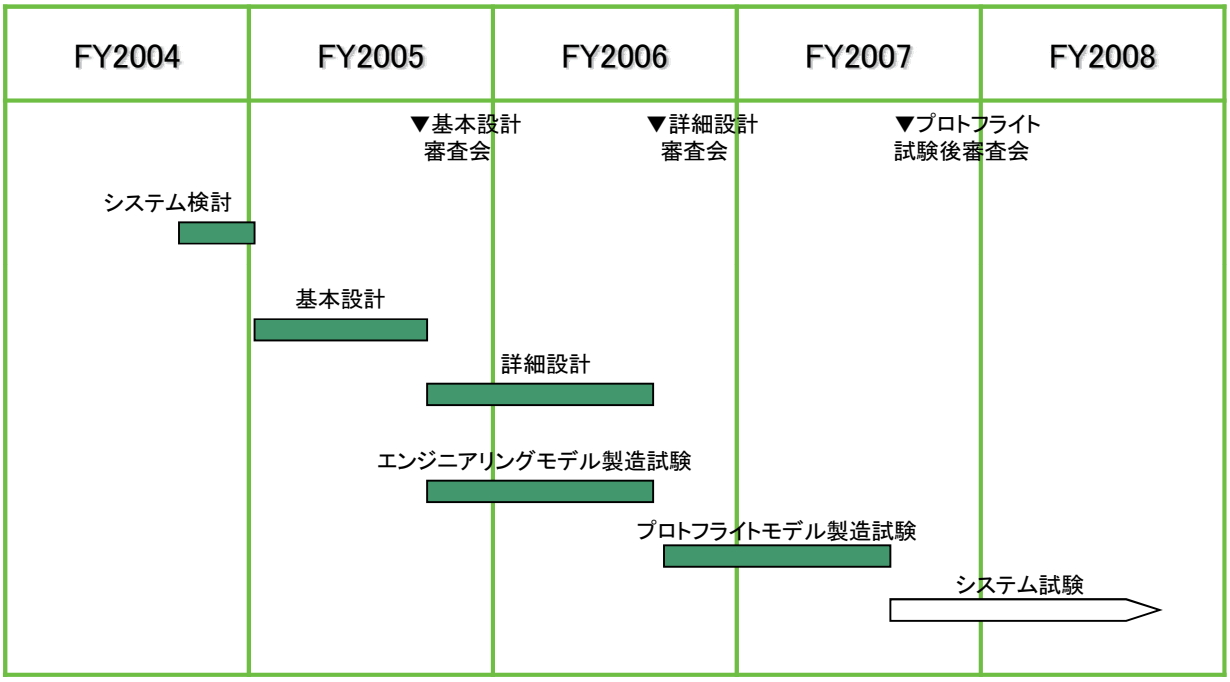

装置の構成

- 技術データ取得装置は、以下の放射線観測装置で構成されている。
  - □軽粒子観測装置(LPT)
    質量の小さい粒子(電子、陽子、ヘリウム)を観測する。
  - □重イオン観測装置(HIT)
    質量の大きい粒子(重イオン)を観測する。

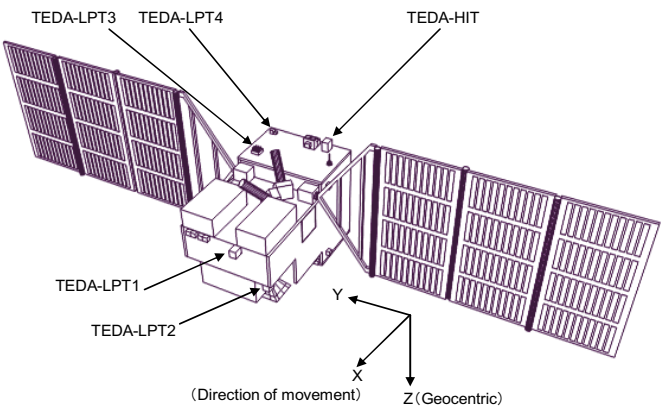

観測装置の搭載位置

軽粒子観測装置(LPT)

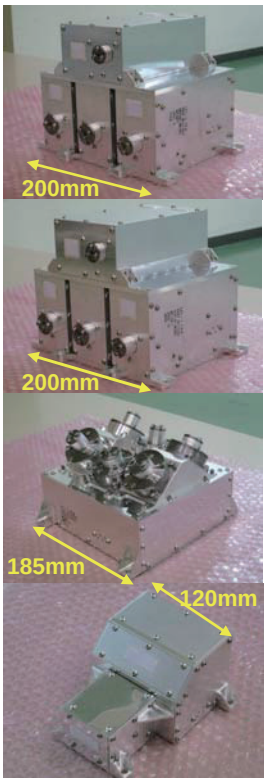

- 電子、陽子、重陽子、三重陽子、ヘリウム3、ヘリウム4を弁別し、エネルギーを計測する。
- LPTはシリコン検出器とシンチレータから構成される5種類のセンサユニットから構成される。

	LPT-1	LPT-2	LPT-3	LPT-4
低エネルギー電子観測センサ(ELS-A)	○	○	○	
高エネルギー電子観測センサ（ELS-B)	○	○		
低エネルギーアルファ陽子観測センサ(APS-A)	○	○	○	
中エネルギーアルファ陽子観測センサ(APS-B)	○	○		
高エネルギーアルファ陽子観測センサ(APS-C)				○

- 合計質量： 13kg
- 合計電力： 22W

軽粒子観測装置(LPT)

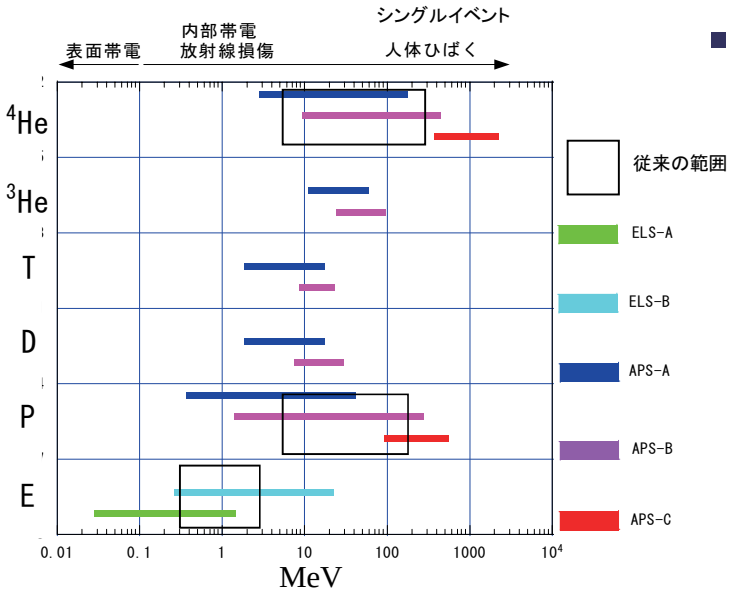

LPTの観測範囲

- 高性能の検出器と低ノイズの回路系をもつ5種類のセンサユニットを組み合わせることにより観測範囲を従来よりも大幅に拡大した。
  - 電子：0.03MeV - 20MeV
  - 陽子：0.4MeV - 500MeV
  - He4：0.8MeV/n～500MeV/n

軽粒子観測装置(LPT)

捕捉放射線の最悪環境、ピッチ角分布(*)、更に太陽フレアの際に発生する粒子の影響を計測するように視野を設定した。

(*)ピッチ角：　地磁気の方向と粒子の運動方向とのなす角

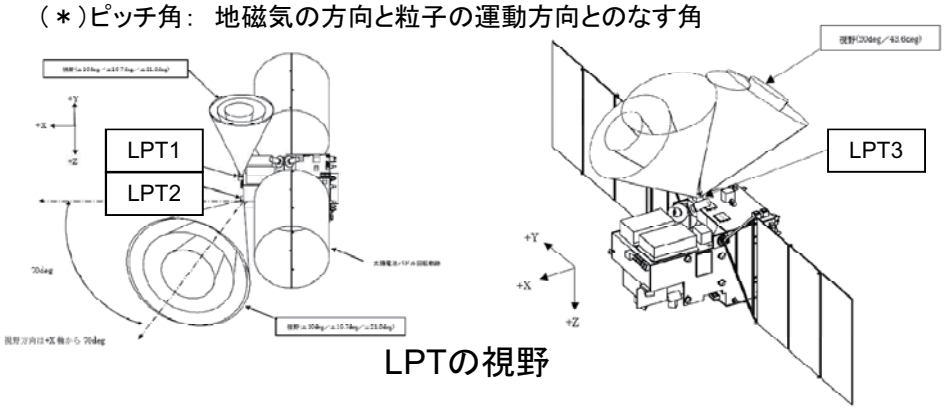

LPTの視野

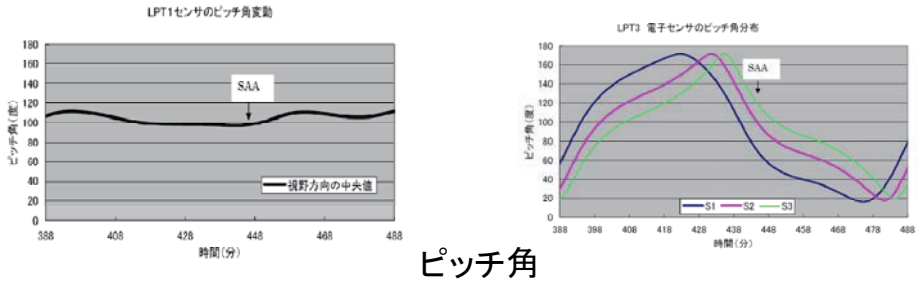

ピッチ角

重イオン観測装置(HIT)

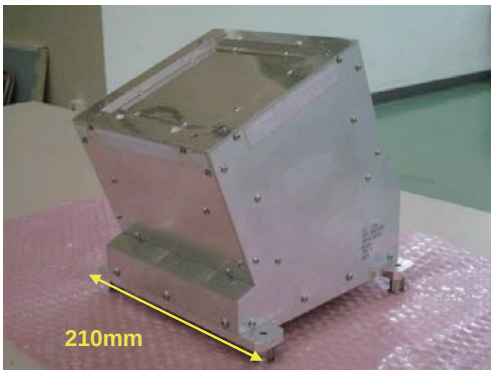

- 重イオン(He～Fe)の核種、エネルギー、入射方向を計測する。
  - He：7MeV/n　～　48MeV/n
  - Li:　8.5MeV/n　～　56MeV/n
  - C:　13MeV/n　～　90MeV/n
  - O:　16MeV/n　～　106MeV/n
  - Fe:　28MeV/n　～　201MeV/n
- MDS-1, ALOS搭載装置をベースに部品実装方法の改良、回路構成の簡素化により小型軽量化した。
- 質量：　4kg
- 電力：　6W

重イオン観測装置(HIT)

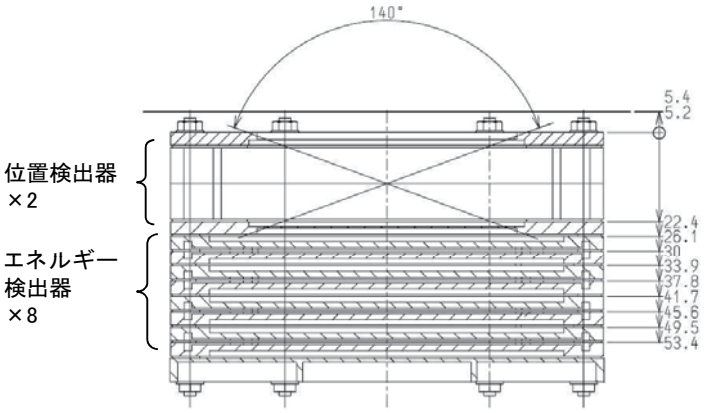

HIT検出部の断面図

- 検出部の構成
  - 二次元位置検出器×2枚
  - エネルギー検出器×8枚
- 観測方式： ΔE×E法
- 各検出器の出力値をテレメトリとして取得しデータ処理する。
- 統計的に精度の高いデータを取得するため、従来の装置よりも幾何学的効率を大きくした。
  - Gファクタ： 60cm^2・sr
  - 従来よりも有感領域の厚い(1.5mm)の半導体検出器を新たに開発し、検出器の個数を減らし、センサ長を短くした。

試験内容

- 照射試験
  - 宇宙環境計測実験室： 電子30～900keV
  - 放医研： He4 25MeV/n、C 430MeV/n、Fe 500MeV/n
  - 理研： 陽子 210MeV, He4 135MeV/n
  - 筑波大学： 陽子 4～20MeV
- プロトフライト試験
  - 初期性能試験
  - 電磁適合性試験
  - 振動衝撃試験
  - 熱真空試験
  - 最終性能試験

照射試験の結果（1）

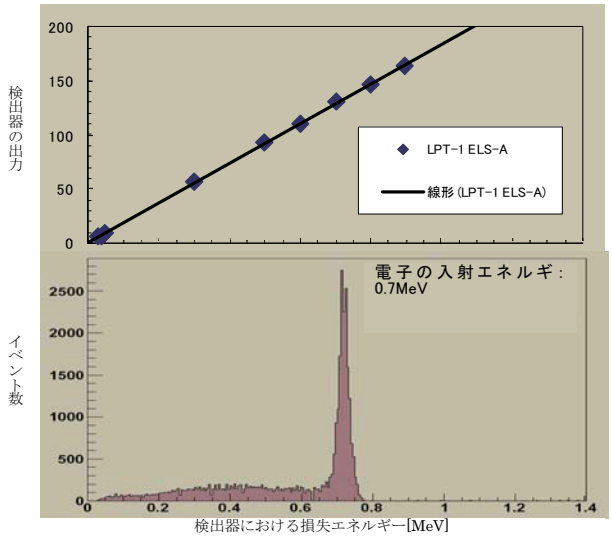

- LPTの試験結果の例として、ELS-Aの電子30keV～900keVの照射試験結果を左図に示す。
- 粒子に対する応答の直線性、分解能が良好であることを確認した。
- その他のセンサユニットの性能についても同様に確認した。

照射試験の結果（2）

- HITの照射試験結果を下図に示す。
- 位置検出器とエネルギー検出器について粒子に対する応答の直線性、分解能が良好であることを確認した。

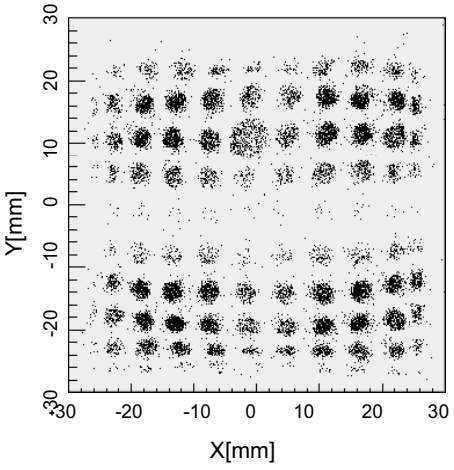

位置検出器の検出パターン

Fe 110MeV/nを6mm間隔の格子状コリメータを通して照射

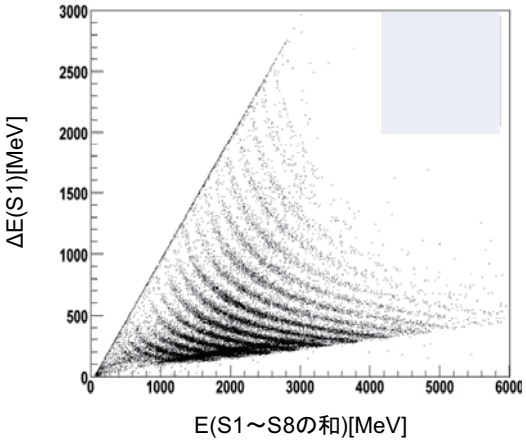

エネルギー検出器のデータ

Fe 500MeV/nの破砕粒子を照射

まとめ

- GOSAT搭載技術データ取得装置は、単体での試験を完了し、目標とする機能性能を満足し、フライト品としての品質を有していることを確認した。
- 今後、衛星システムに組み込まれて、電気試験及び環境試験が実施される。

－ＭＥＭＯ－

付録・講演プログラム

第4回 「宇宙環境シンポジウム」 プログラム

日時:2008年1月22日(火)、23日(水)
場所:日本科学未来館 7階 会議室2
主催:宇宙航空研究開発機構 総合技術研究本部 環境計測グループ
協力:九州工業大学、地球磁気圏・地球惑星圏学会 宇宙飛翔体環境研究分科会、情報通信研究機構
※ 講演時間 特別講演:25分(講演18分＋質疑応答7分) 一般講演:15分(講演12分＋質疑応答3分)
但し、一部の講演は異なる

1月**22**日(火)

13:30 - 13:40
「開会の挨拶」
五家建夫 (JAXA)

特集－世界の宇宙環境の研究最前線－

13:45 - 14:10
「Effects of Low Temperature on Charging of Spacecraft Dielectrics」
○Dale C. Ferguson, Todd A. Schneider, and Jason A. Vaughn (JPL/NASA)

14:10 - 14:35
「Visualizing Root Causes for Satellite Anomalies, Spacecraft Charging, and Mitigation Methods to Prevent ESD」
○Richard Briet (Aerospace Corporation)

14:35 - 15:00
「Spacecraft Plasma Interaction eXperiment in India - an Introductio」
○Suresh Puthanveettil (India)

15:00 - 15:25
「Arcing on Solar Array Surfaces: Ground Tests」
○Boris V. Vayner (GRC/NASA)

15:25 - 15:50
「Space Environment Effects on Thermal Control Materials」
○Weiquan FENG, Yigang DING, Dekui YAN, Xuechao LIU, Wei WANG, Dongmei LI
(Beijing Institute of Spacecraft Environment Engineering)

15:50 - 16:05 休憩

16:05 - 16:30
「Solar Cell R&D activities at ESA」
○Carsten Bauer (ESA)

16:30 - 16:55
「Charge/discharges studies at CNES and ONERA」
○Denis Payan (CNES), Virginie Inguimbert, Jean-Charles.Mateo_Velez (ONERA)

16:55 - 17:15
「Measurement of near Earth Radiation Environment in JAXA -Overview and Plan-」
○Tateo Goka (JAXA)

17:15 - 17:35
「Spacecraft design Guideline in JAXA」
○Kumi Nitta (JAXA), Japanese Spacecraft Design standardization WG1, WG5, WG8

宇宙環境計測・宇宙天気**(1)**

17:35 - 17:50
「Highly Energetic Electron Environment in the Inner Magnetosphere」
○T.Obara (NiCT), H.Matsumoto, K.Koga, H.Koshiishi and T.Goka (JAXA)

17:50 - 18:05
「Statistical Data Analysis of the Aurora Electrons and Thermal Ions for Spacecraft Charging Analysis」
○Takamitsu Hamanaga, Mengu Cho (Kyushu Inst. of Tech.)
18:05 - 18:20
「Electron flux enhancements in the pre-noon sector of GEO」
○Masao Nakamura (Osaka Prefecture Univ.)

18:30 - 20:30 意見交換・交流会

1月23日(水)
帯電・放電実験
9:30 - 9:45
「Threshold measurement of secondary arc on solar arrays for Japanese spacecraft charging guideline」
○Kazuhiro Toyoda, Takayuki Ose, Hirokazu Masui, and Mengu Cho (Kyushu Inst. of Tech.)
9:45 - 10:00
「Metal halide lamps - Simulation of power generating solar arrays for secondary arc investigation
○Andreas Kroier, Teppei Okumura, Kazuhiro Toyoda, Mengu Cho (Kyushu Inst. of Tech.)
and Erich Leitgeb (Graz Univ. of Tech.)
10:00 - 10:15
「ESD Test for Triple-Junction solar cells with monolithic diode 」
○Yukishige Nozaki (NTSpace), Hirokazu Masui, Kazuhito Toyoda, Mengu Cho (Kyushu Inst. of Tech.)
10:15 - 10:30
「Influence of solar cell degradation due to ESD to solar array power generation」
○Teppei Okumura, Kazuhiro Toyoda (Kyushu Inst. of Tech.) Mitsuru Imaizumi (JAXA),
Mengu Cho (Kyushu Inst. of Tech.)
10:30 - 10:45
「Measurement of photoelectron emission characteristic by vacuum ultraviolet ray irradiation」
○Shugo Okamura, Toru Iwao, Motoshige Yumoto (Musashi Inst. of Tech.),
Hiroaki Miyake, Kumi Nitta (JAXA)

10:45 - 11:00 休憩

11:00 - 11:15
「Estimation of volume resistivity of dielectric films under electron irradiation」
○Rikio Watanabe(Musashi Inst. of Tech.), Hiroaki Miyake and Kumi Nitta(JAXA)
11:15 - 11:30
「Experimental measurement of secondary arc plasma parameter on solar array」
○Takayuki Ose, Hirokazu Masui, Kazuhiro Toyoda and Mengu Cho (Kyushu Inst. of Tech.)
11:30 - 11:45
「Plasma and solar array arcing caused by space debris impact」
○Shinya Fukushige, Yasuhiro Akahoshi (Kyushu Inst. of Tech.), Keiko Watanabe (Osaka Univ.),
Toshikazu Nagasaki, Kenshou Sugawara, Takao Koura, Mengu Cho (Kyushu Inst. of Tech.)
11:45 - 12:00
「Preliminary ESD Ground Tests on Meter-Class Solar panels in Simulated GEO Environments」
○Hideto Mashidori, Minoru Iwasa, Atsushi Wada, Kumi Nitta (JAXA)
Masayuki Nomura, Kazuhiro Toyoda (Kyushu Inst. of Tech.)

12:00 - 13:30 昼食

宇宙環境計測・宇宙天気(2)

13:30 - 13:45
「STEREO Data applied to Space Weather Forecasting」
○Tsutomu Nagatsuma, Maki Akioka, Kazuhiro Ohtaka (NiCT)

13:45 - 14:00
「Development of a light weight, large area in-situ impact ionization dust/debris detector」
○Hideo Ohashi, Takayuki Hirai (Tokyo University of Marine Science and Technology),
Sho Sasaki (National Astronomical Observatory of Japan), Hiromi Shibata (Kyoto University)
Ken-ichi Nogami (Dokkyo Medical Unversity) and Takeo Iwai (University of Tokyo)

14:00 - 14:15
「Forecast of high-energy electron flux at geosynchronous orbit using neural network」
○Shinichi Watari (NiCT), Masahiro Tokumitsu (Toyohashi Univ. of Tech.),
Kentarou Tokumitsu (Tokuyama Coleage of Tech.) and Yoshiteru Ishida (Toyohashi Univ. of Tech.)

材料物性

14:15 - 14:30
「Erosion properties of polyimide as a monitoring material of atomic oxygen environment in space (3): Synergistic effect of atomic oxygen and ultraviolet」
○Masahito Tagawa and Kumiko Yokota (Kobe University)

14:30 - 14:35 休憩

以上の発表は英語での発表

以下の発表は日本語での発表

14:35 - 14:50
「衛星用表面材料の光電子放出電流分布の測定」
○岡野拓哉 (埼玉大), 仁田工美 (JAXA), 山納康, 小林信一 (埼玉大)

14:50 - 15:05
「衛星用絶縁材料の真空中における表面抵抗率・体積抵抗率測定」
○小宮山丈行 (埼玉大), 仁田工美 (JAXA), 山納康, 小林信一 (埼玉大)

15:05 15:20
「絶縁体への電子線照射効果の各種分光法による評価」
○廣川紫月, 西川宏之 (芝浦工大), 三宅弘晃 (JAXA)

15:20 - 15:35
「小型表面帯電分布計測システムの開発」
○籾山弘行, 鈴木祥太, 田中康寛, 高田達雄 (武蔵工大)

15:35 - 15:50
「電子線を照射した各種ポリマーの内部帯電現象」
○長澤健一郎, 本城正人, 田中康寛, 渡邉力夫, 高田達雄 (武蔵工大)

15:50 - 16:05 休憩

軌道上観測結果・シミュレーション

16:05 - 16:20
「静止軌道上帯電データ解析・評価の状況」
○古賀清一、上田裕子、五家建夫(JAXA)、八田真児、金正浩(MUSE)

16:20 - 16:35
「宇宙機環境プラズマシミュレータによる「れいめい」電流モニタの校正」
○上田裕子, 村中 崇信 (JAXA), 臼井英之 (京大), 篠原育 (JAXA), 岡田雅樹 (NIPR)

16:35 - 16:50
「だいち衛星(ALOS)軌道に於ける宇宙放射線環境評価」
○丸山健太 (鹿児島大), 越石英樹, 松本晴久, 五家建夫 (JAXA)
16:50 - 17:05
「GEOTAIL衛星より発生した光電子の非対称分布とその原因」
下田忠宏, ○町田忍(京大), 向井利典, 齋藤義文 (JAXA), 笠羽康正 (東北大), 早川基 (JAXA)
17:05 - 17:20
「能動的プラズマ放出による極域衛星帯電緩和に関するPICシミュレーション」
○臼井英之, 今里康二郎 (京大)
17:20 - 17:35
「JASON2搭載技術データ取得装置について」
○込山立人(JAXA)
17:35 - 17:50
「GOSAT搭載技術データ取得装置について」
○佐々木康友 (JAXA)

17:50 - 18:05
総評・閉会

(以上)

宇宙航空研究開発機構特別資料　JAXA−SP−07−030

発　　行　　平成20年3月31日
編集・発行　　宇宙航空研究開発機構
〒182-8522 東京都調布市深大寺東町7-44-1
URL : http://www.jaxa.jp/
印刷・製本　　㈱ビー・シー・シー・

本書及び内容についてのお問い合わせは、下記にお願いいたします。
宇宙航空研究開発機構 情報システム部 研究開発情報センター
〒305-8505 茨城県つくば市千現2-1-1
TEL:029-868-2079　FAX:029-868-2956

本書は再生紙を使用しております。